8.1 Introduction

Stratospheric ozone is known to vary in response to a number of natural factors, such as the seasonal and the 11-year cycles in solar irradiance, the Quasi-Biennial Oscillation (QBO), El Niño Southern Oscillation (ENSO), variations in transport associated with large-scale circulations (*i.e.*, Brewer-Dobson circulation) and dynamical variability associated with the annular modes. Aerosols from volcanic eruptions can also affect stratospheric ozone, although their effects depend on the background atmospheric composition. Ozone observations have demonstrated variations on a large number of spatial and temporal scales. To quantify the impact of anthropogenic perturbations to the ozone layer, and to make reliable projections of future ozone abundances, it is necessary to understand and to quantify the underlying natural ozone variations.

The goal of this chapter is to evaluate how well CCMs simulate natural stratospheric ozone variability, based on our current knowledge of the links between ozone variations and natural forcings. Fundamental questions are:

- Do the models realistically simulate natural ozone variations?
- Which processes are key in determining natural variability in stratospheric ozone?
- Do models that reproduce natural variations in ozone do so because these key processes are well simulated?

The response to these questions will inform the assessment of whether the models simulate natural ozone variations for the correct reasons.

The relative importance of the different sources of natural variability in stratospheric ozone is assessed here primarily by means of multiple linear regression analyses. When possible, the connection between the sources of natural variability and ozone is addressed by analysing the processes that determine it (see **Table 8.1**). Systematic inter-comparisons of ozone as simulated by the CCMs, as well as individual model studies, are considered. Evaluation of the CCMVal-2 REF-B1 simulations makes up the core of the assessment, while comparison of CCMVal-2 results with those from CCMVal-1 simulations is carried out when possible.

This chapter aims to synthesize the results of parts A and B of this report with respect to natural ozone variations. Trends related to anthropogenic ozone depletion are considered, in order to address the problem of how natural ozone variations are modelled but the discussion of the effects of these trends is left to Chapter 9.

8.2 Data and Methodology

8.2.1 Data

In the following, a brief description is provided of the key ozone and temperature observations employed to validate and assess the ability of the CCMs to simulate observed variability. To take into account the spread between available observational data sets and individual estimates of measurement errors, several data sets have been used, when possible.

The ground-based zonal mean column ozone data set from Fioletov *et al*. (2002; ***ftp://ftp.tor.ec.gc.ca/Projects-Campaigns/ZonalMeans/***) and the merged satellite column ozone data set (TOMS/SBUV) from the Total Ozone Mapping Spectrometer (TOMS) and Solar Backscatter Ultraviolet 2 (SBUV/2) instruments (Stolarski and Frith, 2006; ***http://acdb-ext.gsfc.nasa.gov/Data_services/merged/***) are used, because together they provide a long-term data set, ranging from 1964 to 2008. To construct the continuous data set, the ground-based data are used where no satellite data are available (1964-1979) and satellite data are employed where available (1980-2008). Gaps in the satellite data are filled with ground-based data (Fioletov *et al*., 2002). This data set is referred to as "TOMS+gb". The NIWA combined total column ozone database 1 for the shorter period 1980-2007 (updated from Bodeker *et al*., 2005) is also employed, hereafter referred to as NIWA-column. The comparison of ground-based, merged satellite data, TOMS/SBUV data as well as the NIWA-column ozone data shows good correspondence between the 5 data sets and maximum differences of +1 to -1% (Fioletov *et al*., 2002).

Several ozone profile data sets are employed. The Randel&Wu data set (Randel and Wu, 2007; 1979-2005) is based on output from a regression model applied to ozone anomalies from SAGE satellite data (referred to as Randel&Wu or SAGE in the following). The regression model includes a decadal trend (EESC: equivalent effective stratospheric chlorine), the QBO, 11-year solar cycle and an ENSO basis function, which are fitted to SAGE I and II satellite ozone anomalies. The regression output is added to a seasonal mean, zonal mean, vertically resolved ozone climatology (Fortuin and Kelder, 1998). The NIWA-3D data set (1980-2007) is based on satellite (SAGE I and II, POAM II, and III, HALOE) and ozone-sonde profiles where regression constrained interpolation has been used to produce a gap free data set (Hassler *et al*., 2009). The NIWA-3D data set is similar to the Randel&Wu data set, in the sense that it is also the output of a regression model.

For the seasonal cycle studies of ozone, the Microwave Limb Sounder (MLS) data from the NASA Aura satellite (Waters *et al*., 2006; Froidevaux *et al*., 2008) are also em-

Table 8.1: List of diagnostics employed to evaluate the modelling of natural stratospheric ozone variability by the CCMs participating in CCMVal-2.

Process	Diagnostic	Variables	Data	References
Annual Cycle in Ozone				
Chemistry	Annual cycle at selected locations	O_3, T	MLS, HALOE	*Eyring et al. (2006)*
Chemistry & Dynamics	MLR analysis	O_3	NIWA-3D	*Bodeker et al. (1998)*
	Annual cycle in column ozone	O_3 column	NIWA-column	*Eyring et al. (2006)*
Interannual Polar Ozone Variability				
Dynamics & Transport	Monthly standard deviations and climatology	O_3 column	NIWA-column	
	Heat flux relationship with column ozone	v'T', T	ERA-Interim, NIWA-column	*Weber et al. (2003)*
	Annular Mode relationship to column ozone	Z_g, O_3	NCEP/NCAR, NIWA-column	*Hu and Tung (2002)*
Solar Cycle in Ozone				
Dynamics, Chemistry & Radiation	MLR analysis	T, O_3	ERA-40, SSU, RICH, NIWA-3D, Randel&Wu	*Austin et al. (2008)*
Chemistry & Transport	MLR analysis	O_3 column	NIWA-column, TOMS+gb	*Austin et al. (2008)*
Radiation & Chemistry	MLR analysis	SWHR - Shortwave heating rates	-	
QBO in Ozone				
Chemistry & Dynamics	Monthly standard deviations	U, O_3	ERA-40, SAGE	*Baldwin et al. (2001)*
	MLR analysis	O_3	NIWA-3D, Randel&Wu	
Transport, Dynamics & Chemistry	MLR analysis	O_3 column	NIWA-column, SAGE, TOMS+gb	
ENSO Signal in Ozone				
Dynamics & Transport	MLR analysis	T, O_3	ERA-40, RICH, NIWA-3D, Randel&Wu ozone	*Free and Seidel (2009); Randel et al. (2009b)*
	Composite analysis	T, O_3 column	ERA-40, NIWA-column	*Cagnazzo et al. (2009)*
Volcanic Aerosols				
Radiation & Chemistry	Composite analysis	T, O_3 column	ERA-40, NIWA-column, TOMS+gb	*Timmreck et al. (2003)*
	MLR analysis	T	ERA-40, SSU, RICH, NIWA-3D, Randel&Wu	
Chemistry & Transport	Composite analysis	ClO, O_3		

ployed. The MLS instrument has made global measurements nearly every day since August 2004 and is therefore ideal for examining the seasonal cycle at various pressure levels. Monthly averaged values of MLS ozone are computed for 6-degree latitude bins. The ozone climatology for the period 1991-2002 from the Halogen Occultation Experiment (HALOE) onboard the Upper Atmosphere Research Satellite (UARS; Russell *et al*., 1993) is also used. Data after September 2002 have not been included because of the unusual major warming in the Antarctic in 2002, and because the observations have been less frequent since 2002 (Grooß and Russell, 2005).

Various temperature data sets are used: 1) SSU (Stratospheric Sounding Unit) temperature data for the middle and upper stratosphere (Randel *et al*., 2009a; 1979-2005), 2) the Radiosonde Innovation Composite Homogenization (RICH) data set that uses the ERA-40 reanalysis to identify break points, which are then adjusted using neighboring radiosonde observations in the lower stratosphere and troposphere (Haimberger *et al*., 2008; ***http://www.sparc.sunysb.edu/html/updated_temp.html***; 1960-2004), and 3) the ERA-40 reanalysis temperature data (Uppala *et al*., 2004; 1979-2001). The reanalyses are used to allow comparison of similar spatial coverage as in the CCMs, keeping in mind the uncertainties related to possible spurious trends in this data set (for a discussion see *e.g*., Randel *et al*., 2009a).

8.2.2 Multiple Linear Regression Analysis

Multiple linear regression (MLR) analyses is a commonly used method to assess the relative contributions of different drivers of variability in geophysical time series, *e.g*., near global total column ozone (Chapter 3 in WMO, 2007). Here we compare results from an MLR analysis applied to monthly ozone and temperature fields from the REF-B1 simulations of CCMVal-2 with results from an identical analysis of the appropriate observational data sets described above. Although the focus is on sources of natural variability (annual cycle, solar cycle, QBO, ENSO, and volcanoes), a secular term is also required to account for the substantial trend in ozone and temperature over the period examined. For the ozone regression, the secular term is represented by the EESC (equivalent effective stratospheric chlorine), while for the temperature regression, a linear trend is used instead. The MLR analysis is based on the method described in Bodeker *et al*. (1998, 2001) to model a time dependent variable, *e.g*., ozone:

$$y(t) = \beta_{offs(N=4)} \times offset + \beta_{EESC(N=2)} \times EESC(t) + \beta_{QBO(N=2)} \times QBO(t) + \beta_{QBO_or(N=2)} \times QBO_orthog(t) + \beta_{sol(N=0)} \times solar(t) + \beta_{ENSO(N=2)} \times ENSO(t) + \beta_{Ag(N=2)} \times Agung(t) + \beta_{Elc(N=2)} \times ElChichon(t) + \beta_{Pin(N=2)} \times Pinatubo(t) + R(t)_{t=1,n}$$

The first term in the regression model (β_{offs} coefficient times the offset basis function) represents a constant offset and, when expanded in a Fourier expansion, represents the mean annual cycle. In this case, with four Fourier pairs (*N=4* in the equation above), the annual cycle is modelled as a summation of 12, 6, 4, and 3 month harmonics each of variable phase. All basis functions are de-trended except for the EESC, the trend and volcano basis functions; and the offset is removed from the respective basis functions except for the volcanoes. The sensitivity of the basis functions to different numbers of Fourier pairs was tested. The two Fourier pair expansion for the EESC fit coefficients was chosen to account for the strong seasonal cycle in the effect of EESC on ozone, particularly in the polar regions. For all other basis functions the results are not significantly influenced by changing the number of Fourier expansions of their fit coefficients.

The EESC basis function represents the total halogen loading of the stratosphere effective in ozone depletion, appropriately weighted by the mean age of air (age 3.0 years and width 1.5 years has been selected for the global average investigated here). For most of the CCMs, the EESC has been calculated using the formula suggested by Newman *et al*. (2007): $Cl_y + 60Br_y$ (in volume mixing ratio (vmr)) and the global monthly mean values at 50 hPa, and is referred to as effective stratospheric chlorine (ESC) in Eyring *et al*. (2007). Some CCMs do not provide Cl_y and/or Br_y and therefore for these CCMs the observed EESC is used (E39CA, NiwaSOCOL, UMUKCA-METO, and UMUKCA-UCAM). The EESC fit coefficient (β_{EESC}) represents the anthropogenic part of the signal and is not discussed until the Chapter 9. Note that an additional linear trend term for the ozone regression is not included, because it is assumed that all long-term secular changes within the last 50 years are captured by the EESC basis function.

The QBO basis function is specified as the monthly mean 50 hPa zonal wind (except for AMTRAC3 where 10 hPa and UMSLIMCAT where 30 hPa is used) for each individual model realisation. Since the phase of the QBO varies with latitude and altitude a second QBO basis function is included, which is orthogonal to the first, as described by Austin *et al*. (2008). For the CCMs in Group A of Table 8.4, the QBO basis function is neglected, given their lack of interannual variability in the tropics (see Figure 8.14).

The observed Nino 3.4 sea surface temperature (SST) anomalies are used for the ENSO basis function without a time shift. The F10.7cm radio flux is employed for the 11-year solar cycle basis function. The volcanic aerosol basis functions for Agung, El Chichón and Pinatubo are taken from Bodeker *et al*. (2001). To account for the autocorrelation in the residuals, an autoregressive model of *R* (the residual) is used: First a fit to the time series is performed and a residual calculated. Then the autocorrelation coefficient is calculated using Equation 6 in Bodeker *et al*. (1998) and

used to transform the basis functions and the regression time series. The MLR analysis is then applied a second time and now includes the effects of autocorrelation in the residuals. Uncertainties are expressed as the square root of the sum of the squared diagonal elements of the covariance matrix.

In summary, only the QBO and the EESC basis functions are formed from model output. All the other basis functions are common to the MLR analyses of both the time series from the CCMs and observational data.

In **Figure 8.1** the contribution of the various natural as well as anthropogenic contributions to global (60°S-60°N) column ozone variations is shown for the ground-based data set in Dobson units. Figure 8.1 shows that the observed long-term decrease in column ozone is almost completely explained by the trend due to increased atmospheric halogen loading. However, natural variability is not negligible. The annual cycle dominates the natural variability with an amplitude of ~12 DU, followed by the 11-year solar cycle with ~6 DU between solar maximum and solar minimum, the QBO with ~4 DU between maximum QBO easterlies and westerlies, a small component associated with ENSO of ~1 DU, and the volcanic contribution which has distinct and unevenly distributed contributions of up to 6 DU. Note that the residual, especially before the satellite era is relatively large (up to ±5 DU) and we can only speculate that this has to do with the data quality. Also we emphasize that the atmosphere is highly non-linear, so the residual represents to some extent also the failure of a linear regression analysis to account for non-linear processes in the atmosphere.

The results of the MLR analysis are presented in the following Sections (8.3-8.8), together with process oriented studies. For most CCMVal-2 models the whole time series from 1960 to 2004 is considered (although some only provide data up to 2000). Comparisons with observations are also described, employing data for the same time period (1960-2004) or only from the satellite era (1979-2007), as appropriate. In these cases, the sensitivity of the MLR analysis to the selected time period has been tested (but is not shown); unless otherwise stated, the essential results are not substantially affected by the shortened period, although the amplitude of the signal is usually larger.

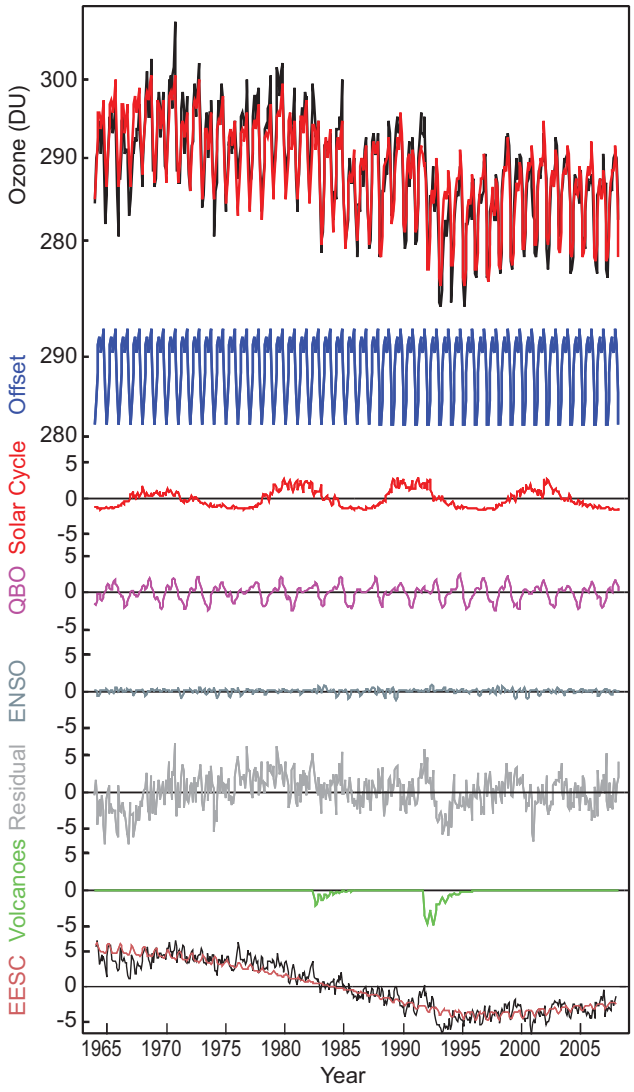

Figure 8.1: Ozone variations for 60°S-60°N in DU estimated from ground-based measurements (Fioletov et al., 2002) and individual components that comprise ozone variations, from 1964 to 2008. From top to bottom: Original data (black) and fitted with a multiple linear regression (MLR) model (red); annual cycle (blue); 11-year solar cycle (red); QBO (purple); ENSO (light blue); residual (grey); and the EESC (red) curve scaled to fit the data from 1964-2008. The residual is the difference between the original and the fitted time series. See text for details on the MLR analyis.

8.3 Annual Cycle in Ozone

Pronounced variations in stratospheric ozone are caused by annual variations in transport and photochemistry. The transport variations are driven by dynamical processes (Chapters 4 and 5) and can affect ozone either directly or indirectly (through changed transport of ozone-depleting substances). Photochemical production of ozone depends on annual variations in the solar irradiance (Chapters 3 and 6). The resulting annual cycle in column ozone is characterized by (a) low amounts in the tropics year-round, (b) maxima in the spring of Northern Hemisphere (NH) high latitudes and Southern Hemisphere (SH) middle latitudes, and (c) larger hemispheric-mean amounts in the NH *versus* the SH. This annual evolution of column ozone reflects the dominant influence of transport processes on lower stratospheric ozone.

8.3.1 Annual cycle at selected locations in the stratosphere

The photochemical time scale for ozone varies seasonally as a function of latitude and pressure. In the lower stratosphere the time scale is long and the seasonal cycle is largely controlled by transport. In the upper stratosphere, the time scale is short and the ozone mixing ratio reflects a near balance between production and loss. Since the time scales for transport and for photochemical processes both vary seasonally, in some parts of the stratosphere both types of process contribute to the stratospheric concentration of ozone. For example, in winter transport processes control the seasonal build-up of ozone through descent at the edge of the vortex and this is then moderated at high latitudes during cold winters by chemical loss associated with polar processes. In summer, transport effects are minimal and the photochemical time scale decreases from several years to 30 days or less, producing a summer minimum that varies little from year to year.

In **Figure 8.2** the annual cycle in ozone mixing ratios simulated by 16 CCMs is compared with MLS observations. At 1 hPa the time evolution of monthly-mean, zonal-mean ozone is shown at 40°S, the Equator and 40°N. At 46 hPa corresponding plots are shown for 72°S, the Equator, and 72°N. Four separate years of MLS observations are shown in the SH and equatorial plots (January 2005-December 2008) and three years (July 2005-June 2008) are shown in the NH; the NH observations are phase shifted to align the seasons with those of the SH observations. From the models, only a single year's annual cycle is shown, taken from the early 2000s for consistency with the data. Examination of up to an additional 10 years per model (not shown) has demonstrated that the comparisons are representative. The annual mean has been subtracted in all figures to emphasize the seasonal variation in both observations and simulations.

Although the ozone column is dominated by mixing ratios in the lower stratosphere and hence its annual cycle is barely affected by the evolution of upper stratosphere

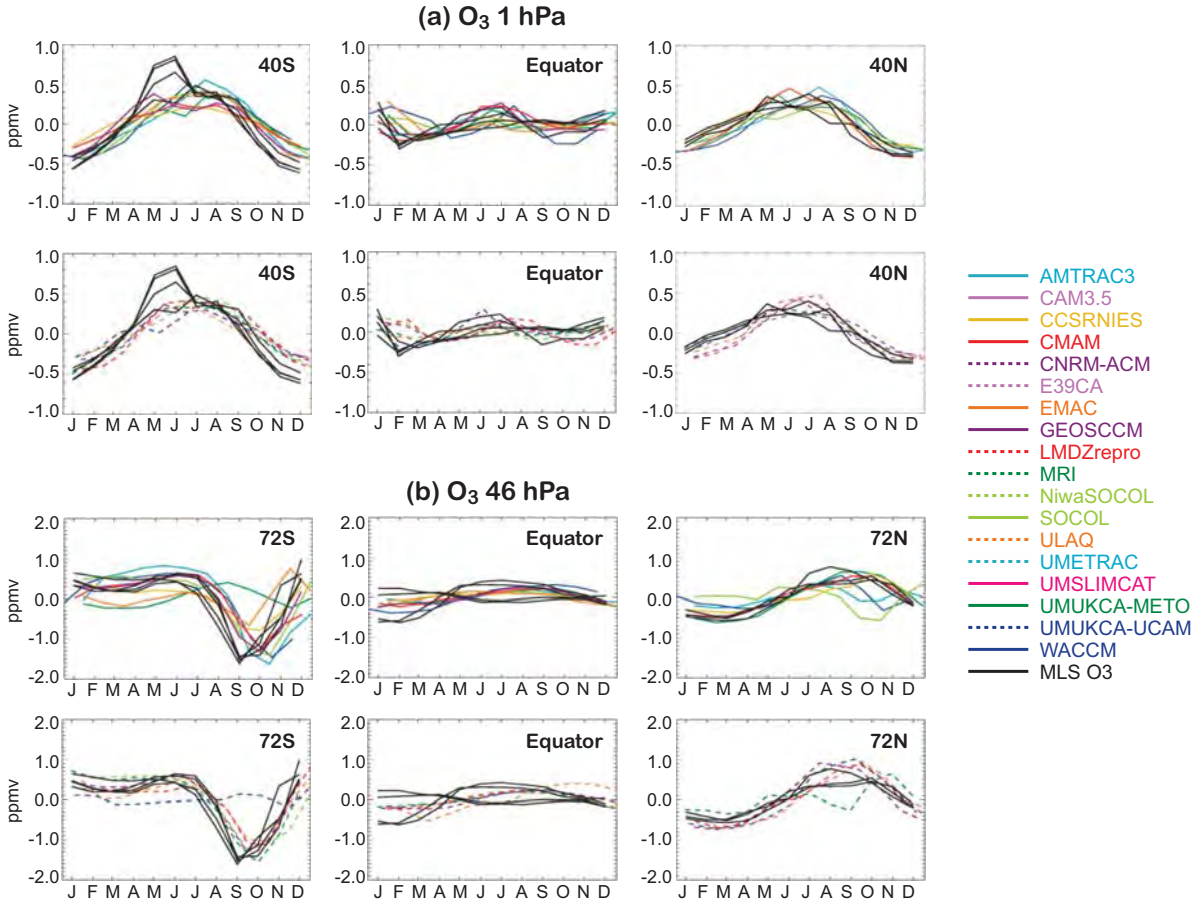

Figure 8.2: (a) Monthly mean ozone mixing ratios (ppmv) at 1 hPa throughout the year, 40°S (left), equator (middle) and 40°N (right) from several years of MLS observations (black lines) and for the CCMVal-2 CCMs (monthly zonal-mean ozone in the early 2000s from selected years). MLS data are averaged for a six degree latitude band centred on the selected latitudes. (b) Same as 8.2a but at 46 hPa, 72°S (left), Equator (middle) and 72°N (right).

mixing ratios, a comparison at 1 hPa provides a simple check on the performance of the photochemical schemes implemented in the various models (see also the more detailed comparison of photochemical schemes in Chapter 6). The simulated annual cycle at both 40°S and 40°N generally approximates the MLS data. The simulated annual cycle in temperature also agrees with observations (Figure S8.1 in the supplementary material), so this comparison verifies the simulated sensitivity to temperature. A positive anomaly in the SH during May and June in the MLS data is not reproduced by any model. A similar (negative) feature in temperature mirrors this anomaly. In the tropics, a small semi-annual oscillation is also seen in the observations. Many of the models also reproduce this semi-annual variation but with differences in the timing. This phase difference between models and observations is also seen in the temperature variations (Figure S8.1) and therefore explains the mismatch in ozone. To summarize, the models exhibit the appropriate sensitivity to temperature, so, when the simulation reproduces (or does not reproduce) the temperature variation, a corresponding match or mismatch is seen in the ozone variations.

At 46 hPa during winter and spring in the high latitude SH, the ozone mixing ratio anomaly is dominated by polar ozone loss. Figure 8.2 (bottom) shows that the models generally reproduce this variation, except for UMUKCA-METO and UMUKCA-UCAM. For both of these models, there is polar ozone loss, but it does not extend as far equator-ward as 72°S. Note that these models perform better further south. While observations show a peak ozone loss in September, the CCMs response is shifted by one to two months. At the equator, the MLS data show a seasonal variation that depends on the phase of the QBO and is not fully captured by the models (see Section 8.6). In the NH, transport and polar ozone destruction processes control the evolution during winter/spring. Both contribute to the substantial observed variability in ozone during these seasons. Interannual variability in winter/spring is so large (see Section 8.4) that differences between the observations and simulations are not significant. However, during the

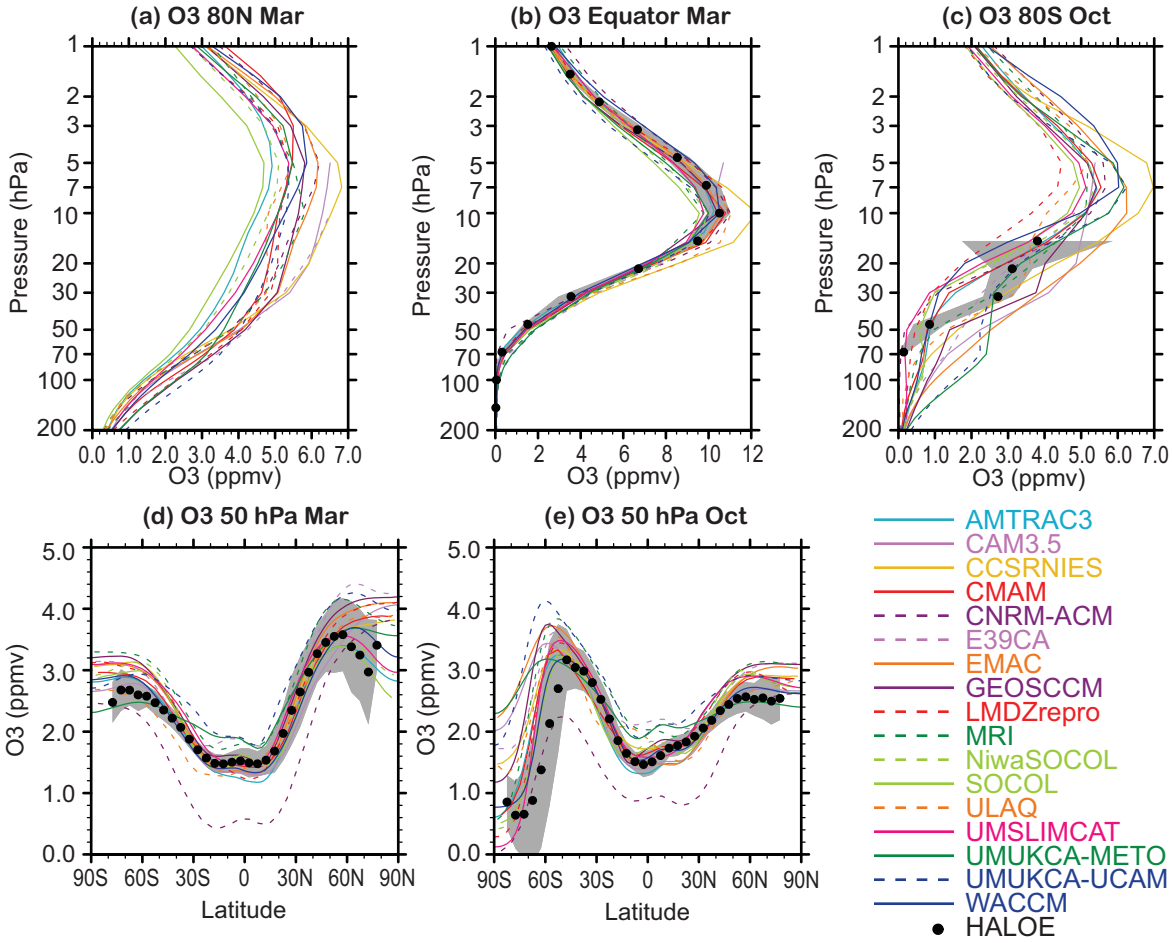

Figure 8.3: Climatological zonal mean O_3 mixing ratios from the CCMVal-2 CCMs and HALOE in ppmv. Vertical profiles at (a) 80°N in March, (b) 0° in March, and (c) 80°S in October. Latitudinal profiles at 50 hPa in (d) March and (e) October. The grey area shows HALOE ±1 standard deviation (s) about the climatological zonal mean. Same as Figure 13 for CCMVal-1 CCMs in Eyring et al. (2006).

summer the photochemical time scale decreases to 30-60 days, the circulation is near zonal with little horizontal or vertical mixing and the ozone mixing ratio is close to photochemical balance. The interannual variability of the observed ozone mixing ratio during this period is minimal. In the models, there is a relatively large spread during this period (and also during January-February-March in the SH), which likely reflects the spread of temperatures between the models (see Chapter 4). Nevertheless, the simulated ozone mixing ratios return to values that are the same each year within a few percent in each of the last 10 years of the integrations (not shown), in agreement with the observations, thus demonstrating that models make a reasonable transition to photochemical control in summer. This variation decreases with increasing pressure; at 70 hPa the models reproduce the observed small annual variation in ozone mixing ratio (not shown).

8.3.2 Springtime ozone values

Figure 8.3 compares climatological mean vertical ozone profiles and latitudinal cross-sections in March and October derived from the CCMVal-2 models and HALOE observations (see Figure 13 from Eyring *et al*., 2006 for the CCMVal-1 models). At the equator, most models agree well with HALOE observations and lie within one standard deviation of the HALOE mean, except for the CCSRNIES model that shows unusually large ozone peak values at 10 hPa. At higher latitudes during NH and SH spring there is a larger spread between the models and only a few lie within one standard deviation of the HALOE mean. This is especially true in the lower stratosphere/upper troposphere where CCMVal-1 simulations showed very good agreement with observations but CCMVal-2 simulations show a much larger spread. This may be simply because more CCMs now participate in CCMVal-2; see also Chapter 7 for a detailed discussion on UTLS performance of each model.

In the SH spring, the vertical profiles of CCSRNIES, CAM3.5, EMAC, UMUKCA-METO, and UMUKCA-UCAM are biased high, while LMDZrepro is biased low. In the NH, again CCSRNIES and CAM3.5 are biased high, while SOCOL is biased low. For the CCSRNIES model, the overestimation of peak ozone values in the tropics and polar regions was already evident in CCMVal-1 and is related to overestimation of O_2 photolysis rates at this altitude (see PhotoComp results in Chapter 6, *e.g*., Figure 6.1). The pronounced ozone bias that was evident in LMDZrepro in CCMVal-1 has been improved but this model is still biased low due to the warm temperature bias in the SH (Chapter 4).

The lower panels of Figure 8.3 show that the latitudinal representation of ozone in the lower stratosphere in spring-time of each hemisphere has improved since CCMVal-1. Between 60°S and 60°N most models lie within one standard deviation of the HALOE data. The CNRM-ACM is a clear outlier and substantially under-estimates the values. At polar latitudes more than half of the CCMs significantly overestimate the HALOE ozone values, possibly related to their low potential for chlorine activation (PACl; Chapter 6, Table 6.5). SOCOL, NiwaSOCOL, AMTRAC3, UMSLIMCAT, and WACCM agree best with observations at northern high latitudes in March, while at southern high latitudes CNRM-ACM and LMDZrepro are equally good compared to observations.

8.3.3 Annual cycle metrics

Differences between modelled and observed annual cycles in ozone can be further quantified by means of normalised Taylor diagrams (Taylor, 2001). The usefulness of the Taylor diagrams is their compact representation of pattern statistics between two fields, thus providing a straightforward methodology to quantify and compare results from a large number of fields (model diagnostics) with respect to a reference field (observations). The pattern statistics computed are correlations and normalised spatial standard deviations, respectively giving information on the differences in phase and magnitude, between each model result and the observation. In the Taylor diagram, the correlation is given by the cosine of the angle from the x-axis, and the normalised spatial standard deviation is the radial distance from the origin. The observation (reference) point therefore lies on the x-axis, with standard deviation equal to 1 and correlation equal to 1. The distance from the reference point (curved dashed lines with the origin at the reference point) measures the centred root mean square error.

The normalised Taylor diagram for the annual and the semi-annual harmonics of the zonal-mean ozone from the MLR analysis is shown in **Figure 8.4**. Since the focus is on stratospheric ozone, the pattern statistics are computed for the latitude-pressure sections ranging respectively from the South to the North poles, and from 500 to 1 hPa pressures; and the pattern statistics calculation includes area weights, but no weighting in pressure. Therefore, Figure 8.4 evaluates the latitude-pressure patterns of the modelled annual and semi-annual harmonics, namely the fields shown in the supplementary material (Figures S8.2-S8.4). Figure 8.4 shows that both the annual and the semi-annual harmonics in zonal mean ozone are very well represented for the majority of models, with respect to the NIWA-3D ozone data set. All models are characterized by correlations higher then 0.8, except for one model, E39CA in the case of the annual harmonic and CAM3.5 in the case of the semi-annual harmonic. Interestingly, both E39CA and CAM3.5 are the models with low tops (Chapter 2), suggesting that the top boundary conditions applied in these models may slightly degenerate the performance of their annual cy-

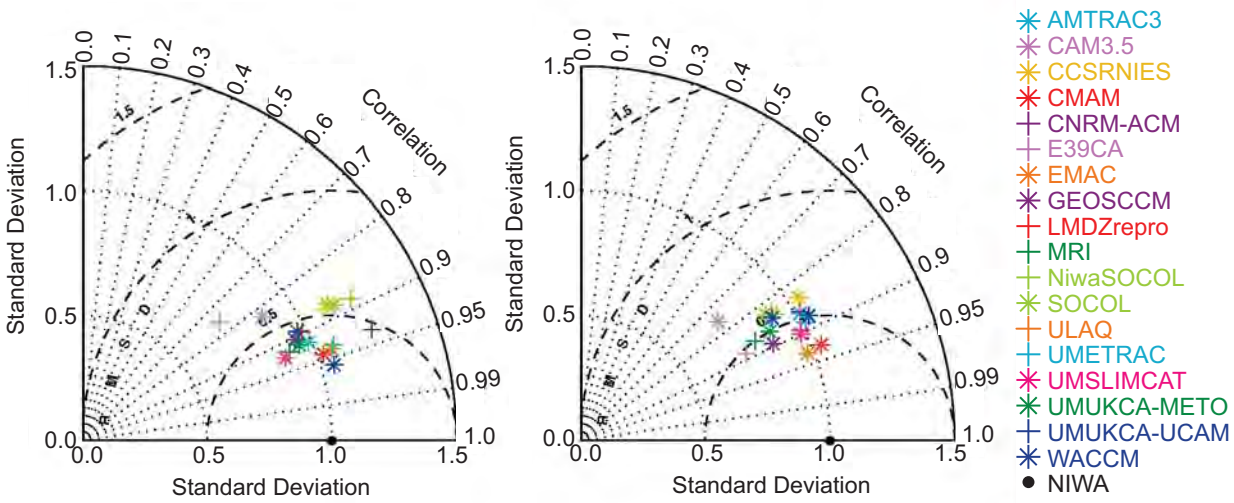

Figure 8.4: Normalised Taylor diagram of the annual (left) and semi-annual (right) harmonics of the zonal-mean ozone, latitude-pressure distribution, for the NIWA-3D data set and the CCMVal-2 models. The corresponding fields are shown in the supplementary material (Figures S8.2-S8.4). The pattern statistics have been computed for the 1-500 hPa, 90°S-90°N range.

cle in ozone. The relative clustering of the model points around one standard deviation demonstrates also that the magnitudes of the modelled spatial ozone variations compare well to those of the NIWA-3D data set.

For comparison with the performances of the annual and semi-annual cycle, the normalised Taylor diagram of the annual zonal-mean ozone coefficients from the MLR analysis is reported in the supplementary material (Figure S8.5). In this case, the very close clustering of the model signatures around the black solid point on the x-axis, which is the reference observation, demonstrate that the annual zonal-mean ozone field is extremely well simulated by all models.

The evaluation of the annual cycle in column ozone is performed on the monthly-mean zonal-mean model data. For the models, only data from 1980 to the end of the REF-B1 simulations (which vary model by model between 2000 and 2007) are considered, to better match the period of the NIWA-column ozone data set (1980-2007) used as the reference field. A second data set, the TOMS+gb column ozone since 1980 has also been used to provide an estimate of the uncertainty in the observations. In addition, plotting each available realization from the models shows the sample uncertainty. The normalised Taylor diagram from these data, using NIWA-column ozone as the reference, is shown in **Figure 8.5**. Therefore, Figure 8.5 evaluates the latitude-month patterns of the modelled column ozone fields, shown in supplementary material (Figure S8.6). Note that the Taylor diagram is computed only for data between 60°S and 60°N (for the annual cycle in polar ozone, see Section 8.4). Figure 8.5 demonstrates that most models capture the phase of the annual cycle and the latitudinal distribution of the total ozone quite well. All models are characterized by correlations close to or above 0.9. Only UMUKCA-UCAM overestimates the spatial standard deviation substantially (factor 1.5), while CNRM-ACM under-estimates it. As a group, the models display a slight overestimation of the seasonal variations of the zonal mean column ozone (most model points have standard deviations between 1 and 1.5)

In the computation of the Taylor diagram, the mean bias is excluded. The relative mean bias, (model – observation)/observation, is shown for the near global column ozone and the northern and southern polar caps in **Table**

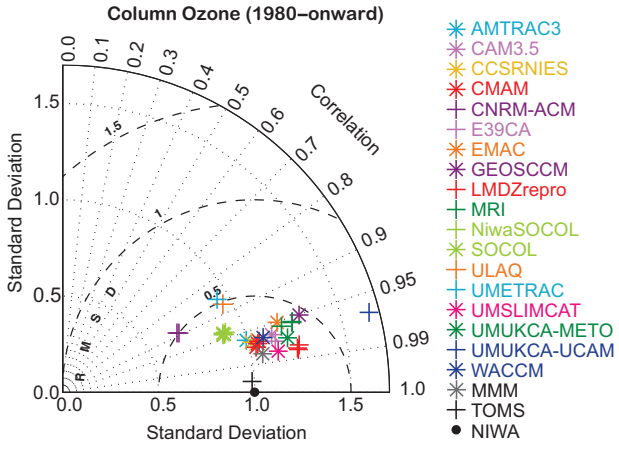

Figure 8.5: Normalised Taylor diagram of the annual cycle of the zonal-mean column ozone, latitude-month distribution, for the NIWA-column and TOMS+gb data sets and the CCMVal-2 models. The corresponding fields are shown in the supplementary material (Figure S8.6). The pattern statistics have been computed for the 60°S-60°N range.

8.2. The NIWA-column ozone is used as the reference observations. For most models, the relative mean bias is small, within a few percent. Defining as outliers the models with an absolute relative mean bias larger than 10%, it is found that E39CA and UMUKCA-UCAM overestimate the near-global ozone and both the North and South polar ozone; UMSLIMCAT slightly under-estimates only the near global ozone; GEOSCCM and UMUKCA-METO overestimate ozone over both polar caps; LMDZ-repro and UMETRAC respectively over- and under-estimate ozone only in the northern polar cap; CAM3.5, EMAC, and MRI overestimate ozone and CNRM-ACM under-estimates ozone over the southern polar cap.

8.4 Interannual Polar Ozone Variability

In the extra-tropics, interannual natural variations in stratospheric ozone are largest in the polar regions and tend to maximise during the spring season. **Figure 8.6a** (top panels) shows the monthly interannual standard deviation of column ozone averaged over the polar caps (60°N-90°N at left and 60°S-90°S at right), from the CCMVal-2 models and the NIWA-column ozone data. The corresponding annual cycle in the column ozone climatology is shown in Figure 8.6b. These results have been calculated for the time period from 1980 to the end of the REF-B1 simulations (varying model by model, between 2000 and 2007) and for 1980-2007 for the NIWA-column data. For the models, similar results were obtained if the calculation is performed from 1960 (not shown). Prior to the calculation of the diagram shown in Figure 8.6a, decadal trends were removed from the data. This was accomplished by calculating a low-pass filtered version of the data (the time filter consists of Gaussian-weighted running means with a full width at half maximum of 9 years) and by removing it from the original time series. The resulting time series therefore, contain only variability on time scales from 1 to about 10 years. Model performance with respect to the NIWA-column data is quantified by corresponding Taylor diagrams (Figure 8.6 lower panels).

Figure 8.6a shows that the interannual variability of the NIWA-column ozone exhibits a pronounced annual cycle and maximises during the dynamically active late winter and early spring periods of each hemisphere (January-April in the NH; August-November in the SH). The simulation of this observed seasonality represents an important model benchmark. Figure 8.6a demonstrates that all models show a minimum in variability in the late summer and fall (upper panels) and that the correlation coefficient is above 0.7-0.8 for most of the models (lower panels). Better agreement with the NIWA-column data may not be warranted, because at polar latitude during winter the NIWA-column data are mostly estimates (Bodeker *et al.*, 2001, 2005).

Table 8.2: Total ozone model bias in % for different latitude ranges.

CCM	60°S-60°N	60°N-90°N	90°S-60°S
AMTRAC3	-3.77	-6.57	-0.36
CAM3.5	-3.64	1.79	11.07
CCSRNIES	5.86	1.51	9.12
CMAM	-2.18	0.04	-1.18
CNRM-ACM	-5.81	-3.12	-14.95
E39CA	15.14	19.07	16.04
EMAC	2.02	2.71	13.94
GEOSCCM	3.33	15.72	19.37
LMDZrepro	4.31	10.67	2.30
MRI	8.88	9.92	15.11
NiwaSOCOL	0.77	-3.34	-4.42
SOCOL	-1.49	-5.85	-6.49
ULAQ	3.29	-1.65	-4.45
UMETRAC	-3.95	-13.95	-0.03
UMSLIMCAT	10.34	-4.80	-5.87
UMUKCA-METO	6.61	12.84	16.65
UMUKCA-UCAM	14.07	26.26	34.40
WACCM	-2.35	2.26	-5.68
MMM	1.71	3.53	5.25

During the NH active period (Figure 8.6a left panel), the amplitude of the annual cycle is well simulated by most models, with notable exceptions for MRI, which exhibits very large variability and standard deviation larger than 2 in the Taylor diagram, and also UMUKCA-UCAM and WACCM, both with standard deviation close to 1.5 in the Taylor diagram. The rest of the models are close together and slightly under-estimate the observed total ozone variability, suggesting a possible systematic bias. The results for individual ensemble members of MRI (not shown) are very similar, indicating that its high variability is not due to sampling uncertainty. The interannual variability of the WACCM model, in addition to be biased high, is characterized by a prolonged period of high variability, extending into June (low correlation, below 0.6).

During the SH active period (Figure 8.6a right panel), the model results tend to surround the observations. Models with particularly low variability are CNRM-ACM, E39CAA, GEOSCCM, and UMUKCA-UCAM. Models with particularly high variability, suggesting an early start of the active period, are CAM3.5 and EMAC, while CMAM has excessive variability in November.

The annual cycle of the column ozone climatology averaged over the polar caps (Figure 8.6b) shows the NH

spring time column ozone build up and the seasonality of the SH ozone hole. The timing of the NH ozone build up is well simulated by all models, as quantified by correlations above 0.8 for all models (bottom panel). A weak build up is noted for NiwaSOCOL, SOCOL, and possibly AMTRAC3 and MRI. In the SH, the situation is complicated by the presence of the ozone hole, an anthropogenic modification of the annual cycle. Therefore, factors such as the size of the polar vortex (a dynamical process), the strength of the polar barrier, as well as heterogeneous chemistry (a chemical process) play a role in determining the large spread of modelled column ozone minimum in September-October, as discussed in Chapter 6. Particularly low correlations (below 0.5) are displayed by E39CA, EMAC, UMUKCA-METO, UMUKCA-UCAM, and WACCM. Of these models, only WACCM reproduces the dip in ozone, *albeit* with a 2-month delay. The other highlighted outliers instead fail to model the impact of the ozone hole on the annual cycle. Among the models that better reproduce the column ozone annual cycle, NiwaSOCOL, MRI, and SOCOL overestimate its amplitude (standard deviations larger than 1.5, bottom panels). Note that the CAM3.5 model is not plotted, because it falls outside the Taylor diagram (standard deviation: 0.8; correlation coefficient: -0.4).

In addition, Figure 8.6b (upper panels) shows that a number of models are affected by a mean bias in polar column ozone, which cannot be quantified by the Taylor diagram. In the NH, E39CA and UMUKCA-UCAM column ozone fields are biased high, while UMETRAC column ozone is biased low (see Table 8.2), in spite of their high correlations and standard deviations close to 1 (implying well simulated phase and magnitude of the annual cycle). These biases may be related to excessive stratosphere to troposphere ozone transport and/or tropospheric chemistry. In the SH, the E39CA, EMAC, GEOSCCM, MRI, UMUKCA-METO, and UMUKCA-UCAM ozone fields are all biased high (see Table 8.2).

The winter and spring evolution of the interannual variability in column ozone is associated with the seasonality of planetary wave activity and its influence on the strength of polar descent in the Brewer-Dobson circulation (Fusco and Salby, 1999, Randel *et al*., 2002). When planetary wave activity is high, diabatic descent at high latitudes is strengthened, leading to increased transport of ozone-rich air from the tropical middle stratosphere (where ozone is photochemically produced) to the polar

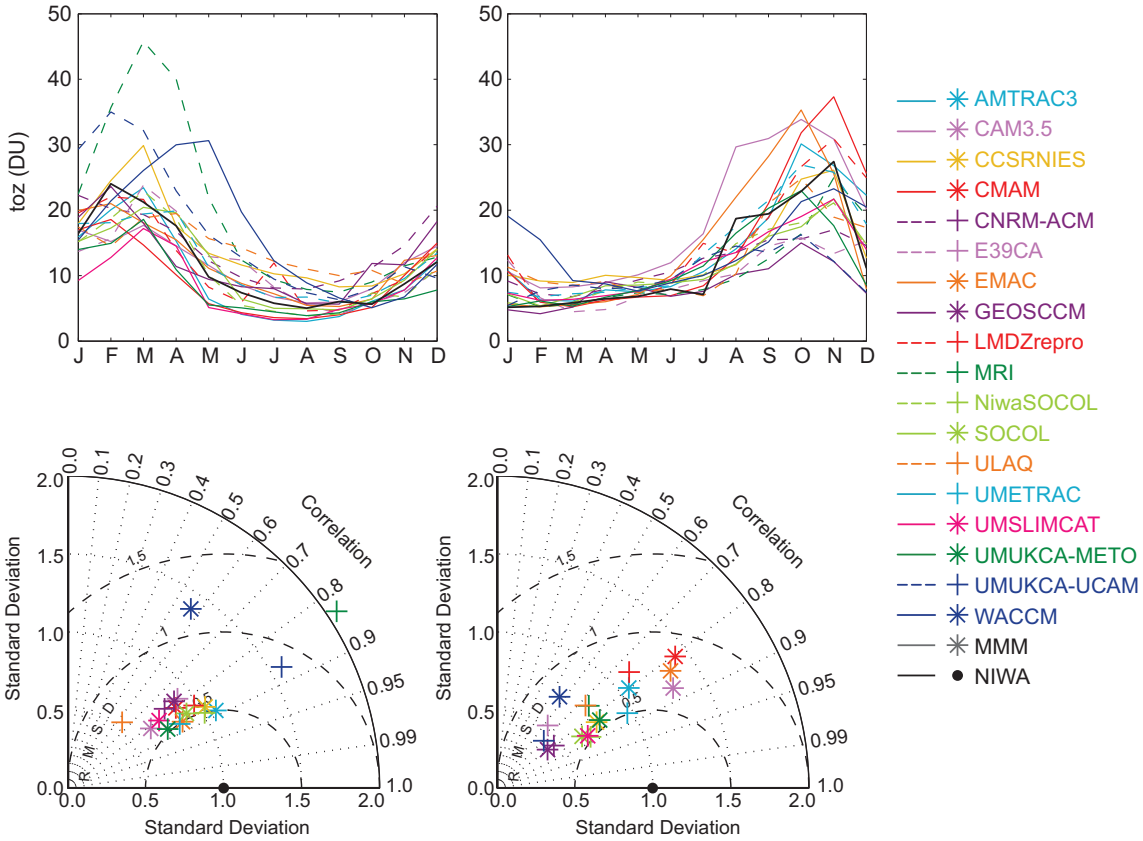

Figure 8.6a: Interannual variability of polar cap averaged column ozone (DU, upper panels) and corresponding normalised Taylor diagrams (lower panels) for NH (left) and SH (right) over the period onward of 1980. Legend for model results in the upper panels: Star (cross) symbols correspond to solid (dashed) lines. Black solid line represents NIWA-column data.

lower stratosphere. In addition, increased wave activity leads to a more disturbed polar vortex and hence to higher polar temperatures, creating less favourable conditions for chemical depletion of ozone due to heterogeneous processes. To evaluate the modelled connections between ozone variability and dynamical variability (the latter discussed in Chapter 4), the relationships between column ozone and, respectively, meridional heat fluxes, temperature and the stratospheric annular mode are reported in the following sections.

8.4.1 Heat flux and column ozone

Weber *et al*. (2003) show a compact relationship between the spring-to-fall ozone ratio in each hemisphere and the winter-time mean heat flux. In this section the presence of a similar relationship is investigated. The models are compared to observations using winter-time mean 100 hPa meridional heat fluxes from the ERA-Interim data set and the spring-to-fall ratio in column ozone from the NIWA-column ozone data. Column ozone ratios are for March/September in the NH and September/March in the SH, using area weighted averages between 60° and the pole. Heat fluxes are averaged between 45° and 75°, using extended winter means: September-March (NH) and March-September (SH). SH data are de-trended as previously for Figure 8.6a. To calculate the spring-to-fall ozone ratio it is necessary to add a climatological ozone field to the filtered time series: a 10 year mean, monthly column ozone amount (1990-2000) was employed for this, since it is a period common to both the data and models. The analysis is performed for every year of model data from 1960 to the end of each simulation (which varies from model to model, between 2000 and 2007) and for 1980-2007 for NIWA-column and ERA-Interim data.

Results from the individual scatter plots (see supplementary material Figures S8.7) are summarized in **Figure 8.7**, where the slope parameter of the linear fit of each scatter plot is plotted against the mean spring-to-fall ozone ratio for each model or data set, along with the 95% confidence interval of the slope parameter. The slope of the scatter plot describes the typical response of the spring-to-fall ozone ratio to a one-unit increase in the absolute value of 100 hPa meridional heat flux. Since the absolute value of the heat flux is proportional to the upward component of the Eliassen-Palm flux, the slope diagnoses the response

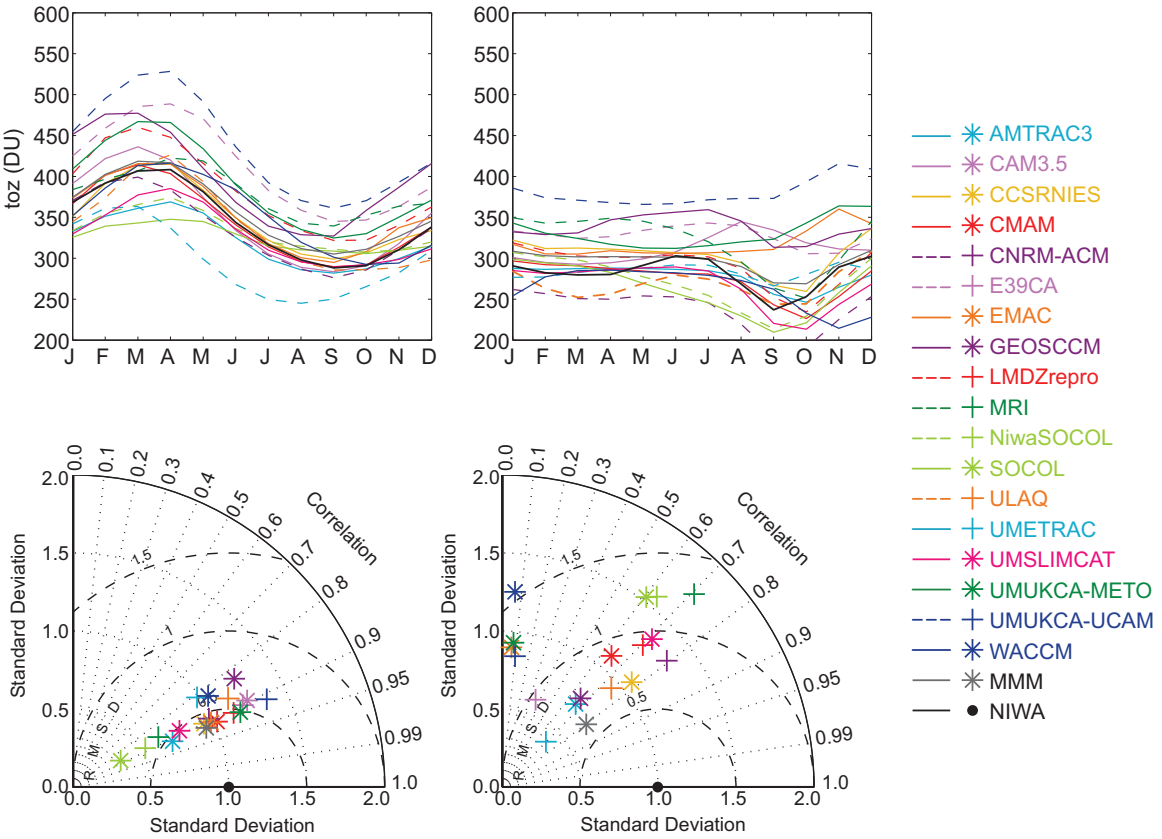

Figure 8.6b: Mean polar cap averaged column ozone (DU, upper panels) and corresponding normalised Taylor diagrams (lower panels) for NH (left) and SH (right) over the period onward of 1980. Legend for model results in the upper panels: Star (cross) symbols correspond to solid (dashed) lines. Black solid line represents NIWA-column data.

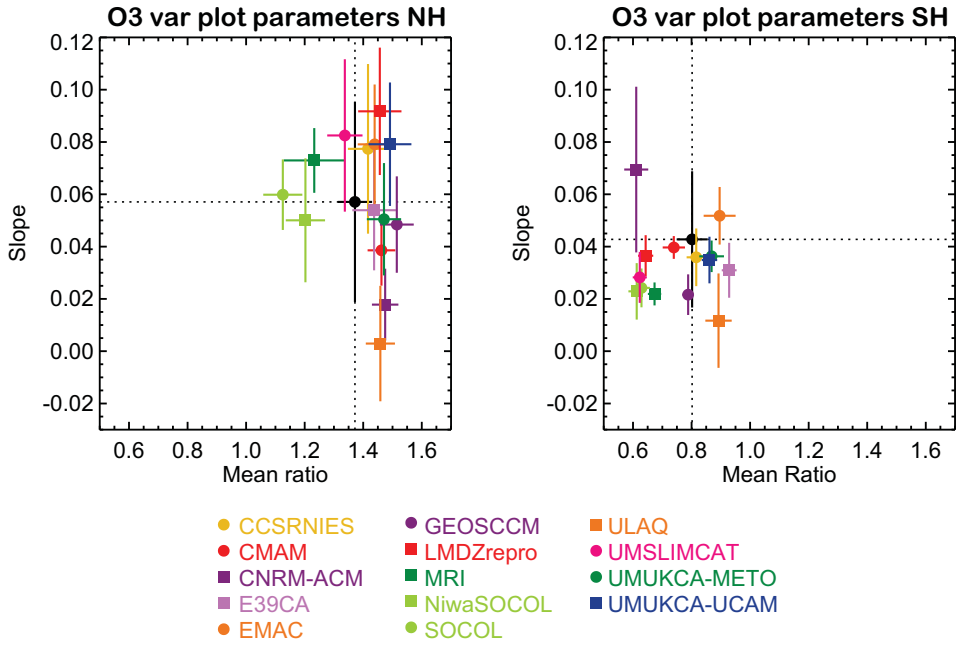

Figure 8.7: Slope parameter (1/ K ms^{-1}) of the linear fit to the scatter plots of the Spring/Autumn ozone ratio versus the 100 hPa winter heat flux, plotted against the mean Spring/Autumn ozone ratio for each model. NH (left) and SH (right). Black symbols represent ERA-Interim and NIWA-column data. Each model is plotted with a single coloured dot or square, 95% confidence intervals for the slope parameters are shown in solid lines.

of ozone over each polar cap to changes in the amount of planetary wave activity entering the lower stratosphere. The mean ratio of the spring-to-fall ozone concentration diagnoses the average seasonality in ozone concentrations present in each model. This is a more useful measure of the position of the model on each scatter plot than the intercept of the regression line, which is usually a large distance from the centre of the cloud of points for each model.

Figure 8.7 shows that for most of the models the slope parameter is within the sampling uncertainty of the observations, for both hemispheres. Only the slope parameter of the ULAQ model is indicative of a much weaker relationship (close to zero in the NH) between the heat flux and spring-to-fall ozone ratio, possibly related to the limited horizontal resolution of the ULAQ model. Note that ULAQ is also characterized by a weak relationship between lower stratospheric temperature and heat fluxes, in the NH (Chapter 4). The CNRM-ACM result is for 10 years only so could be different to the rest of the model results for this reason. In the NH (Figure 8.7 left panel), there is a larger spread and a larger uncertainty in the slope parameter than in the SH (right panel), possibly because of the larger NH interannual variability in planetary wave activity (Chapter 4). In the NH, Chapter 4 reports a tendency for enhanced sensitivity in the lower stratospheric polar temperature to the winter heat fluxes. This Chapter 4 result is consistent with the slight overestimation of the ozone sensitivity to the heat flux suggested by the cluster of the model points, located above the value of the slope parameter of the observations (once CNRM-ACM, because it is based on a shorter data set, and ULAQ, since it is an outlier are excluded). In the SH, most of the models show a smaller inter-model spread and tend to under-estimate the slope parameter. This result is not entirely consistent with the temperature sensitivity reported in Chapter 4, which shows both higher and lower modelled sensitivity of the lower polar stratospheric temperature to the heat fluxes. Concerning the mean spring-to-fall ozone ratio in the models, in the NH the NIWA-column data fall approximately in the middle of the model range. Very weak transport of ozone into the vortex is implied for the MRI, NiwaSOCOL and SOCOL models, explaining the low NH spring time column ozone previously noted. In the SH, there is a relatively large spread in the mean ratio of the September/March column ozone between the models, with about half of the models with smaller or larger ratio than observed (consistent with Figure 8.6b right). Given that the September/March ratio is less than 1.0 because of polar ozone depletion, *i.e.*, the ratio is influenced by chemistry and not just dynamics. This suggests that biases in the modelling of polar chemical processes (Chapter 6) can contribute to this spread in model results. It is also possible that the advection of ozone rich air into the polar cap, which would tend to produce a September/March ratio above 1, is weaker in most models than in the reanalysis, although analysis of some of the same models in Chapter 4 did not suggest that the strength

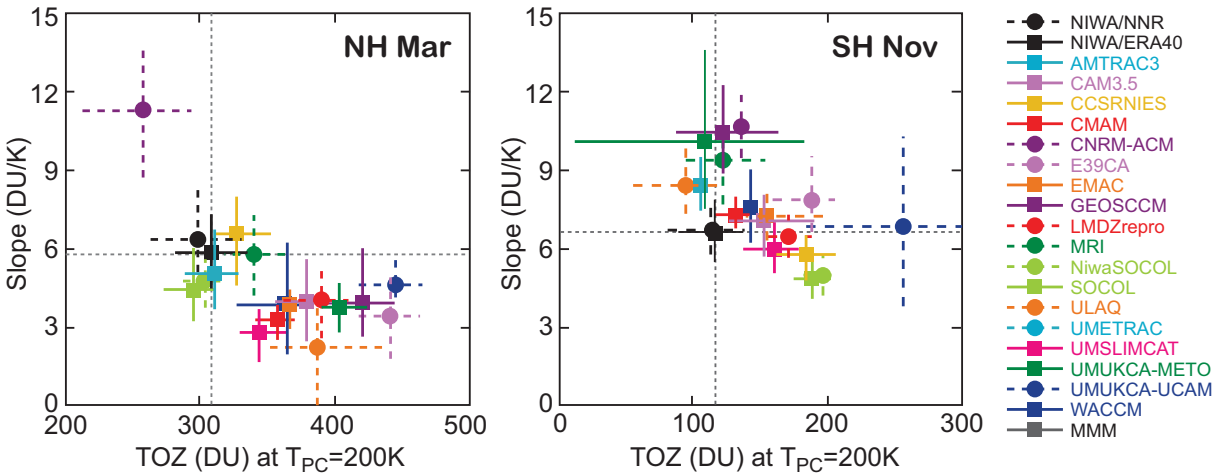

Figure 8.8: Slope parameter (DU/K) of the linear fit to the scatter plots of the polar cap averaged column ozone versus 50 hPa temperature, plotted against the column ozone value of the linear fit at T = 200 K for each model. NH (left) and SH (right). Black solid (open) symbols represent NNR (ERA-40) reanalysis and NIWA-column data. Each model is plotted with a single coloured symbol, 95% confidence intervals for the slope parameters are shown in solid or dashed lines.

of their Brewer-Dobson circulation was too weak. There is some indication in Chapter 5 that models with a much lower ratio of September/March ozone in the SH perform poorly in diagnostics of their polar isolation (LMDZrepro, MRI, NiwaSOCOL, SOCOL). However, it is also true that some models with good transport diagnostics also show low spring-to-fall ozone ratios here.

8.4.2 Temperature and column ozone

The tight relationship between heat flux and temperature (Newman *et al.*, 2001, see also Chapter 4) motivates an extension of the analysis presented in Figure 8.7 by evaluating the relationship between column ozone and lower stratospheric temperatures. The existence of such a relationship has previously been identified by Newman and Randel (1988) and Fortuin and Kelder (1996).

In this section, polar cap averaged (60°-90°) monthly temperatures at 50 hPa are compared against polar cap averaged total column ozone. The analysis is focused on spring (March for the NH and November for the SH), which is the time when the cumulative effects of wave activity during the previous winter on ozone and temperature are most pronounced. The analysis is performed for every year of model data from 1960 to the end of each simulation and for the common periods between the NIWA-column ozone and, respectively, the NCEP/NCAR reanalysis (hereafter: NNR, updated from Kalnay *et al.*, 1996) and the ERA-40 reanalysis.

Figure 8.8 displays the slope parameter of the linear fit between column ozone and temperature and its 95% confidence intervals. The slope parameter indicates how sensitive column ozone is to a given temperature perturbation. On the x-axis is reported the ozone amount of the linear fit at a temperature of 200 K, which is used as a second parameter to describe the goodness of the fits.

The results shown in Figure 8.8 indicate that the models perform adequately over both polar caps, in the sense that all slopes are positive showing that column ozone increases when temperatures are anomalously warm. However, for the NH (March, left panel), only 5 models (AMTRAC3, CCSRNIES, MRI, NiwaSOCOL, SOCOL) reproduce the observed relationship reasonably well. UMUKCA-UCAM does not under-estimate the slope significantly, but has a large amount of ozone at the temperature of 200 K. One model (CNRM-ACM) considerably overestimates the observed slope. The rest of the models under-estimate the slope up to a factor of two, indicating that for most models the simulated ozone is less sensitive to a given temperature perturbation than in the observations. In November (SH, right panel), the number of models that either over- or under-estimate the observed slope is quite evenly distributed around the observations. The slope is overestimated for CNRM-ACM, GEOSCCM, MRI, and UMUKCA-METO.

Figure 8.8 also indicates that the x-axis values, the amount of ozone at a temperature of 200 K, are too large for most models. This is consistent with the column ozone systematic bias seen in Figure 8.6b. The positive ozone bias is particularly large for the UMUKCA-UCAM model in November, and consequently this model stands out in the SH plot.

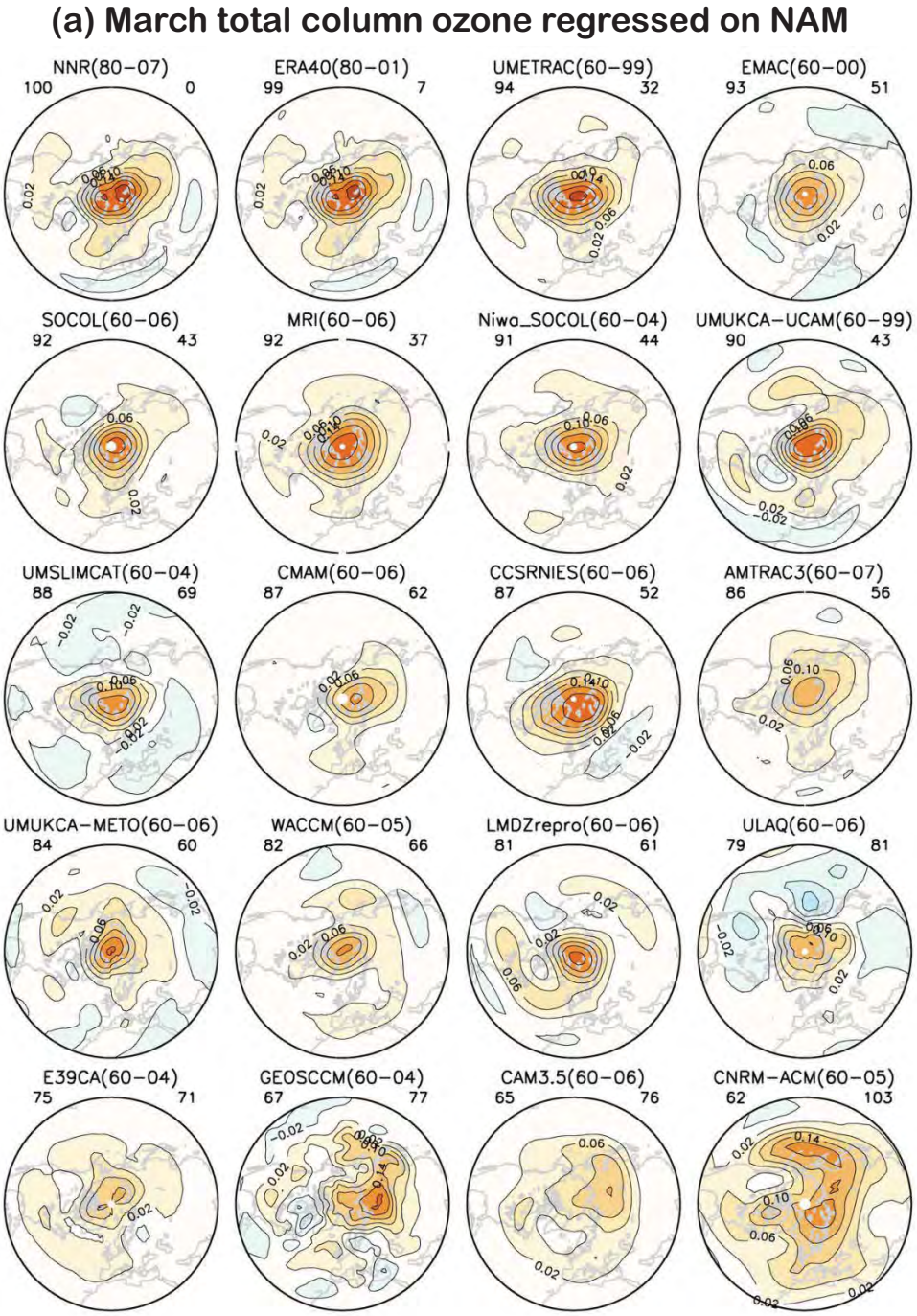

Figure 8.9a: Regression of column ozone on the simplified annular mode for NH March. Contour interval is 0.04 DU/gpm. The numbers on top of each map represent (left) pattern correlations (x100) and (right) nrms-errors (x100) between results from the individual models and those from the NIWA-column and NNR. Numbers in parenthesis indicate the period (years) included in the calculations.

8.4.3 Stratospheric annular mode and column ozone

On interannual time scales the strength of the annular mode in the lower stratosphere and the heat fluxes at 100 hPa are closely connected (Hu and Tung, 2002). Therefore, a relationship should also exist between the column ozone variation and the annular mode. This possibility is investigated by regressing the monthly mean column ozone time series on to a relatively simple definition of the annular mode (AM) index at 50 hPa. The 50 hPa level is chosen because column ozone is mostly affected by variations in the

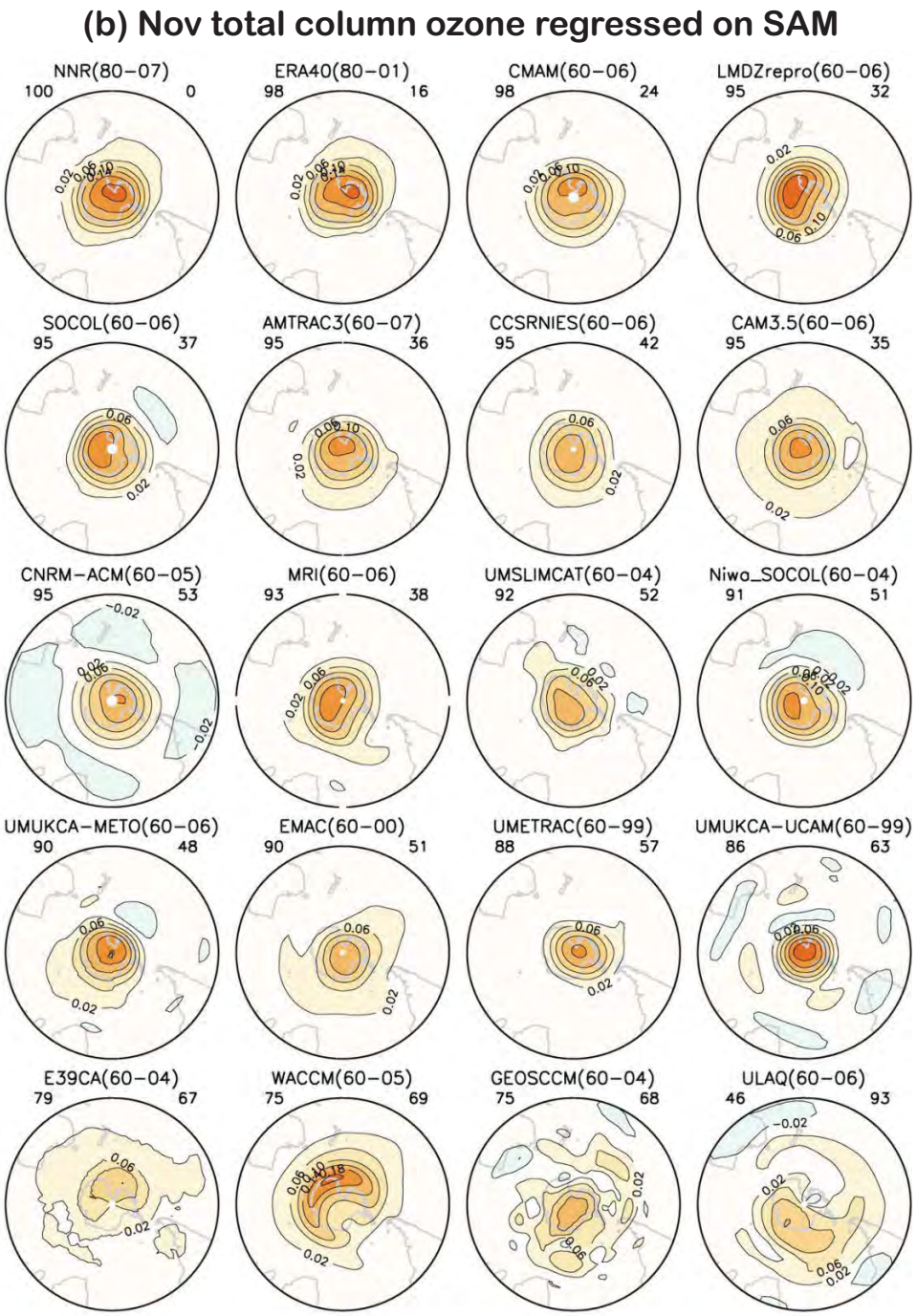

Figure 8.9b: Regression of column ozone on the simplified annular mode for SH November. Contour interval is 0.04 DU/gpm. The numbers on top of each map represent (left) pattern correlations (x100) and (right) nrms-errors (x100) between results from the individual models and those from the NIWA-column and NNR. Numbers in parenthesis indicate the period (years) included in the calculations.

lower stratosphere. The simple AM definition is based on polar cap averages (60°-90°) of monthly mean zonal mean geopotential height anomalies at 50 hPa, and is a good approximation of the traditional AM index (Baldwin and Thompson 2009). The simple AM is employed, because it represents an absolute measure and thus avoids possible ambiguities associated with the polarity and magnitude of the EOF-based approach. Note that, however, it has the opposite polarity from the EOF-based AM. Prior to the analysis, all data are de-trended as previously done for Figure 8.6a. Concerning the observations, the NIWA-column ozone data are used and the AM index is derived from the

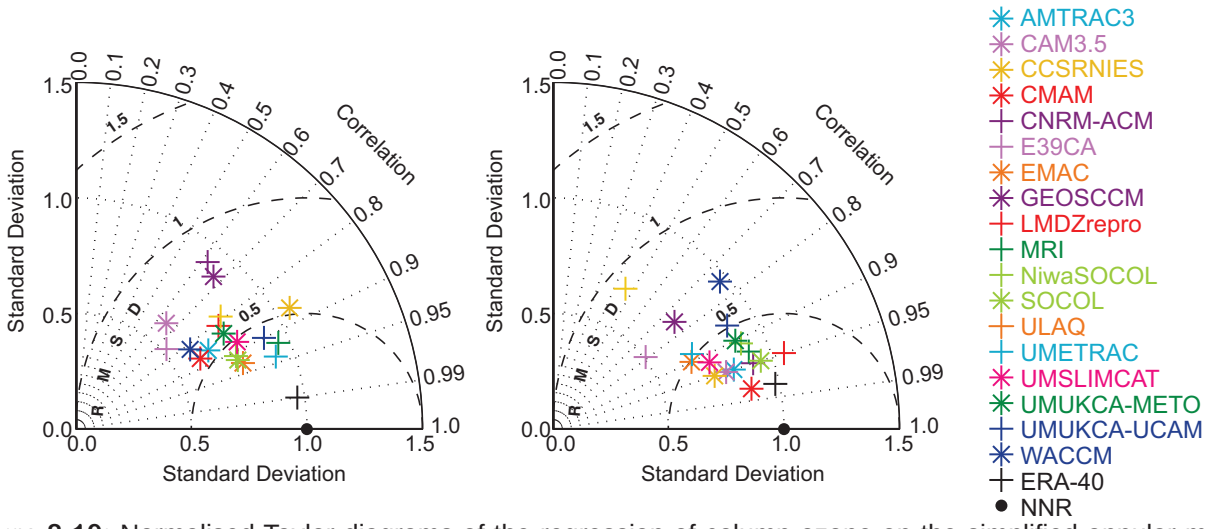

Figure 8.10: Normalised Taylor diagrams of the regression of column ozone on the simplified annular mode for NH March (at left) and SH November (at right). The corresponding fields are shown in Figure 8.9a and 8.9b, respectively.

NNR or the ERA-40 reanalysis, as in Section 8.4.2.

The regression coefficients between local variations of column ozone and the AM index for each model and observations are shown for NH March in **Figure 8.9a** and for SH November in Figure 8.9b, the dynamically active seasons (section 8.4.1) and a time when this relationship is expected to be robust. The corresponding Taylor diagrams quantifying model performance with respect to NIWA/NNR are shown in **Figure 8.10**. Therefore, Figure 8.10 (left) evaluates the longitude-latitude pattern of the modelled ozone versus annular mode regression for NH March, and Figure 8.10 (right) the one for SH November. As expected, using the simple AM leads to positive regressions over the polar regions. Column ozone is high when the AM is positive, *i.e.*, when the geopotential height anomalies over the pole are positive, indicative of a warm and weak vortex, increased wave activity, and an anomalously strong descending branch of the Brewer-Dobson circulation at polar latitudes.

Figure 8.10 (left) shows that for NH March, most models reproduce the basic structure of the observed regression patterns in the sense that most models have a correlation coefficient with NIWA/NNR larger than 0.7. The three outliers (CAM3.5, CNRM-ACM, and GEOSCCM) still have relatively high correlations larger than 0.6. The amplitude of the observed regression pattern is less well simulated, with most of the models tending to under-estimate it (standard deviation less then 1).

In the SH, Figure 8.10 (right) shows a better simulation of the observed pattern for SH November. In this case, the outlier is ULAQ, because of its very small correlation (smaller than 0.5), while E39CA, GEOSCCM, and WACCM have correlations between 0.7 and 0.8, and the rest of the models have correlations close to or higher than 0.9. The decrease in the spread of the model results is due to the improvement in the structure of the modelled regression pattern, while the performance in its amplitude (measured by the standard deviation) is comparable in the two hemispheres. Possibly, the better simulation of the structure of the regression pattern in the SH is related to the more zonal character of the large scale stratospheric dynamics there.

8.5 Solar Cycle

The 11-year solar cycle has a direct impact on ozone *via* radiation and chemistry in the upper stratosphere and indirect effects on dynamics, transport and chemistry throughout the stratosphere (*e.g.*, review by Gray *et al.*, 2010). The direct effect in the upper stratosphere depends on a good representation of solar radiation processes in both the radiative transfer and in the photochemistry parameterisations (see Chapters 3 and 6 for a comparison of radiation codes and photochemical schemes respectively). These were reasonably well simulated by the CCMVal-1 models (Austin *et al.*, 2008). However, the indirect dynamical effects in the tropical lower stratosphere and extra-tropical stratosphere and the extension of the signal into the troposphere (see *e.g.*, Haigh, 1999; Kodera and Kuroda, 2002; Matthes *et al.*, 2004; Haigh *et al.*, 2005; Kodera, 2006; Matthes *et al.*, 2006; Gray *et al.*, 2010) are more challenging to reproduce. Matthes *et al.* (2003) suggested that a realistic representation of the model's climatology is an important pre-requisite for reproducing the indirect dynamical effects. Other suggested important "ingredients" are a QBO, time-varying solar irradiances, and realistic interannual variability in the SSTs. Another

remaining challenging task is to understand the observed modulation of the solar signal with the tropical oscillations (QBO and SAO) at the equatorial as well as at the high-latitude stratosphere (see *e.g.*, Labitzke, 1987; Labitzke and van Loon, 1988; Gray *et al.*, 2001). This interaction is still difficult to investigate since the number of observed events when separated into solar and QBO phases is small and only some of the CCMs reproduce an internally generated QBO, a prerequisite to study the full solar/QBO interaction. On the other hand there is still considerable uncertainty in the observed solar cycle signal, so an understanding of the modelled responses might help to understand the observed response. In the following section the solar cycle response is examined without considering the more complicated tropospheric responses and extra-tropical interactions, which are beyond the scope of the current report.

Five models (GEOSCCM, ULAQ, UMECTRAC, UMUKCA-METO, UMUKCA-UCAM; referred to as the non-sc group) do not prescribe a solar cycle in irradiances and are therefore not included in the following analysis. **Table 8.3** shows a comparison of the solar regression coefficients from the MLR in total column ozone from 60°S to 60°N compared with the observed solar regression coefficient from the NIWA total column ozone data set. While the models from the non-sc group consistently show a solar regression coefficient around zero, most of the models that impose a solar cycle show a solar regression coefficient that is 70% to 80% of the observed value. WACCM, MRI, and UMSLIMCAT show the best agreement with the observed values, while CAM3.5 is biased low and CCSRNIES and CNRM-ACM are biased high. These high biases in CCSRNIES and CNRM-ACM may be related to biases in their ozone climatologies (*e.g.*, Figures 8.2-8.5). Differences in the radiation schemes and the input data (either spectrally resolved solar UV data and/or total solar irradiance (TSI) data) are discussed in Chapter 3, Section 3.6. The difference between the two low-top models E39CA and CAM3.5 that do not include the whole stratosphere is surprising. While CAM3.5 shows a 53% correspondence with observations, a value that might be expected from a low top model, E39CA performs very well (82%). Note also that there are substantial uncertainties from observations. While only the NIWA-column estimate is shown in comparison with the models, Randel *et al.* (2007, Figure 12) showed a factor of two difference among TOMS, SBUV, SAGE, and ground-based estimates.

8.5.1 Vertical structure of temperature and ozone signal in the tropics

Considerable discrepancies exist between the various observational estimates of the vertical structure of the tropical solar signal (Gray *et al.*, 2010) as well as between observations and models (WMO, 2007), especially below 10 hPa. Austin *et al.* (2007; 2008) showed that recent model studies have achieved an improved vertical structure in this region and speculated that it may be related to (a) the introduction of time-varying solar cycle irradiances instead of the constant solar min/max simulations that had previously been performed because of limited computer resources or (b) an aliasing effect of the SSTs with the solar cycle. Marsh and Garcia (2007) discuss the inability of the MLR technique to take into account autocorrelation between *e.g.*, the solar and the ENSO signal, although the MLR analysis employed here should be able to handle this since the autocorrelation in the residual is taken into account (*e.g.*, Crooks and Gray, 2005). Nevertheless, the real atmosphere is highly non-linear and it may be difficult to capture the solar signal completely with the linear method used here. Another factor that complicates the solar signal is the QBO. Lee and Smith (2003) and Smith and Matthes (2008) discuss an aliasing effect of the QBO (and volcanoes) with the solar cycle. Frame and Gray (2010) have recently demonstrated that the volcanic influence is unlikely to be important. Recently, Matthes *et al.* (2010) showed that in their model the observed vertical structure in the tropical solar ozone and temperature signal in the middle and lower stratosphere can be reproduced only when a QBO is present.

Figure 8.11 shows the annual mean of the tropical vertical solar signal in temperature and ozone from the

Table 8.3: Solar regression coefficient for total column ozone from 60°S to 60°N for the CCMs that impose a solar cycle compared to observations (NIWA-column).

CCM	Solar regression coefficient/100 units of F10.7 cm solar flux	%
AMTRAC3	2.8	74
CAM3.5	2.0	53
CCSRNIES	6.5	171
CMAM	3.2	84
CNRM-ACM	7.3	192
E39CA	3.1	82
EMAC	2.7	71
LMDZrepro	2.9	76
MRI	4.1	108
NiwaSOCOL	2.7	71
SOCOL	2.8	74
UMSLIMCAT	3.4	89
WACCM	3.8	100
observations NIWA column	3.8	-

MLR analyses. The relative uncertainties have been calculated by dividing the uncertainty from the MLR (square root of the sum of the squares of the diagonal elements in the covariance matrix) by the solar regression coefficient and normalising it. Therefore, relative uncertainty values below one indicate statistically significant results. The largest and statistically significant temperature and ozone solar response occurs in the upper stratosphere around 1 and 3 hPa, respectively. This is the direct solar effect due to enhanced UV absorption during solar maxima that leads to higher temperature and greater ozone production, which in turn increases the temperature. Most of the models produce a temperature response of about 0.6 K per 100 units of the F10.7 cm radio flux (multiply with 1.3 to get the difference between solar maximum and minimum of the solar cycle) around the stratopause, although the values range from up to 1.1 K in CNRM-ACM, 0.9 K in WACCM, down to ~0.35 K in LMDZrepro and SOCOL. Note that UMSLIMCAT shows a larger warming of about 1 K higher up near 0.3 hPa. The majority of the modelled temperature responses in the upper stratosphere are similar to the SSU observations, although the ERA-40 data show a slightly larger temperature signal of 1.3 K.

The modelled temperature responses are consistent with the shortwave heating rate responses shown in **Figure 8.12**. Models with the largest differences of about 0.15 K/day (EMAC, WACCM, CMAM, CCSRNIES) produce the largest temperature responses around the stratopause. However, even though MRI has the largest shortwave heating rate difference, it does not show an especially large temperature response. The results are also consistent with the offline solar radiation calculation results in Chapter

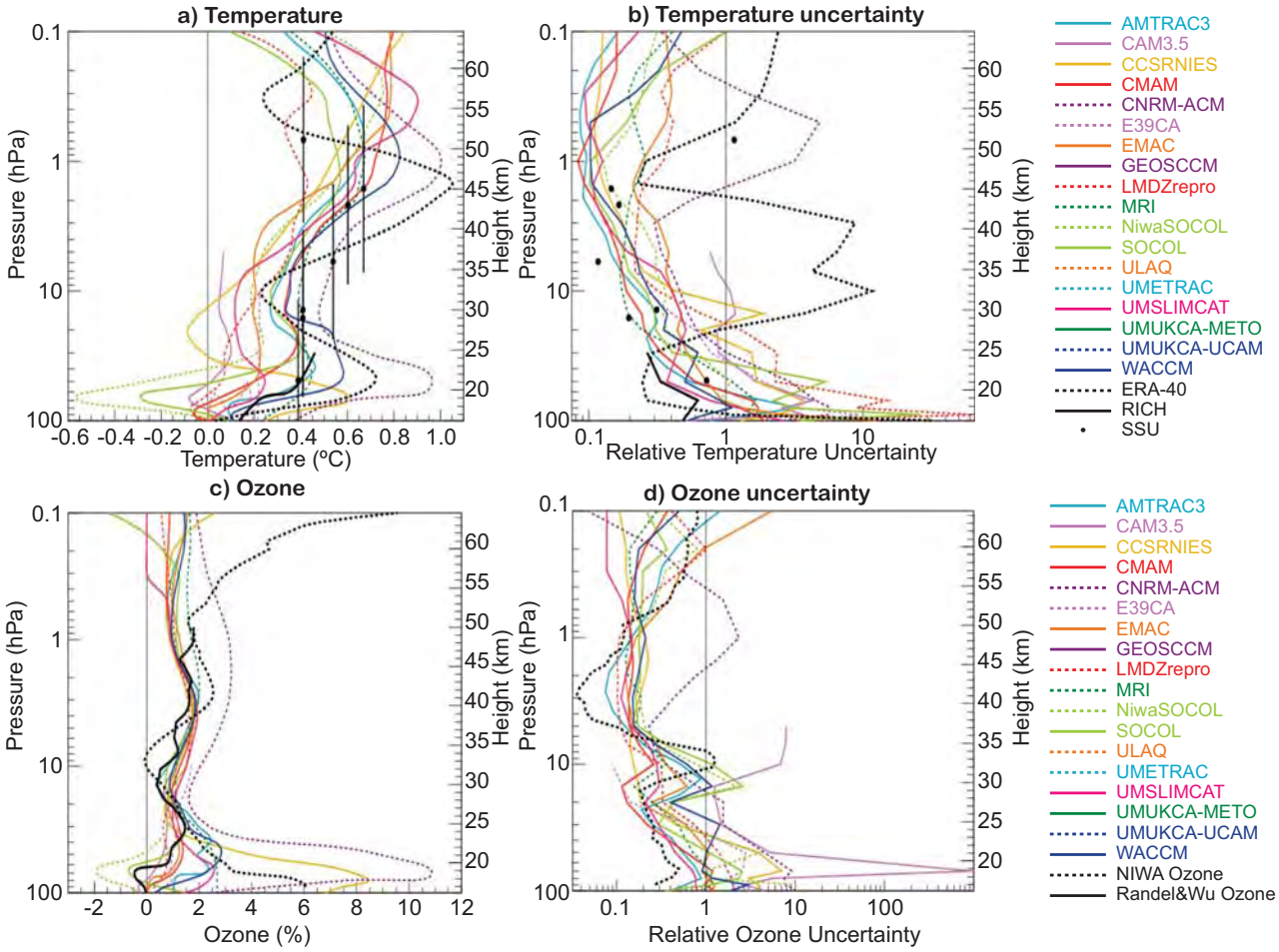

Figure 8.11: Annual mean tropical (25°S-25°N) solar regression coefficients for (a) temperature in Kelvin per 100 units of the F10.7cm radio flux, (b) the relative uncertainty (uncertainty from MLR divided by the regression coefficient and normalised) temperature, (c) ozone in %/100 F10.7cm units, and (d) the relative uncertainty in ozone. From CCMVal-2 CCMs (1960-2004) and observations (NIWA-3D ozone, 1979-2004, Randel&Wu ozone (1979-2005), RICH radiosonde data (1960-2004), ERA-40 (1979-2001), and SSU data (1979-2005)) from 100 to 0.1 hPa. Note that the Randel&Wu ozone data are displayed in DU/km, whereas the CCMs and the NIWA-3D ozone data are on pressure levels.

3 (although note that the offline radiation calculations in Chapter 3 do not necessarily correspond to model results in Figure 8.12; *e.g.*, UMUKCA-UCAM does not have a solar cycle in the REF-B1 simulation and is therefore in the non-sc group in this chapter, although it shows shortwave heating rate differences from the offline radiation calculations in Section 3.6 that are related to solar induced ozone changes in the offline calculations only). LMDZrepro only prescribes total solar irradiance changes, so under-estimates the shortwave heating (Figure 8.12) and therefore the solar temperature response (Figure 8.11). Some of the models with large shortwave heating response (MRI and EMAC in Figure 8.12) show smaller temperature signals (Figure 8.11) than models with smaller shortwave heating responses (*e.g.*, WACCM). In summary, the solar induced temperature responses in Figure 8.11 are produced by a combination of solar UV radiation changes and solar induced ozone changes, which depend both on the prescription of spectrally resolved or total solar irradiance changes in the radiation and on the photochemical schemes and their individual performances (see Chapters 3 and 6).

Discrepancies between the models themselves and with the observations increase below 10 hPa consistent with larger relative uncertainties (Figure 8.11b). Some CCMs show a positive solar temperature signal (Figure 8.11a) that increases with increasing height in good agreement with the SSU data, whereas others such as AMTRAC3, WACCM, SOCOL, CCSRNIES and EMAC show a relative minimum in the middle stratosphere like the ERA-40 data although the height of their respective minima differs. Some models (AMTRAC3, CMAM, CNRM-ACM, CCSRNIES, MRI, and WACCM), show a distinct secondary temperature maximum in the lower stratosphere, which

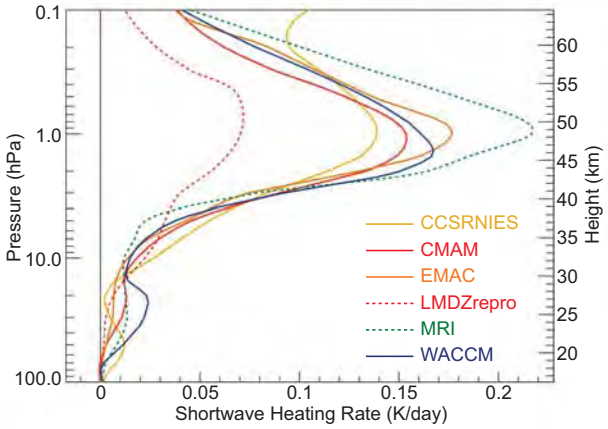

Figure 8.12: Solar cycle shortwave heating rate differences in Kelvin per day in 100 units of the F10.7cm solar flux (multiply by 1.3 to obtain the difference between solar maximum and solar minimum) averaged between 25°S and 25°N for those CCMs that prescribed a solar cycle and provided data.

is also present in the RICH radiosonde data (0.4-0.5 K) and the ERA-40 data (~0.7 K). But as noted above these changes are not statistically significant.

The vertical structure of the solar signal in ozone is much better represented in the models compared to observations, than in the case for temperature (Figure 8.11c). The models compare well with the Randel&Wu ozone data in the middle and upper stratosphere while the agreement between the models, and between the models and observations, deteriorates in the lower stratosphere due to the increased uncertainties (Figure 8.11d). The NIWA-3D data set shows a clear upper stratospheric maximum, a minimum in the middle stratosphere, and a secondary maximum in the lower stratosphere. A secondary peak in ozone in the lower stratosphere between 20 and 25 km, a region where the largest ozone column changes occur, is simulated by AMTRAC3, CNRM-ACM, CCSRNIES, MRI, and WACCM. Except for AMTRAC3 and CNRM-ACM these models have variability related to a (prescribed) or internally generated QBO-like oscillation. Similar to the temperature response, the ozone response and its uncertainties in the lower stratosphere for CCSRNIES and CNRM-ACM are very large compared to the other models and observations. These models were also outliers in the ozone climatology inter-comparison (Figure 8.3), CCSRNIES was graded low for nearly all photolysis rates in the PhotoComp inter-comparison (Chapter 6), and both models showed very fast tropical ascent rates in the transport comparison (Chapter 5).

Note that both low-top CCMs (CAM3.5 and E39CA) produce only a small solar signal in temperature since they do not include the stratopause region where the initial solar signal appears. CAM3.5 produces a similarly small signal in ozone, whereas E39CA shows a relative large solar ozone signal consistent with the largest signal in column ozone in Table 8.3.

8.5.2 Latitudinal structure of the solar signal in temperature and ozone

The latitudinal structure of the amplitude of the solar cycle in temperature and ozone is shown in **Figure 8.13** at 1 and 3 hPa, respectively. Apparent is the large spread of model results which is larger for temperature than for ozone. The modelled solar signals in ozone are similar in the tropics and mid-latitudes while large differences occur at northern and southern high latitudes due to large interannual variability (see Section 8.4). The models agree well with the Randel&Wu data but are lower than the NIWA-3D solar ozone signal in the tropics. EMAC and WACCM show the largest latitudinal variations; in the SH this agrees well with the NIWA-3D ozone. Again, CNRM-ACM is biased high from 60°S to 60°N.

The solar temperature signal shows more variabil-

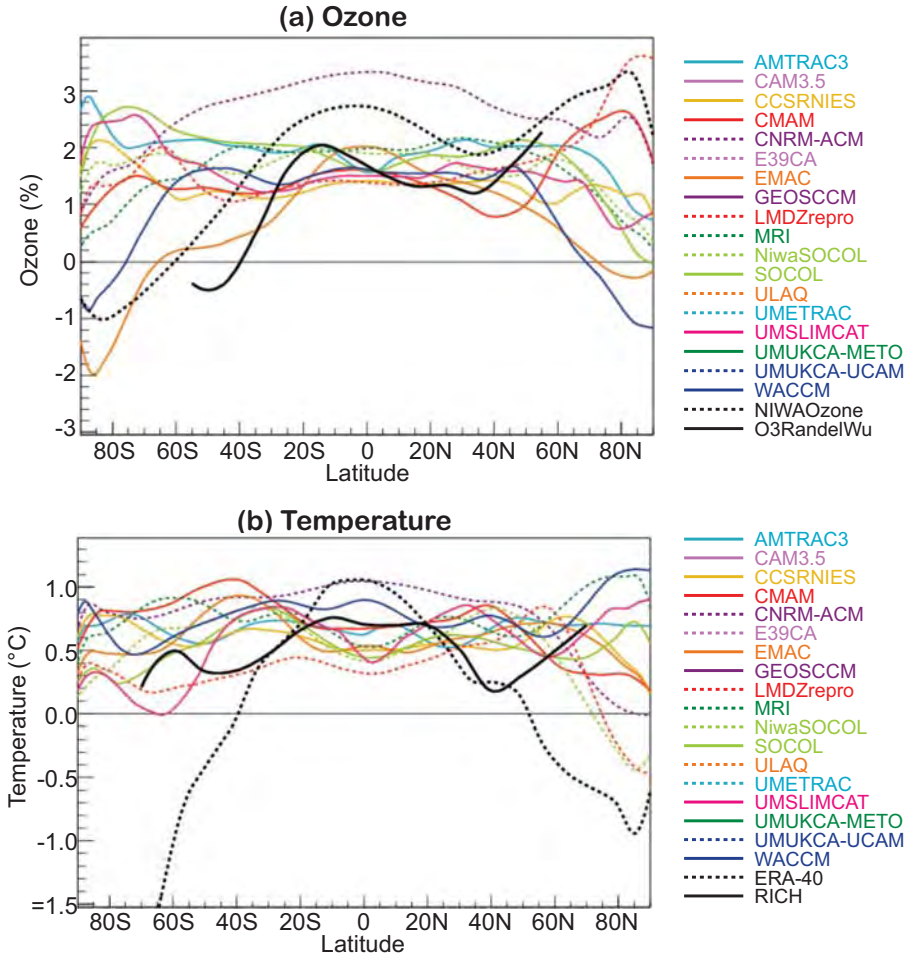

Figure 8.13: Amplitude of the solar cycle in the upper stratosphere over latitude for ozone at 3 hPa in %/100 units of the F10.7cm radio flux (top) and temperature at 1 hPa in K/100 units of the F10.7 cm radio flux (bottom). Note that the Randel&Wu data represents the 40 km height values, and the SSU data the 45 km values.

ity between the CCMs than the ozone signal. Most models show a relatively flat response of about 0.5 K between 60°S and 60°N. The ERA-40 response, on the other hand, shows a peak response at equatorial latitudes and decreases to higher latitudes. As with the ozone data sets, there is significant variation between the different observational data sets (Gray *et al*., 2010). However, neither observational data set demonstrates statistical significance poleward of ~30°, so validation of the models at these latitudes is difficult. The difficulty of reproducing the latitudinal structure of the solar signal is also apparent in the latitudinal structure of the annual-mean solar regression coefficient for column ozone (see supplementary material, Figure S8.8). The spread in model responses is especially large at high northern latitudes due to dynamical interactions. Very large deviations are seen for EMAC and WACCM at high latitudes. These differences might be related to differences in the transport schemes, because transport and dynamical processes in lower stratospheric ozone dominate the distribution of column ozone variations. Both models have a large cold bias in the SH (Chapter 4) and too low Cl_y in the vortex. In addition, WACCM has too much mixing in the TLS and EMAC has subtropical and polar lower stratospheric barriers that are too weak (Chapter 5).

Since the spread in both the modelled and observed solar cycle signal is so large, especially at high latitudes, no further diagnostics are presented to investigate dynamical feedback mechanisms (Kodera and Kuroda, 2002), such as those shown by Matthes *et al*. (2003) who investigated GCMs in which the ozone solar signal was imposed. Recent model studies (*e.g*., Matthes *et al*., 2006; Gray *et al*., 2006; Ito *et al*., 2009; Matthes *et al*., 2010) suggest that these dynamical feedback mechanisms are particularly difficult to reproduce, because of possible non-linear interaction with the QBO, and are currently best investigated in more idealised model studies in which the various influences can be examined separately.

Several studies have highlighted the limitations of the MLR analysis with respect to the time period chosen and the difficulty of separating autocorrelated signals such as

the solar and the QBO, volcanic or ENSO signal in the equatorial lower stratosphere (*e.g.*, Smith and Matthes, 2008; Marsh and Garcia, 2007; Austin *et al.*, 2008; Frame and Gray, 2010). The sensitivity of the MLR analysis presented here has been tested using different time periods, *i.e.*, 1960-2004 and 1979-2004. The details of the results are not very sensitive to the period chosen, apart from the magnitude of the response changes, which is larger for the shorter time period. This allows confidence in the performance of the MLR method, provided careful representation is made of all possible basis functions as well as an autocorrelation of the residuals.

8.6 QBO in Ozone

In the tropical stratosphere, the QBO in zonal wind is a major driver of ozone variability (see Baldwin *et al.*, 2001). Typically, however, general circulation models of the atmosphere have difficulties in spontaneously simulating the QBO. In order to simulate a realistic QBO, a model should be able to support a realistic spectrum (temporal and spatial) of upward propagating waves in the tropics. This is a major challenge, because this spectrum of waves depends on many technical aspects of an atmospheric general circulation model, such as tropical convection parameterisation, stability of the troposphere, SSTs, vertical and horizontal resolutions and atmospheric gravity wave parameterizations (*e.g.*, Scaife *et al.*, 2000; Giorgetta *et al.*, 2002, 2006; Shibata and Deushi, 2005).

A model that does not appropriately simulate the QBO in zonal wind, also severely misrepresents the natural ozone variations associated with the QBO (Punge and Giorgetta, 2008). Therefore some modelling groups have imposed the QBO by assimilation techniques (*i.e.*, nudging, see Chapter 2) of either the equatorial zonal winds or the vorticity. The models that assimilate the QBO in the REF-B1 simulation are shown in Chapter 2 (Table 2.8), and referred to as Group C in **Table 8.4**. Although the assimilation of the QBO should alleviate the biases in the ozone distribution associated with the problem of properly representing the QBO, it unfortunately removes the predictive capability of a model. While it is therefore possible to evaluate the response of ozone to a prescribed QBO forcing, a prediction of future ozone behaviour related to the QBO is impossible with this methodology.

Table 8.4: Tropical variability in the CCMVal-2 models. Models in Group A and Group B do not assimilate the QBO. Models in Group C assimilate the QBO (via nudging of the zonal winds or vorticity). Group A models have basis functions in the MLR analysis set to zero. Models in Group B and C are included in the MLR analysis.

GROUP A	GROUP B	GROUP C
CMAM	AMTRAC3	CAM3.5
CNRM-ACM	MRI	CCSRNIES
GEOSCCM	UMETRAC	E39CA
LMDZrepro	UMUKCA-METO	EMAC
	UMUKCA-UCAM	NiwaSOCOL
	UMSLIMCAT	SOCOL
		ULAQ
		WACCM

8.6.1 Equatorial Variability and the QBO signal in the stratosphere

Figure 8.14 shows the vertical profile of the variability of zonal-mean zonal wind (left) and ozone in DU/km (right) at the Equator (average 5°S-5°N) computed as the standard deviation of the monthly values for the period 1960-1999. In both model and observational data, the linear trend and the annual cycle have been removed. In addition, a band pass filter has been applied to the time series to extract only those oscillations with periods between 9-48 months. The upper panels include only the models with nudged QBO (Group C of Table 8.4), while the bottom panels include the rest of the models (both Groups A and B of Table 8.4).

The models in Group C are characterized by substantial variability, from ~10 m/s up to ~18 m/s in zonal-mean zonal wind and in the range 0.7 to 1.5 DU/km in ozone, as expected because of the assimilation. In addition to the main peak near 20 hPa in zonal-mean zonal wind, some models (NiwaSOCOL, SOCOL, and to a lesser extent WACCM) show a secondary peak in zonal wind variability near 1 hPa. This variability could be excessive QBO modulation of the SAO at these altitudes, a possible side effect of the applied nudging.

In the models that did not assimilate the QBO (lower panels), the zonal wind variability clusters into two groups: 4 models (GEOSCCM, LMDZrepro, CNRM-ACM, and CMAM) have variability less than 5 m/s (Group A); and 6 models (AMTRAC3, MRI, UMETRAC, UMUKCA-METO, UMUKCA-UCAM, and UMSLIMCAT) have variability in the range 7 to 22 m/s (Group B). Group A severely under-estimates the zonal wind variability, leading to the conclusion that the QBO in zonal wind is not internally generated to a sufficient degree in these models. For consistency in these models the QBO basis functions in the MLR analysis are set to zero (see Table 8.4). The variability in Group B is much more realistic when compared with ERA-40 reanalysis, although the maximum amplitude is both overestimated (UMETRAC and UMSLIMCAT) and under-estimated (AMTRAC3, MRI, UMUKCA-METO, UMUKCA-UCAM) and tends to be located at lower pres-

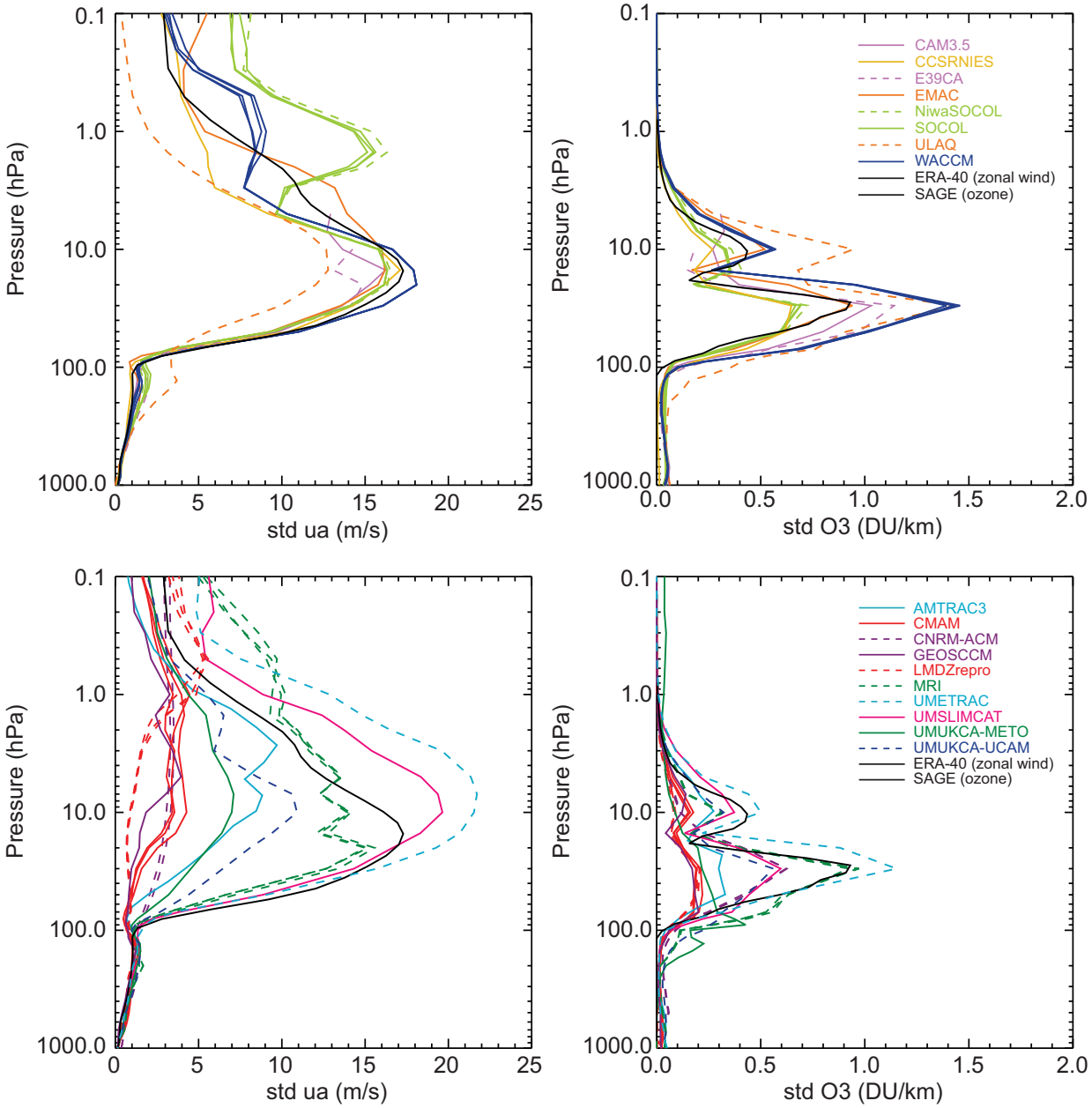

Figure 8.14: Monthly zonal-mean standard deviation of zonal-mean zonal wind (left, m/s) and ozone (right, DU/km) averaged from 5°S to 5°N. Results from the CCMVal-2 CCMs (in colour), ERA-40 (left, black), and SAGE data (right, black). From de-trended, de-seasonalised and filtered (9-48 months) time series. Top panels: Group C CCMs, bottom panels: Groups A and B CCMs.

sure (*i.e.*, higher in the atmosphere) than observed.

The observed interannual variability of ozone (right panels) shows two maxima (10 and 30 hPa). These maxima are due to the modulation of the ozone chemistry in the middle stratosphere (10 hPa, see Chapter 6) and the advection of ozone by the secondary meridional circulation (30 hPa, see Chapter 5) in the lower stratosphere (Gray and Chipperfield 1990). The models with a nudged QBO (Group C, upper right panel) show the clear double peak structure, in phase with the Randel&Wu observations, although with a wide range of magnitudes. The models without QBO nudging (lower panel) that showed little variance in wind at the equator also simulate little variance in ozone (Group A). The exception in Group A is the CNRM-ACM model, with a 0.6 DU/km peak in ozone variability at 30 hPa. The time series of the ozone vertical distribution is shown in the supplementary material (Figure S8.9) for CNRM-ACM. It shows that these variations are not downward propagating, consistent with the fact that this model does not simulate the QBO. Possibly, these variations are

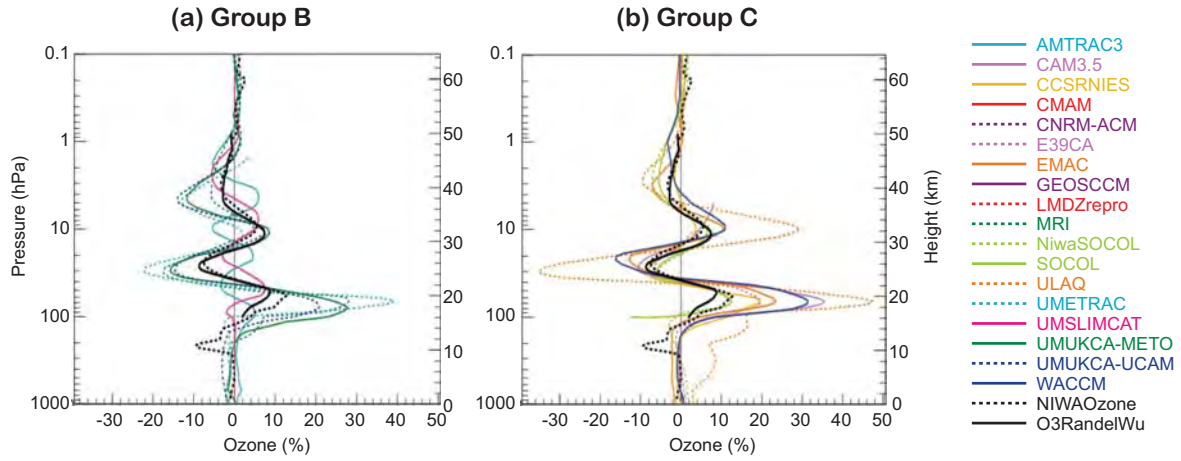

Figure 8.15: Annual mean QBO regression coefficient (multiplied by 30 m/s) in ozone in percent at equatorial latitudes (5°S-5°N) from the CCMVal-2 CCMs (1960-2004) and observations (NIWA-3D ozone, 1979-2004; Randel&Wu ozone, 1979-2005). (a) Group B CCMs. (b) Group C CCMs.

associated with ENSO, which can still be present in the applied band pass filter (9-48 months). A similar behaviour was previously reported for a CCMVal-1 model (Punge and Giorgetta, 2008). With the exception of UMUKCA-METO, the models in Group B show the double peak in ozone variability, each of them to a different degree.

Apart from this very broad comparison, there does not seem to be a linear relationship between the variability in zonal winds and ozone in Groups B and C, suggesting a range of sensitivity of the ozone to the zonal wind QBO, which is independent of whether it is imposed or internally generated. In particular, in Group B the UMSLIMCAT model appears to be characterized by low ozone sensitivity, given its higher than observed wind variability but half than observed ozone variability at 30 hPa. In Group C, the ULAQ and WACCM models appear to have a higher than observed ozone sensitivity, while the NiwaSOCOL and SOCOL sensitivity is lower than observed. Note that the two SOCOL models and WACCM are very close to observations in their zonal wind variability at 30 hPa, while they differ by a factor of two in their ozone variability.

An alternative measure of the models' representation of the ozone QBO is the vertical distribution of the annual mean equatorial (5°S-5°N) QBO regression coefficient from the MLR analysis (which is represented in terms of ozone mixing ratios for all models and NIWA-3D observations and ozone density for the Randel&Wu ozone). One coefficient is shown in **Figure 8.15a** (the orthogonal one is not shown) for the models in Group B (internal QBO-like oscillation) and in Figure 8.15b for models with nudged QBO (Group C). For a better comparison of the QBO signal between the models and observations, the QBO regression coefficient has been multiplied by the typical mean QBO amplitude of 30 m/s. Most of the models in both groups capture well the vertical structure of the QBO signal, but tend to overestimate the magnitude of the response, especially in the lower stratosphere. In the case of ULAQ, this overestimation is particularly evident (more than a factor 2

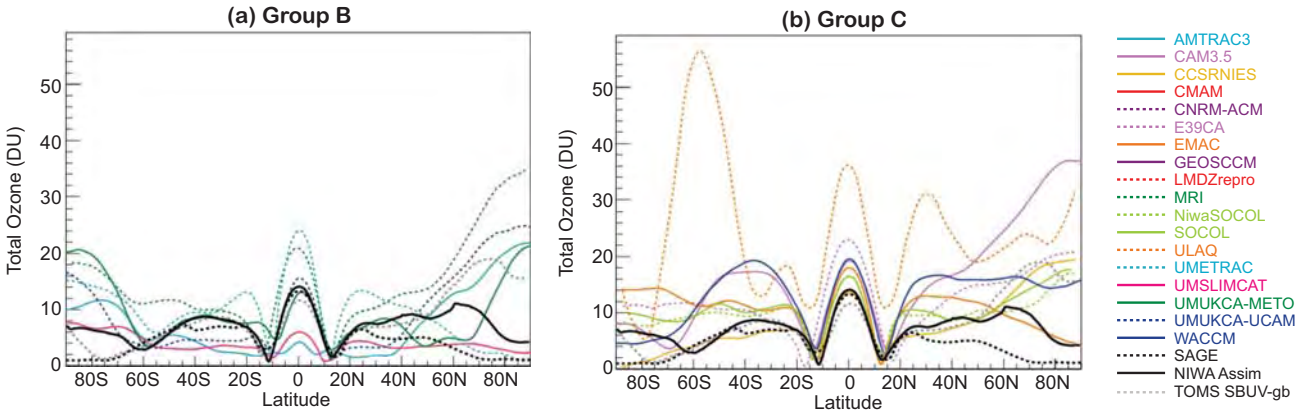

Figure 8.16: Latitudinal distribution of the annual mean QBO amplitude (multiplied by 30 ms-1) in column ozone (DU) from the CCMVal-2 CCMs (1960-2004) and the following observations: TOMS/SBUV+gb (1964-2004), SAGE (1979-2005), and NIWA-column ozone (1979-2007). (a) Group B CCMs. (b) Group C CCMs.

throughout the stratosphere). Among the Group B models, AMTRAC3 and UMSLIMCAT under-estimate the magnitude of the response, and AMTRAC3 also clearly misrepresents the vertical phase of the pattern. The rest of the models in both groups capture the vertical phasing well, and this is particularly true for the nudged QBO models.

8.6.2 QBO signal in column ozone

The latitudinal distribution of the annual mean QBO amplitude from the MLR analysis of column ozone amounts is presented in **Figure 8.16**. All models show a maximum at the equator and minima in the subtropics, in good agreement with observations. Poleward of 20° in both hemispheres, the spread of model results clearly increases. Considering both groups, the equatorial amplitude of the QBO signal in column ozone is within the range of the observations for CCSRNIES, UMUKCA-METO and UMUKCA-UCAM, while it is severely under-estimated by AMTRAC3 (also featuring a flat latitudinal distribution) and UMSLIMCAT and overestimated by the rest (*i.e.*, the majority) of the models. ULAQ shows the largest QBO amplitude variations, consistent with the overestimation of both variability peaks in Figure 8.14 (right), but inconsistent with the under-estimation of the wind variability. For the nudged QBO models, problems with the nudging techniques might contribute to the highlighted differences. In general, however, many biases can contribute, such as errors in the QBO-induced residual mean circulation in the lower to mid-stratosphere, the latitudinal extension of the QBO, as well as errors in the vertical gradient of ozone in the vicinity of the induced motions.

Figure 8.17 shows the temporal evolution of the time series reconstruction of the QBO signal from the MLR analysis of column ozone (averaged from 5°S-5°N) for the models and TOMS+gb, Randel&Wu and NIWA-column data. As expected, models that nudge the QBO closely follow the phase of the observed QBO in column ozone,

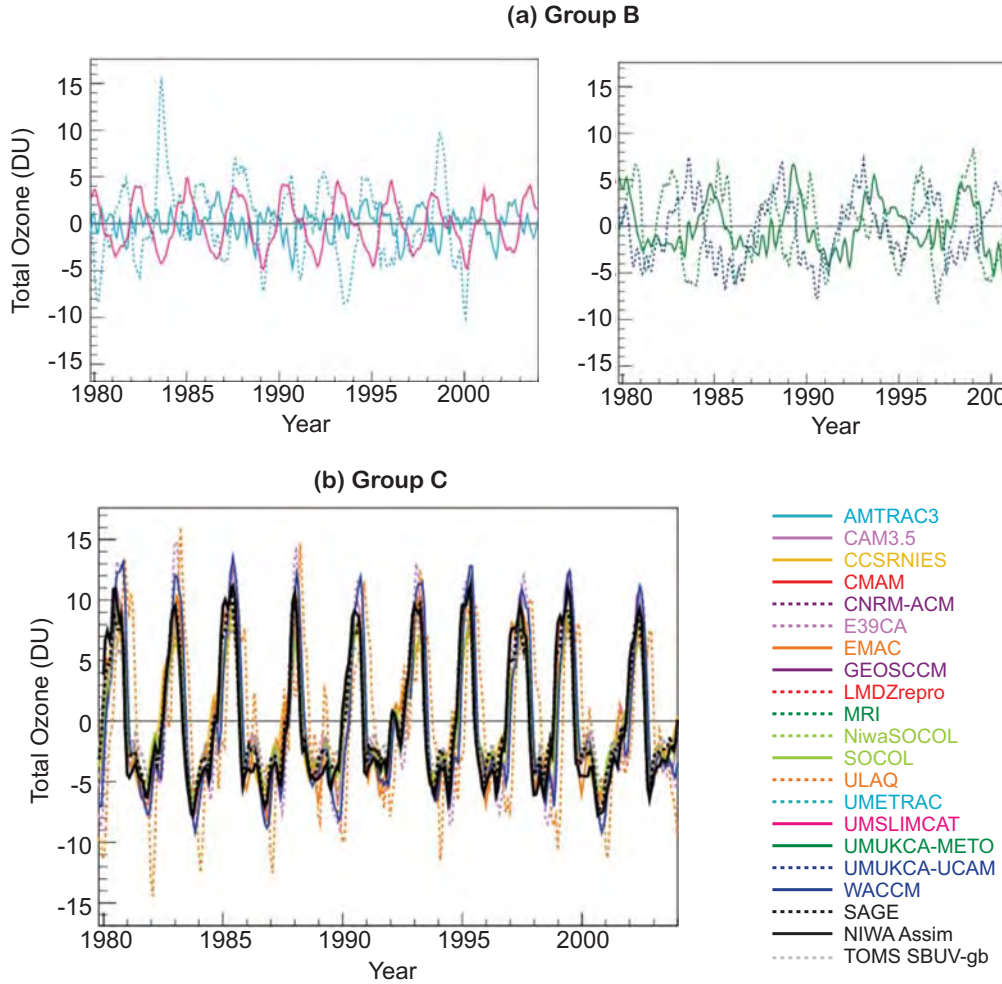

Figure 8.17: Reconstruction of the QBO contribution to the monthly zonal mean column ozone (DU) averaged from 5°S to 5°N. Results from the CCMVal-2 CCMs (in colour; 1960-2004) and the TOMS/SBUV+gb data (1964-2004), SAGE data (1979-2005), and NIWA-column ozone (1979-2006). (a) Group B CCMs. (b) Group C CCMs.

although some of them overestimate the amplitude, consistent with Figure 8.16 and right panels in Figure 8.14. The variability in the Group B models is not expected to be in phase with observations. For the Group B models, Figure 8.17 provides information on the period of the modelled QBO variability in ozone. Among this group, MRI, UMETRAC, UMSLIMCAT show a period close to the observed (~28 months), while UMUKCA-METO and UMUKCA-UCAM overestimate (by almost a factor 2) the typical QBO periodicity. Also note that UMETRAC shows some sporadic large amplitude episodes. AMTRAC3 shows higher frequency (~ 1 year^{-1}) small oscillations and Figure 8.17 therefore confirms that the variability diagnosed in AMTRAC3 is not consistent with the known features of the QBO signal in ozone. From this it can be concluded that the QBO signal in ozone is not represented in AMTRAC3.

8.7 ENSO Signal in Ozone

The El Niño Southern Oscillation (ENSO) is a tropical atmosphere-ocean phenomenon and a source of large-scale climate variability for the atmosphere–ocean system. Its influence on the stratosphere has been increasingly recognised, with the advent of ensemble modelling and with the availability of longer observational data sets. Most of the published work has focused on the polar lower stratosphere, because of the established teleconnections between the warm phases of ENSO and the mid-latitude North Pacific region (*e.g.*, Hoerling *et al.*, 1997) which can favour the enhancement of mid-latitude planetary waves

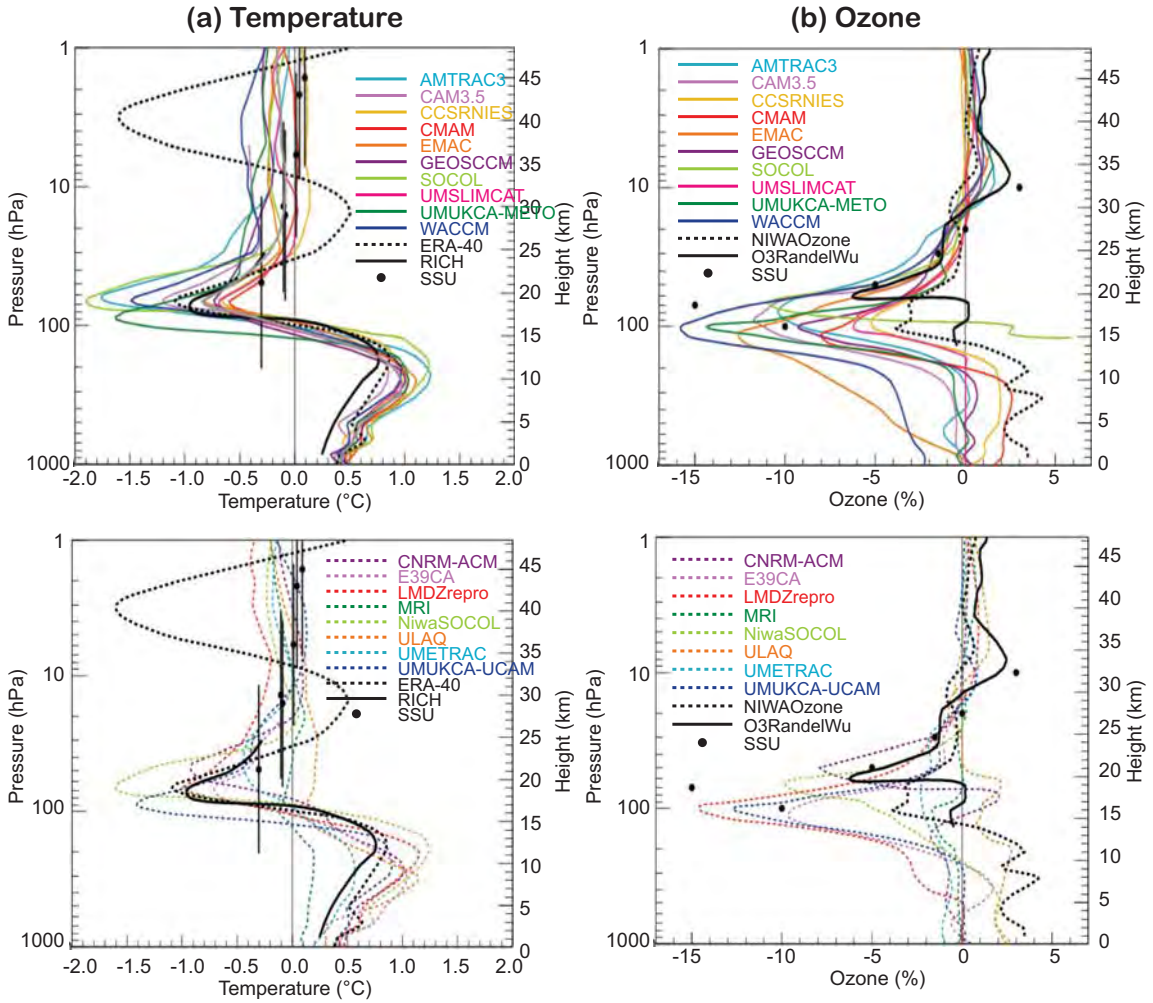

Figure 8.18: Annual mean tropical (25°S-25°N) ENSO regression coefficients from 1000 to 1 hPa for (a) temperature (K) and (b) ozone (%) from the CCMVal-2 CCMs (1960-2004) and observations: RICH radiosonde data (1960-2004), SSU data (1979-2005), and ERA-40 data (1979-2004); NIWA-3D ozone (1979-2004); Randel&Wu ozone (1979-2005). The ENSO coefficients have been multiplied by 2.5 K. In order to better distinguish, the CCMs solid (top) and dashed (bottom) lines have been separated. Black dots represent the Randel&Wu ozone data analysis from Randel et al. (2009).

and their upward propagation into the stratosphere. Due to this increase in extra-tropical stratospheric planetary wave activity, warm ENSO events have been found to be associated with anomalous warming and anomalously high geopotential heights in the polar stratosphere, both from observations (van Loon and Labitzke, 1987; Brönnimann *et al*., 2004; Camp and Tung, 2007; Garfinkel and Hartmann 2007) and comprehensive modelling of the troposphere-stratosphere system (Sassi *et al*., 2004; Manzini *et al*., 2006; Garcia-Herrera *et al*., 2006). These signals in temperature are consistent with signals in ozone during ENSO events (Fischer *et al*., 2008; Steinbrecht *et al*., 2006; Brönnimann *et al*., 2006). The ENSO signal in column ozone for the CCMVal-1 models is discussed in Cagnazzo *et al*. (2009). The polar warming and enhanced ozone associated with warm ENSO events are a manifestation of a stronger Brewer-Dobson circulation during ENSO and a negative signal in both temperature and ozone is therefore also expected in the tropics (Free and Seidel, 2009; Randel *et al*., 2009; Manzini, 2009).

The ENSO tropical signals in annual mean temperature (left) and ozone (right) from the MLR analysis are shown in **Figure 8.18**. The maximum ENSO temperature and ozone signals occur in the lower stratosphere (~70 hPa), and the patterns are qualitatively similar between models and observations. Most models show a cooling in the lower stratosphere that surrounds the observed cooling of ~1 K, and values from the CCMs vary over approximately a factor of two, with MRI and ULAQ the only outliers. In the upper troposphere, the observed ENSO warming is about 0.6 K and generally lower than that estimated by the models. The node at the tropopause level (where the regression temperature coefficient changes sign) is well reproduced by the models. The modelled ENSO tropical signal in temperature is therefore consistent with Free and Seidel (2009). Between 150 and 50 hPa a reduction in ozone, ranging from -5 to -15%, is found for most models (with MRI and ULAQ again outliers). The comparison with observations shows results from the NIWA-3D and Randel&Wu data sets, and also results from the SAGE I+II data reported in Randel *et al*. (2009). The difference between the latter two results are mainly due to the differences in detail of the respective regression models (the MLR here uses volcanic proxies, while Randel *et al*. (2009) omit volcanic periods). It therefore appears that the ENSO signal is especially sensitive to these differences, because of the overlap of ENSO warm events with the El Chichon (1982) and Pinatubo (1991) volcanic eruptions (Randel *et al*., 2009). In summary, the model results in Figure 8.18 are broadly consistent with Randel *et al*. (2009), while the ENSO ozone signals derived from the NIWA-3D and Randel&Wu data are somewhat smaller. These differences in the observations serve to highlight the sensitivity to the regression analysis for the ENSO signal and the possibility that the NIWA-3D and Randel&Wu continuous data time series derived from MRL analysis might not contain all of the observable signals. Note also that ozone variability in the lower tropical stratosphere arises from the combined effects of a number of factors, the QBO, ENSO, the solar cycle and volcanic aerosols: A clear challenge for the MLR analysis approach.

To evaluate the ENSO signal in ozone for the northern polar cap, the methodology developed for the CCMVal-1 models by Cagnazzo *et al*. (2009) has been applied to the CCMVal-2 models. The results are shown in **Figure 8.19**, for the relationship between the February-March averaged north polar cap ENSO response in the temperature and column ozone fields. As in Cagnazzo *et al*. (2009), the ENSO signal has been extracted by calculating difference fields between composites of warm ENSO and NEUTRAL years. Warm ENSO years are defined as the four largest events in the period 1980-1999 and NEUTRAL years are the remaining years when both the four largest warm and cold ENSO events have been excluded. During the period (1980-1999), the cold ENSO events are smaller in magnitudes and have not been found to significantly affect the stratosphere (Manzini *et al*., 2006).

In agreement with Cagnazzo *et al*. (2009), a clear positive correlation is found between the modelled column ozone and temperature anomalies at high latitude (0.87, significant at more than 99.9%) supporting the idea that anomalies in temperature and column ozone are influenced by the same (Brewer-Dobson circulation) mechanism. This linear relationship is consistent with the one expected from interannual variability: the slope parameter deduced from Figure 8.19 (about 5.5 DU/K) is comparable, within the sampling uncertainity, to the slope calculated using the ERA-40 temperature and NIWA-column ozone from the individual years (Figure 8.8), as well as the one deduced from the CCMVal-1 models, shown in Cagnazzo *et al*. (2009). Therefore, Figure 8.19 also shows that the spread in the CCMVal-2 model responses is due to internal variability. However, for the CCMVal-2 models there is a less distinct dominance of the cases clustered in the upper-right quadrant (where the signature of observations is located), suggesting that a smaller percentage of the models achieve positive temperature anomalies and increased ozone during ENSO, than the CCMVal-1 models discussed by Cagnazzo *et al*. (2009).

Cagnazzo *et al*. (2009) have shown that CCMVal-1 model simulations that did not have a strong enough extra-tropical ENSO teleconnection pattern in the troposphere did not report a temperature and ozone signal in the stratosphere. This result is found also for the CCMVal-2 models, although in the case of CCMVal-2, models with a significant tropospheric ENSO teleconnection also show negative temperature and decreased ozone responses (not shown). The spread of the CCMVal-2 modelled response therefore

appears to be influenced more by internal variability than that of the CCMVal-1 models. Distinguishing the role of internal variability and model biases in the ENSO response is therefore less straightforward for the CCMVal-2 models. The inclusion and/or a more detailed representation of additional forcings that may interfere with the ENSO signal, such as the QBO, the solar cycle and aerosols from volcanic eruptions, could possibly explain the differences between CCMVal-1 and CCMVal-2 simulations. Given the close connections between the CCMs that participated in both projects, the CCMVal-1 and CCMVal-2 results are not actually statistically different.

8.8 Volcanic Aerosols

Volcanic eruptions can have a significant impact on stratospheric ozone. Eruptions of sufficient strength inject SO_2 into the stratosphere, which is then chemically converted to sulphate aerosols. Volcanic induced ozone changes are related to the effect of volcanic sulphate aerosols on the chemical composition and the radiative balance of the lower stratosphere. Volcanic aerosols provide surfaces for heterogeneous reactions to occur, which can alter the partitioning of catalytic ozone destroying families including NO_x and ClO_x. Volcanic aerosols also reflect and scatter incident solar radiation, leading to changes in the photolysis of chemical species, and absorb outgoing longwave radiation, leading to additional heating of the lower stratosphere.

Observed column ozone reduction after the Mt. Pinatubo and the El Chichón eruptions range from about 2% in the tropics to about 5% (Pinatubo) and 2-3% (El Chichón) in mid-latitudes (Angell, 1997; Solomon *et al*., 1998). Very large ozone losses were observed after the Mt. Pinatubo eruption at high northern latitudes in February and in March, for example Randel *et al*. (1995) found losses of 10% in total column ozone in 1992 northward of 60°N and 10-12% in 1993. Ozone-sonde profiles after the Mt. Pinatubo eruption show that the concentration did not decrease uniformly at all altitudes (Hofmann *et al*., 1993; Grant *et al*., 1994). After the Agung eruption in 1963 a slight increase in global total column ozone was found (Angell, 1997), possibly due to the suppression of nitrogen oxides in the low-chlorine conditions (Tie and Brasseur, 1995).

The methods used to simulate the volcanic impact in the models have been introduced in detail in Chapter 2. Heterogeneous chemical reactions on the volcanic aerosol surfaces are calculated using a prescribed zonal-mean aerosol surface area density (SAD) time series. In the CCMVal-2 model runs, most models have prescribed SADs using the data set compiled and made available through the SPARC Assessment of Stratospheric Aerosol Properties (Thomason and Peter, 2006). The radiative effects of volcanic aerosols have been incorporated into the model in a number of different ways or, in some cases, completely neglected. Chapter 2 (Table 2.18) summarizes the different methods used by the different models, which include (1) no simulation of direct radiative effects, (2) prescribed heating rate anomalies based on offline radiative calculations, (3) online radiative calculations using

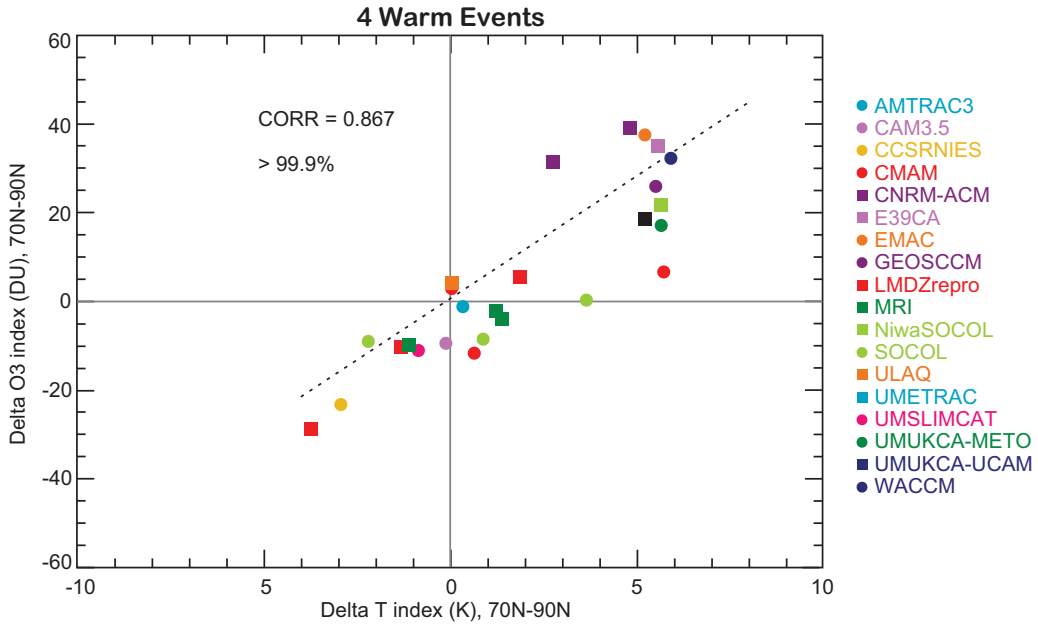

Figure 8.19: Scatter plot of the February-March polar cap ENSO anomaly in column ozone (DU) versus temperature (K, 30-70 hPa average). Black star: NIWA-column ozone versus ERA-40 temperature signature. Colours: CCMVal-2 CCMs. The polar cap averages are computed over 70°N-90°N.

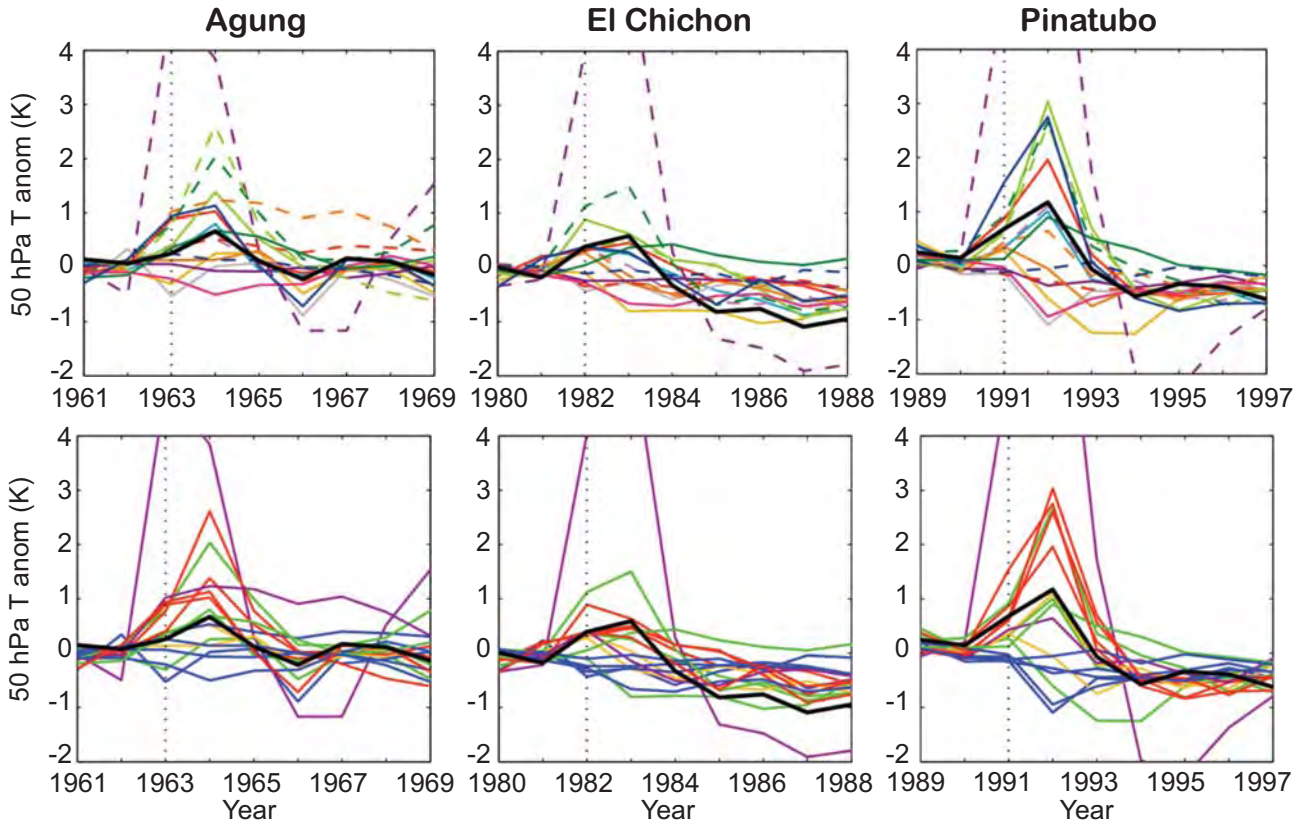

Figure 8.20: Annual mean global mean 50 hPa temperature anomalies from pre-volcanic conditions for the Agung, El Chichón and Pinatubo eruptions. Top: model results colour-coded by model. Bottom: results colour-coded by type of volcanic heating parameterisation used, including: optical properties derived from SADs (red), optical properties from SAGE/GISS data set (green), prescribed heating rate anomalies (yellow), none (blue), full aerosol microphysics (purple). ERA-40 50 hPa temperature anomalies are shown in both plots in black.

aerosol properties estimated from observations, (4) online radiative calculations using optical depths derived from the SPARC SAD data set (also based on observations) and (5) full microphysical modelling of volcanic aerosols based on prescribed stratospheric influx of volcanic SO_2.

8.8.1 Global mean temperature response

The result of volcanic forcing on stratospheric temperatures can be seen most simply through inspection of global-mean annual-mean temperature time series. These are shown at 50 hPa in **Figure 8.20** (top panel), as anomalies from pre-volcanic conditions for the three eruptions of the 1960-2000 time period: Agung (1963), El Chichón (1982) and Mt. Pinatubo (1991). The anomalies are calculated as deviations from the mean of the 5 years (3 years for Agung) preceding the year of the eruption. There is a considerable spread in the post-volcanic eruption temperatures in the models. For example, in 1992 after the Pinatubo eruption, the changes in 50 hPa temperature range from +9 to -1 K, while the observations show a +1 K change. CNRM-ACM appears as an outlier in this diagnostic, with temperature increases much larger than the other models or the observations. This is related to how the radiative scheme responds to the volcanic aerosols. Subsequent runs of the CNRM-ACM model, in which the aerosol properties have been modified to exhibit less absorption, have shown temperature evolution in the range of that of the CCMVal-2 CCMs (Martine Michou, personal communication, 2009). The temperature response in all of the models is strongly dependent on the parameterisation method employed to simulate the direct radiative effects of volcanic aerosol loading. In the lower panel of Figure 8.20 the anomalies have been replotted, but colour-coded by parameterisation method. This plot shows that using aerosol optical depths derived from the SPARC SADs (red: NiwaSOCOL, SOCOL, WACCM, CMAM) leads, at least in the Pinatubo and Agung eruptions, to anomalously large temperature perturbations compared to those estimated from the ERA-40 data set. Those models that did not include radiative effects of volcanic aerosols (blue: CAM3.5, GEOSCCM, LMDZrepro, UMSLIMCAT, UMUKCA-UCAM) show little change in 50 hPa temperature, although two models show modest (~1 K) decreases after the Pinatubo eruption,

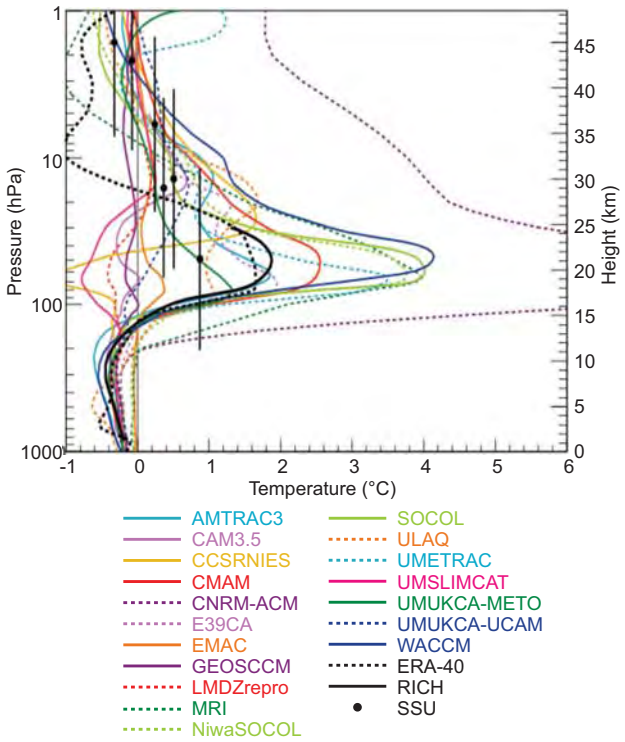

Figure 8.21: Annual mean tropical (25°S-25°N) contribution from the volcanic basis function from CCMVal-2 CCMs (1960-2004) and observations (ERA-40, SSU and RICH) to temperature in Kelvin (K) for Pinatubo (averaged over 24 months after the eruption) from 1000 to 1 hPa.

as might be expected due to chemical induced ozone decreases. Finally, the models which employ optical depth estimates from GISS (green: AMTRAC3, CCSRNIES, MRI, UMUKCA-METO) and those which use prescribed heating rates (yellow: E39CA, EMAC) show (for some models, *i.e.*, AMTRAC3, E39CA, and UMUKCA-METO) quite good agreement with the observations. However, there are also some outliers: *e.g.*, the CCSRNIES model shows cooling after the El Chichón and Pinatubo eruptions even though aerosol radiative heating is included.

8.8.2 Vertical temperature response

Inspection of the vertical structure of the temperature anomalies can help evaluate the reason for the discrepancies between models. **Figure 8.21** shows the annual mean tropical contribution from the volcanic basis function for Pinatubo (responses for Agung and El Chicón are shown in Figure S8.10) averaged over 24 months after the eruption for temperature in the tropics, where the temperature increases are largest. The structure of the anomalies is generally consistent between the models, with maximum heating at ~50 hPa (20 km), in good agreement with observations. There is excellent agreement between the models that show the largest response in the region of maximum heating in Figure 8.21 and those that show the largest temperature response in Figure 8.20. The models which include no direct aerosol heating show a negative sign in their temperature response. A number of outliers in Figure 8.20 also show deviations from the general vertical structure. For example, CCSRNIES, which showed post-volcanic cooling at 50 hPa shows a positive response in Figure 8.21 only at heights above 40 hPa, and negative ones between 50 and 100 hPa. On the other hand, the EMAC response is small and restricted to heights below 50 hPa, which helps explain why the EMAC anomalies of Figure 8.20 are different from the other models using prescribed heating rates. The latitude-height structure of the Pinatubo temperature response is shown in Figures S8.11 and S8.12.

8.8.3 Ozone response

Figure 8.22 shows global-mean, annual-mean total-column ozone anomalies compared with pre-volcanic conditions. Local minima in the years after the El Chichón and Pinatubo eruptions are associated with the effects of the

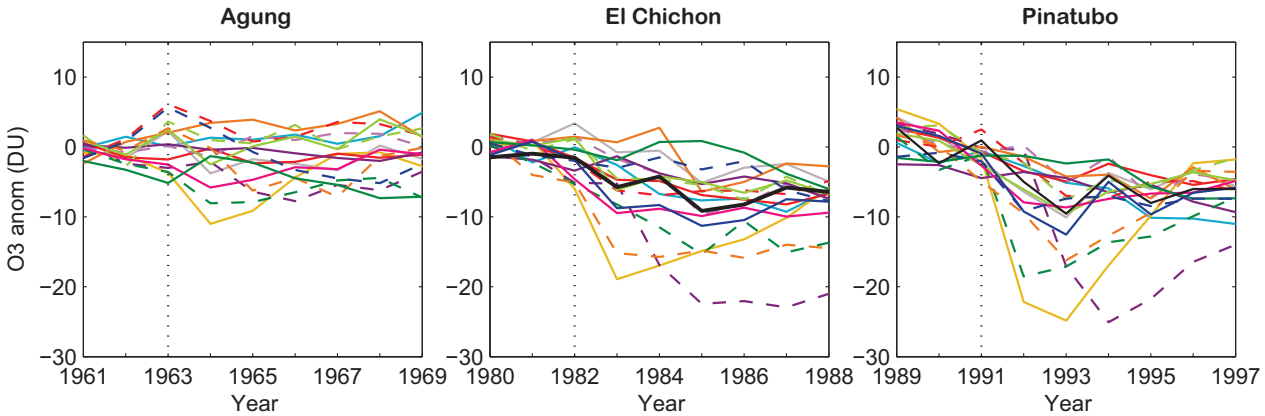

Figure 8.22: Annual mean global mean column ozone anomalies from pre-volcanic conditions for the Agung, El Chichón and Pinatubo eruptions. Ozone anomalies from the TOMS+gb data set are shown in black.

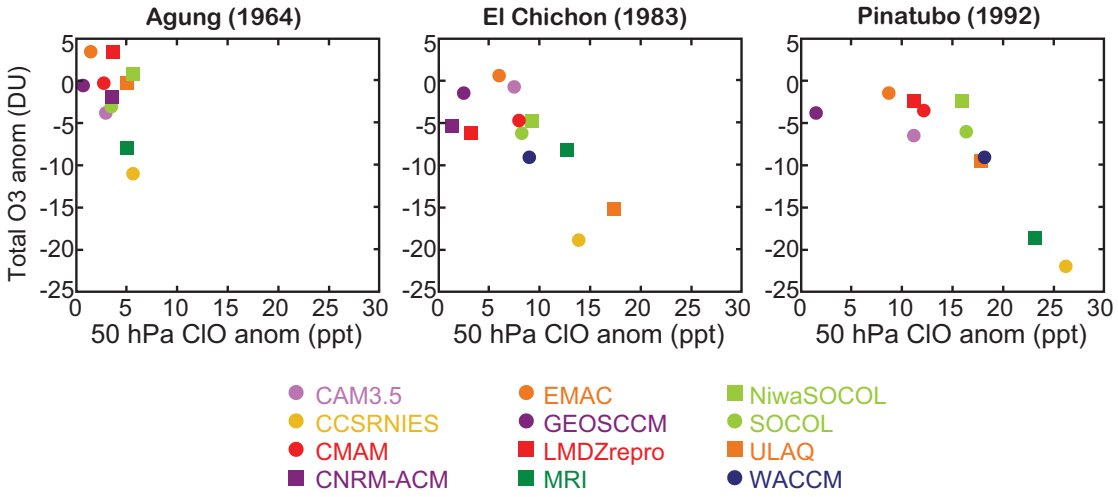

Figure 8.23: Post volcanic eruption annual mean global mean anomalies of column ozone as a function of similarly calculated anomalies in ClO at 50 hPa, for the models that have reported ClO mixing ratios.

volcanic aerosols. Note that in these plots the anomalies are the result of a number of factors including volcanic effects, but also the EESC related trend and the QBO. The observed anomalies after the El Chichón and Pinatubo eruptions were of the order of 10 DU. There is a large degree of scatter in the model results, ranging from some models showing post-volcanic decreases of up to 15-20 DU (CCSRNIES, MRI, ULAQ) and, for El Chichón, small post-eruption increases (EMAC, UMUKCA-METO). For the Agung eruption, some models show a slight increase in the year of the eruption, however, it is impossible to attribute any ozone changes to the volcanic effects, as the spread in modelled values stays relatively constant over the time span shown. Slight differences in the vertical structure of the ozone response (Figure S8.13) can help shed light on why the global-mean total ozone time series in Figure 8.22 differ. The models generally show the largest ozone loss at 30 hPa (25 km). After Pinatubo, two models (CCSRNIES and ULAQ) show responses at lower heights than the other models and these two models are among the models with the largest total ozone losses. The latitudinal distribution of total ozone losses is shown in the supplementary material (Figure S8.14).

Since a large amount of volcano-related ozone loss is related to heterogeneous chemistry, one would expect the models with largest ozone loss to have the largest amounts of chlorine activation. **Figure 8.23** confirms this, showing the ozone anomaly in the year following each eruption as a function of the anomaly in ClO at 50 hPa. For each eruption, there is a relatively linear relationship between ozone loss and chlorine activation. Note that by choosing to look only at the year after each eruption, the relationship between ClO and ozone for CNRM-ACM is not well represented by these plots, since this model displays maximum ClO and ozone anomalies three years after each eruption, and in fact shows negative ClO anomalies for the first year after the Mt. Pinatubo eruption (with large increases afterwards). Latitude-time plots of ClO (not shown) and total ozone abundances (Figure S8.14) confirm that the models with largest total ozone loss, including CCSRNIES and ULAQ, are characterized by chlorine activation and ozone loss extending from the tropics to the high latitudes. Thus, the cause of the anomalous ozone loss in these models is the anomalous chlorine activation, which may itself be related to biases in total chlorine since both models received low grades representing Cl_y in the middle stratosphere (Chapter 6) or too low stratospheric temperatures (Chapter 4).

An interesting feature of the observed ozone loss after the Mt. Pinatubo eruption is the hemispheric asymmetry: NH ozone levels (especially in mid-latitudes) have been observed to decrease after the eruption, while levels in the SH were relatively unperturbed (WMO, 2007). None of the CCMVal-2 models reproduce the observed hemispheric asymmetry in post-Pinatubo ozone loss, for either full hemispheric means or for mid latitudes (see Figures S8.15 and S8.16). Most models have post-Pinatubo SH ozone loss which is comparable to or greater than that observed, while NH ozone loss is less than that observed. Whether or not the models have a QBO (internally generated or nudged) does not appear to have an appreciable effect on this result.

8.9 Conclusions

Although the MLR analysis is a powerful tool for synthesizing the relative influence of the variability sources on natural ozone variation, it cannot take into account the fact that the net effect of the natural variations on ozone is usually a non-linear combination of the single contributions of variability factors. Non-linearities have been reported for

the combined ENSO and QBO signal (Calvo *et al*., 2009), the solar-QBO and volcanic signals (Lee and Smith, 2003), solar-QBO signals (Smith and Matthes, 2008; Camp and Tung, 2008; Matthes *et al*., 2010), the solar-SST signal (Marsh and Garcia, 2007; Austin *et al*., 2008), and ENSO, QBO, and solar interconnections (*e.g*., Kryjov and Park, 2007; Kuroda, 2007; Kodera *et al*., 2007). Many of these inter-connections of the natural variability sources are objectives of current research.

Another limitation of the assessment in this chapter is the relatively short observational record which limits the statistical significance of many of the responses to individual components. This is especially true for the 11-year solar cycle, where only data for two and a half cycles are available, and for ENSO, a relatively sporadic event, usually occurring with a wide variety of amplitudes. Additionally, large volcanic eruptions coincided with solar maximum phases of the solar cycle. Another limitation of the available ozone observational time series is that they are reconstruction by statistical models (usually MLR analysis) in order to provide a continuous time series without missing data. Therefore, there is the possibility that the MLR analysis of the reconstructed time series might return signals affected by the periods with missing data.

Because of these limitations, it is still very difficult to quantitatively evaluate (grade) the model performance by individual natural variability factor, especially for the solar cycle, ENSO and volcanoes, and relate their relative importance to the evolution and prediction of stratospheric ozone. Note that Dameris *et al*. (2006) show a delay of ozone recovery due to solar cycle effects.

Given that estimates of the annual cycle in ozone are the most reliable, the quantitative evaluation of the model performance is carried out only for the climatology and interannual variability of the annual cycle in ozone (**Figure 8.24**, **Table 8.5**). The performance of the QBO signal in ozone could be a second candidate for a quantitative evaluation. However, the modelling of this phenomenon in CCMs is in a too primitive stage to apply performance metrics.

For the case of the ozone annual cycle climatology and interannual variability, the model performance is quantified following Taylor (2001). The respective correlations and normalised standard deviations discussed in Sections 8.3 and 8.4 are combined in one grade by means of Equation 5 of Taylor (2001). The results are summarized in matrix form in Figure 8.24. Thereafter, the information in Figure 8.24 is used in the following summaries, by variability factor and model-by-model.

8.9.1 Summary by process

Summary on annual cycle

The comparison with MLS data shows that the processes leading to the annual cycle in the upper stratosphere are well captured by the models: the anti-correlations between temperature and ozone at 1 hPa are broadly captured and provide a simple check of photolysis scheme (Section

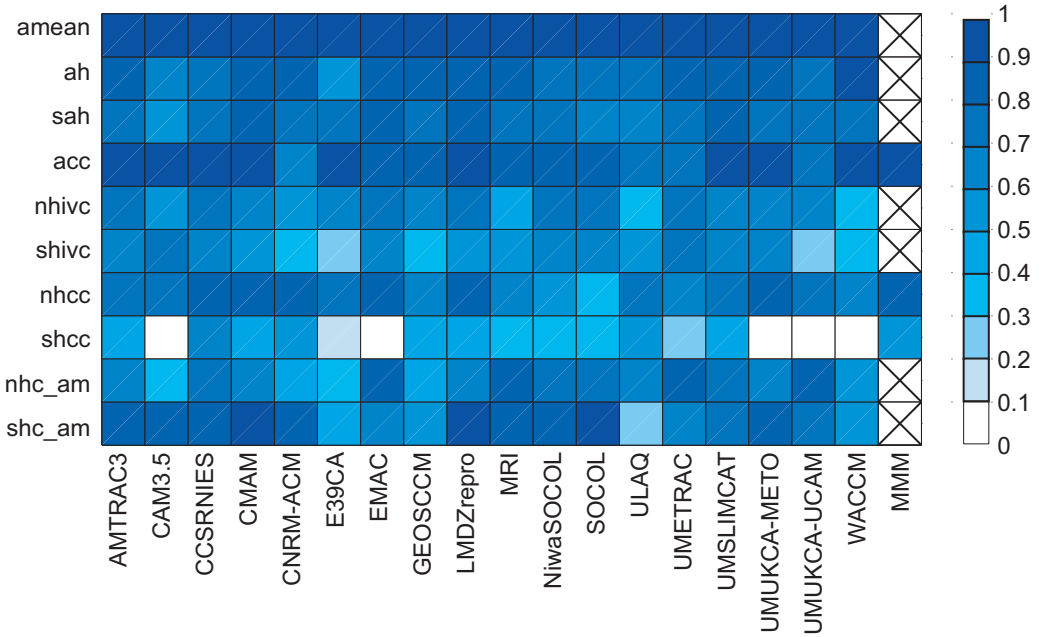

Figure 8.24: Matrix displaying the model performance (see colour bar), following Equation 5 of Taylor (2001), for the normalised Taylor diagrams discussed in the chapter. See Table 8.5 for definitions of the assessment factors.

Table 8.5: List of metrics used in Chapter 8.

Metric	Description	Details
amean	Annual zonal-mean ozone	500-1 hPa, 90°S-90°N
ah	Annual harmonic in ozone from the MLR analysis	500-1 hPa, 90°S-90°N
sah	Semiannual harmonic in ozone from the MLR analysis	500-1 hPa, 90°S-90°N
acc	Annual cycle of near global column ozone	60°S-60°N, January to December climatology
nhivc	Monthly standard deviation of column ozone	60°N-90°N, January to December
shivc	Monthly standard deviation of column ozone	60°S-90°S, January to December
nhcc	Column ozone climatology	60°N-90°N, January to December
shcc	Column ozone climatology	60°S-90°S, January to December
nhc_am	Northern annular mode - ozone relationship	60°N-90°N, March
shc_am	Southern annular mode - ozone relationship	60°S-90°S, November

8.3). The magnitude of the annual cycle and the transition to summer conditions are also well reproduced by the models. However, in the lower stratosphere a few models (UMUKCA-METO and UMUKCA-UCAM) do not reproduce the anthropogenic deviation of the annual cycle (polar ozone depletion) that dominates the late winter and spring in the SH.

In comparison with HALOE, the CCMVal-2 models show a larger spread in their response to the annual cycle, in the NH and SH spring, upper troposphere and lower stratosphere, than the CCMVal-1 models. This may simply be due to the fact that more CCMs participated in this evaluation. CCMVal-2 model outliers are CCSRNIES, which shows unusually large ozone values at 10 hPa in March at the equator and in October at 80°S, and CNRM-ACM at 50 hPa which shows unusually small values at all except polar latitudes.

The assessment of the performance of the models for the annual cycle in ozone that is summarized in Figure 8.24 (ah and sah diagnostics), implies that the vertical and latitudinal distribution of the annual cycle in stratospheric zonal monthly mean ozone is very well represented by the majority of the models. There are only two outliers, CAM3.5 and E39CA, respectively showing poor performance in the semi-annual and annual harmonic ozone diagnostics, possibly because of their low top. Concerning the annual mean (amean diagnostic) and the annual cycle in near global column ozone (acc diagnostic), all models perform very well. However, this result does not translate in to a lack of global mean ozone bias, as reported in Table 8.2. Major outliers in global mean bias are E39CA and UMUKCA-UCAM, which both overestimate the near-global ozone as well as the North and South polar ozone.

Summary on interannual polar variability

The observed annual cycle in polar column ozone variability is well reproduced by all models, in the sense that all show a minimum in variability in the summer seasons (Section 8.4). In the NH dynamically active period, most of the models under-estimate the interannual polar variability, indicating a common bias. With the exception of CAM3.5, Figure 8.24 (nhivc and shivc diagnostics) shows that models (CNRM-ACM, MRI, ULAQ and WACCM) with poor performance in interannual variability in the NH also perform poorly in the SH, suggesting basic problems in the dynamical core of the models, possibly related to resolution and the parameterisation of the effects of unresolved gravity waves. The model performance in the annual cycle in polar ozone climatology (nhcc and shcc) shows instead a marked hemispheric asymmetry, with good to very good performance in the North polar cap, but poor to very poor in the Southern polar cap. The latter case is therefore highlighted as a systematic bias, due to persistent problems in the combined representation of the chemical and dynamical processes characterizing the morphology of the ozone hole.

The majority of models reproduce quite well the relationship between winter mean heat flux and spring-to-fall ozone ratio in both the NH and SH. This result suggests that the sensitivity of ozone to the heat fluxes is realistic. The only outlier is the ULAQ model, which appears to severely under-estimate the relationship in the NH. The models reproduce the observed ozone-temperature relationship quite well; although in the NH the ozone is less responsive to temperature perturbations in a number of the models than in the observations. Among the models with low sensitivity is again ULAQ, while the relationship is substantially overestimated by CNRM-ACM. In the SH, the spread of the models surrounds the observations, as in the case of the ozone standard deviation. When the parameters of heat flux versus ozone and heat flux versus temperature fits are compared (not shown) there is a good correlation (>0.6) between them in both hemispheres. This indicates that models with enhanced polar temperature sensitivity to planetary wave activity also exhibit an enhanced sensitivity of polar ozone to planetary wave activity.

The regression of the column ozone on to the simplified AM index further confirms that the modelled interannual polar ozone variations are due to the known dynamical processes affecting the variability of the stratospheric vortex and that these processes and their connection to ozone are generally well simulated for the majority of the models. Figure 8.24 shows that models previously highlighted with poor performance in interannual variability, are those that tend to perform poorly also in the ozone variations associated with the annular mode (nhc_am and shc_am).

Summary on 11-year solar cycle

Most models imposed a solar cycle in the CCMVal-2 REF-B1 simulations (sc group), with only five that did not (no-sc group, *i.e.*, GEOSCCM, ULAQ, UMUKCA-METO, UMUKCA-UCAM, UMETRAC, Section 8.5). The solar cycle in total column ozone is qualitatively well represented in the sc group, although with some amplitude spread. Most models reproduce 70-80% of the observed solar total column ozone variations from 60°S to 60°N. MRI, UMSLIMCAT and WACCM show best agreement with observations, while CNRM-ACM, CCSRNIES, CAM3.5, and ULAQ show the worst agreement. The vertical structure of the tropical solar signal in ozone and temperature is more difficult to model. While the direct solar response in temperature and ozone in the upper stratosphere is well represented (best for WACCM, CMAM, AMTRAC3, and UMSLIMCAT, worst for LMDZrepro) the vertical structure in the tropics below 10 hPa varies a lot among the models but also among different observational data sets. Especially in the lower stratosphere uncertainties are large and might be related to non-linear interactions with a number of signals (solar, QBO, ENSO, volcanos) that might not be handled correctly in a MLR as discussed earlier. Another limiting factor might be the fact that we only used one simulation from each model. An ensemble mean for the models that delivered several simulations might reduce the large uncertainties in the middle and lower stratosphere as shown by Austin *et al*. (2008). In general the agreement between the models and between the models and observations is better for ozone than for temperature. The latitudinal representation of the solar response in total column ozone shows improved representation compared with CCMVal-1 but a large spread especially at mid- to high latitudes due to large interannual variability.

Compared to CCMVal-1, the way in which the solar cycle in radiation and chemistry is represented has been improved, by prescribing daily varying spectrally resolved irradiance data from the SOLARIS project (Matthes *et al*., 2007) instead of scaling to the F10.7 cm solar radio flux as used in CCMVal-1. Nevertheless, the modelled responses still show large differences that might be related to differences in the performance of the radiation schemes (compare Chapter 3, Section 3.6), the photolysis schemes (compare Chapter 6) or to dynamical and transport differences that are very difficult to separate.

Summary on QBO

Metrics are not computed for the QBO signal in ozone because the status of the modelling of the QBO in CCMs is still at a primitive stage (Section 8.6). Some AGCMs in recent years have been able to simulate a quite realistic QBO in zonal winds and related dynamical quantities, but it does not seem that this expertise has passed to the CCMs, possibly because of the computational and/or developmental constraint of the additional chemical modelling. The QBO modelling in the CCMs as implemented for CCMVal-2 therefore remains an outstanding problem.

In summary, there are three groups of models: Group A with negligible tropical variability, Group B with intermediate to large tropical variability, and the Group C models, with externally imposed tropical variability (Table 8.4). The QBO signal in ozone is not simulated by any of the Group A models nor by the AMTRAC3 model of Group B. Although AMTRAC3 showed some signal in tropical variability, it fails in all diagnostics. The rest of the models in Group B, namely MRI, UMETRAC, UMSLIMCAT, and UMUKCA-METO, and UMUKCA-UCAM, and all models of Group C, show a QBO signal in ozone, *albeit* with some biases. From the MLR analysis, it is found that these models show a comparable spread in the amplitude of the QBO signal in ozone. Among the models with nudged QBO variability, large overestimations of the amplitude of ozone variations are found for ULAQ, indicating a problem with the nudging specification. Among the models with internal QBO variability, MRI, UMETRAC, UMSLIMCAT show a periodicity close to the observed average, while UMUKCA-METO and UMUKCA-UCAM overestimate (by almost a factor 2) the typical QBO periodicity.

Summary on ENSO

For most models, the tropical ENSO signal in temperature is consistent with that estimated by available observations in the lower stratosphere and upper troposphere, in the sense that the model results envelop the observed signatures (Section 8.7). Most models show a comparable response in ozone, although with a spread. In this case, it is hard to judge if the modelled ozone variations are consistent with the observations, because of the large uncertainty in the observational data used. By looking at column ozone a clear picture emerges, with the spread of the model responses explained by interannual variability. Note indeed that the slope (from the ensemble of models) deduced by Figure 8.19 is consistent with the slope estimated by observations in Figure 8.8.

It is concluded that an ENSO signal in temperature and ozone is emerging from the models, especially in the tropical lower stratosphere, where most of the models show a cooling and an ozone reduction. However, because of the large role of interannual variability and the uncertainty in the observations, it is not possible to measure the model performance in the simulation of the ENSO signal in ozone.

Summary on volcanic aerosols

The models show a considerable spread in their simulated response to volcanic eruptions (Section 8.8), as seen in modelled temperature and ozone responses. The fact that many fundamentally different methods have been employed to parameterise the direct effect of volcanic aerosols on the radiative transfer of the stratosphere (Figure 8.21) helps explain, at least in part, the wide range of post-eruption temperature anomalies seen in the different models. For example, models that estimate aerosol optical depth from the SAD data set of WMO (2007) consistently overestimate lower stratospheric temperatures after the Mt. Pinatubo eruption compared to the ERA-40 data set. On the other hand, models which use the GISS aerosol optical depth data set lead to wide ranging estimates of lower stratospheric heating. Post-eruption changes in total column ozone are well correlated with changes in lower stratospheric ClO. It thus appears that while most models use a common aerosol SAD data set to drive anomalous post-eruption chemistry, the models display differing degrees of sensitivity to those aerosols, leading to differing amounts of chlorine activation and associated ozone loss. None of the CCMVal-2 models reproduce the observed hemispheric asymmetry in post-Pinatubo ozone loss, for either full hemispheric means or for mid-latitudes.

8.9.2 Model by model summary

A model by model summary is provided that is based on the grading of the metrics listed in Table 8.5 as well as some approximate grading for the remaining variability factors considered. In a few cases, the evaluation of the modelled key processes responsible for natural ozone variations has not been possible, because the respective external forcing was not included in the models. Three broad groups are identified: (1) models that simulate natural ozone variations well with better or mean performance in most diagnostics, (2) models that simulate natural ozone variations and with mixed and/or limited success, and (3) models that are outliers in many diagnostics for natural ozone variations.

AMTRAC3 accurately represents the annual mean and the annual cycle in ozone, in near global and northern polar column ozone. The variability of column ozone in both polar caps is well represented, while the annual cycle in southern polar cap column ozone is poor. It has a good representation of the solar cycle in ozone and temperature. This model fails to reproduce the QBO signal in ozone. The tropical ENSO signal in temperature and ozone is within the cluster of model responses. The model compares quite well with the observed volcanic effects (optical properties from SAGE/GISS are used for the volcanic aerosols). Overall, AMTRAC3 simulates natural ozone variations well, with better or mean performance in most diagnostics.

CAM3.5 performs well to very well for the annual mean and the annual cycle in ozone, in near global and North polar column ozone, but it shows a poorer performance in the ozone semi-annual harmonic and in the column ozone variability for both polar caps than other models. It does not accurately represent solar cycle effects in temperature and ozone. The amplitude of the ozone response to the nudged QBO is moderately overestimated. The tropical ENSO signal in temperature and ozone is within the cluster of model responses. This model does not use a parameterisation of volcanic effects and therefore it does not show a volcanic response. CAM3.5 is an outlier in many diagnostics for natural ozone variability possibly related to its low top.

CCSRNIES performs very well for the annual mean and the annual cycle in ozone, in near global and northern polar column ozone. The annual cycle in southern polar cap column ozone and the variability in both polar caps are well represented. It shows unusually large ozone peak values at 10 hPa that might be related to its fast tropical ascent (Chapter 5), and/or its poor performance for nearly all photolysis rates (Chapter 6). This model uses spectrally resolved data to represent the solar cycle and consistently shows large shortwave heating rates. However the solar response in temperature is biased low compared to most models and large biases occur in the solar ozone and temperature signal in the tropical lower stratosphere which lead to large biases in the solar response of total column ozone. The ozone response to the nudged QBO is excellent. The tropical ENSO signal in temperature and ozone is within the cluster of model responses. The model uses SAGE/GISS data to model the effect of volcanoes but fails to reproduce the observed volcanic signals in temperature and ozone. Overall, CCSRNIES simulates natural ozone variations with mixed and/or limited performance in most diagnostics.

CMAM accurately represents the annual mean and the annual cycle in ozone, in near global and northern polar column ozone. The variability of column ozone in both polar caps is well represented, while the annual cycle in southern polar cap column ozone is poor. It uses spectrally

resolved data to represent the solar cycle and is among the best performing models for the solar cycle in the upper stratosphere, but shows larger discrepancies in the middle and lower stratosphere in the tropical ozone signal. This model does not have a QBO signal in ozone. The tropical ENSO signal in temperature and ozone is within the cluster of model responses. This model uses optical properties from SADs to represent volcanic aerosols and tends to overestimate its effects. Overall, CMAM simulates natural ozone variations well, with better or mean performance in most diagnostics.

CNRM-ACM performs well to very well for the annual mean and the annual cycle in ozone, in near global and polar column ozone, while the variability of column ozone in both polar caps is poor. The 50 hPa ozone concentrations in NH spring and autumn are biased low. The solar signal in temperature and ozone is substantially overestimated and is the largest among all models. This model does not have a QBO signal in ozone. The tropical ENSO signal in temperature and ozone is within the cluster of model responses. This model includes full volcanic aerosol microphysics, but due to the way the radiative scheme responds to volcanic aerosols, it produces anomalously large temperature responses to volcanic effects. CNRM-ACM is an outlier in many of the diagnostics for natural ozone variability shown in this chapter.

E39CA performs well to very well for the annual mean and the annual cycle in ozone, in near global and northern polar column ozone. The variability of column ozone in the polar caps is well represented in the north but very poor in the south. The model shows a poorer performance in the ozone annual harmonic and it fails to reproduce the annual cycle in southern polar cap column ozone. It also shows poorer performance in the ozone variations associated with the annular mode, suggesting that the good performance in NH ozone variability might be the results of compensating errors. The global mean column ozone is biased high everywhere. Similarly to CAM3.5, it does not capture the solar temperature signal, possibly due to its low lid. The amplitude of the ozone response to the nudged QBO is slightly overestimated. The tropical ENSO signal in temperature and ozone is within the cluster of model responses. To mimic the effects of volcanic aerosols, prescribed heating rate anomalies are used that provide temperature reactions close to the observed ones. Overall, E39CA simulates natural ozone variations with mixed and only limited success, possibly related to its low lid.

EMAC accurately represents the annual mean and the annual cycle in ozone, in near global and northern polar column ozone. The variability of column ozone in both polar caps is well represented. The model fails to reproduce the annual cycle in southern polar cap column ozone. It has a good representation of solar induced ozone changes and their effect on heating but shows smaller temperature and ozone responses than most models which result in a lower than observed solar regression coefficient for total column ozone. The amplitude of the ozone response to the nudged QBO is less overestimated than for the rest of the models with nudged QBO, possibly because of the biased low variability in the lower stratosphere. The tropical ENSO signal in temperature and ozone is within the cluster of model responses. EMAC uses prescribed heating rates to simulate the effect of volcanoes but fails to represent it correctly. Overall, EMAC simulates natural ozone variations well, with better or mean performance in most diagnostics.

GEOSCCM accurately represents the annual mean and the annual cycle in ozone, in near global and northern polar column ozone, but shows a poor performance in the annual cycle in southern polar cap column ozone. The variability of column ozone in the polar caps is well represented in the north but very poor in the south. It also shows poor performance in the ozone variations associated with the annular mode. This suggests that the good performance in NH ozone variability might be the result of compensating errors. The global mean column ozone is biased high, in both polar caps. It does not prescribe a solar cycle in irradiance, has no QBO signal in ozone, and did not include radiative effects of volcanic aerosols, and hence does not show a volcanic signal in temperature or ozone. The tropical ENSO signal in temperature and ozone is within the cluster of model responses. Overall, GEOSCCM simulates natural ozone variations with limited success.

LMDZrepro accurately represents the annual mean and the annual cycle in ozone, in near global and northern polar column ozone. The variability of column ozone in the polar caps is well represented in the north but poor in the south. The annual cycle in southern polar cap column ozone is poor. It prescribes solar cycle variations as total solar irradiance (TSI) changes in the heating and spectrally resolved in the photolysis leading to a small short wave heating and therefore largely under-estimates temperature changes when compared to the majority of the models. Solar induced ozone variations are well reproduced. This model does not have a QBO signal in ozone. The tropical ENSO signal in temperature and ozone is within the cluster of model responses. It does not include any volcanic forcing; hence it does not show a response. Overall, LMDZrepro simulates natural ozone variations moderately well, with mean or limited performance in most diagnostics.

MRI accurately represents the annual mean and the annual cycle in ozone, in near global and northern polar column ozone, while the variability of column ozone in both polar

caps is poor. The model fails to reproduce the annual cycle in southern polar cap column ozone. It prescribes spectrally resolved solar irradiance variations leading to the highest shortwave heating rates and relatively large solar cycle temperature and ozone responses as compared with other models, especially in the upper stratosphere. Both the amplitude and the period of the QBO signal in ozone are well represented. However, this model is one of the few that under-estimates the tropical ENSO signal in temperature and ozone. It uses optical properties from SAGE/GISS and overestimates the volcanic effect on temperatures by a factor of almost two. Overall, MRI simulates natural ozone variations with mixed and limited success.

NiwaSOCOL performs well to very well for the annual mean and the annual cycle in ozone, in near global column ozone, and in the variability of column ozone in the northern polar cap. The annual cycle in northern polar cap column ozone is poor and the model fails in the southern polar cap column ozone and variability. The solar response in temperature and ozone is less than in most other models. The amplitude of the ozone response to the nudged QBO is well represented. The tropical ENSO signal in temperature and ozone is within the cluster of model responses. To represent volcanic effects, the model uses optical properties derived from SADs and, except for El Chichón, the volcanic signals are largely overestimated. Overall, NiwaSOCOL simulates ozone variations with mixed and limited success.

SOCOL performs well to very well for well for the annual mean and the annual cycle in ozone, in near global column ozone, and in the variability of column ozone in the Northern polar cap. The model fails to represent the annual cycle in polar column ozone and variability. Compared to NiwaSOCOL it shows a slightly larger solar response in temperature and ozone and very similar QBO and volcanic signals. The tropical ENSO signal in temperature and ozone is within the cluster of model responses. Overall, SOCOL simulates natural ozone variations with mixed and limited success.

ULAQ performs well to very well for the annual mean and the annual cycle in ozone and in near global and northern polar ozone, but it shows a poorer performance in southern polar ozone. The model fails to reproduce the variability of column ozone in both polar caps. It does not prescribe a solar cycle, and the amplitude of the ozone response to the nudged QBO is substantially overestimated. This model under-estimates the tropical ENSO signal in temperature and ozone. The model uses full aerosol microphysics to represent volcanic effects. Except for Agung, the correspondence with observations is remarkable. Overall, ULAQ is an outlier in many of the diagnostics for natural ozone variability shown in this chapter.

UMETRAC performs well to very well for the annual mean and the annual cycle in ozone, in near global and northern polar column ozone, but fails to reproduce the annual cycle in southern polar column ozone. The variability of column ozone in both polar caps is well represented. The global mean in northern polar column ozone is biased low. It does not prescribe solar cycle changes. The period of the internally generated QBO signal in ozone is well represented, while the amplitude is biased high. The tropical ENSO signal in temperature and ozone is within the cluster of model responses. It was not evaluated in the volcanic section since data were delivered too late. Overall, UMETRAC simulates natural ozone variations with mixed and/or limited success.

UMSLIMCAT accurately represents the annual mean and the annual cycle in ozone, in near global column ozone. The variability of column ozone in both polar caps and the annual cycle in northern polar column ozone are well represented, but the model fails to reproduce the annual cycle in southern polar column ozone. It includes spectrally resolved data and shows larger than average solar temperature and ozone signals, leading to a good correspondence in the total column ozone solar regression coefficient. The period of the internally generated QBO signal in ozone is well represented, while the amplitude is biased low. The tropical ENSO signal in temperature and ozone is within the cluster of model responses. It does not include radiative effects of volcanic aerosols and shows modest decreases after the Pinatubo eruption, as expected from chemical induced ozone decrease. Overall, UMSLIMCAT simulates natural ozone variations well, with better or mean performance in most diagnostics.

UMUKCA-METO accurately represents the annual mean and the annual cycle in ozone, in near global and northern polar column ozone. The variability of column ozone in both polar caps is well represented. The model fails to reproduce the annual cycle in southern polar cap column ozone. In the polar caps, the global mean column ozone is biased high. It does not prescribe solar cycle effects. The amplitude of the internally generated QBO signal in ozone is well represented, while the period is biased high. The tropical ENSO signal in temperature and ozone is within the cluster of model responses. The model uses optical properties from GISS and gives a close representation of observed ozone changes after volcanic eruptions. Overall, UMUKCA-METO simulates natural ozone variations well, with better or mean performance in most diagnostics.

UMUKCA-UCAM performs well to very well for the annual men and annual cycle in ozone, in near global and northern polar column ozone. The variability of column ozone in the northern polar caps is well represented. The

model fails to reproduce the annual cycle in southern polar cap column ozone and variability. The global mean column ozone is biased high, everywhere. It only prescribes TSI changes and therefore misrepresents solar cycle effects. The amplitude of the QBO signal in ozone is well represented, while the period is biased high. The tropical ENSO signal in temperature and ozone is within the cluster of model responses. It does not include radiative effects of volcanic aerosols and it does not show a volcanic response. Overall, UMUKCA-UCAM simulates natural ozone variations with mixed and/or limited success.

WACCM accurately represents the annual mean and the annual cycle in ozone and in near global column ozone. The annual cycle in northern polar cap is well represented. The model fails to reproduce the annual cycle in the southern polar cap column ozone and in the variability of column ozone in both polar caps. It uses spectrally resolved solar irradiance data and is the model that best represents the solar cycle signal among the models considered here. The amplitude of the ozone response to the nudged QBO is moderately overestimated. The tropical ENSO signal in temperature and ozone is within the cluster of model responses. To represent volcanoes it uses optical properties derived from SPARC SADs and largely overestimates the temperature response after the Agung and Pinatubo eruptions. Overall, WACCM simulates natural ozone variations with mixed or in some diagnostics limited success.

References

Angell, J. K., 1997. Estimated impact of Agung, El Chichón and Pinatubo volcanic eruptions on global and regional total ozone after adjustment for the QBO, *Geophys. Res. Lett.*, **24**, 647-650.

Austin, J., L. L. Hood, and B. E. Soukharev, 2007. Solar cycle variations of stratospheric ozone and temperature in simulations of a coupled chemistry-climate model, *Atmos. Chem. Phys.*, **7**, 1693-1706.

Austin, J., K. Tourpali, E. Rozanov, H. Akiyoshi, S. Bekki, G. Bodeker, C. Brühl, N. Butchart, M. Chipperfield, M. Deushi, V.I. Fomichev, M.A. Giorgetta, L. Gray, K. Kodera, D. Kinnison, E. Manzini, D. Marsh, K. Matthes, T. Nagashima, K. Shibata, R.S. Stolarski, H. Struthers, and W. Tian, 2008. Coupled chemistry climate model simulations of the solar cycle in ozone and temperature, *J. Geophys. Res.,* **113**, doi:10.1029/2007JD009391.

Baldwin, M. P., L. J. Gray, T. J. Dunkerton, K. Hamilton, P. H. Haynes, W. J. Randel, J. R. Holton, M. J. Alexander, I. Hirota, T. Horinouchi, D. B. A. Jones, J. S. Kinnersley, C. Marquardt, K. Sato, and M. Takahashi, 2001. The Quasi-Biennial Oscillation, *Rev. Geophys.*, **39**, 179-229.

Bodeker, G. E, J. C. Scott, K. Kreher, and R. L. McKenzie, 2001. Global ozone trends in potential vorticity coordinates using TOMS and GOME intercompared against the Dobson network: 1978-1998, *J. Geophys. Res.*, **106**, 23,029-23,042.

Baldwin, M. P. and D. W. J. Thompson, 2009. A critical comparison of stratosphere-troposphere coupling indices, *Quart. J. Roy. Meteorol. Soc.,* **135**, 1661–1672.

Bodeker, G. E., I. S. Boyd and W. A. Matthews, 1998. Trends and variability in vertical ozone and temperature profiles measured by ozonesondes at Lauder, New Zealand 1986-1996, *J. Geophys. Res.*, **103**, 28,661-28,681.

Bodeker, G. E., Shiona, H., and Eskes, H., 2005. Indicators of Antarctic ozone depletion, *Atmos. Chem. Phys.*, **5**, 2603–2615.

Brönnimann, S., J. Luterbacher, J. Staehelin, T. M. Svendby, G. Hansen, and T. Svenoe, 2004. Extreme climate of the global troposphere and stratosphere in 1940 – 42 related to El Nino, *Nature*, **431**, 971 – 974.

Brönnimann, S., M. Schraner, B. Müller, A, Fischer, D. Brunner, E. Rozanov and T. Egorova, 2006. The 1986-1989 ENSO cycle in a chemical climate model, *Atmos. Chem. Phys.*, **6**, 4669–4685.

Cagnazzo, C., E. Manzini, N. Calvo, A. Douglass, H. Akiyoshi, S. Bekki, M. Chipperfield, M. Dameris, M. Deushi, A. Fischer, H. Garny, A. Gettelman, M. A. Giorgetta, D. Plummer, E. Rozanov, T. G. Shepherd, K. Shibata, A. Stenke, H. Struthers, and W. Tian, 2009. Northern winter stratospheric temperature and ozone responses to ENSO inferred from an ensemble of Chemistry Climate Models. *Atmos. Chem. Phys. Discuss.*, **9**, 12141–12170,

Calvo, N., M. A. Giorgetta, R. Garcia-Herrera, and E. Manzini, 2009. Nonlinearity of the combined warm ENSO and QBO effects on the Northern Hemisphere polar vortex in MAECHAM5 simulations, *J. Geophys. Res.*, **114**, doi:10.1029/ 2008JD011445.

Camp, C. D., and K.-K. Tung, 2007. Stratospheric polar warming by ENSO in winter: A statistical study, *Geophys. Res. Lett.*, **34**, doi:10.1029/2006GL028521.

Crooks, S. A., and L. J. Gray, 2005. Characterization of the

11-year solar signal using a multiple regression analysis of the ERA-40 data set, *J. Clim.*, **18**, 996-1015.

Dameris, M., S. Matthes, R. Deckert, V. Grewe, and M. Ponater, 2006. Solar cycle effect delays onset of ozone recovery, *Geophys. Res. Lett.*, **33**, doi:10.1029/2005GL024741.

Eyring, V., N. Butchart, D. W. Waugh, H. Akiyoshi, J. Austin, S. Bekki, G. E. Bodeker, B. A. Boville, C. Brühl, M. P. Chipperfield, E. Cordero, M. Dameris, M. Deushi, V. E. Fioletov, S. M. Frith, R. R. Garcia, A. Gettelman, M. A. Giorgetta, V. Grewe, L. Jourdain, D. E. Kinnison, E. Mancini, E. Manzini, M. Marchand, D. R. Marsh, T. Nagashima, P. A. Newman, J. E. Nielsen, S. Pawson, G. Pitari, D. A. Plummer, E. Rozanov, M. Schraner, T. G. Shepherd, K. Shibata, R. S. Stolarski, H. Struthers, W. Tian, and M. Yoshiki, 2006. Assessment of temperature, trace species, and ozone in chemistry-climate model simulations of the recent past, *J. Geophys. Res.*, **111**, doi:10.1029/2006JD007327.

Eyring, V., D. W. Waugh, G. E. Bodeker, E. Cordero, H. Akiyoshi, J. Austin, S. R. Beagley, B. A. Boville, P. Braesicke, C. Brühl, N. Butchart, M. P. Chipperfield, M. Dameris, R. Deckert, M. Deushi, S. M. Frith, R. R. Garcia, A. Gettelman, M. A. Giorgetta, D. E. Kinnison, E. Mancini, E. Manzini, D. R. Marsh, S. Matthes, T. Nagashima, P. A. Newman, J. E. Nielsen, S. Pawson, G. Pitari, D. A. Plummer, E. Rozanov, M. Schraner, J. F. Scinocca, K. Semeniuk, T. G. Shepherd, K. Shibata, B. Steil, R. S. Stolarski, W. Tian, and M. Yoshiki, 2007. Multi-model projections of ozone recovery in the 21st century, *J. Geophys. Res.*, **112**, doi:10.1029/2006JD008332.

Fioletov, V. E., G. E. Bodeker, A. J. Miller, R. D. McPeters and R. Stolarski, 2002. Global and zonal total ozone variations estimated from ground-based and satellite measurements: 1964-2000, *J. Geophys Res.*, **107**, doi:10.1029/2001JD001350.

Fischer, A. M., D. T. Shindell, B. Winter, M. S. Bourqui, G. Faluvegi, E. Rozanov, M. Schraner, and S. Brönnimann, 2008. Stratospheric winter climate response to ENSO in three chemistry-climate models, *Geophys. Res. Lett.*, **35**, doi:10.1029/2008GL034289.

Fortuin, J. P. F., and H. Kelder, 1996. Possible links between ozone and temperature profiles, *Geophys. Res. Lett.*, **23**, 1517-1520.

Fortuin, J. P. F., and H. Kelder, 1998. An ozone climatology based on ozonesonde and satellite measurements, *J. Geophys. Res.*, **103**, 31709-31734.

Frame, T. H. A., and L.J. Gray, 2010. The 11-year solar cycle in ERA-40 data: an update to 2008, J. Climate, in press.

Free, M. and D. Seidel, 2009. The observed ENSO temperature signal in the stratosphere. (accepted J. Geophys. Res.)

Froidevaux, L., Y. B. Jiang, A. Lambert, N. J. Livesey, W. G. Read, J. W. Waters, R. A. Fuller, T. P. Marcy, P. J. Popp, R. S. Gao, D. W. Fahey, K. W. Jucks, R. A. Stachnik, G. C. Toon, L. E. Christensen, C. R. Webster, P. F. Bernath, C. D. Boone, K. A. Walker, H. C. Pumphrey, R. S. Harwood, G. L. Manney, M. J. Schwartz, W. H. Daffer, B. J. Drouin, R. E. Cofield, D. T. Cuddy, R. F. Jarnot, B. W. Knosp, V. S. Perun, W. V. Snyder, P. C. Stek, R. P. Thurstans, P. A. Wagner, 2008. Validation of Aura Microwave Limb Sounder stratospheric ozone measurements, *J. Geophys. Res.*, **113**, doi:10.1029/2007JD008771.

Fusco, A. C., and Salby, M. L., 1999. Interannual variations of total ozone and their relationship to variations of planetary wave activity, *J. Clim.*, **12**, 1619 – 1629.

Garcia-Herrera, R., N. Calvo, R. R. Garcia, and M. A. Giorgetta, 2006. Propagation of ENSO temperature signals into the middle atmosphere: A comparison of two general circulation models and ERA-40 reanalysis data, *J. Geophys. Res.*, **111**, doi:10.1029/2005JD006061.

Garfinkel, C. I., and D. L. Hartmann, 2007. Effects of El Nino-Southern Oscillation and the Quasi-Biennial Oscillation on polar temperatures in the stratosphere, *J. Geophys. Res.*, **112**, doi:10.1029/2007JD008481.

Giorgetta, M. A., E. Manzini, and E. Roeckner, 2002. Forcing of the quasi-biennial oscillation from a broad spectrum of atmospheric waves, *Geophys. Res. Lett.*, **29**, doi:10.1029/2002GL14756.

Giorgetta, M.A., E. Manzini, E. Roeckner, M. Esch, and L. Bengtsson, 2006. Climatology and Forcing of the Quasi-Biennial Oscillation in the MAECHAM5 Model, *J. Clim.*, **19**, doi:10.1175/JCLI3830.1.

Grant, W. B., E. V. Browell, J. Fishman. V. G. Brackett. R. E. Veiga, D. Nganga. A. Minga, B. Cros. C. F. Butler. M. A. Fenn, C. S. Long, and L. L Stowe, 1994. Aerosol-associated changes in tropical stratospheric

ozone following the eruption of Mount Pinatubo, *J. Geophys. Res.*, **99**, 8197-8211.

Gray, L. J., J. Beer, M. Geller, J. D. Haigh, M. Lockwood, K. Matthes, U. Cubasch, D. Fleitmann, G. Harrison, L. Hood, J. Luterbacher, G. A. Meehl, D. Shindell, B. van Geel, and W. White, 2010. Solar Influences on Climate, Reviews of Geophysics, in press.

Gray, L. J. and M. P. Chipperfield, 1990. On the interannual variability of trace gases in the middle atmosphere, *Geophys. Res. Lett.*, **17**, 933-936.

Gray, L. J., S. J. Phipps, T. J. Dunkerton, M. P. Baldwin, E. F. Drysdale, and M. R. Allen, 2001. A data study of the influence of the equatorial upper stratosphere on northern hemisphere stratospheric sudden warmings, *Quart. J. Roy. Meteorol. Soc.*, **127**, 1985-2003.

Gray, L. J, S. A. Crooks, M. A. Palmer, C. L. Pascow, and S. Sparrow, 2006. A possible transfer mechanism for the 11-year solar cycle to the lower stratosphere, *Space Sci. Rev.*, **125**, 357-370.

Grooß, J.-U., and J. M. Russell III, 2005. Technical note: A stratospheric climatology for O3, H2O, CH4, NOx, HCl and HF derived from HALOE measurements, *Atmos. Chem. Phys.*, **5**, 2797– 2807.

Haigh, J. D., M. Blackburn, and R. Day, 2005. The Response of Tropospheric Circulation to Perturbations in Lower-Stratospheric Temperature, *J. Clim.*, **18**, 3672-3685.

Haigh, J. D., 1999. Modelling the impact of solar variability on climate. *J. Atmos. Sol. Terr. Phys.*, **61**, 63-72.

Haimberger, L., C. Tavolato, S. Sperka, 2008. Towards elimination of the warm bias in historic radiosonde temperature records — some new results from a comprehensive intercomparison of upper air data. *J. Clim.*, **21**, 4587-4606.

Hassler, B., G.E. Bodeker, I. Cionni, and M. Dameris, 2009. A vertically resolved, monthly mean ozone database from 1979 to 2100 for constraining global climate model simulations, *International Journal of Remote Sensing*, **30**, 4009–4018.

Hoerling, M. P., Kumar, A. and Zhong, M., 1997. El Niño, La Niña, and the nonlinearity of their teleconnections. *J. Clim.*, **10**, 1769–1786.

Hofmann, D. J., S. J. Oltmans, J. M. Harris, W. D. Komhyr, J. A. Lathrop, T. DeFoor, and D. Kuniyuki, 1993. Ozonesonde measurements at Hilo, Hawaii following the eruption of Pinatubo, *Geophys. Res. Lett.*, **20**, 1555-1558.

Hu, Y. and K.-K.Tung, 2002. Interannual and Decadal Variations of Planetary Wave Activity, Stratospheric Cooling, and Northern Hemisphere Annular Mode. *J. Clim.*, **15**, 1659-1673.

Ito, K., Y. Naito, and S. Yoden, 2009. Combined effects of QBO and 11-year solar cycle on the winter hemisphere in a stratosphere-troposphere coupled system, *Geophys. Res. Lett.*, **36**, doi:10.1029/2008GL037117.

Kalnay, E., M. Kanamitsu, R. Kistler, W. Collins, D. Deaven, L. Gandin, M. Iredell, S. Saha, G. White, J. Woollen, Y. Zhu, A. Leetmaa, R. Reynolds, M. Chelliah, W. Ebisuzaki, W. Higgins, J. Janowiak, K. C. Mo, C. Ropelewski, J. Wang, R. Jenne, and D. Joseph, 1996. The NCEP/NCAR 40-Year Reanalysis Project. *Bull. Amer. Meteor. Soc.*, **77**, 437-471.

Kodera, K., and Y. Kuroda, 2002. Dynamical response to the solar cycle, *J. Geophys. Res.*, **107**, doi:10.1029/2002JD002224.

Kodera, K., 2006. The Role of Dynamics in Solar Forcing, *Space Sci. Rev.*, **125**, 319-330.

Kodera, K., K. Coughlin, and O. Arakawa, 2007. Possible modulation of the connection between the Pacific and Indian ocean variability by the solar cycle, *Geophys. Res. Lett.*, **34**, doi:10.1029/2006GL027827.

Kryjov, V. N. and C.-K. Park, 2007. Solar Modulation of the El Nino/Southern Oscillation impact on the Northern Hemisphere Annular Mode. *Geophys. Res. Lett.*, **34**, doi: 10.1029/2006GL028015.

Kuroda, K., 2007. Effect of QBO and ENSO on the Solar Cycle modulation of winter North Atlantic Oscillation. *J. Met. Soc. Japan*, **85**, 889-898.

Labitzke, K., 1987. Sunspots, the QBO and the stratospheric temperature in the north polar region, *Geophys. Res. Lett.*, **14**, 535-537.

Labitzke, K., and H. van Loon, 1988. Associations between the 11-year solar cycle, the QBO and the atmosphere, Part I: The troposphere and stratosphere in the northern hemisphere in winter, *J. Atmos. Terr. Phys.*, **50**, 197-206.

Lee, H. and A. K. Smith, 2003. Simulation of the combined effects of solar cycle, quasi-biennial oscillation, and volcanic forcing on stratospheric ozone changes in recent decades, *J. Geophys. Res.*, **108**, doi:10.1029/2001JD001503.

Manzini, E., 2009. ENSO and the stratosphere. *Nature*

Geosci., **2**, 749-750.

Manzini, E. M. A. Giorgetta, M. Esch, L. Kornblueh, and E. Roeckner, 2006. The influence of sea surface temperatures on the Northern winter stratosphere: Ensemble simulations with the MAECHAM5 model, *J. Clim*., **19**, 3863-3881.

Marsh, D. R., and R. R. Garcia, 2007. Attribution of decadal variability in lower-stratospheric tropical ozone, *Geophys. Res. Lett*., **34**, doi:10.1029/2007GL030935.

Matthes, K., Y. Kuroda, K. Kodera, and U. Langematz, 2006. Transfer of the solar signal from the stratosphere to the troposphere: Northern winter, *J. Geophys. Res*., **111**, doi:10.1029/ 2005JD006283.

Matthes, K., K. Kodera, L.J. Gray, et al., 2007: Report on the first solar influence for SPARC (SOLARIS) workshop in Boulder/CO October 3-6 2006, SPARC Newsletter 28.

Matthes, K., U. Langematz, L.J. Gray, K. Kodera, and K. Labitzke, 2004. Improved 11-Year Solar Signal in the Freie Universität Berlin Climate Middle Atmosphere Model (FUB-CMAM), *J. Geophys. Res*., **109**, doi:10.1029/2003JD004012.

Matthes, K., D. R. Marsh, R. R. Garcia, D. Kinnison, F. Sassi, and S. Walters, 2010. The role of the QBO in modeling the influence of the 11-year solar cycle on the atmosphere using constant forcings, revised for J. Geophys. Res.

Matthes, K., K. Kodera, J.D. Haigh, D.T. Shindell, K. Shibata, U. Langematz, E. Rozanov, and Y. Kuroda, 2003. GRIPS solar experiments intercomparison project: Initial results, *Pap. Meteorol. Geophys*., **54**, 71-90.

Newman, P. A., J. S. Daniel, D. W. Waugh, and E. R. Nash, 2007. A new formulation of equivalent effective stratospheric chlorine (EESC), *Atmos. Chem. Phys*., **7**, 4537-4552.

Newman, P., E. Nash, and J. Rosenfield, 2001. What controls the temperature of the Arctic stratosphere during the spring?, *J. Geophys. Res*., **106**, 19999-20010.

Newman, P., and W. J. Randel, 1988. Cohoerent ozone dynamical changes during the Southern hemisphere spring, 1979-1988. *J. Geophys. Res*., **93**, 12585-12606.

Punge, H.J., and M. A. Giorgetta, 2008. Net effect of the QBO in a chemistry-climate model, *Atmos. Chem. Phys*., **8**, 6505–6525.

Randel, W. J., Wu, F., and Stolarski, R., 2002. Changes in column ozone correlated with the stratospheric EP flux, *J. Meteorol. Soc. Japan*, **80**, 849–862.

Randel, W. J. and F. Wu, 2007. A stratospheric ozone profile data set for 1979-2005: variability, trends, and comparisons with column ozone data, *J. Geophys. Res*., **112**, doi:10.1029/2006JD007339.

Randel, W. J., K. P. Shine, J. Austin, J. Barnett, C. Claud, N. P. Gillett, P. Keckhut, U. Langematz, R. Lin, C. Long, C. Mears, A. Miller, J. Nash, D. J. Seidel, D. W. J. Thompson, F. Wu, and S. Yoden, 2009a. An update of observed stratospheric temperature trends, *J. Geophys. Res*., **114**, doi:10.1029/2008JD010421.

Randel, W. J., R. R. Garcia, N. Calvo, and D. Marsh, 2009b. ENSO influence on zonal mean temperature and ozone in the tropical lower stratosphere, *Geophys. Res. Lett*., **36**, doi:10.1029/2009GL039343.

Randel, W. J, F. Wu, J. M. Russell III, J. W. Waters, and L. Froidevaux, 1995. Ozone and temperature changes in the stratosphere following the eruption of Mount Pinatubo, *J. Geophys. Res*., **100**, 16753-16764.

Russell, J. M., III, L. L. Gordley, J. H. Park, S. R. Drayson, W. D. Hesketh, R. J. Cicerone, A. F. Tuck, J. E. Frederick, J. E. Harries, P. J. Crutzen, 1993. The Halogen Occultation Experiment, *J. Geophys. Res*., **98**, 10,777–10,797.

Sassi, F., D. Kinnison, B. A. Boville, R. R. Garcia, and R. Roble, 2004. Effect of El Nin"o–Southern Oscillation on the dynamical, thermal, and chemical structure of the middle atmophere, *J. Geophys . Res*., **109**, doi:10.1029/2003JD004434.

Scaife, A., N, Butchart, C. Warner, D. Staniforth, W. Norton, and J. Austin, 2000. Realistic Quasi-Biennial Oscillation in a simulation of the global climate, *Geophys. Res. Lett*., **27**, 3481-3484.

Shibata, K., and M. Deushi, 2005. Partitioning between resolved wave forcing and unresolved gravity wave forcing to the quasi-biennial oscillation as revealed with a coupled chemistry-climate model, *Geophys. Res. Lett*., **32**, doi:10.1029/2005GL022885.

Solomon, S., R. W. Portmann, R. R. Garcia, W. Randel, F. Wu, R. Nagatani, J. Gleason, L. Thomason, L. R. Poole, and M. P. McCormick, 1998. Ozone depletion at mid-latitudes: coupling of volcanic aerosols and temperature variability to anthropogenic chlorine, *Geophys. Res. Lett*., **25**, 1871-1874.

Smith, A. K., and K. Matthes, 2008. Decadal-Scale Periodicities in the Stratosphere Associated with the 11-Year Solar Cycle and the QBO, *J. Geophys. Res.*, **113**, doi:10.1029/2007JD009051.

Steinbrecht, W., Hassler, B., Brühl, C., Dameris, M., Giorgetta, M. A., Grewe, V., Manzini, E., Matthes, S., Schnadt, C., Steil, B., and Winkler, P., 2006. Interannual variation patterns of total ozone and temperature in observations and model simulations, *Atmos. Chem. Phys.*, **6**, 349– 374.

Stolarski, R. S. and S. Frith, 2006. Search for evidence of trend slow-down in the long-term TOMS/SBUV total ozone data record: the importance of instrument drift uncertainty and fingerprint detection, *Atmos. Chem. Phys.*, **6**, 3883-3912.

Taylor, K. E., 2001. Summarizing multiple aspects of model performance in a single diagram, *J. Geophys. Res.*, **106**, 7183-7192.

Thomason, L., and T. Peter, 2006. Assessment of Stratospheric Aerosol Properties (ASAP), SPARC Report No. 4., WCRP-124, WMO/TD-No. 1295.

Tie, X. X., and G. P. Brasseur, 1995. The response of stratospheric ozone to volcanic eruptions: Sensitivity to atmospheric chlorine loading, *Geophys. Res. Lett.*, **22**, 3035-3038.

Timmreck, C., H.-F. Graf and B. Steil, 2003. Aerosol chemistry interactions after the Mt. Pinatubo eruption, in Volcanism and the Earth's Atmosphere, eds. A. Robock and C. Oppenheimer, AGU Monograph,Vol. 139, p213-225.

Uppala, S., et al., 2004. ERA-40: ECMWF 45-year reanalysis of the global atmosphere and surface conditions 1957–2002: ECMWF Newsletter, Vol. 101, ECMWF, Reading, United Kingdom, 2–21.

Van Loon, H., and K. Labitzke, 1987. The southern oscillation. Part V: The anomalies in the lower stratosphere of the Northern Hemisphere in winter and a comparison with the quasi-biennial oscillation. *Mon. Wea. Rev.*, **115**, 357–369.

Waters, J. W., Froidevaux, L., Harwood, R.S., Jarnot, R.F., Pickett, H.M., Read, W.G., Siegel, P.H., Cofield, R.E., Filipiak, M.J., Flower, D.A., Holden, J.R., Lau, G.K., Livesey, N.J., Manney, G.L., Pumphrey, H.C., Santee, M.L., Wu, D.L., Cuddy, D.T., Lay, R.R., Loo, M.S., Perun, V.S., Schwartz, M.J., Stek, P.C., Thurstans, R.P., Boyles, M.A., Chandra, K.M., Chavez, M.C., Gun-Shing Chen, Chudasama, B.V., Dodge, R., Fuller, R.A., Girard, M.A., Jiang, J.H., Yibo Jiang, Knosp, B.W., LaBelle, R.C., Lam, J.C., Lee, K.A., Miller, D., Oswald, J.E., Patel, N.C., Pukala, D.M., Quintero, O., Scaff, D.M., Van Snyder, W., Tope, M.C., Wagner, P.A., and Walch, M.J., 2006. The Earth Observing System Microwave Limb Sounder (EOS MLS) on the Aura Satellite, *IEEE Trans. Geosci. Remote Sens.*, **44**, 1075-1092.

Weber, M., S. Dhomse, F. Wittrock, A Richter, B.-M. Sinnhuber and J. P. Burrows, 2003. Dynamical control of NH and SH winter/spring total ozone from GOME observations in 1995-2002, *Geophys. Res. Lett.*, **30**, doi:10.1029/2002GL016799.

World Meteorological Organization (WMO)/United Nations Environment Programme (UNEP), 2007. *Scientific Assessment of Ozone Depletion: 2006*, World Meteorological Organization, Global Ozone Research and Monitoring Project, Report No. 50, Geneva, Switzerland.

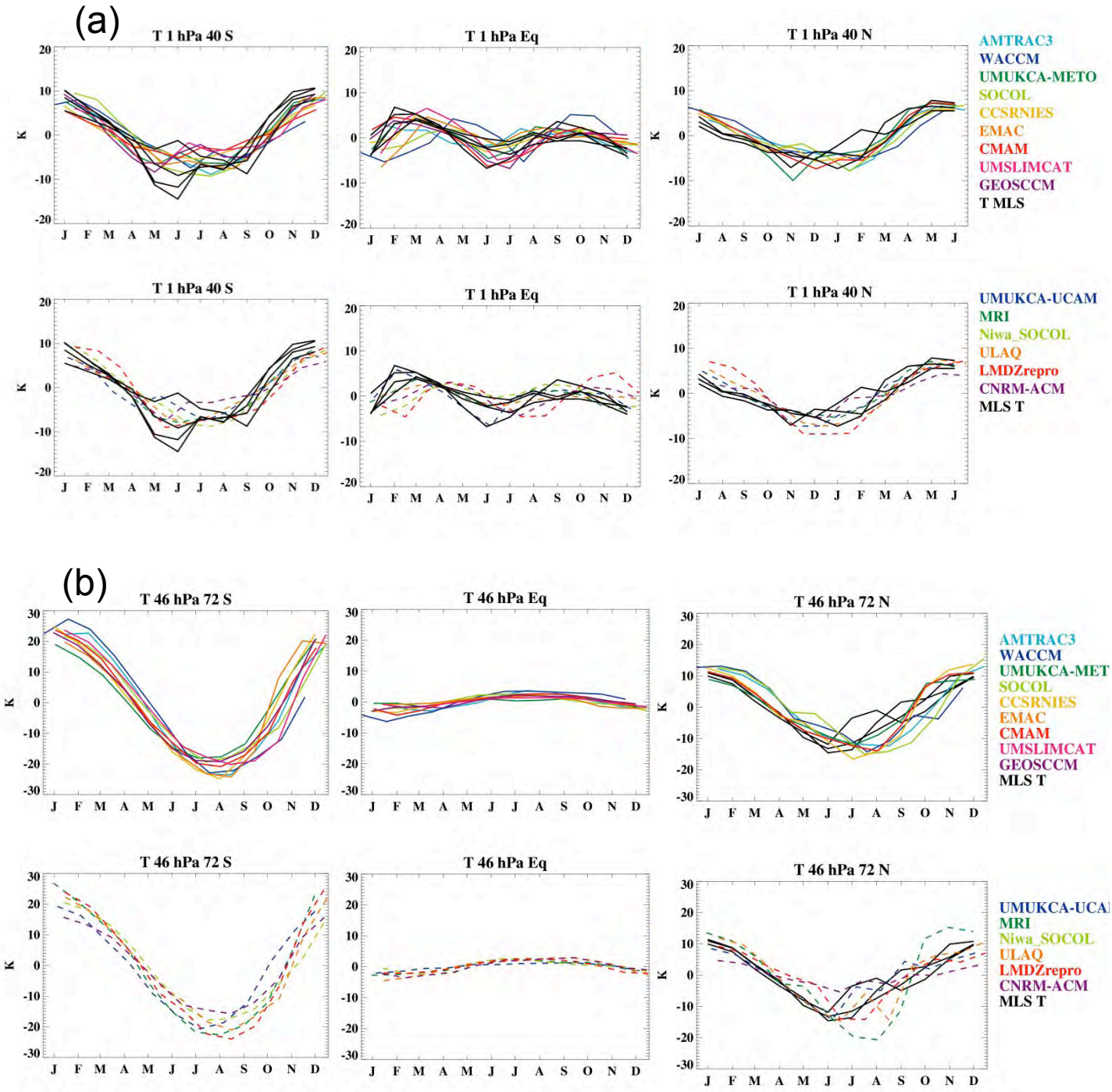

Figure S8.1: Monthly mean temperature annual cycle corresponding to the ozone mixing ratio annual cycle shown in Figures 8.2 a,b.

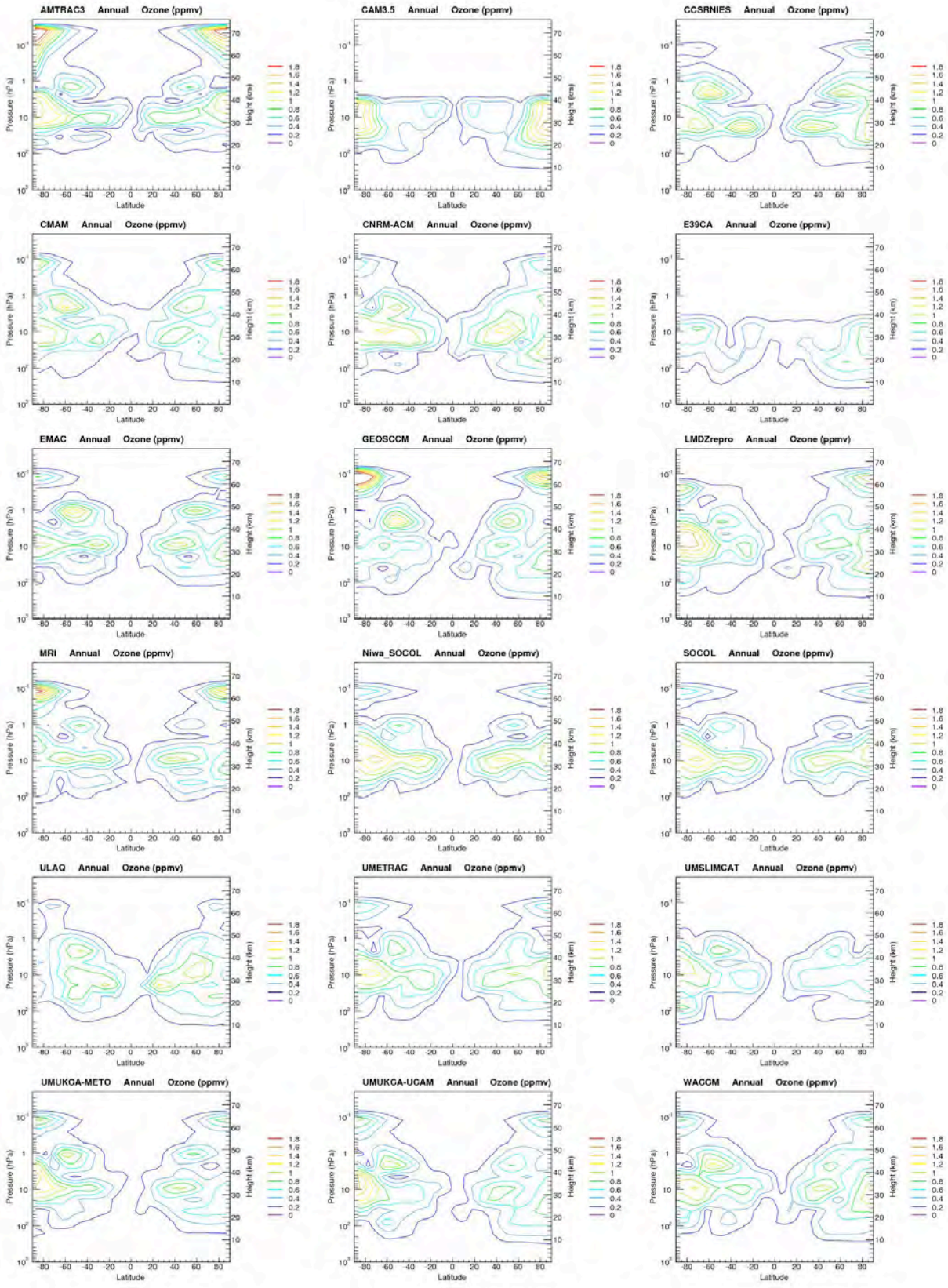

Figure S8.2: Latitude-height section of the annual harmonic from the MLR analysis for the CCMVal-2 CCMs (1960-2004).

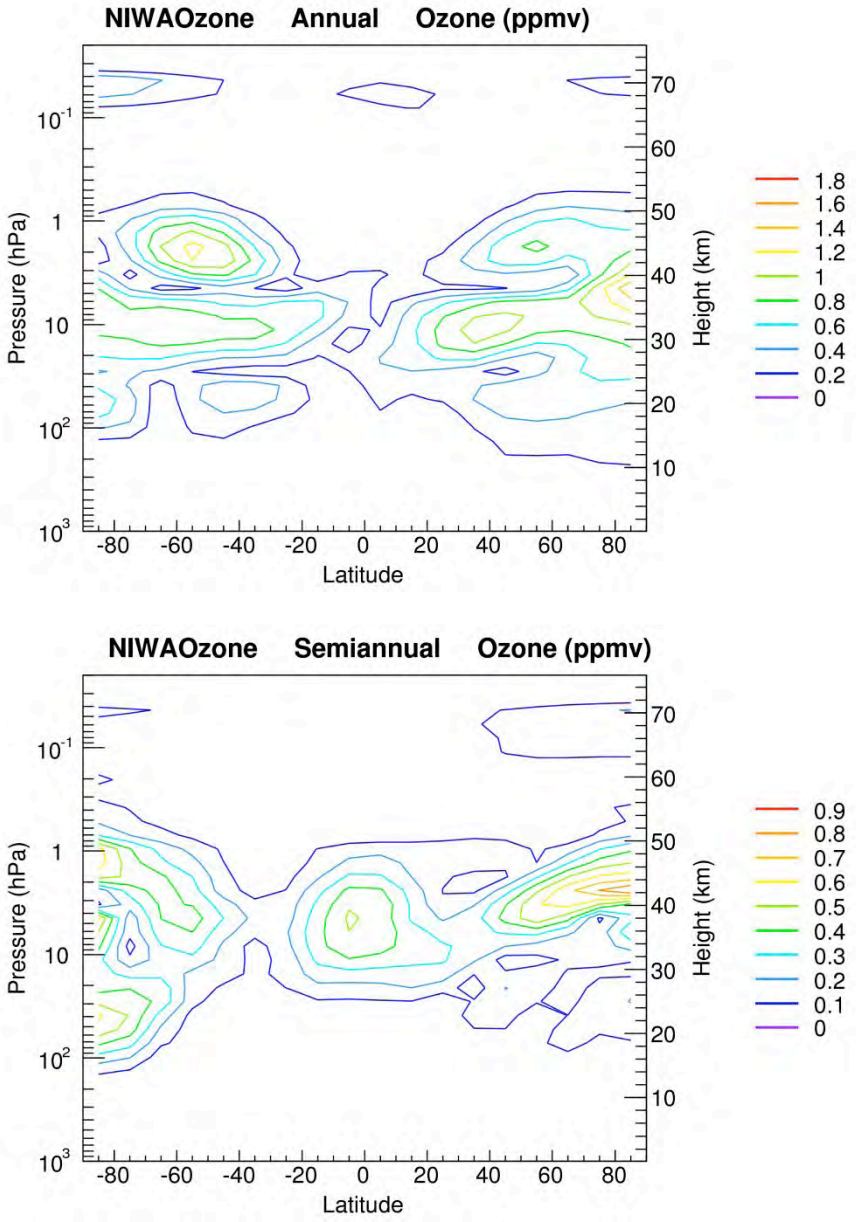

Figure S8.3: Latitude-height sections of the annual and semiannual harmonics from the MLR analyis for the NIWA-3D data (1979-2006).

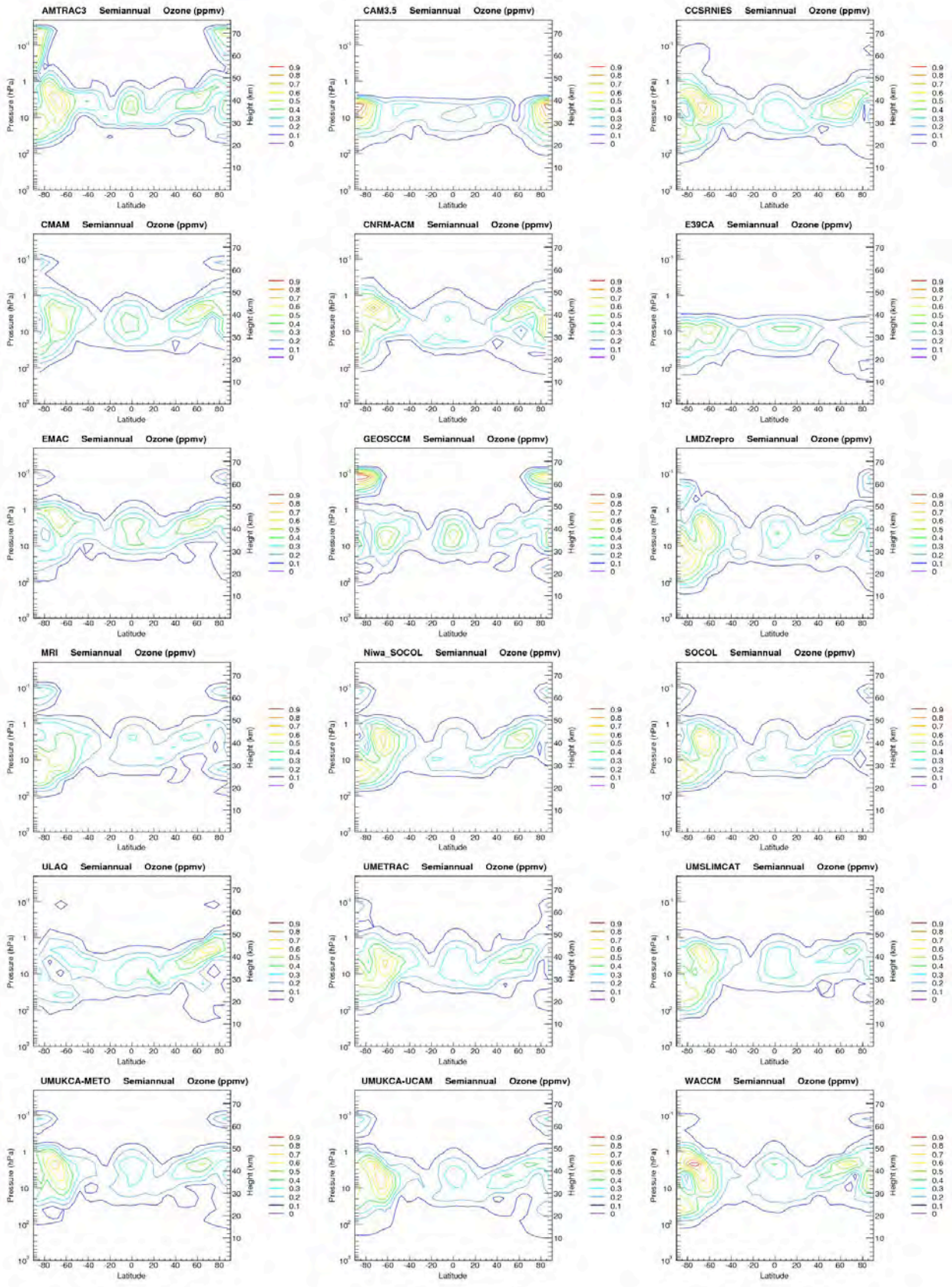

Figure S8.4: Latitude-height sections of the semiannual harmonic from the MLR analysis for the CCMVal-2 CCMs (1960-2004).

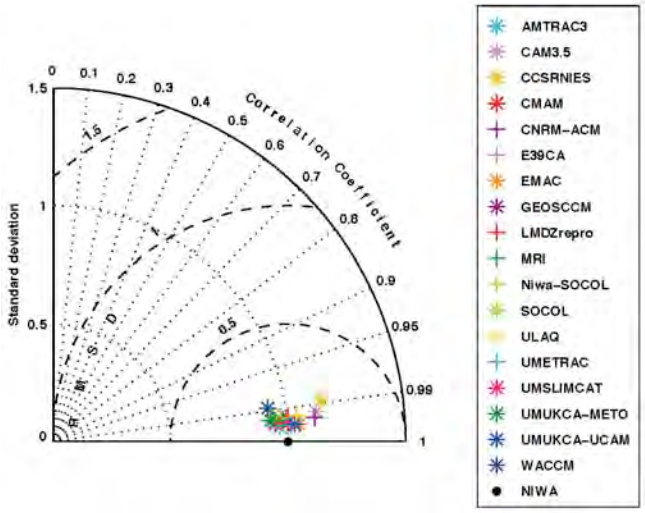

Figure S8.5: Normalized Taylor diagram of the annual zonal mean ozone, latitude-pressure distribution, for the NIWA-3D dataset and the CCMVal-2 models. The pattern statistics have been computed for the 1-500 hPa, 90°S-90°N range.

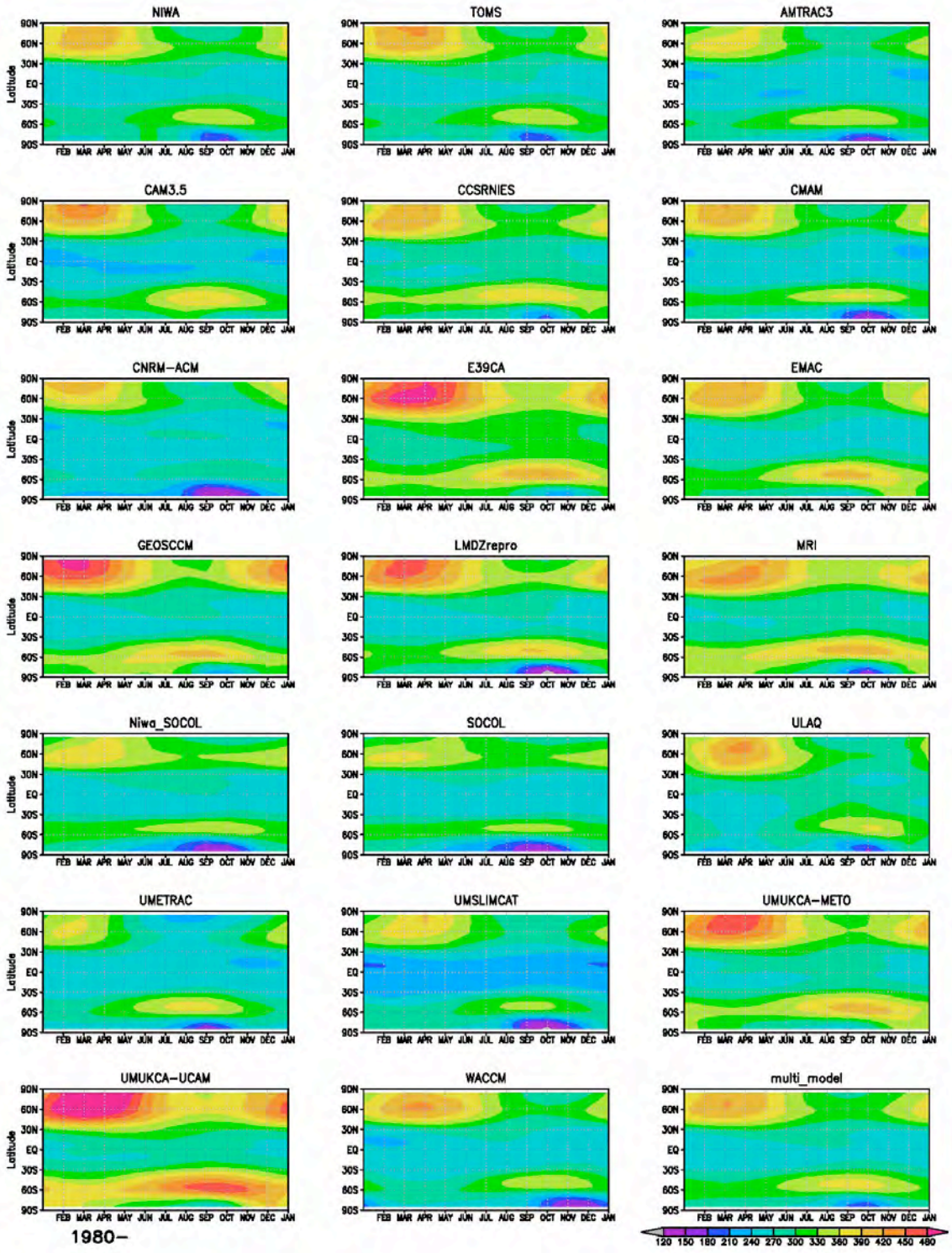

Figure S8.6: Annual cycle of the monthly zonal mean column ozone for the NIWA-column, TOMS+gb datasets and the CCMVal-2 models.

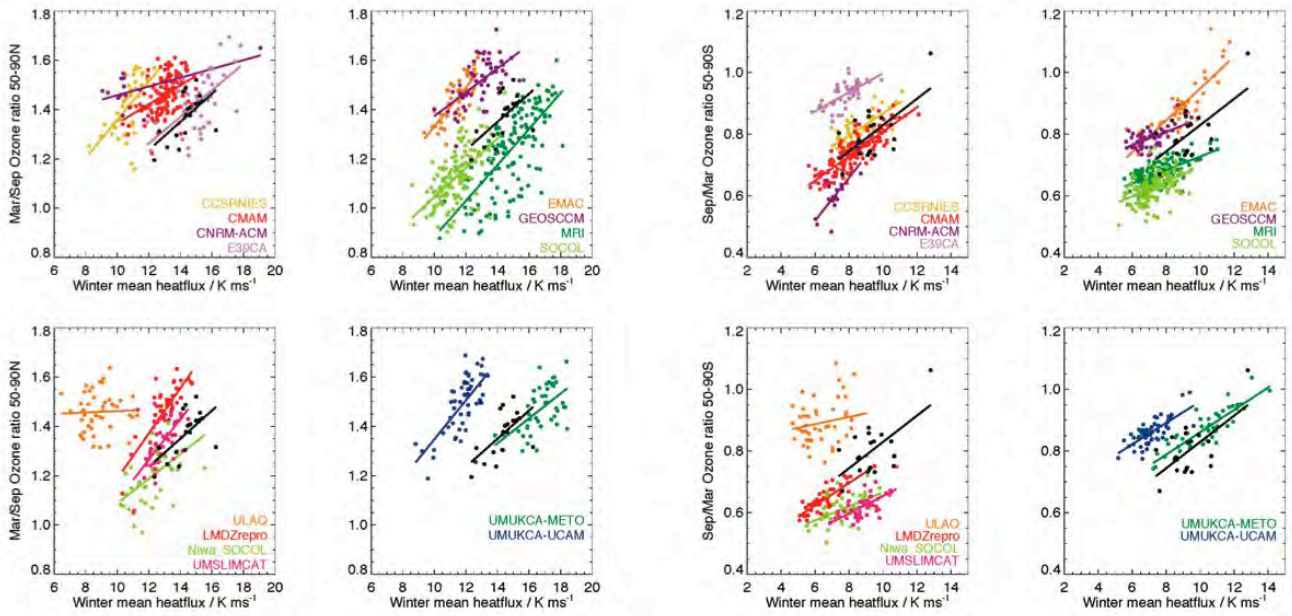

Figure S8.7: Scatter plot of the spring-to-fall column ozone ratio versus the 100 hPa winter mean heat flux (K ms-1) for each model and for the observations. Black color is used for the observations (NIWA-column ozone data and ERA-interim heat flux). Dot represent a single year of data. Solid lines represent the linear fit to the respective data. NH results: 4 panels at left. SH results: 4 panels at right.

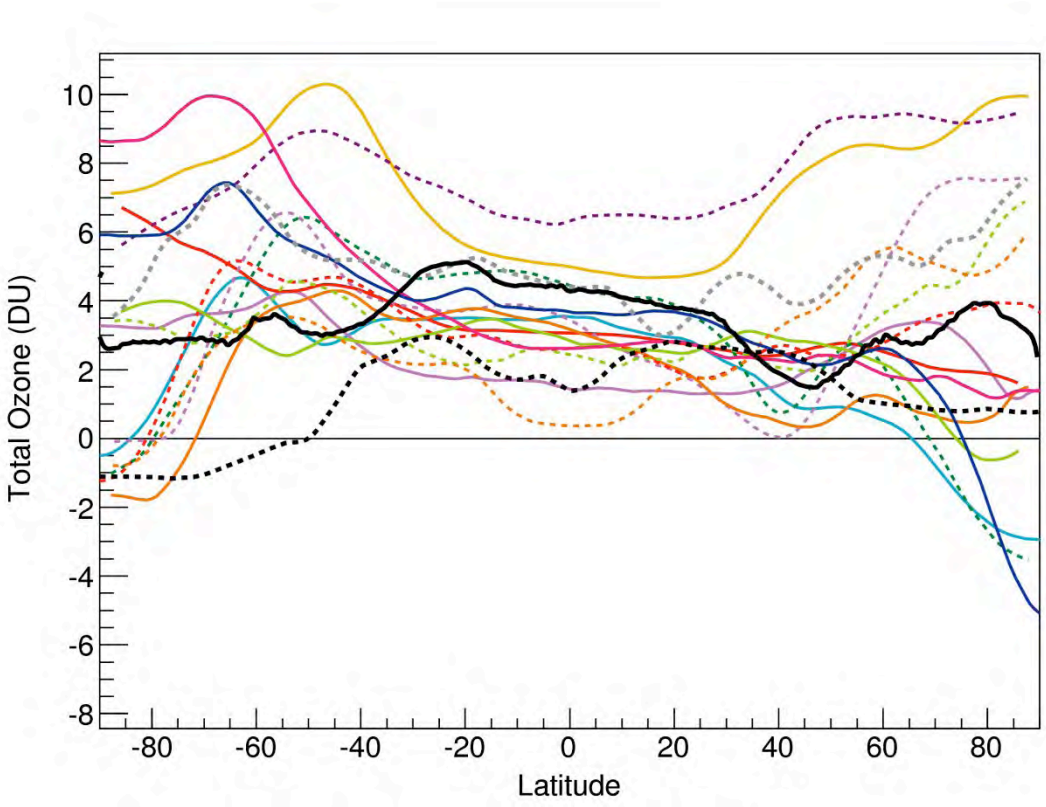

Figure S8.8: Annual mean latitude distribution of the solar coefficient (%/100 units of the F10.7cm radio flux) for column ozone for the CCMVal-2 CCMs and TOMS+gb, SAGE, and NIWA-column ozone observations.

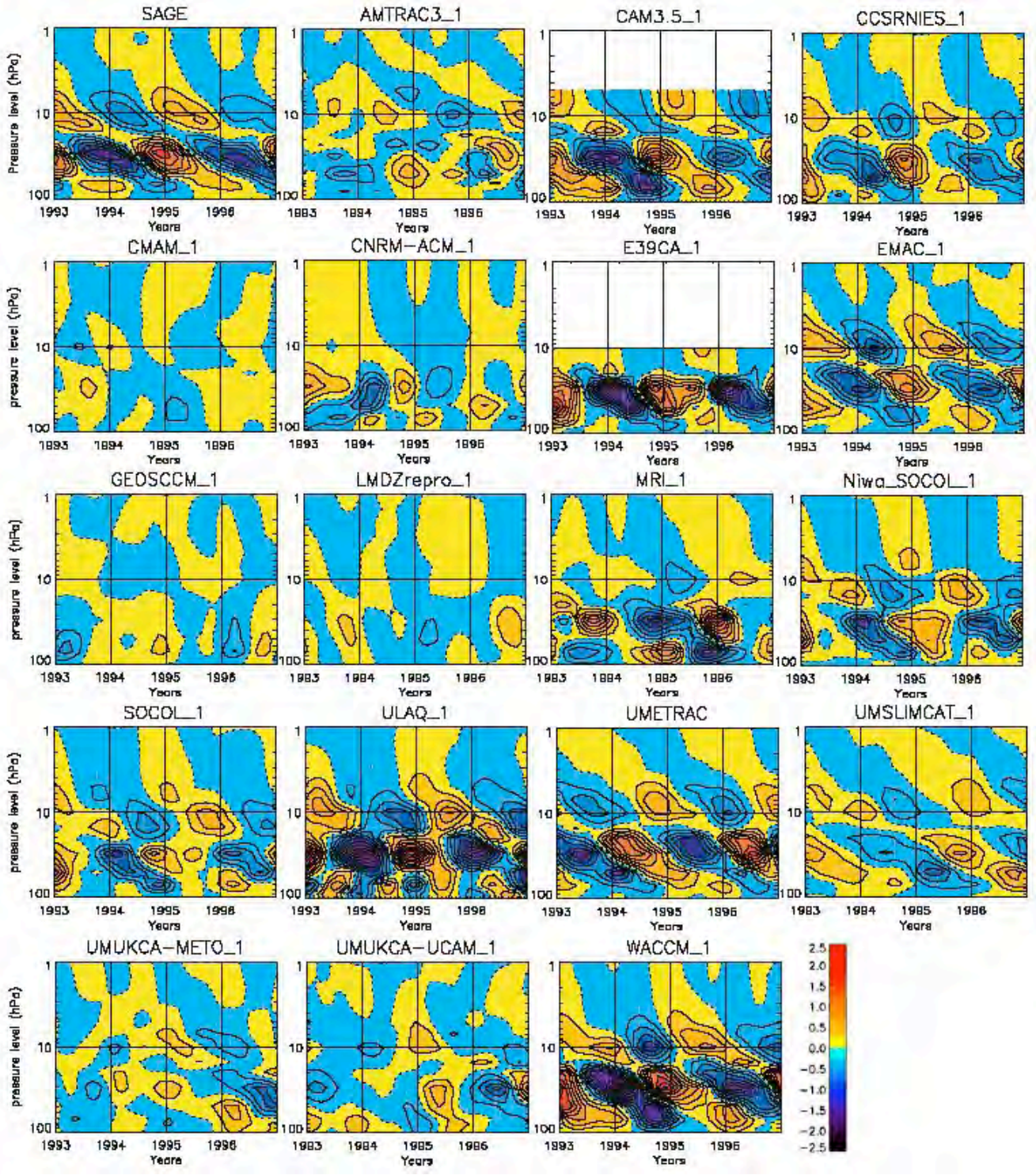

Figure S8.9: Latitude-time series of monthly zonal mean ozone concentration (DU/km) from 1993 to 1996 (data treated as Figure 8.14) for SAGE observations and the CCMVal-2 CCMs

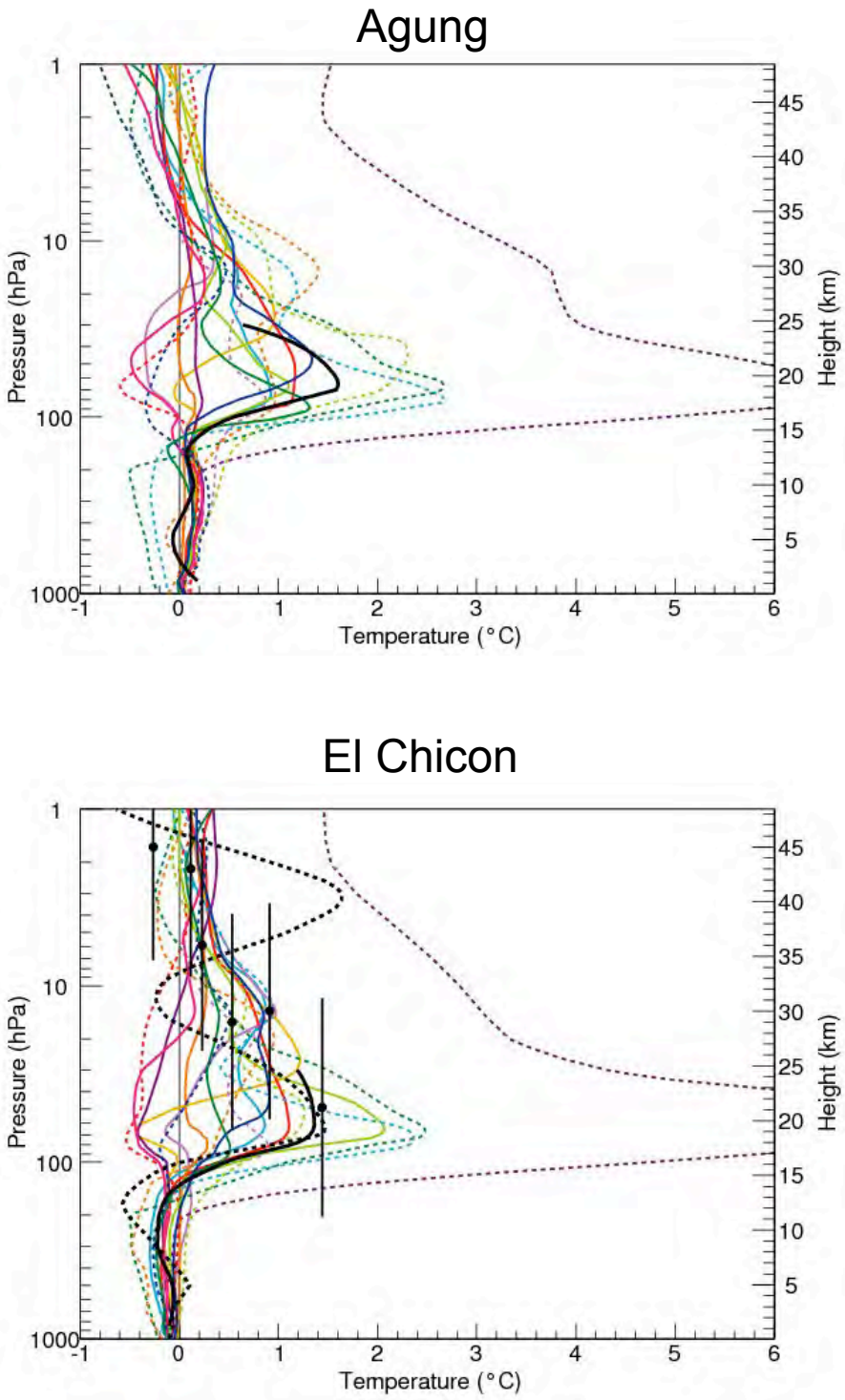

Figure S8.10: As Fig. 8.21 but for Agung (top) and El Chicon (bottom) (averaged over 24 months after the eruption) from 1000 to 1 hPa, temperature (K) for the CCMVal-2 CCMs and the ERA40, SSU and RICH observations.

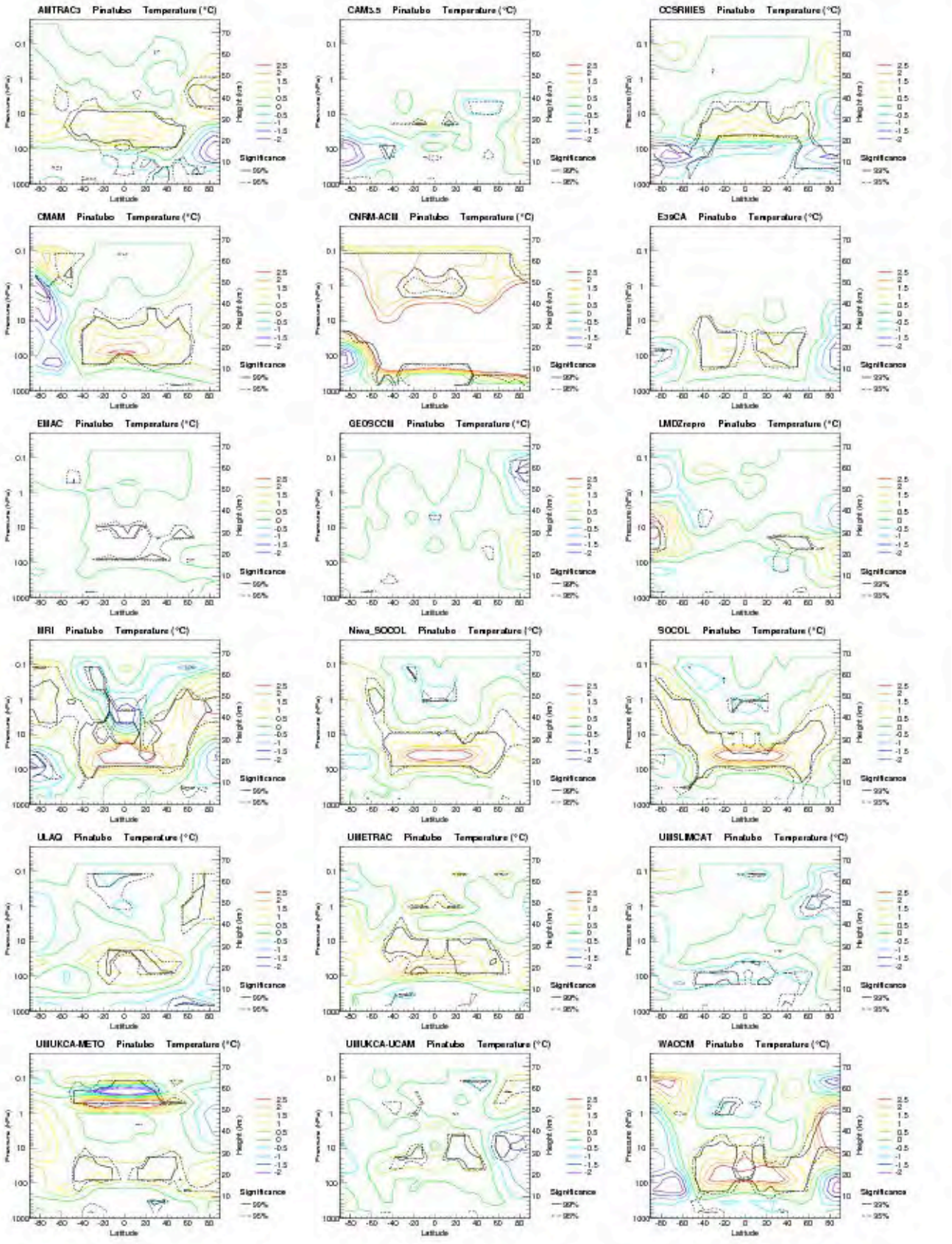

Figure S8.11: Latitude-height distribution of the volcanic response contribution from CCMVal-2 CCMs (1960-2004) for Pinatubo (averaged over 24 months after the eruption) from 1000 to 1 hPa. Temperature in K.

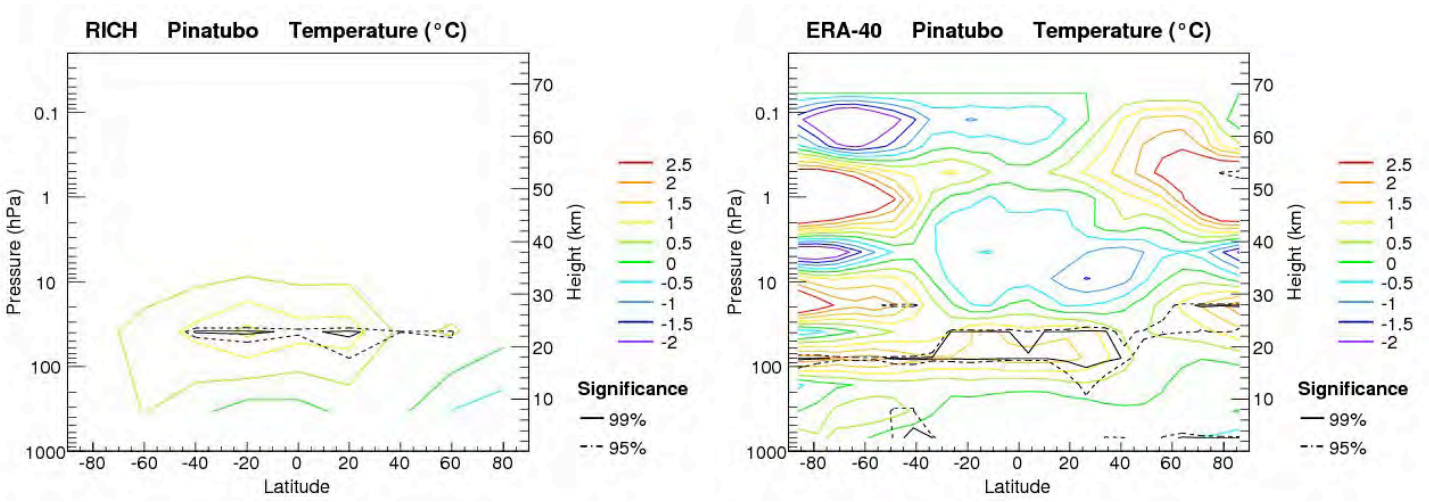

Figure S8.12: same as Fig. S8.11, but for observations (left panel RICH and right panel ERA-40).

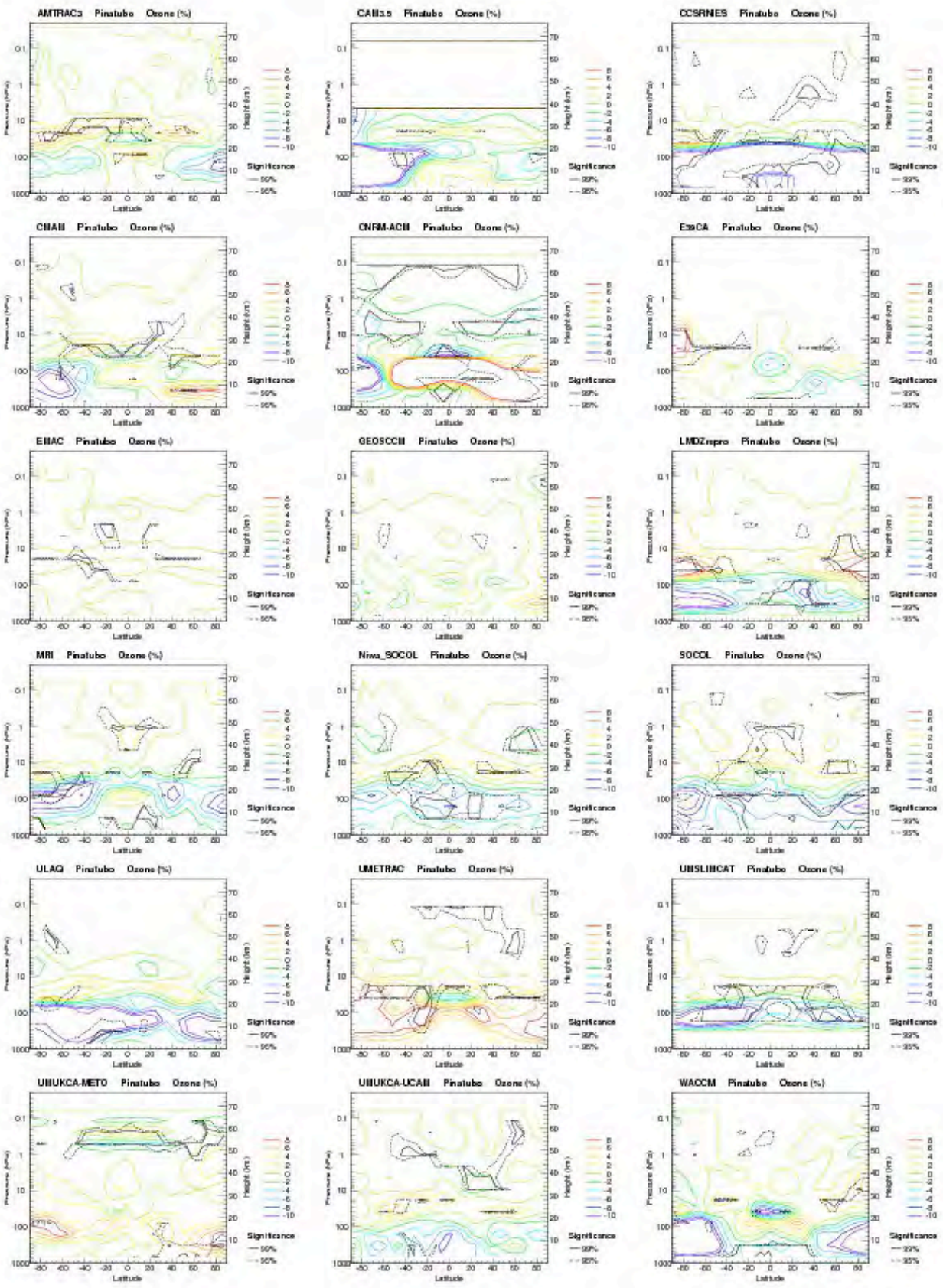

Figure S8.13: Same as Figure S8.11 but for ozone in %.

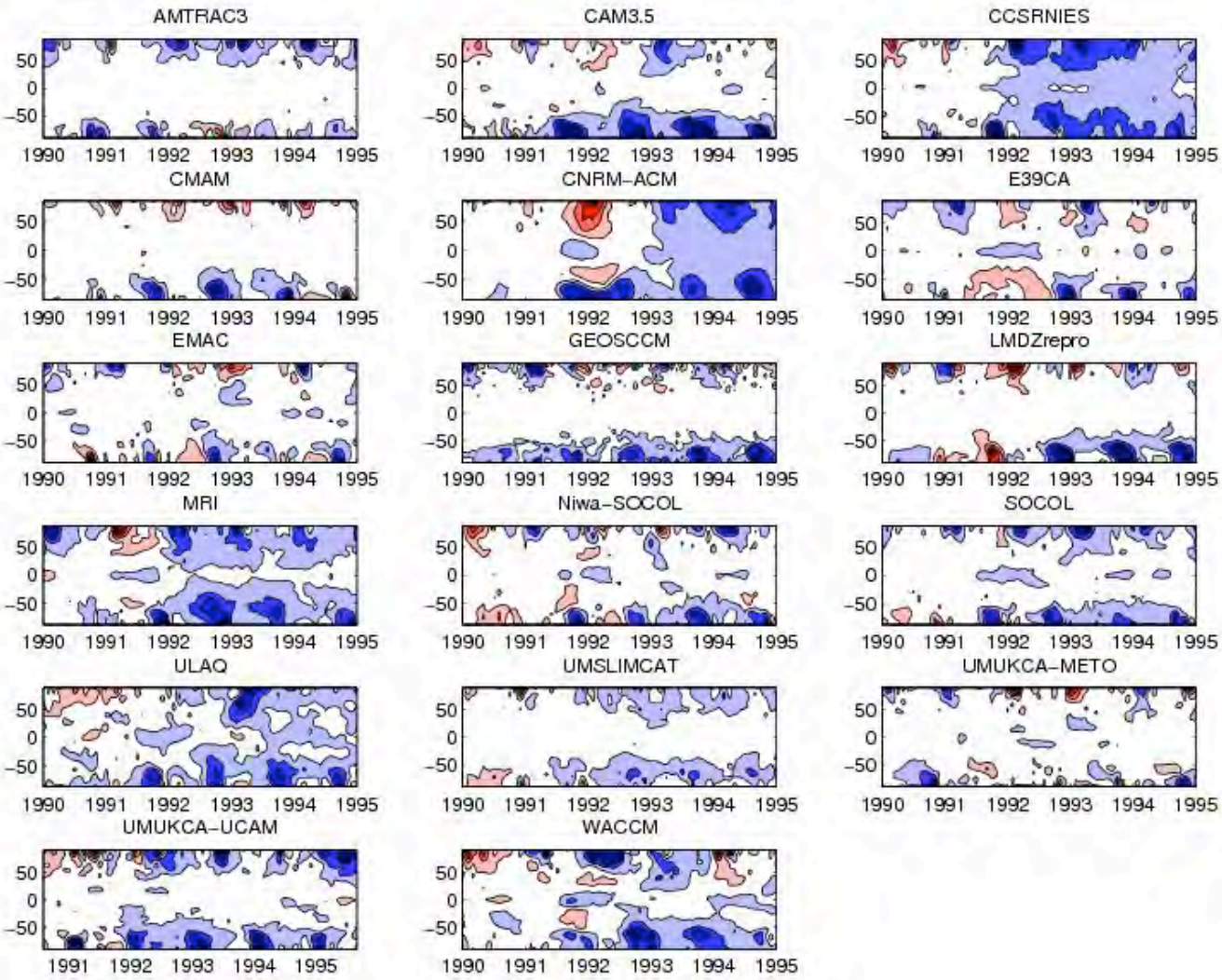

Figure S8.14: Latitude-time contour plots of column ozone differences from the 1985-1990 mean climatology over the years 1990-1995. Contours are spaced by 20 DU, with colored contours beginning at -10 and +10 DU. Note that an increase in the strength of ozone loss in the Antarctic spring is expected even without volcanic influence (see behavior for GEOSCCM, which does not include any volcanic forcing), due to the increasing levels of EESC over this time period.

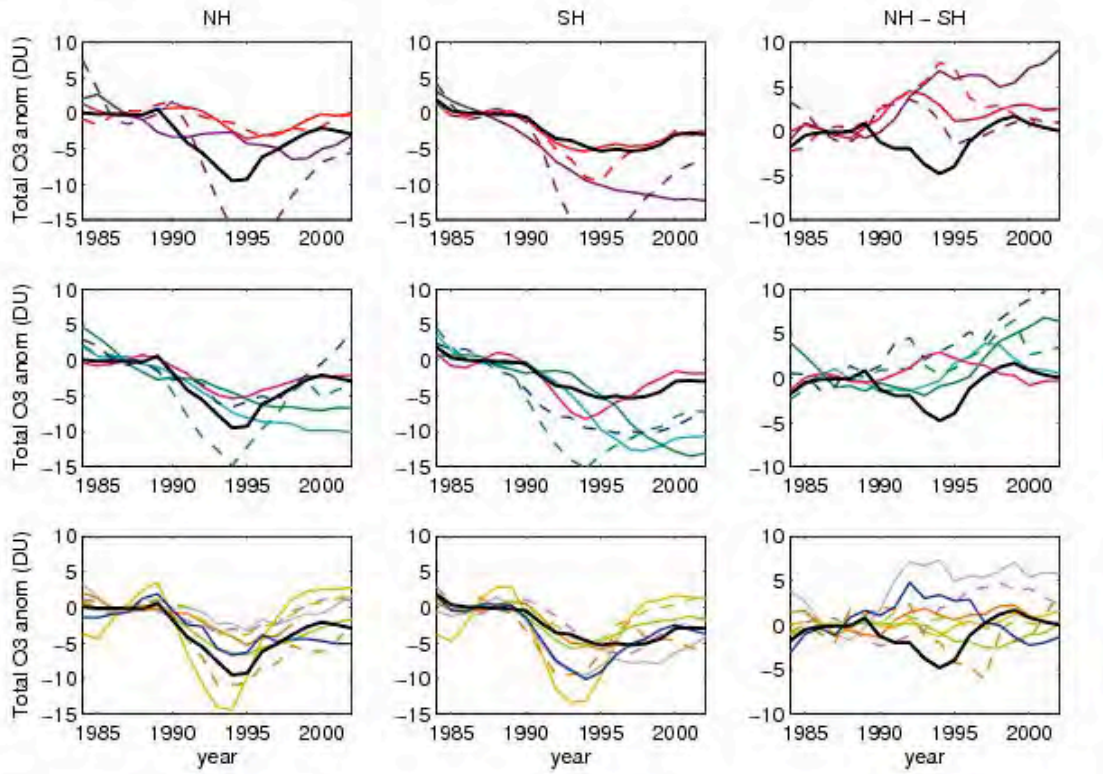

Figure S8.15: Total ozone anomalies from pre-Mt. Pinatubo eruption period (1985-1990) for NH (left column), and SH (middle column), smoothed by a five-year box-car function. Right column shows differences between the two hemisphere anomalies (NH-SH). Rows separate models with respect to Group A (top row), Group B (middle row) and Group C (bottom row) of the QBO Table 8.4 . Observations (TOMS+gb, black) show more post-Pinatubo ozone loss in the NH than in the SH, which is not well simulated by the CCMVal models.

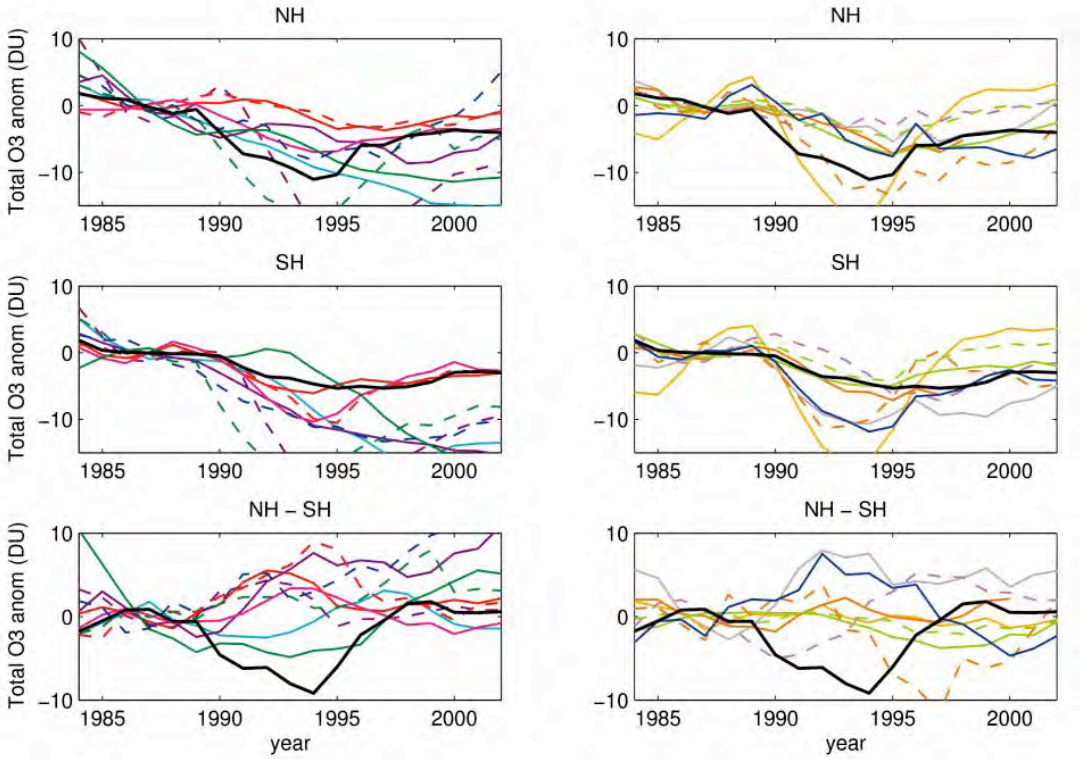

Figure S8.16: Same as S8.15 but for midlatitude (30°-60°) regions of each hemisphere.

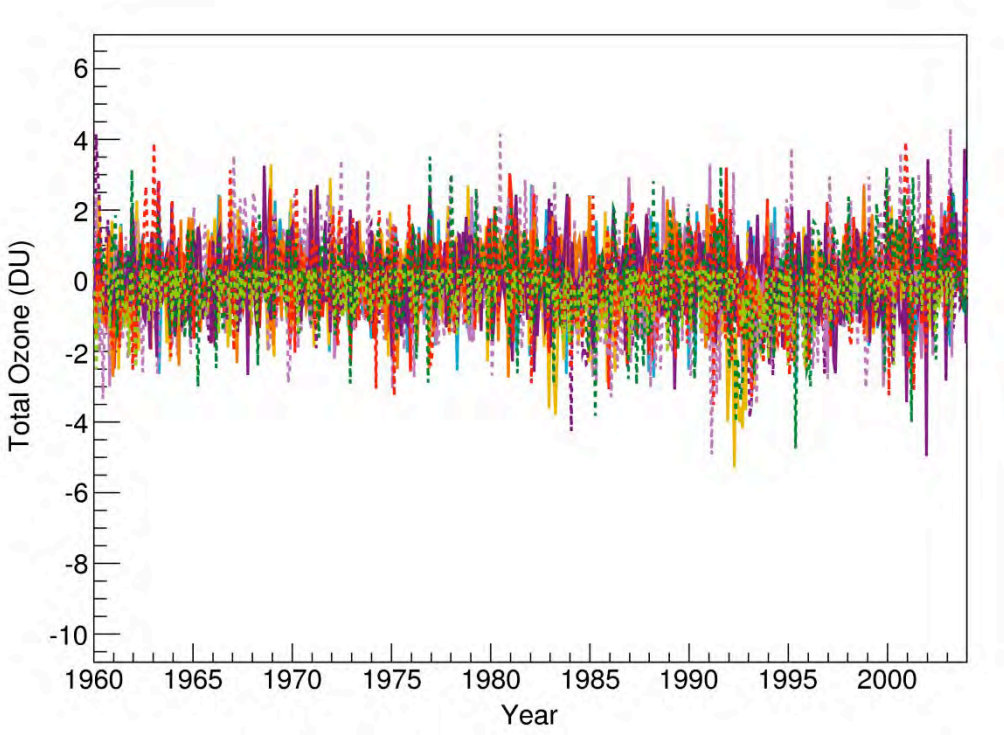

Figure S8.17: Residual (difference between original and fitted data) for column ozone for the CCMVal-2 CCMs.

Chapter 9

Long-term projections of stratospheric ozone

Lead authors: John Austin & John Scinocca

Co-authors: Trevor Bailey
Luke Oman
David Plummer
David Stephenson
Hamish Struthers

9.1 Introduction

The long-term evolution of ozone is influenced by a wide variety of factors that may be broadly separated into radiative, dynamical, transport, chemical and external forcing processes. Many of the processes are also coupled in the sense that, for example, dynamical changes lead to chemical changes, which feed back onto the dynamics. Therefore, although it is convenient to try to separate the effects of individual processes on ozone amounts, to some extent this can be a matter of definition and the stratosphere needs to be treated as a whole.

Radiative effects related to ozone were discussed in Chapter 3. Stratospheric temperature (and hence ozone chemistry) is influenced by radiative processes through changes in the long-lived greenhouse gases (GHGs) (Shine *et al*., 2003); primarily CO_2, although CH_4, H_2O, and N_2O are minor contributors. The stratospheric temperature also has an important influence on the formation of polar stratospheric clouds, which are implicated in polar ozone destruction. Ozone itself is a radiative gas. The radiative effects combined — due to GHGs and ozone — induce temperature changes. In turn this changes the planetary wave driving of the Brewer-Dobson (BD) circulation, which on climate time scales leads to increased transport (Butchart and Scaife, 2001).

Dynamical effects related to ozone were discussed in Chapter 4. Ozone amounts are influenced by both resolved and parameterised wave forcing. Resolved waves include synoptic scale and planetary waves, which have in particular a direct effect on the polar vortex. Most models include parameterisations for both orographic and non-orographic gravity waves (Chapter 2), which are crucial to simulate realistic polar vortex strength. For those models that have sufficient vertical resolution, there is the potential to model a spontaneous Quasi-Biennial Oscillation (QBO) (Takahashi, 1996). The QBO is an important part of the tropical variability, but also contributes to interannual variability in high latitude stratospheric winds by the well-known Holton-Tan effect (Holton and Tan, 1980). These processes have a direct effect on ozone amounts through transport. Dynamical processes also influence temperatures which in turn affect the chemistry of ozone because of the temperature dependence of the reaction rates.

Transport effects were discussed in Chapter 5. The net ozone change is essentially the balance between transport and chemistry, and small changes such as those due to the changes in the BD circulation (Shepherd, 2008) can have important direct changes on ozone as well as influencing the concentrations of long-lived species, in particular Cl_y and NO_y, which produce further chemical changes (Douglass *et al*., 2008).

Chemical effects related to ozone were discussed in Chapter 6. Chemical processes in recent decades have been dominated by the evolution of halogen loading (Eyring *et al*., 2006), which will also remain the focus of attention for several decades to come. While chlorine remains present in high concentrations in the atmosphere, volcanic eruptions will also play an important role through the supply of sites for heterogeneous reactions (Tie and Brasseur, 1995). Changes in water vapour concentration have a dual role; in changing the concentration of HO_x radicals, and in changing the amount of polar stratospheric clouds (PSCs). HO_x catalytically destroys ozone and changes the balance of other chemical species. Increases in PSC amounts lead to enhanced ozone destruction in the presence of high halogen amounts. N_2O increases lead to increased NO_y, and future ozone loss (Portmann and Solomon, 2007).

The UTLS region (Chapter 7) is important to ozone since, for example, water vapour concentrations in the stratosphere depend on the tropical tropopause temperature. The tropical pipe (Plumb, 1996) is also a source of very short-lived species which contribute to ozone depletion (WMO, 2007, Chapter 2).

Forcings external to the atmosphere also contribute to ozone change and were discussed in Chapter 8. At the top of the atmosphere, solar cycle variability leads to changes in ultraviolet (UV) flux which contributes to ozone variability *via* changes in photolysis rates (Austin *et al*., 2008). Unlike most other processes considered, though, this is cyclic rather than systematic, apart from historical periods such as the Maunder Minimum of several centuries ago. The lower boundary of the atmosphere is coupled to the sea surface, which will influence and be influenced by tropospheric dynamics, which in turn can affect stratospheric wave propagation (Garnkel and Hartman, 2007). Volcanic aerosols also affect ozone through heterogeneous chemical effects and *via* radiative heating (Chapter 3). Finally, the extent to which sea-surface temperatures (SSTs) and the troposphere influence the stratosphere will be determined in small part by the effect of the stratosphere on climate (Chapter 10).

The degree to which all of these factors combined influence the future evolution of ozone is investigated using the simulations of CCMVal-2, described in Chapter 2. The two sets of results from experiments REF-B1 and REF-B2 are used. In REF-B1, sea surface temperatures (SSTs) and external forcing parameters including the solar cycle, were specified from observations. In REF-B2, the greenhouse gas (GHG) scenario SRES A1b and the halogen scenario A1 from WMO (2007) were used to investigate the future behaviour of stratospheric ozone until the end of the 21st century. The results are found to depend broadly on latitude and hence it is most natural to divide the results into tropical, mid-latitude, and polar regions. For each of these regions the goal of this Chapter will be:

- To review and update our understanding of the dominant factors that affect ozone depletion and recovery in that region.
- To present the projected past and future ozone change from the new (CCMVal-2) CCM simulations and compare this with the projected ozone change from the previous (CCMVal-1) CCM simulations.
- To pull together "future-change" information for these factors from the relevant chapters of this report to understand the evolution of ozone and to estimate the relative importance of any competing factors.
- To identify outstanding modelling issues that are central to the accurate prediction of long-term ozone in that region.

In addition, in Section 9.6 the results from the different regions are brought together to address the issue of ozone recovery and its timing. The 2006 Ozone assessment (WMO, 2007) expressed ozone recovery in terms of ozone increase relating to a reduction in ozone depleting substances (ODSs). Here, we need to consider a more generalised ozone recovery, which takes account of changes in GHGs as well. In this respect ozone recovery can be considered in the same way as tropospheric temperature change, and attribution analyses can be undertaken to determine the cause of ozone recovery, whether it is chemical (*via* ODS reduction for example), radiative (*via* temperature change on the reaction rates) or dynamical (*via* chang-

es in transport). Hence, we use the term "ozone recovery" to imply the process of an increase in ozone. We avoid terms such as "full recovery" and "super-recovery", which imply the need for an ozone or ODS benchmark. Instead, we refer to points along the path of ozone increase as "recovery to 1980 levels" or "return to 1980 levels". We also consider other reference dates, such as 1960, reflecting the loss of ozone that likely occurred prior to the availability of extensive satellite measurements of ozone.

9.2 Analysis methods

The CCMVal results are investigated using two distinct analysis methods. In Section 9.2.1 we present a multi-model time series analysis method which is used to document the evolution of total column ozone and chlorine amounts. In Section 9.2.2 we summarize the multi-linear regression methodology that is used to attribute individual model sensitivities to chemistry and temperature.

9.2.1 Multi-Model Time Series Analysis

Ideally, a comparison between CCMVal-1 and CCMVal-2 projections would be based on analyses that produced quantitative predictions and uncertainty estimates of ozone and ozone related indices. In previous studies, time series analysis of CCMVal simulations (WMO 2007, Eyring *et al*., 2007) have provided mostly qualitative results making it difficult to formulate and utilize multi-model projections. Instead, we formulate a new analysis procedure based on a statistical framework that employs a nonparametric additive model to estimate individual-model trends (IMT) and multi-model, trends (MMT). Here, the term "trend" refers to a smooth trajectory passing through the time series data representing the "signal", leaving a "noise" field as the residual. The goal in this procedure is the definition of the simplest nonparametric additive model whose trend estimate produces residuals that satisfy assumed properties of noise (*e.g*., that it be an independent normally distributed random variable). The use of a statistical framework based on a probabilistic model allows the trend estimates to be used to make formal inference (*e.g*., calculation of confidence and prediction intervals). We shall refer to this new time series additive-model analysis as the "TSAM" analysis. Attractive properties of the TSAM analysis include: the production of smooth trend estimates out to the ends of the time series, the ability to model explicitly interannual variability about the trend estimate, and the ability to make rigorous probability statements. Because the TSAM analysis is based on a testable probabilistic model, the suitability of the particular nonparametric additive model used can be validated.

The TSAM analysis adopted here consists of three steps: estimation of individual model trends (IMT), baseline adjustment of these trends, and the weighted combination of the IMT estimates to produce a multi-model trend (MMT) estimate. Much of the development effort of the TSAM analysis has gone into the final weighting step. The formulation allows the specication of prior model weights if this is desired (*e.g*., metric-based performance weighting, although in the present application of the TSAM, this feature was not used) in the evaluation of the final MMT estimate. Two types of uncertainty intervals are constructed for the MMT estimate. The first is the point-wise 95% confidence interval. This interval has a 95% chance of overlapping the true trend, representing the local uncertainty in the trend at each year. The second interval, larger by construction, is the 95% prediction interval. This interval is a combination of uncertainty in the trend estimate and uncertainty due to natural interannual variability about the trend. It gives an idea of where an ozone value for a given year might reasonably lie.

A complete description of the TSAM is provided in Appendix B. along with detailed examples of its application. A supplement to the chapter has been created in which a more complete set of TSAM diagnostics are provided along with an analysis of its sensitivity to outliers and a comparison with the simpler methods of time series analysis employed for CCMVal-1.

In the following sections, three types of figures will be presented that relate to the application of the TSAM analysis on ozone related time series. The first (*e.g*., Figure 9.1 left-hand column) represents initial IMT estimates of the raw time series data. This initial smooth fit is used to define a baseline value for each model, and a multi-model mean baseline value for a specified reference year. Taking the reference year as 1980 for example, anomaly time series would be constructed by taking the raw time series and subtracting their respective 1980 baseline values. Finally, to each anomaly time series the multi-model mean 1980 baseline value would be added. In this example, we would refer to these as "1980 baseline-adjusted" time series. The second type of figure (*e.g*., Figure 9.1 right-hand column) displays IMT estimates of the baseline-adjusted time series and it is these that are used to define the MMT estimate in the final step of the TSAM analysis. The third type of figure (*e.g*., Figure 9.2) shows the baseline-adjusted MMT estimate (heavy dark-grey line) along with its 95% confidence, and 95% prediction intervals (light- and dark-grey shading respectively). Further details may be found in Appendix B and a complete set of these figures appears in Section 9S.1 of the supplement to this chapter. The final MMT estimates are suitable for the production of multi-model estimates of return dates and this is discussed in Section 9.6.

9.2.2 Multi-linear regression analysis

Multiple linear regression (MLR) is used to deter-

mine the relationship between ozone amounts and physical parameters to try to obtain the reasons for the modelled ozone trends. We concentrate on the middle and upper stratosphere, where the processes are more amenable to this analysis. The method used here is based on Oman *et al*. (2010) which separates the contributions of explanatory variables to changes in extra-polar ozone. As discussed in Oman *et al*. (2010), the MLR method focuses on the variables contributing to ozone change rather than the specific surface forcings (*e.g*., CO_2, N_2O, CH_4, and Halogens). The explanatory variables are temperature, NO_y, HO_x and $Cl_y + \alpha Br_y$. For those models which did not supply HO_x (AMTRAC3 and UMUKCA-UCAM) this term was not included in the analysis. Likewise, several models (CAM3.5, CNRM-ACM, UMSLIMCAT, and UMUKCA-UCAM) did not supply bromine, or bromine was not included in the simulations, and so the bromine component of $Cl_y + \alpha Br_y$ was set to zero.

The purpose of the analysis is to estimate the contribution of the different chemical mechanisms to the simulated changes in ozone. The principal analysis method used is multiple linear regression (MLR), which for a given location is applied to determine the coefficients m_x such that

$$\Delta O_3(t) = \Sigma_j m_{x_j} \Delta x_j(t) + \varepsilon(t) \qquad (9.1)$$

where the x_j are the independent parameters of the regression and $\varepsilon(t)$ is the residual. Four explanatory variables x_j are used: $Cl_y + \alpha Br_y$, $NO_y = NO + NO_2 + NO_3 + 2N_2O_5 + HNO_3 + HNO_4 + ClONO_2 + BrONO_2$, $HO_x = OH + HO_2$, and temperature, T. m_{x_j} is later referred to as the 'sensitivity' of O_3 to the independent parameter x_j. Each of the product terms on the right hand side of Equation 9.1, $m_{x_j} \Delta x_j(t)$, represents the contribution of x_j to the ozone change. For the term $Cl_y + \alpha Br_y$, α is taken to be 5, the appropriate value for the upper stratosphere (Daniel *et al*., 1999), which is the region of the atmosphere considered here.

The MLR analysis is more difficult to interpret in the lower stratosphere, where photochemical time scales are comparable to the dynamical time scales. Hence temperature changes can induce chemical changes in ozone as well as reflecting dynamical variations which induce transport changes in ozone. Since these effects are often opposed, the resulting regression fit is poorer.

9.3 Tropical Ozone

9.3.1 From the 2006 WMO assessment:

- A small (2%) increase in column ozone is expected from 2000 to 2020.
- The 2050 column ozone is expected to be slightly lower than 1980 values.
- Decreased ozone occurs in the lower stratosphere, due to the enhancement of the BD circulation, which is expected to bring up ozone-poor air from the troposphere.

9.3.2 Further analysis of the CCMVal-1 runs

The strength of the BD circulation is expected to increase on climate time scales (Butchart and Scaife, 2001; Butchart *et al*., 2006; McLandress and Shepherd, 2009a), driven by increases in GHGs. Li *et al*. (2008) and Oman *et al*. (2009) show that the BD circulation is also driven in part by changes in ozone, with the circulation changing fastest during the last two decades when ozone depletion was strongest. In the future, as ozone recovers, the BD circulation is expected to increase less rapidly (Li *et al*., 2008; Oman *et al*., 2009). Model simulations agree well with calculations of upwelling derived from radiosonde observations (Yang *et al*., 2008), although it is not currently feasible to determine observed trends because of the quality of the data. An indirect way of estimating the trend in upwelling is *via* the age of air, which should decrease due to climate change (*e.g*., Austin and Li, 2006; Garcia *et al*., 2007). However, although measurements do not show a trend in age of air (Engel *et al*., 2009), because of their large uncertainties, they do not necessarily contradict CCM results (Waugh, 2009).

The change in the BD circulation gives rise to upward transport of ozone and other constituents in tropical regions, leading to lower tropical ozone in particular (*e.g*., Shepherd, 2008). The decrease of column ozone due to transport is comparable to the increase in the upper stratosphere due to stratospheric temperature change (*e.g*., Li *et al*., 2009).

Recent work has also investigated trends in the position of the tropopause (Son *et al*., 2008; Gettelman *et al*., 2009; Austin and Reichler, 2008). These studies show that the tropopause height is expected to increase in the future at a similar rate as the increase of the past few decades. The tropopause pressure is also simulated to decrease at a similar rate in the future as in the past. Austin and Reichler (2008) also show that in AMTRAC, the BD circulation is closely related to tropopause pressure and that their model simulates larger tropopause pressure trends than observed. These studies combined indicate that models with larger trends in upwelling give rise to larger trends in tropopause pressure, and that the mean of the models considered by Son *et al*. (2008), which included both small BD trends as well as large trends, is in good agreement with observations. In independent calculations, Fomichev *et al*. (2007) also show that an increase in SSTs leads to a warmer and higher tropopause. A plausible physical mechanism for the tropical SST influence is the strengthening of tropical upwelling *via* deep convection (Deckert and Dameris, 2008).

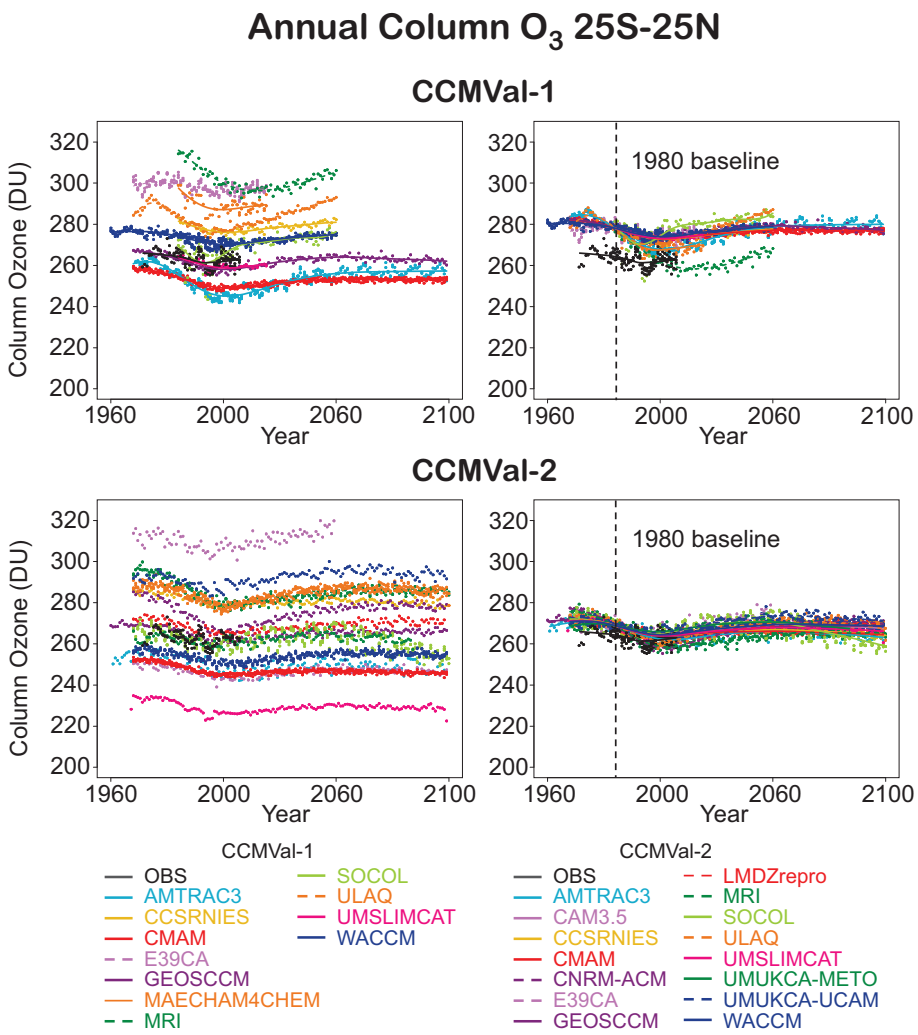

Figure 9.1: Raw time series data of annually averaged total ozone for the latitude range 25°S-25°N and initial individual model trend (IMT) estimates (left-hand panels), and 1980 baseline-adjusted time series data and 1980 baseline-adjusted IMT estimates (right-hand panels) for the TSAM analysis of CCMVal-1 (top) and CCMVal-2 (bottom). Observations are shown in black for four observational data sets (see text). A lowess fit (with smoother span f=0.4) to the observations appears as a black line in all panels. The observations are not baseline-adjusted in the right-hand panels.

The implication of the trend in tropopause pressure is to reduce ozone at a given pressure just above the tropical tropopause. This would also follow directly from the increased upwelling in that region. A reduction in ozone has been observed in that part of the atmosphere (Randel and Wu, 2007) exceeding 6%/decade since 1980, which is too large to be understood on the basis of known chemistry, as radical concentrations are considered too small to have had a significant impact. The trend in ozone in this region has an important radiative impact, which leads to temperature trends in the tropopause region that are in much better agreement with observations than the simulations of the Coupled Model Intercomparison Project 3 (Forster *et al.*, 2007). The advantage of a CCM is that ozone is reasonably accurate in the vicinity of the tropopause, whereas in models with specified ozone, the connection between the local tropopause and the ozone amount is lost, and this has a significant impact on net heating rates (Forster *et al.*, 2007).

9.3.3 Tropical TSAM analysis

The TSAM analysis is applied to both the CCMVal-1 and current CCMVal-2 tropical total column ozone and 50 hPa total inorganic chlorine to identify any changes or improvements in moving to the newer models. In the left-hand column of **Figure 9.1** we present the raw time series data and the initial TSAM individual-model-trend (IMT) estimates for the annual total column ozone in the latitude band 25°S-25°N for 11 CCMVal-1 models (top) and 15 CCMVal-2 models (bottom). These initial IMT estimates

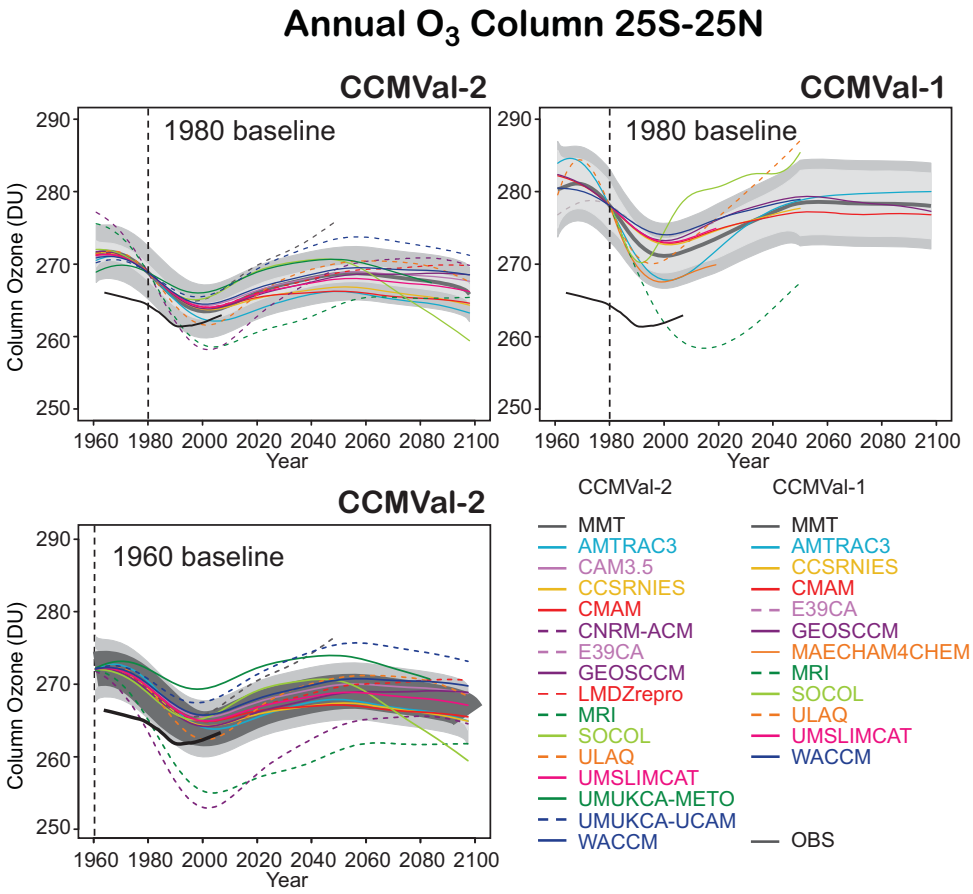

Figure 9.2: 1980 baseline-adjusted multi-model trend (MMT) estimates of annually averaged total ozone for the latitude range 25°S-25°N (heavy dark grey line) with 95% confidence and 95% prediction intervals appearing as light- and dark-grey shaded regions about the trend (upper panels). The baseline-adjusted IMT estimates, and unadjusted lowess fit to the observations are additionally plotted. CCMVal-2 results appear on the left and CCMVal-1 results appear on the right. The lower panel shows the same analysis of CCMVal-2 data but for a baseline adjustment employing a 1960 reference date.

employ the nonparametric additive model discussed in Appendix B and were verified by an analysis of the residuals (*e.g.*, see Appendix B.3). Observations of total ozone from four data sets are also presented in Figure 9.1 (black lines and symbols). These include ground-based measurements (updated from Fioletov *et al.* (2002)), merged satellite data (Stolarski and Frith, 2006), the National Institute of Water and Atmospheric Research (NIWA) combined total column ozone database (Bodeker *et al.*, 2005), and from Solar Backscatter Ultraviolet (SBUV, SBUV/2) retrievals (updated from Miller *et al.* (2002)).

Both the CCMVal-1 and CCMVal-2 time series display a wide range of background total ozone values over the entire REF-B2 period, which extend significantly above and below the observed values in this region. While the biases of most models have remained unchanged between the two inter-comparison projects, two models show significant differences from CCMVal-1 to CCMVal-2: WACCM has changed from a positive bias to a negative bias and UMSLIMCAT has changed from a near zero bias to a signicant negative bias.

As described in Sections 9.2.1 and Appendix B, relative to a selected reference date, baseline-adjusted time series and IMT estimates are computed in the second step of the TSAM analysis to facilitate a closer comparison of the predicted evolution of ozone indices between models. Analogous to the analysis performed in Chapter 6 of WMO (2007) and Eyring *et al.* (2007), anomaly time series are created for each model about a baseline value prior to significant ozone loss. Here, the baseline value is taken to be the initial IMT estimate at a selected reference date for each model (*e.g.*, 1980).

The baseline-adjusted time series are then formed by adding a constant so that each anomaly time series goes through the multi-model average of the IMT estimates at the reference date. Since the multi-model average of the IMT estimates is a close approximation to the final multi-model trend (MMT) estimate derived in the third step

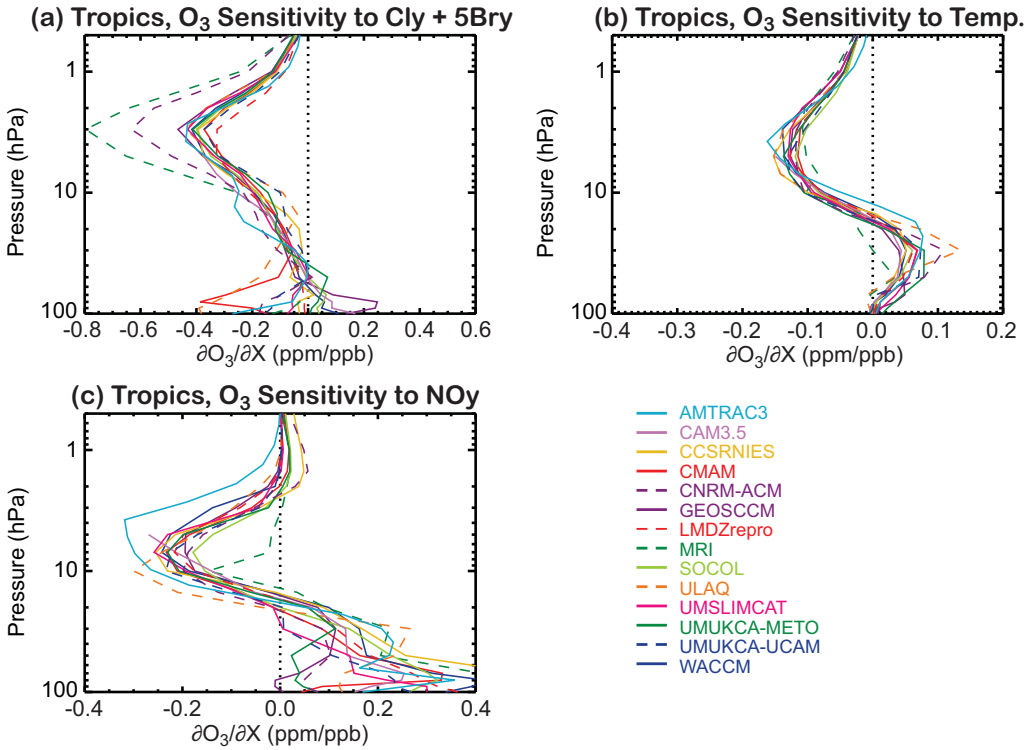

Figure 9.3: Results of the MLR analysis for the CCMVal-2 models in the latitude band 25°S-25°N. (a) Sensitivity of the model ozone to halogen, (b) sensitivity of the model ozone amounts to temperature and (c) sensitivity of the model ozone amounts to NO_y .

of the TSAM analysis, the baseline adjustment may be viewed simply as forcing the anomaly time series to go roughly through the final MMT estimate at the reference date. The baseline-adjusted IMT estimates employing a reference date of 1980 are presented in the right-hand panels of Figure 9.1. Comparing the left- and right-hand panels of this figure it can be seen that the TSAM analysis has been very effective at providing a common reference for the total ozone time series allowing a clearer comparison of the predicted evolution between models. The baseline-adjusted time series employing a reference date of 1980 show improved agreement with observations for CCMVal-2 relative to CCMVal-1. From the left-hand panels of Figure 9.1 it can be seen that this improvement in CCMVal-2 is fortuitous in that it has not come from a reduction in the spread of models but rather through a more even spread about the observations.

In the two top panels of **Figure 9.2** the 1980 baseline-adjusted MMT estimates (thick grey line) computed in the final step of the TSAM analysis for the 25°S-25°N total column ozone in CCMVal-2 (left) and CCMVal-1 (right) are presented. The 95% confidence and 95% prediction intervals for the MMT estimate are also displayed in these panels as the light and dark-grey shaded intervals respectively and the IMT estimates are superposed on top of the MMT estimate. A comparison of the MMT estimates in this figure reveals a reduced uncertainty and closer agreement with the observations for CCMVal-2 relative to CCMVal-1. The tighter confidence intervals for the CCMVal-2 MMT estimate have two sources. The first is that more models in CCMVal-2 submitted data that extended over a greater portion of the requested period (1960-2100). The second is that several of the models (*e.g.*, AMTRAC3 and WACCM) have improved. In AMTRAC3 the improvements have arisen from the reduction in lower stratospheric chlorine.

The MMT estimates in the upper panels of Figure 9.2 indicate that the evolution of total ozone in the tropics is relatively unchanged between the CCMVal-1 and CCMVal-2 data sets. There is a general decline from the start of the integrations until about the year 2000. Following a gradual increase until about 2050, column ozone amounts decline slightly toward the end of the century. However, after the year 2000, the secular variation in annual mean tropical ozone is only about 10 DU. Increased transport by the BD circulation is likely one of the largest drivers (Shepherd, 2008; Li *et al.*, 2009), and chlorine only has a small influence. The corresponding TSAM analysis of the 50 hPa Cl_y in this latitude band may by found in Figures 9S.5.8 in the supplement to this chapter.

Finally, in the lower panel of Figure 9.2 we consider the impact of using the earlier reference date of 1960 for the baseline-adjustment of total column ozone time series.

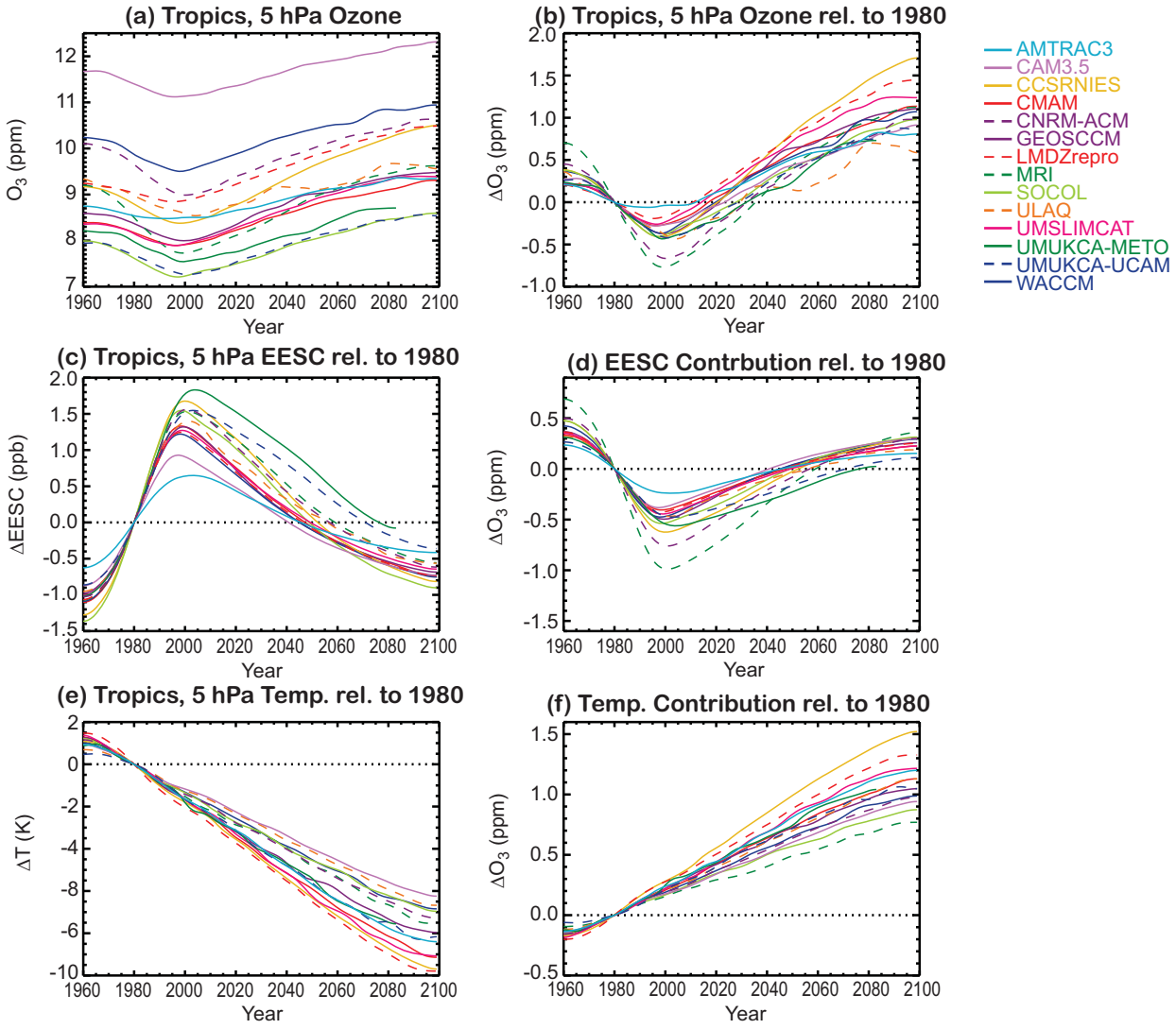

Figure 9.4: Results of the MLR analysis for the CCMVal-2 models in the latitude band 25°S-25°N. (a) Evolution of ozone at 5 hPa, (b) Change in 5 hPa ozone relative to 1980 levels, (c) Evolution of $Cl_y + \alpha Br_y$, (d) Contribution of $Cl_y + \alpha Br_y$ to the ozone change. (e) and (f) are the same as (c) and (d), except for temperature. Curves in this figure were smoothed with a 1:2:1 filter applied iteratively 30 times.

This is only possible for the CCMVal-2 data. It can be seen that the use of an earlier reference date for the pre-ozone-hole baseline causes a significant increase in the spread of the anomaly time series particularly at the time of maximum ozone depletion. Relative to using a 1980 reference date for the baseline adjustment, the use of 1960 causes the MRI and CNRM-ACM to be larger outliers having excessive ozone depletion in all years. SOCOL is an outlier for both 1960 and 1980 baselines after about 2050. This is due to the BC circulation and trend being particularly large in that model, as indicated in Figure 9.6 (see also Chapters 4 and 5). The use of reference dates spanning the range 1970-1980 for both total column ozone and 50 hPa Cl_y is presented in Section 9S.1 of the supplement to this chapter.

9.3.4 Multiple linear regression analysis

Figure 9.3 shows the sensitivity of tropical (25°S - 25°N) ozone to temperature, $Cl_y + 5Br_y$ and NO_y. There is general agreement among models in the middle to upper stratosphere with the exception of MRI and CNRM-ACM, which show higher ozone sensitivities to $Cl_y + \alpha Br_y$, and AMTRAC3 which has more sensitivity to NO_y than most models. The MRI results are consistent with the findings of Chapter 6 showing a much higher than expected ClO/Cl_y ratio. However, at this time it is not clear why CNRM-ACM and AMTRAC3 show these higher sensitivities.

Figures 9.4a and b show the evolution of ozone and its change relative to 1980 at 5 hPa in the tropics (25°S - 25°N). There is a large spread in the time-mean values of

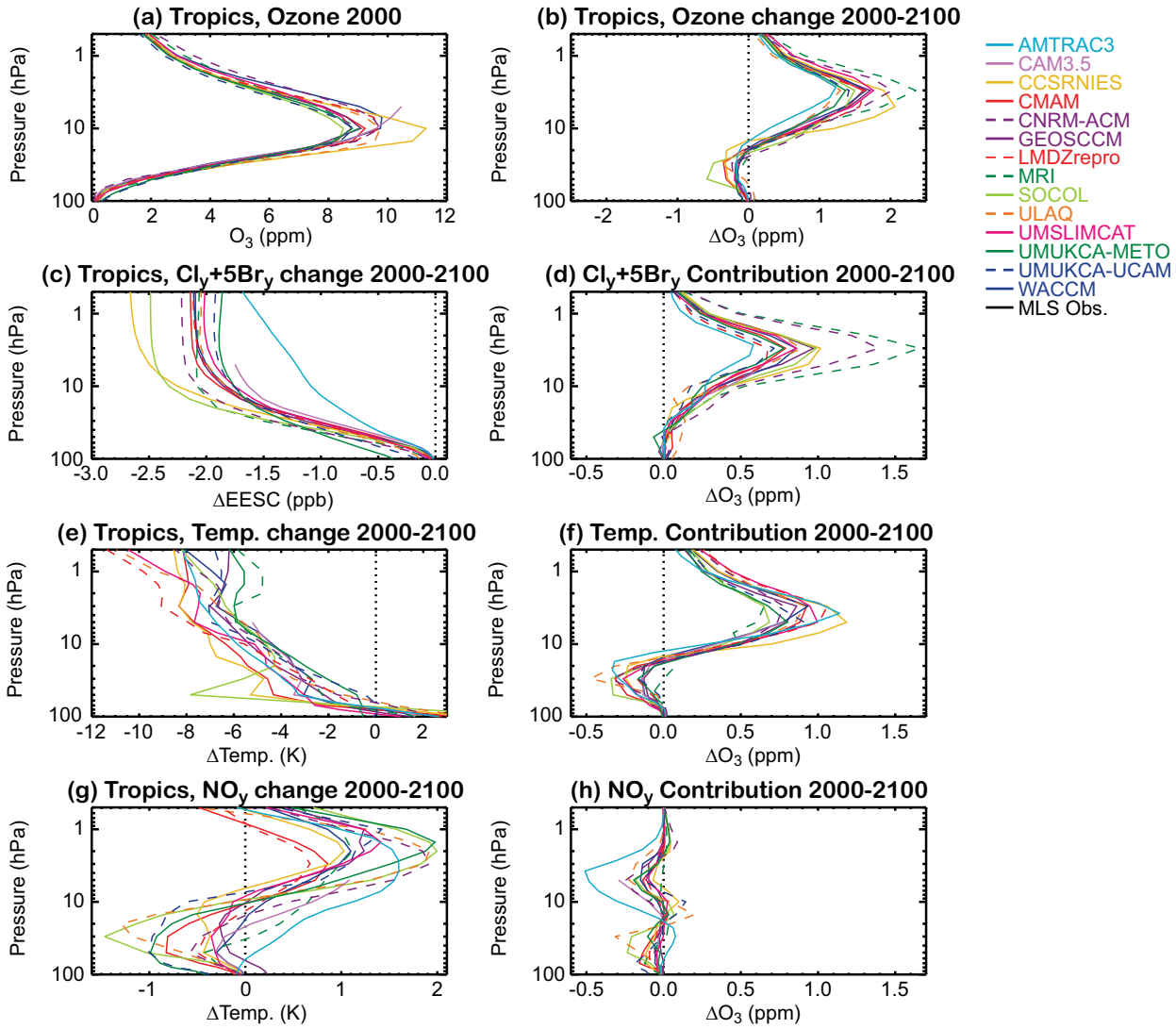

Figure 9.5: Vertical profile results of the MLR analysis for the CCMVal-2 models in the latitude band 25°S-25°N. (a) Ozone in the year 2000, (b) Ozone change from 2000 to 2100, (c) Cl_y + αBr_y change from 2000 to 2100, (d) Contribution of the Cl_y + αBr_y change to the ozone change. (e) and (f) are the same as (c) and (d), except for temperature, and (g) and (h) are the same as (c) and (d), except for NO_y.

ozone, from 8 to 12 ppmv, and the change relative to 1980 levels also varies substantially. Most models show a peak ozone loss of about 0.25 to 0.5 ppmv by the year 2000 and exceed 1980 levels around the year 2020, and 1960 levels by about 2040. MRI and CNRM-ACM have larger than average peak ozone loss, whereas AMTRAC3 has less than average. Generally, those models with a smaller ozone loss recover earlier, and those with a larger loss recover later.

Similar variations can be seen in the change in Cl_y + αBr_y (Figure 9.4c), suggesting that differences in peak ozone loss and date of return to 1960 and 1980 levels can be explained partially by differences in contributions from Cl_y + αBr_y. However, this relationship is not the only relevant factor, as MRI and CNRM-ACM have the largest peak ozone loss, but do not have the largest change in Cl_y + αBr_y. Upper stratospheric ozone is also influenced by temperature, with most models cooling by 7-9 K from 1960-2100. Those models with the largest cooling, 10-11 K (CCSRNIES, CMAM, LMDZrepro, UMSLIMCAT) also have some of the largest temperature contributions to the ozone change. The contributions of Cl_y + αBr_y and temperature to the ozone change, computed from the regression analysis, are shown in Figures 9.4d and f respectively. The term that dominates the trends in ozone at this level varies depending on the time period, but in general Cl_y + αBr_y dominates over the past and beginning of the 21st century, with temperature changes causing the largest ozone changes during the 2nd half of the 21st century. The contributions from NO_y and HO_x under the chosen A1b GHG scenario are negligible in most cases and are not shown.

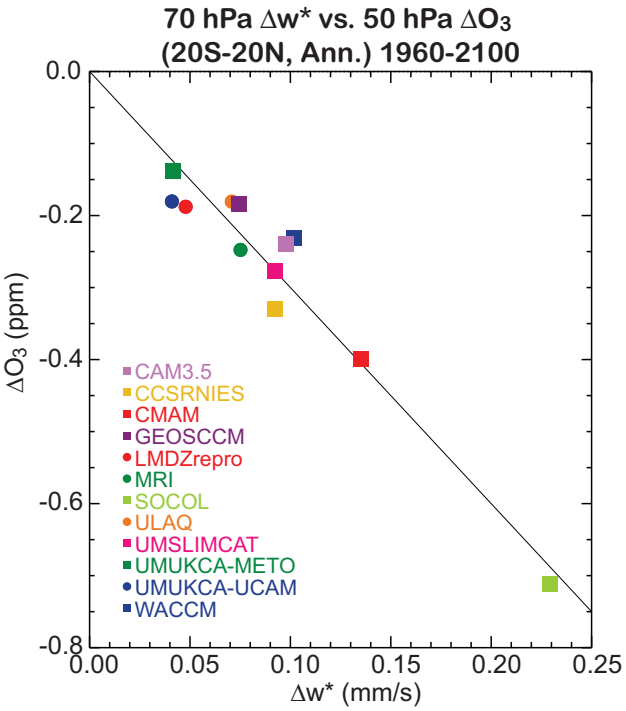

Figure 9.6: Scatter plot showing the differences (from 1960 to 2100) in 70 hPa $\overline{w}^*$ and 50 hPa ozone for those CCMVal-2 models which supplied data. The values are annual averages over the latitude range 25°S-25°N.

The ClO/Cl_y ratio for MRI suggests that the model has much larger amounts of ClO than should be expected (Chapter 6) which leads to the high sensitivity of ozone to $Cl_y + \alpha Br_y$ noted here. The reason for the high sensitivity of CNRM-ACM is not clear. The low $Cl_y + \alpha Br_y$ contribution of AMTRAC3 is due to the parameterisation of Cl_y which is less realistic in the tropical middle stratosphere.

Figure 9.5 shows the results of the MLR analysis for the vertical profile of the ozone change for 2000-2100. The maximum ozone change since 2000 occurs typically at about 3 hPa, with a typical increase of about 1.5 ppmv (Figure 9.5b). Figure 9.5c indicates that in the upper stratosphere of most models, $Cl_y + \alpha Br_y$ decreases by 2 ppbv over this period. CCSRNIES and SOCOL have larger than average decreases in $Cl_y + \alpha Br_y$, and AMTRAC3 has a smaller than average $Cl_y + \alpha Br_y$ change, with a quite different vertical structure for reasons noted previously. Again, MRI and CNRM-ACM have the largest ozone changes due to $Cl_y + \alpha Br_y$ (Figure 9.5d) and AMTRAC3 has a smaller increase. The NO_y increase in most models peaks in the range 1-2 ppbv (Figure 9.5g) and combined with the sensitivities shown in Figure 9.3 most models indicate a very small overall impact on ozone, less than 0.2 ppmv. AMTRAC3 is an exception in showing a much larger impact for reasons that are not clear. Apart from these exceptions, most models show about equal contributions to ozone change from changes in $Cl_y + \alpha Br_y$, temperature and NO_y.

9.3.5 The effect of upwelling on ozone

As indicated in Section 9.2.2, results from MLR are difficult to interpret in the lower stratosphere. Instead we show in **Figure 9.6** the relationship between the change in tropical (25°S - 25°N) ozone at 50 hPa, and the change in the vertical residual velocity, $\overline{w}^*$, at 70 hPa, for the period 1960-2100. All the models for which data were available show an increase in tropical upwelling and a decrease in ozone over this period. A linear regression line through the results goes through the origin, indicating that upwelling is the dominant contributor to ozone reduction at this level. Most models yield an increase in upwelling of 0.04-0.10 mm/s during this period, corresponding to ozone reductions of 0.15-0.35 ppmv. SOCOL is significantly different from the other models in simulating larger increases in upwelling (Chapter 9.3.3 and 4.2.3) and larger ozone losses which both lead to the large cooling seen in Figure 9.5e.

9.3.6 Brief summary

The analysis has shown that the dominant factors that affect ozone evolution in the tropics in the upper stratosphere are changes in $Cl_y + \alpha Br_y$ and temperature. In the lower stratosphere the changes in the evolution of the BD circulation, as diagnosed by an increase in tropical upwelling, are primarily responsible for the modelled ozone changes.

9.4 Mid-Latitude Ozone

9.4.1 From the 2006 WMO assessment:

- In the Northern Hemisphere (NH) column ozone returns to 1980 values by about 2035, well ahead of the return of halogen loading to 1980 values (2035-2050). In the Southern Hemisphere (SH) column ozone returns to 1980 values over the period 2025-2040.
- There is a wide spread in peak Cl_y values simulated for the year 2000.

9.4.2 Further analysis of the CCMVal-1 runs

One of the processes affecting mid-latitude ozone — the increase due to GHG-induced stratospheric cooling — has recently been confirmed as a major process for the mid-latitudes (Waugh *et al*., 2009). The ozone increase occurs in the upper and middle stratosphere. Using the same model, Li *et al*. (2009) estimated that the climate effect led

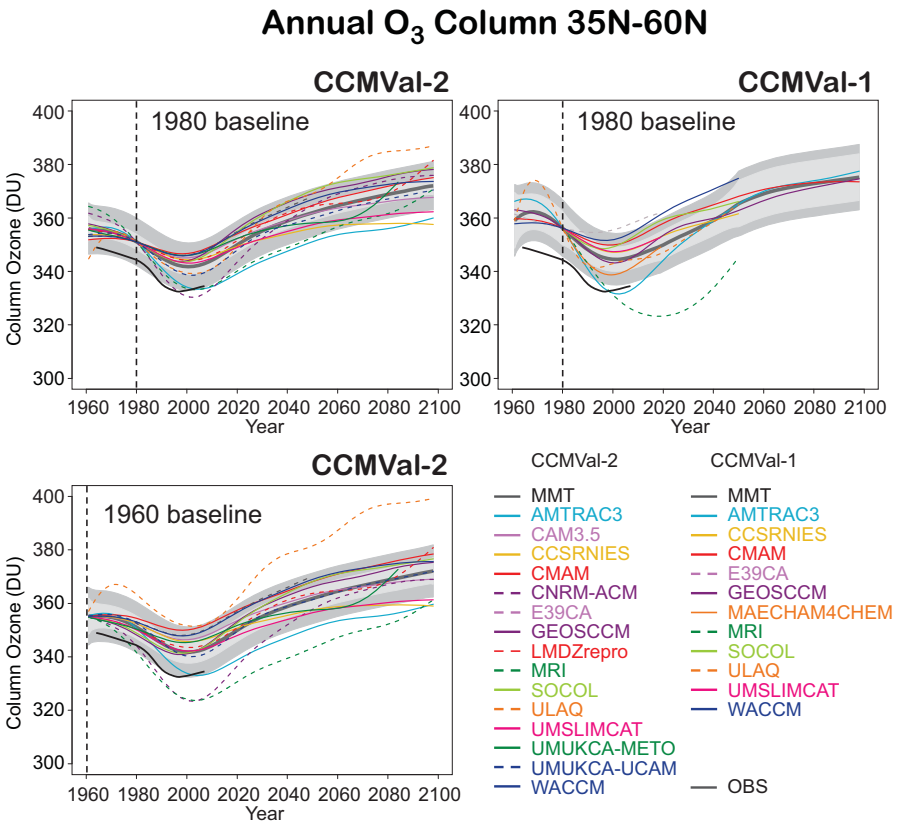

Figure 9.7: As in Figure 9.2 but for the latitude range 35°N-60°N.

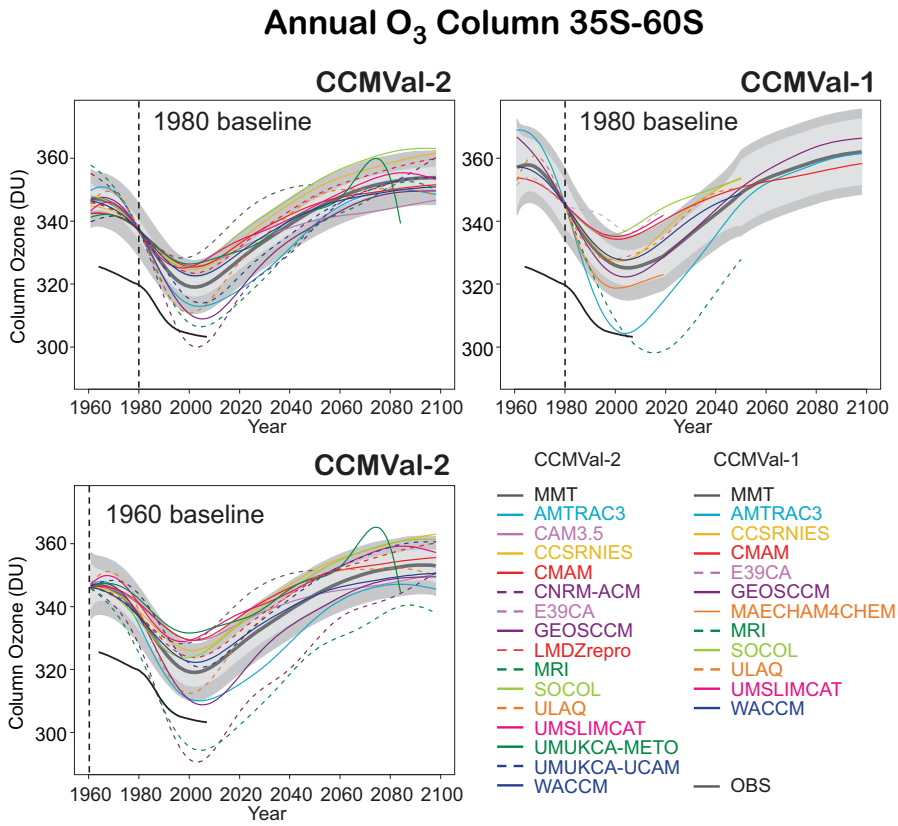

Figure 9.8: As in Figure 9.2 but for the latitude range 35°S-60°S.

to an increase in the extra-tropical ozone column by about 6% in the NH, and about 3% in the SH. These hemispheric differences are likely related to differences in ozone transport.

9.4.3 Mid-Latitude TSAM analysis

In **Figures 9.7** and **9.8**, the 1980 baseline-adjusted IMT and MMT estimates of total column ozone in the latitude bands 35°N-60°N and 35°S-60°S are respectively presented for CCMVal-2 (top left) and CCMVal-1 (top right). These indicate that the multi-model average of total ozone is generally larger than the observations for both CCMVal-1 and CCMVal-2 in these latitude bands with CCMVal-1 displaying the larger error. While the multi-model average of CCMVal-2 more closely corresponds to observations, the raw time series data for both CCMVal-1 and CCMVal-2 show a broad background of total ozone for both hemispheres which spans the range of observations (Figures 9S.9 and 9S.17 of the supplement to the chapter). In both hemispheres, the 1980 baseline-adjusted MMT estimates of ozone indicate that the ozone minimum is reached by roughly the year 2000 and that ozone increases steadily and significantly thereafter. By 2050, northern mid-latitude ozone shows relatively greater increases than southern mid-latitude ozone, probably because of transport from lower latitudes. Other influences such as NO_x- and HO_x-catalysed ozone destruction are likely to have small impacts because the source molecules (N_2O and H_2O) have small trends (Chapter 6).

The 1980 baseline TSAM analysis provides some evidence that improvement has been realised in CCMVal-2 relative to CCMVal-1 with respect to mid-latitude ozone in both hemispheres. Those models which were low outliers in CCMVal-1 for southern latitudes (AMTRAC and MRI) are now more consistent with the other models. The CCMVal-2 1980 baseline analysis in the northern latitudes, however, indicates that these models are at the low end of the range of model results (Figure 9.7), but are consistent with observations from 1980 onwards. The behaviour of the UMUKCA-METO near the end of its IMT estimate (lower panels of Figures 9.7 and 9.8) appears to be an end effect due to an anomalously low data value at the end of its time series in 2084.

In the lower panels of Figures 9.7 and 9.8 the TSAM analysis of mid-latitude ozone employing a 1960 baseline adjustment is presented. The use of the earlier reference date significantly alters the occurrence of outliers in the trend estimates. For example, in both latitude bands, CNRM-ACM and MRI are signicantly low outliers while, in northern latitudes, ULAQ appears as a significant high outlier, with values that greatly exceed all models during

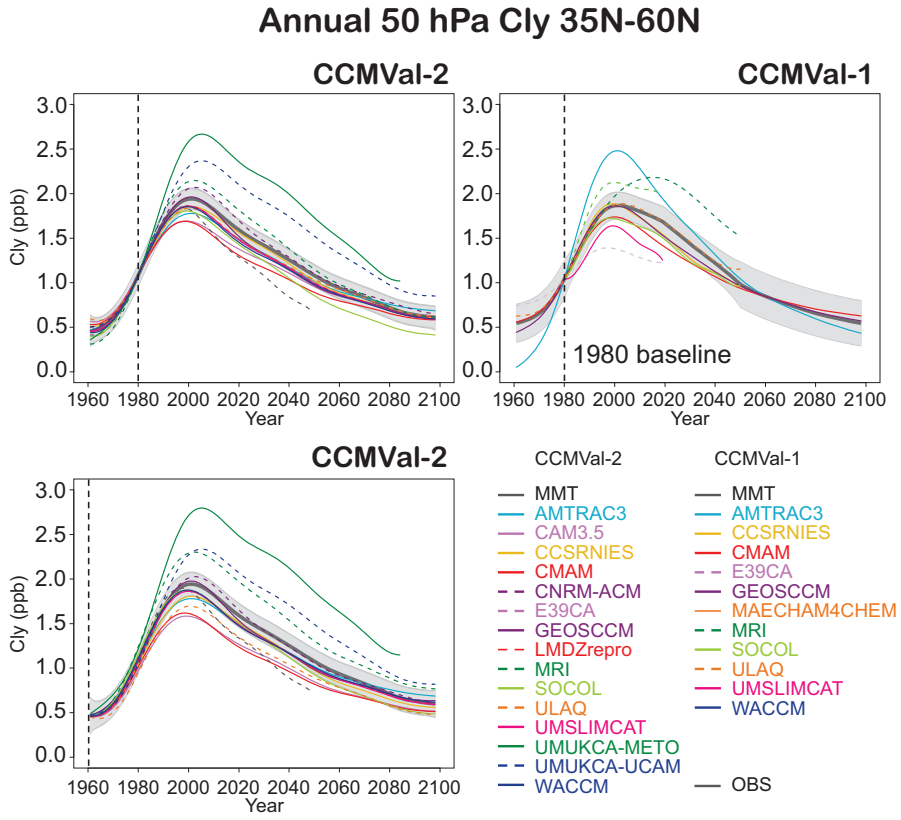

Figure 9.9: As in Figure 9.2 but for 50 hPa Cl_y in the latitude range 35°N-60°N.

the entire period.

In **Figure 9.9** the TSAM analysis for NH mid-latitude 50 hPa inorganic chlorine (Cl_y) is presented. The SH Cl_y appears very similar (see Figure 9S.22 of the supplement). Again, there is a large spread in Cl_y, which maximises near the year 2000. The spread between models in CCMVal-1 and CCMVal-2 is roughly equivalent with each having several outliers. The most significant outlier in the CCMVal-2 set is UMUKCA-METO, which has excessive Cl_y in both hemispheres for all years. While the evolution of ozone generally follows that of chlorine (see Section 9.6.4), the specific behaviour of Cl_y for each model does not appear to account for the outliers of total column ozone identified in Figures 9.7 and 9.8.

9.4.4 Multiple linear regression analysis

The evolution of upper stratospheric ozone, and the contributions of the different chemical mechanisms is very similar in mid-latitudes as in the tropics. **Figures 9.10a**, **b** show the vertical profiles of ozone change in midlatitudes (35°S-60°S and 35°N-60°N) over the 21st century. The ozone increases are similar to those obtained in the tropics, but without the loss in the lower stratosphere in most models. The contributions of $Cl_y + \alpha Br_y$ (Figure 9.10c, d) and temperature (Figures 9.10e, f) are also similar to the results obtained in the tropics. Again MRI and CNRM-ACM reveal much larger contributions of $Cl_y + \alpha Br_y$ to the ozone differences, although the AMTRAC3 parameterisation reveals no clear bias in this region. The contribution to ozone change from NO_y (Figures 9.10g, h) is much smaller than the other terms, and the individual models do not show as wide a range.

9.4.5 Brief Summary

The main factors that affect ozone in mid-latitudes are transport (Chapter 5), and the evolution of halogen amounts, particularly during periods of high aerosol loading following volcanic eruptions (see Chapter 8). In addition, GHG cooling of the stratosphere slows chemical destruction rates leading to an increase in ozone, particularly in the upper stratosphere.

9.5 Polar Ozone

9.5.1 From the 2006 WMO assessment:

- Antarctic ozone is strongly anti-correlated with Cl_y amounts.
- Most models simulate a low bias in Antarctic Cl_y which gives rise to an early return of ozone back to 1980 values.
- Arctic ozone returns to 1980 levels before halogen amounts return to 1980 values and ahead of Antarctic ozone. The main influences on ozone include the enhancement of the BD circulation and the slowing of gas-phase ozone loss in the stratosphere by GHG cooling.

9.5.2 Further analysis of the CCMVal-1 runs

Eyring *et al*. (2006) show that the area of the Antarctic ozone hole, based on the fixed 220 DU threshold, is simulated by CCMs to be smaller than observed. Huck *et al*. (2007) propose an improved method for selecting an ozone threshold for delineating the ozone hole. The discrepancy between observations and models has been explained in part by Struthers *et al*. (2009) who show that some models poorly simulate the size of the polar vortex and confirm that the 220 DU contour is not necessarily appropriate for delineating the region of severe ozone depletion in models with systematic ozone biases. Also, according to WMO (2007, Chapter 2, Figure 2-10), the previous simulations (as well as the CCMVal-2 simulations) were completed with bromine concentrations that were probably too low, because of the neglect of very short-lived species.

Eyring *et al*. (2006) show that the interannual variability of the size of the simulated ozone hole was typically over twice that observed, despite the ozone hole being generally smaller. Comparison of AMTRAC experiments for a 15-year overlap period (Austin and Wilson, 2006), indicated that the observed SSTs gave rise to a smaller, more variable ozone hole than calculations using model SSTs. Although this result is certainly model dependent, the likely reason for the difference is that polar processes are affected by El Niños (*e.g*., Manzini *et al*., 2006; Garnkel and Hartman, 2007) that may not be well simulated by coupled ocean-atmosphere models, particularly those with a simplied stratosphere. The implication is that simulations of the ozone hole and the recovery of Antarctic ozone will depend on the performance of the underlying ocean.

The lower stratospheric temperature arises from the net effect of radiative cooling and heating due to GHGs and ozone respectively, and adiabatic warming from the BD circulation. Hence, the net trend in the lower stratospheric temperature, especially in the Arctic will depend critically on the trend in the BD circulation. For a subset of the CCMVal-1 simulations, the orographic gravity wave drag typically contributed about half of the trend in annual mean tropical upwelling (Li *et al*., 2008; McLandress and Shepherd, 2009a; Garcia and Randel, 2008). However, it should be noted that for CCMVal-2 a wide range of results were obtained in examining the full set of simulations (Chapter 4.2.3).

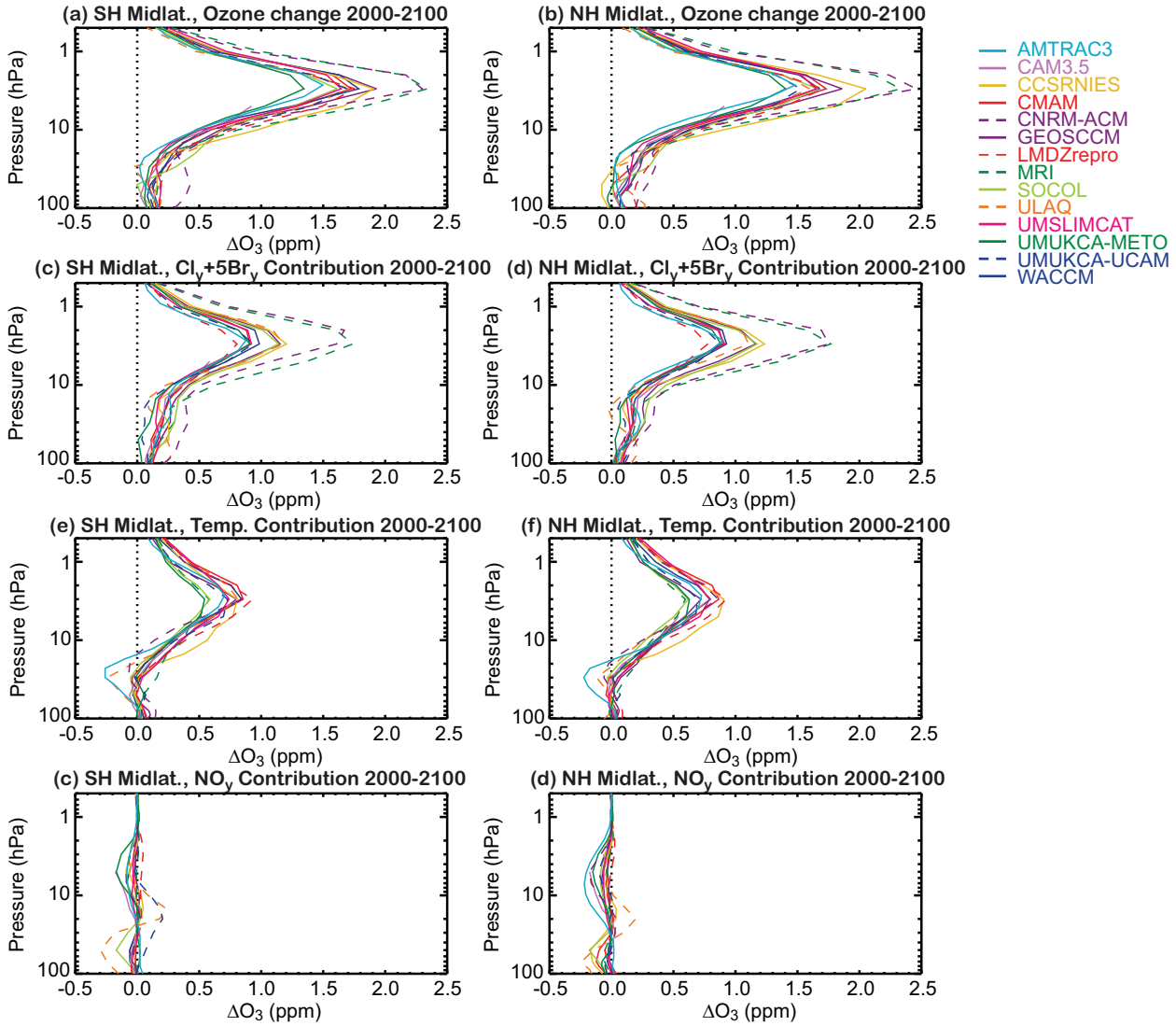

Figure 9.10: Vertical profiles of differences in midlatitude (35°S-60°S and 35°N-60°N) ozone over the the 21st century and the contributions of Cl_y + αBr_y, temperature, and NO_y.

9.5.3 Polar TSAM analysis

The TSAM analyses of spring total column ozone over polar latitudes (60°N-90°N in March and 60°S-90°S in October) are respectively presented in **Figures 9.11** and **9.12**. In Arctic spring, relative to CCMVal-1, CCMVal-2 shows no tendency towards a reduction in model spread (Figure 9S.25 of the supplement). In Antarctic spring, however, the raw time series indicate that the spread of models has increased in CCMVal-2 (Figure 9S.33). This larger spread is associated with a slightly increased negative bias of CMAM relative to its CCMVal-1 contribution, and the inclusion of UMUKCA-UCAM and CAM3.5, which have large positive biases relative to the MMT estimate. This large CCMVal-2 inter-model difference in Antarctic spring background ozone is essentially eliminated in the 1980 baseline-adjusted time series and IMT estimates (Figure 9.12 upper panel and Figs. 9S.33-9S.34). A comparison of the 1980 baseline-adjusted IMT and MMT estimates between CCMVal-1 and CCMVal-2 shows a similar convergence of the models' evolution once the offset in background values of ozone is accounted for (top panels of Figures 9.11 and 9.12), aside from MRI in CCMVal-1.

As was the case for the other latitude bands, employing the earlier reference date of 1960 for the TSAM analysis results in larger inter-model spread for both the Arctic and Antarctic column ozone (lower-left panel of Figures 9.11 and 9.12). Similar to the behaviour in northern midlatitudes, in the Arctic MRI is a low ozone outlier during nearly the entire period (Figure 9.11 and Figures 9S.27-28). In the Antarctic, the use of the earlier 1960 reference date increases the low bias of GEOSCCM, MRI, and

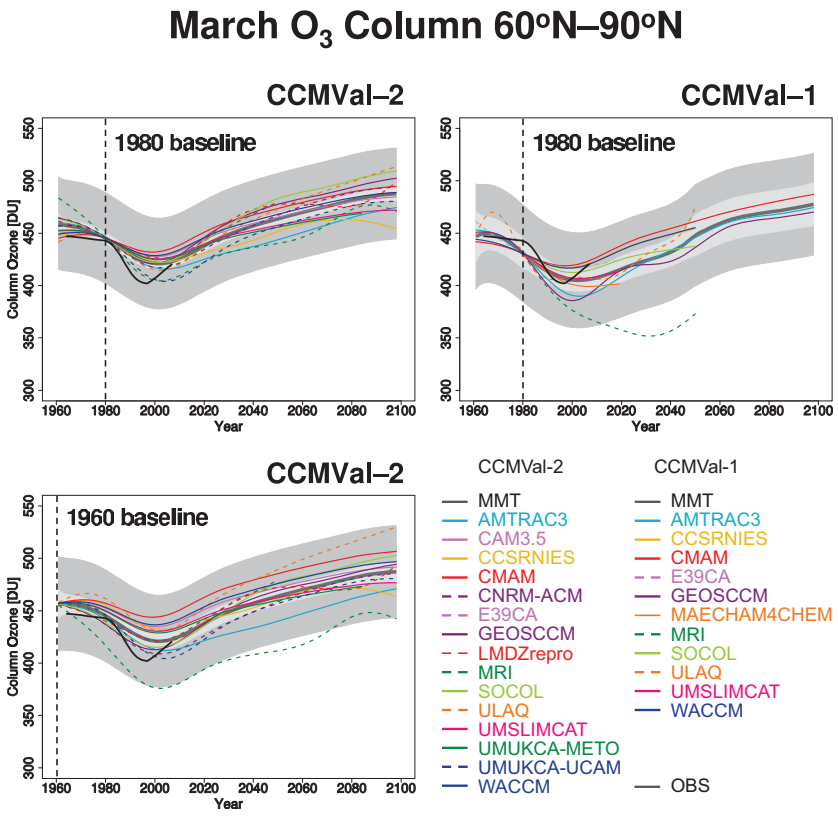

Figure 9.11: As in Figure 9.2 but for the month of March and the latitude range 60°N-90°N.

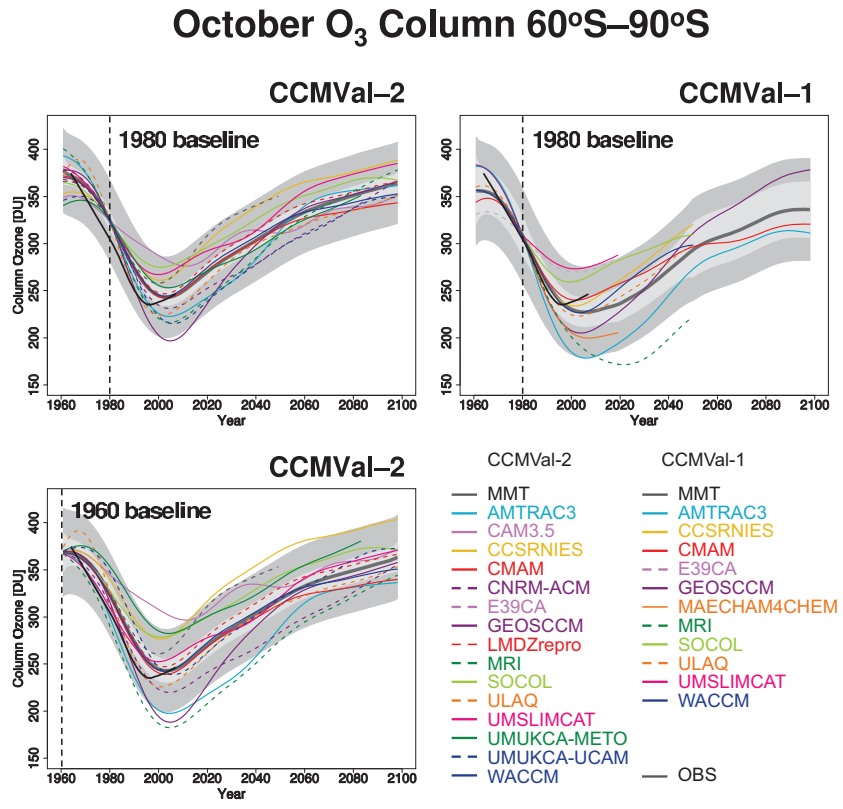

Figure 9.12: As in Figure 9.2 but for the Month of October and the latitude range 60°S-90°S.

AMTRAC3 and the high bias of CAM3.5, CCSRNIES, and UMUKCA-METO near 2000. A comparison of the Arctic and Antarctic spring ozone in Figure. 9.11 and 9.12 indicates the tendency for the Arctic ozone to recover earlier than the Antarctic. This will be quantified from the MMT estimates in Section 9.6 of this chapter.

The results for polar regions, particularly Antarctica, are dominated by chlorine amounts. The IMT and MMT estimates of annual 50 hPa Cl_y over polar latitudes (60°N-90°N and 60°S-90°S) are presented in **Figures 9.13** and **9.14**. Aside from the introduction of UMUKCA-METO, and perhaps UMUKCA-CAM, the CCMVal-2 50 hPa Cl_y at both poles shows less spread than CCMVal-1 when a 1980 baseline is employed (upper panels of Figures 9.13 and 9.14). This is primarily associated with improvement in AMTRAC and the absence of MAECHAM4CHEM (see also Figure 5.11 of Chapter 5). These annual means are very similar to the spring means (not shown) in both the Arctic and Antarctic. Unlike ozone, the use of a 1960 baseline in the derivation of the IMT and MMT estimates does not lead to a significant increase in model spread. The general improvement of Cl_y in CCMVal-2 means that individual model results can no longer be as clearly connected with chlorine amount, as was the case for CCMVal-1. Other processes, such as the strength of the circulation and the lower stratospheric temperature, are likely playing a greater role in the precise differences between model results.

9.5.4 Antarctic ozone hole diagnostics

As the Antarctic ozone hole is frequently used as a proxy for ozone depletion, we explore here in more detail its simulation in the CCMVal-2 models. The ozone hole area is investigated, and discussed in relationship to the cold areas simulated by the models as well as other features which affect model performance.

The perimeter of the Antarctic ozone hole has historically been defined as the 220 DU contour, as values this low rarely occurred in measurements and the 220 DU contour was found to lie close to where ozone gradients across the vortex edge were steepest. Once the ozone hole became prominent, such low values became more common in spring. The problems associated with fixed thresholds for denoting the edge of the ozone hole in model simulations has been discussed by other authors (*e.g.*, Huck *et al.*, 2007; Tilmes *et al.*, 2007; Struthers *et al.*, 2009). Those authors supply algorithms for the reanalysis of the ozone hole which might allow for an improved comparison between different model simulations. Generally this requires the availability of extra data such as potential vorticity and also takes into account whether the temperatures in the vortex are low enough for the formation of PSCs, essential to drive the chemistry. Here we explore two particular diagnostics which investigate whether ozone hole differences might be related to ozone biases, or whether ozone hole differences might be related to dynamical representation of the polar vortex.

Figure 9.15a is the zonal-mean ozone over the 10 year period 1996-2005, averaged over the 20 day period centred on the date of the seasonal Antarctic minimum. To reflect actual model characteristics accurately, this date varies according to the model. While several models are close to that observed, several models (UMUKCA-METO, MRI and CCSRNIES) are biased high, although MRI is close to observations near the edge of the classical ozone hole. In Figure 9.15b the zonal average during the peak ozone hole season has been adjusted relative to the minimum daily value attained throughout 60°S-90°S region for the period 1960-1965. Prior to the introduction of satellite based instruments, there was only limited observational coverage of total ozone in high latitudes. Therefore, we take the value of 220 DU as an appropriate minimum for the 1960 to 1965 period. In the case of AMTRAC3 the 1960-1965 minimum poleward of 60°S was 199 DU. The bias is then taken to be 220 - 199 = 21 DU and the curve has been increased by 21 DU to correct for this bias. After applying an appropriate adjustment to each model, the spread in the model results actually increases, but CCSRNIES has improved. This suggests that most models do not have a clear ozone bias which would impede comparison with observations based on a fixed 220 DU threshold.

We now consider whether the location of the polar vortex might be having an influence on the simulated ozone holes. In observations, the maximum gradient in ozone occurs approximately at the edge of the ozone hole, which is related to the edge of the polar vortex (Bodeker *et al.*, 2002; Newman *et al.*, 2007). **Figure 9.16** shows the meridional gradient in total column ozone (1996-2005 average) for each model considered in comparison with observations and it is seen that the simulations place the maximum gradient in different locations. While several models agree well with observations over a wide latitude range, most models place the peak ozone column polewards of that observed (**Figure 9.17**) which may contribute to an ozone hole smaller than observed (as also found *e.g.*, by Struthers *et al.*, 2009). The latitude of the observed maximum gradient is 64.2°S, with a corresponding ozone value of 273 DU (Figure 9.17). By comparison UMUKCA-METO simulates the position and ozone value at the maximum ozone gradient of 68.5°S and 329 DU respectively. Therefore, by reducing the UMUKCA-METO values by 329 - 273 = 56 DU, an alternative estimate for the ozone hole can be determined. Figure 9.15c shows this adjustment of the model results, and the model spread near the edge of the ozone hole has been reduced.

Figure 9.18 shows the ozone hole area for the different definitions considered. Figure 9.18a shows for each

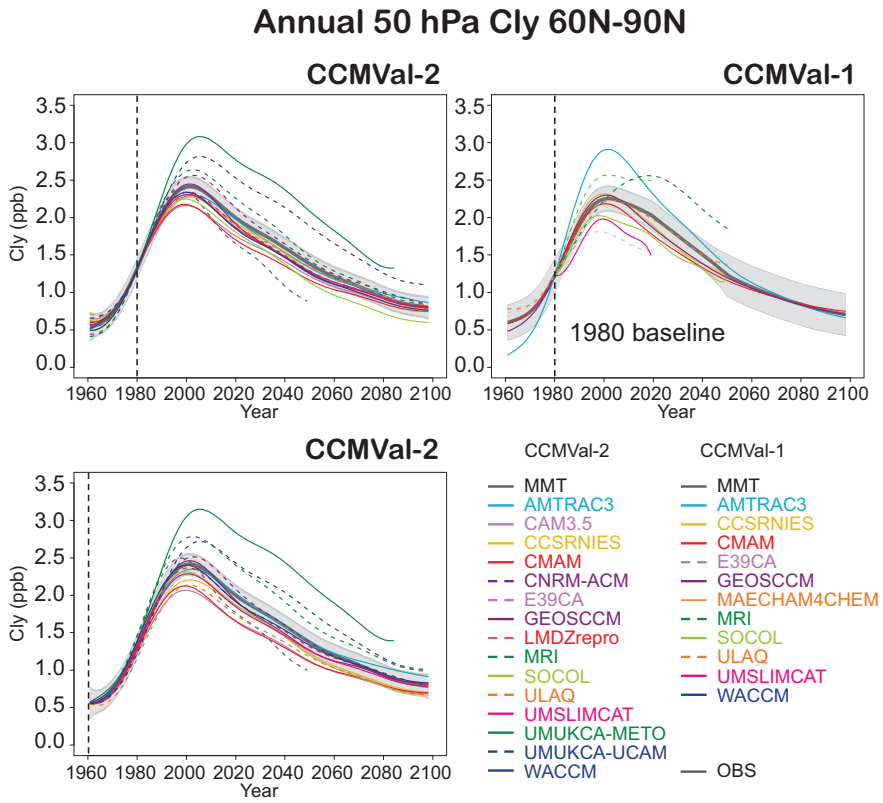

Figure 9.13: As in Figure 9.2 but for 50 hPa Cl_y in the latitude range 60°N-90°N.

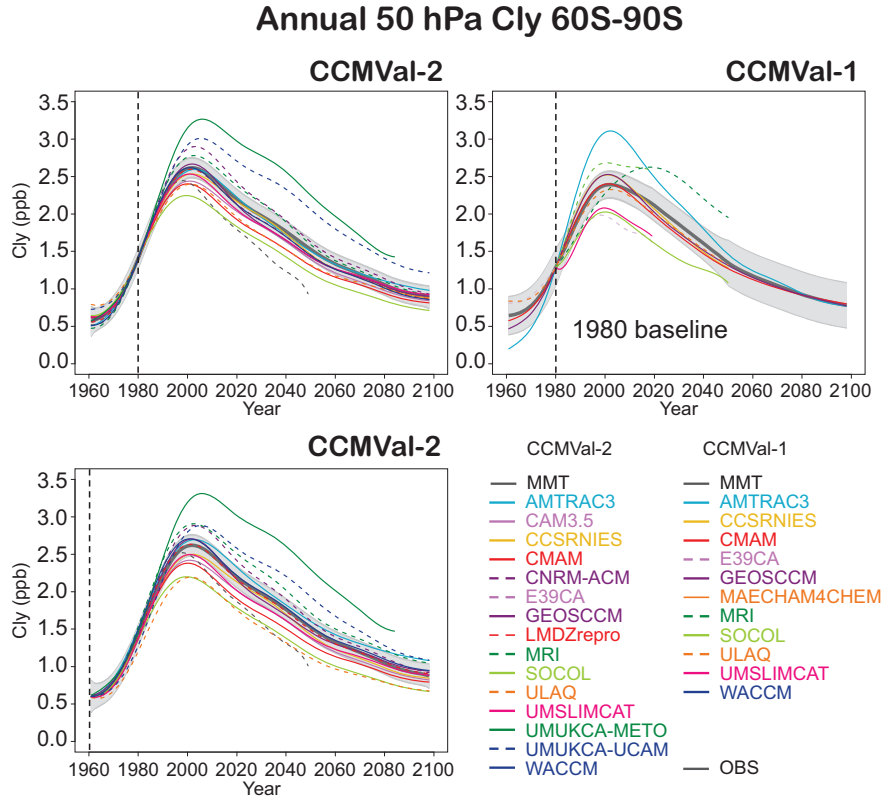

Figure 9.14: As in Figure 9.2 but for 50 hPa Cl_y in the latitude range 60°S-90°S.

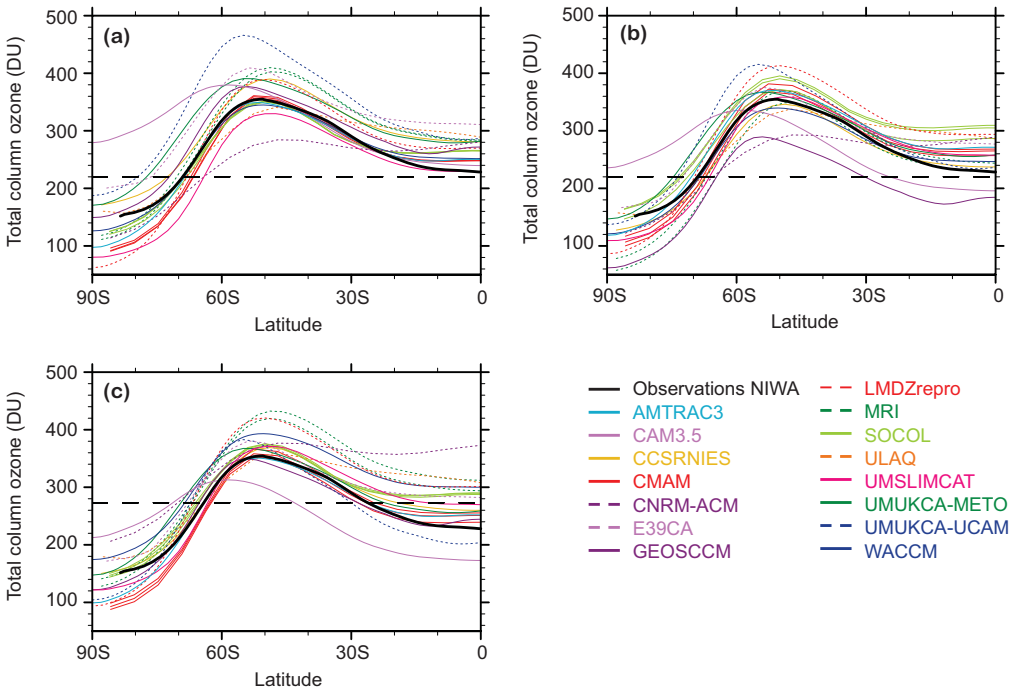

Figure 9.15: Total column ozone as a function of latitude, averaged for the period 1996-2005 for 10 days before and after the minimum column ozone. (a) No adjustments to the model results. (b) Model results have been adjusted relative to the 1960-1965 minimum (see text). (c) Model results have been adjusted relative to the ozone maximum meridional gradient (see text). The results have been obtained from the REF-B2 simulations.

year of the simulations the maximum area for the column ozone less than 220 DU. The agreement with observations is generally poor, with most models under-predicting the size of the ozone hole. If the ozone hole is considered relative to the 1960-1965 minimum, as described for Figure 9.15b, the agreement with observations for several models improves, particularly CCSRNIES and MRI, but SOCOL results are now in poor agreement with observations from 1980 onwards. The improvements arise from the fact that overall these models appear to have a high ozone bias. In comparison SOCOL results are worse under this measure since low ozone occurred in the 1960s due to the dynamics of the model. Figure 9.18c is a measure of the ozone hole relative to the steepest gradients, corresponding to Figure 9.15c. The model simulations are more consistent with each other, primarily because of the substantial correction to the results for UMUKCA-METO. However, most models have ozone holes which remain significantly smaller than observed, by up to 30%. Some models also show very large 'ozone hole' areas prior to 1980 and after 2040 using the steepest gradient criterion. However, there is no implication that the low ozone is necessarily chemistry driven outside the period when halogen levels are expected to be high.

Model Antarctic ozone hole results obtained for the period 1990-2008 for CCMVal-2 (REF-B1) and some statistical comparisons are included in **Tables 9.1** and **9.2**. Compared with observations, most models under-predict the areas of low temperatures (Table 9.1) and therefore the regions of severe ozone depletion are already limited, as shown in Table 9.2. Many models also produce more extreme local ozone loss than observed, since in these models

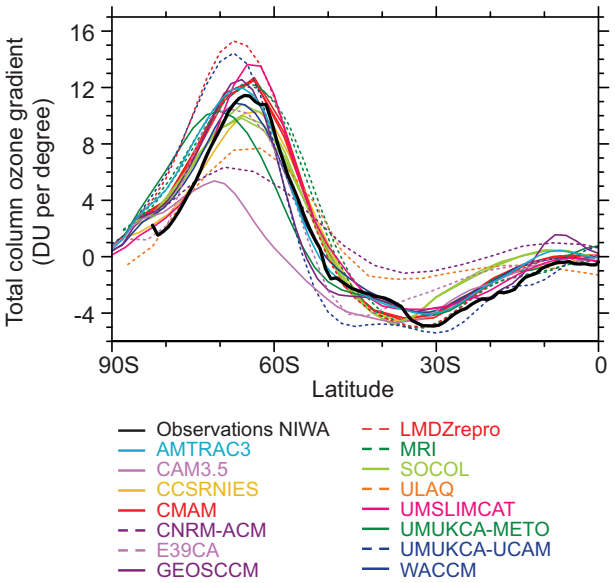

Figure 9.16: Meridional gradient in total column ozone averaged for the period 1996-2005 for the 10 days on either side of the ozone minimum.

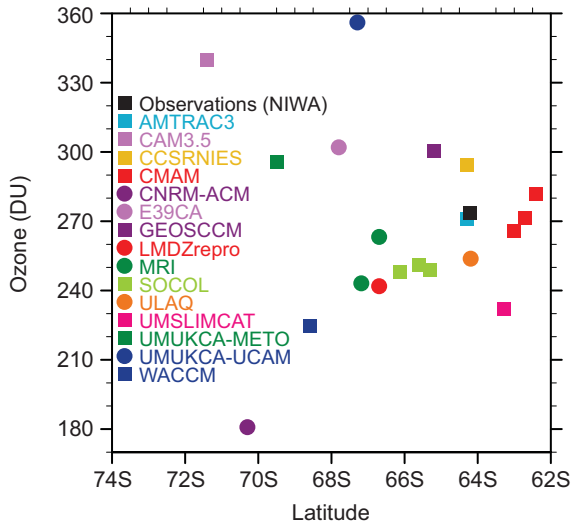

Figure 9.17: Latitude of maximum meridional gradient in total column ozone, as a function of the ozone value at that latitude.

there is a tendency for the ozone hole to extend too high in the atmosphere (not shown). The combination of a low bias in both the ozone minimum and the ozone hole area tends to result in some compensation of errors in the ozone mass deficit, but other models have biases that compound in the ozone mass deficit calculation. Overall, the agreement with observations in most models has not improved appreciably since WMO (2007), despite convergence towards common values for the lower stratospheric Cl_y, and this picture likely remains true regardless of the complexity of the diagnostics adopted. An illustration of the range of results obtained is given by **Figure 9.19**, which shows the mean low temperature (T < 195 K) area averaged for July and September in each of the years 1990-2008 (or the end of the simulation) compared with the area of the ozone hole, based on the 220 DU contour. Almost half the models (AMTRAC3, CMAM, LMDZrepro, NiwaSOCOL, SOCOL, ULAQ, UMSLIMCAT and WACCM) provide a consistent relationship between PSCs (represented by T < 195 K) and the ozone hole, as occurs in the observations. The other models indicate strong biases of background ozone as well as difficulties in simulating sufficient PSCs.

Overall these results suggest that some models do not simulate well the vortex structure, including for example a delay in the final warming (Chapter 4, Pawson *et al.*, 2008). With such a large spread in model results for both 1980 and 2060, predictions of the disappearance of the ozone hole remain unreliable, and in any case, the upper and lower panels of Figure 9.18, indicate that these predictions are likely to be definition dependent.

9.5.5 Brief Summary

The dominant factor which affects ozone evolution in the polar regions is the halogen loading. Although considerable uncertainty still exists in the simulated column ozone trends in the Arctic, models are more consistent

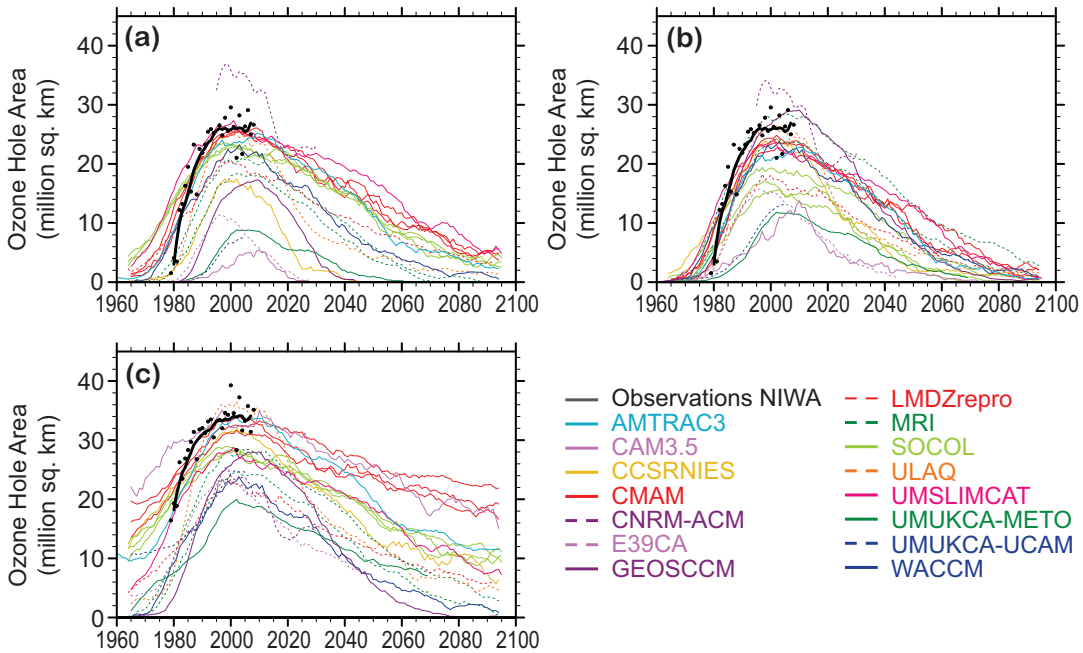

Figure 9.18: Simulated and observed ozone hole areas, based on (a) a fixed, 220 DU amount, (b) the 1960-1965 minimum, and (c) the value at the maximum gradient. The curves indicate 11-year running means of the data for individual years.

Table 9.1: Mean low temperature areas (T < 195 K) for the period July to September for the years 1980-2007 in comparison with observations for the models used in each group of experiments. The uncertainties indicated are approximate 95% confidence intervals for the random error, given by $2s/\sqrt{(n-1)}$,where s is the standard deviation of the annual values and n is the number of years included. The WACCM values are for August and September only.

Model	REF-B1	REF-B2	Model	REF-B1	REF-B2
NCEP data	21.4 ± 0.8	—	LMDZrepro	21.5 ± 0.8	—
AMTRAC3	19.8 ± 0.8	20.4 ± 0.6	MRI	22.6 ± 0.4	22.6 ± 0.5
CAM3.5	17.5 ± 1.5	14.0 ± 1.6	NiwaSOCOL	23.1 ± 0.6	—
CCSRNIES	25.8 ± 0.5	26.4 ± 0.6	SOCOL	21.6 ± 0.4	20.5 ± 0.5
CMAM	19.8 ± 0.6	20.2 ± 0.3	ULAQ	21.7 ± 1.6	21.8 ± 1.5
CNRM-ACM	19.1 ± 1.4	19.3 ± 1.3	UMSLIMCAT	18.9 ± 0.7	19.8 ± 0.9
EMAC	19.0 ± 1.4	—	UMUKCA-METO	14.0 ± 0.8	—
E39CA	24.1 ± 0.7	24.0 ± 0.7	UMUKCA-UCAM	14.7 ± 0.7	16.0 ± 0.6
GEOSCCM	17.5 ± 0.4	—	WACCM	23.9 ± 1.1	21.7 ± 1.6

with each other than in the CCMVal-1 comparisons. Over Antarctica, some models do not simulate well the vortex structure, leading to an ozone hole that is smaller than observed. The ozone hole in many simulations continues to the end of the century.

9.6 Ozone recovery

9.6.1 From the 2006 WMO assessment:

- Full ozone recovery is defined as occurring when ozone depleting substances (ODSs) no longer significantly affect ozone.

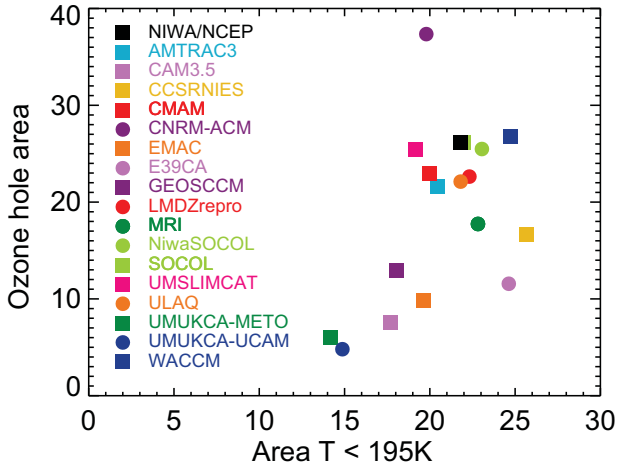

Figure 9.19: Ozone hole area (total column ozone < 220 DU) versus cold area (50 hPa T < 195 K), averaged for July to September for each model compared with observations. The results were calculated from the REF-B1 simulations, and are averaged for the period 1990-2008.

- The return of ozone to 1980 levels is simulated to occur by about 2065 over Antarctica, and up to several decades earlier at other latitudes.

9.6.2 Further analysis of the CCMVal-1 runs

Waugh *et al*. (2009) use simulations of GEOSCCM to examine the impact of climate change on ozone recovery. Waugh *et al*. (2009) conclude that the impact of climate change on ozone recovery depends on the recovery definition and is likely to vary in different atmospheric regions. In particular, for the tropics the total column ozone was found not to return to 1980 values, a commonly used recovery criterion. The results also indicated that full ozone recovery according to the WMO (2007) definition of a negligible impact on ozone due to ODSs would typically not occur before the end of this century.

Austin and Wilson (2006) refer to ozone recovery to 1980 values and suggest that the recovery of the column ozone is advanced relative to Cl_y. This arises from the change in transport, which is larger in the Arctic than in the Antarctic (McLandress and Shepherd, 2009a). Shepherd (2008) and Hitchcock *et al*. (2009) also provide evidence for increased transport effects in the Arctic using temperature and heat flux as a model diagnostic. Possibly related to the increase in the strength of the Brewer-Dobson circulation, simulations also show an increase in stratospheric sudden warmings during the period 1960-2100 of about 50% or more (Charlton-Perez *et al*., 2008; McLandress and Shepherd, 2009b; Chapter 4). This could increase the transport of ozone into the Arctic during winter, as well as increase the interannual variability. Observations of stratospheric sudden warmings are too infrequent and too variable to verify the sudden warming trends obtained in model simulations. An alternative viewpoint is that the increase in

Table 9.2: Commonly used ozone hole diagnostics, averaged over the period 1990-2008, or to the end of the REF-B1 simulations, depending on the model. The uncertainties indicated are approximate 95% confidence intervals for the random error, given by $2s/\sqrt{(n-1)}$, where s is the standard deviation of the annual values and n is the number of years included.

Model	Minimum Antarctic ozone (DU)	Maximum ozone hole area (10^6 km^2)	Ozone mass deficit (Mt)
NIWA data	103 ± 6	26.1 ± 1.2	22.0 ± 2.7
AMTRAC3	74 ± 8	21.8 ± 1.8	24.4 ± 3.8
CAM3.5	187 ± 19	7.5 ± 2.5	1.1 ± 0.5
CCSRNIES	148 ± 10	16.9 ± 2.3	6.6 ± 2.1
CMAM	79 ± 6	23.2 ± 0.8	25.2 ± 2.2
CNRM-ACM	63 ± 4	38.2 ± 3.5	42.4 ± 4.1
EMAC	167 ± 16	10.6 ± 2.5	2.6 ± 1.6
E39CA	121 ± 12	11.7 ± 1.6	3.7 ± 1.1
GEOSCCM	139 ± 8	13.4 ± 1.3	4.6 ± 1.1
LMDZrepro	48 ± 3	22.9 ± 1.1	31.0 ± 2.5
MRI	97 ± 3	14.7 ± 0.6	14.2 ± 1.2
NiwaSOCOL	92 ± 6	26.0 ± 1.6	28.2 ± 3.7
SOCOL	95 ± 4	26.6 ± 0.8	28.7 ± 2.4
ULAQ	102 ± 7	22.5 ± 2.2	15.2 ± 3.4
UMSLIMCAT	79 ± 4	25.0 ± 1.3	34.8 ± 3.5
UMUKCA-METO	168 ± 16	6.2 ± 2.0	2.2 ± 1.1
UMUKCA-UCAM	172 ± 8	5.0 ± 0.8	0.9 ± 0.4
WACCM	101 ± 7	26.4 ± 2.3	22.9 ± 4.3

stratospheric sudden warmings seen in some models over century time scales is representative of a change in climatological state and hence transport effects are relatively unaffected by climate change, apart from the steady increase in the BD circulation (McLandress and Shepherd, 2009b).

9.6.3 Recovery based on TSAM analysis

The IMT and MMT estimates for total ozone and 50 hPa Cl_y presented in Sections 9.3-9.5 may be used to provide individual model, and multi-model estimates of the return to levels associated with a specified reference date. Because the IMT and MMT estimates are smooth curves by construction, the value of ozone and Cl_y for any reference date prior to maximum ozone depletion may be mapped onto a future date based on the return of ozone or Cl_y to the reference date value. The TSAM analysis, therefore, allows the definition of return dates for a continuous set of reference dates. In order to compare recovery predictions from CCMVal-1 with CCMVal-2, we first consider the commonly used reference date of 1980.

Summary diagnostics of total ozone and 50 hPa Cl_y 1980 return dates for the latitude bands discussed in Sections 9.3-9.5 are presented in **Figures 9.20** and **9.21** respectively. In each latitude band, CCMVal-1 return dates are shown on the left and CCMVal-2 return dates are shown on the right. The MMT estimate of return dates is indicated by large black triangles. Error bars on these estimates are associated with the 95% confidence intervals. These two figures provide a concise summary of the ozone and Cl_y discussed in the previous three sections. They allow an overall comparison of CCMVal-1 with CCMVal-2 through the MMT estimates, the change in individual model predictions to be tracked across the two inter-comparison projects, and the comparison of model predictions with the MMT estimates and with each other for each of CCMVal-1 and CCMVal-2.

Initial inspection of these two figures reveals that return dates for Cl_y are more symmetric in latitude, and more certain, than ozone for both CCMVal-1 and CCMVal-2. In general, return dates for Cl_y are very similar between CCMVal-1 and CCMVal-2 being well within the uncertainty bounds of each. Return dates for total ozone, on the other hand, are not symmetric in latitude and, in the tropics not realised by the MMT estimate at all in CCMVal-2. While the CCMVal-1 and CCMVal-2 MMT estimates of return dates for spring polar and annual mid-latitude ozone are seen to be within each other's uncertainty bounds, those for CCMVal-2 appear to be systematically earlier than CCMVal-1. For example, the spring Arctic ozone recovery to 1980 levels is predicted from the MMT estimate to occur near 2025 for CCMVal-2 (2039 for CCMVal-1) while the Antarctic recovery to 1980 levels is predicted to occur much later near 2052 for CCMVal-2 (2062 for CCMVal-1). The asymmetric structure of polar ozone recovery in Figure 9.20 is an indication that, in addition to Cl_y abundance, ozone is affected by dynamical and radiative changes brought about by increased GHG forcing and these have been consistently reproduced in the MMT estimates between CCMVal-1 and CCMVal-2.

In **Figures 9.22** and **9.23** we compare estimates of the return dates to 1960 and 1980 levels for total ozone and 50 hPa Cl_y respectively. In general, the return date for ozone is longer when the earlier reference date of 1960 is used (Figure 9.22). In particular the Antarctic return date changes significantly, from roughly 2055 to nearly 2100. From Figure 9.23 it appears that 50 hPa Cl_y does not return to its 1960 value by the end of the 21st century outside the tropics. Appealing to the earlier reference date of 1960 therefore has significant impact on return dates. However, it must be noted that the use of 1960 as a reference date for the CCMVal-2 comes at the beginning of the time series for many models and some of the sensitivity found here

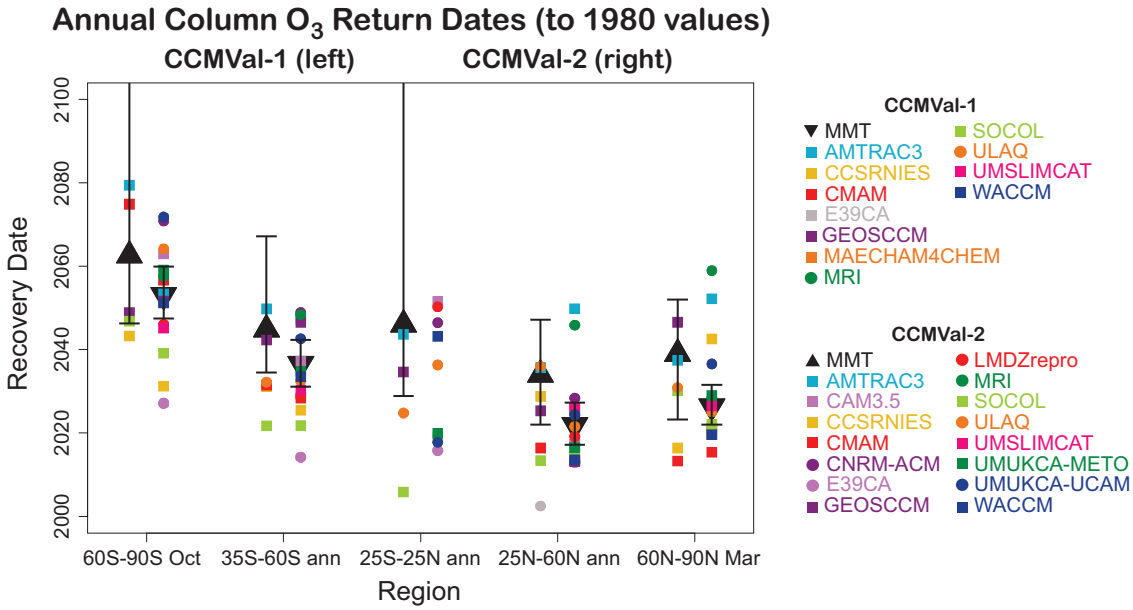

Figure 9.20: Date of return to 1980 values for the annual average (tropical and mid-latitude) and spring (polar) total ozone column derived from the IMT (coloured symbols) and MMT (large black triangles) estimates for CCMVal-1 and CCMVal-2 (left and right respectively in each latitude band). The error bars on the MMT estimate of return date is derived from the 95% confidence interval of the MMT estimates to the 1980 baseline-adjusted time series data.

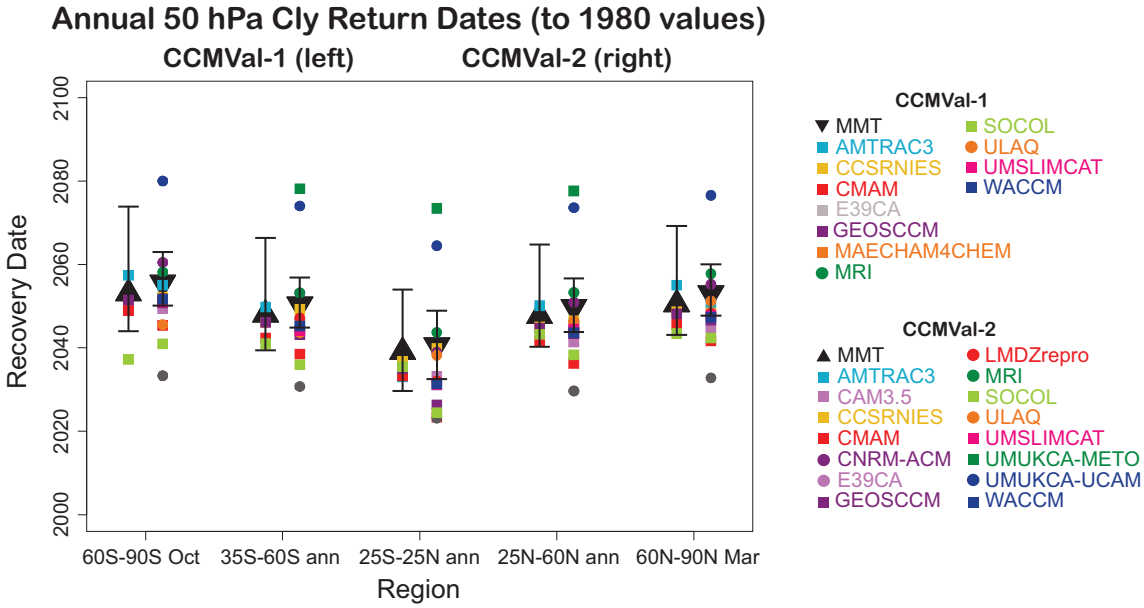

Figure 9.21: Date of return to 1980 values for the annual average 50 hPa Cl_y derived from the IMT (coloured symbols) and MMT (large black triangles) estimates for CCMVal-1 and CCMVal-2 (left and right respectively in each latitude band). The error bars on the MMT estimate of return date is derived from the 95% confidence interval of the MMT estimates to the 1980 baseline-adjusted time series data.

may be associated with spin-up issues at the beginning of the simulations. For example, a number of the models display increasing ozone in the early 1960s prior to their initial decrease in the 1970s and 1980s (*e.g.*, see Figures 9.8 and 9.12). In these models ozone returns to 1960 values both prior to, and after the main loss near year 2000. In these cases the earlier return date was discarded and the later value used. This would appear to be a spin-up issue, or the effect of aerosols following the eruption of Agung (Chapter 8) in these models, suggesting that future experiments should perhaps start even earlier than the period prescribed for CCMVal-2.

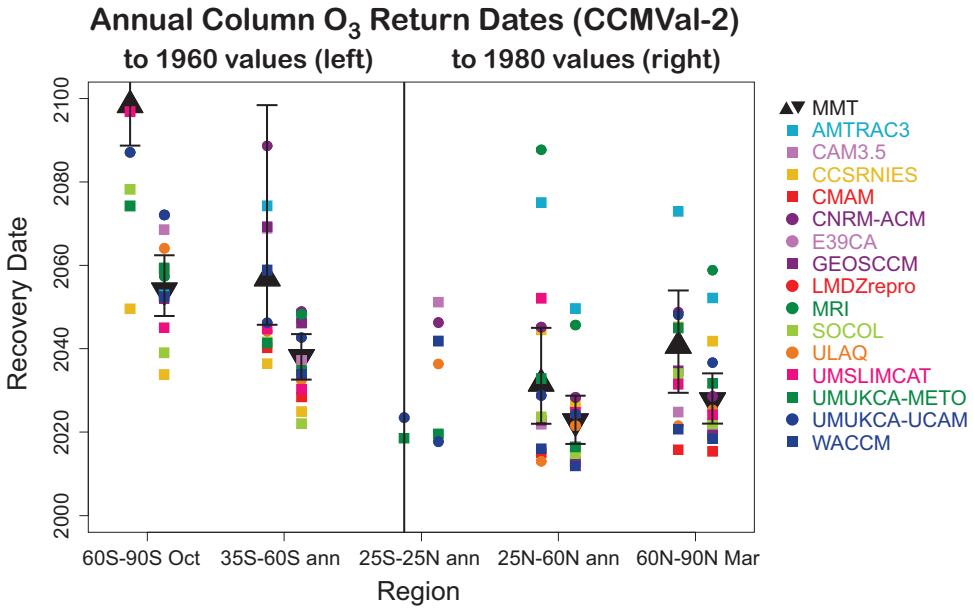

Figure 9.22: Date of return to 1960 (left) and 1980 (right) values for the annual average (tropical and mid-latitude) and spring (polar) total ozone column derived from the IMT (coloured symbols) and MMT (large black triangles) estimates for CCMVal-2. Error bars are as in Figure 9.20.

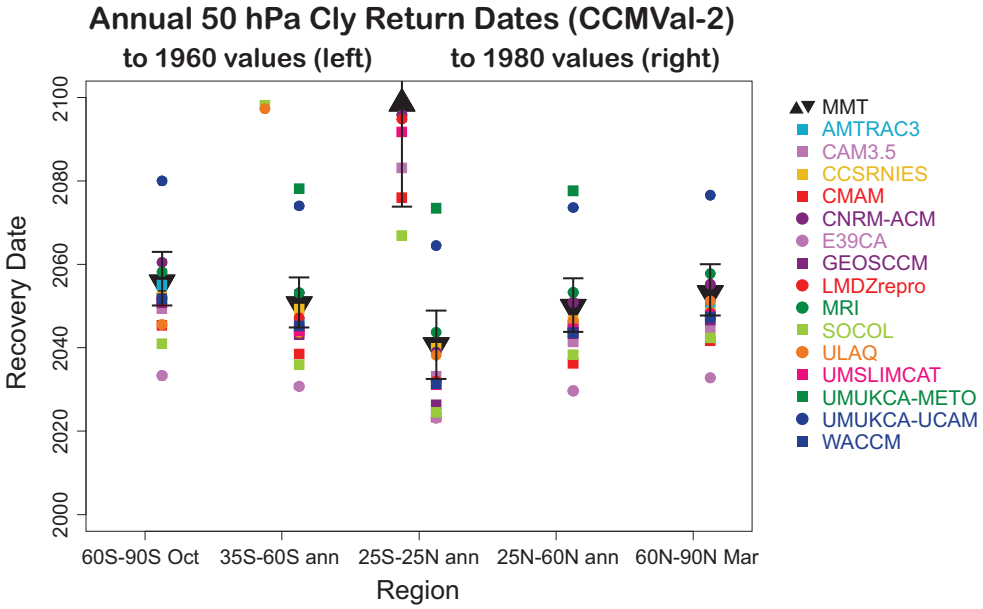

Figure 9.23: Date of return to 1960 (left) and 1980 (right) values for the annual average 50 hPa Cl_y derived from the IMT (coloured symbols) and MMT (large black triangles) estimates for CCMVal-2. Error bars are as in Figure 9.21.

9.6.4 The relationship between O_3 and Cl_y return dates

Figure 9.24 shows the relationship between return date of 50hPa Cl_y and column ozone back to their 1980 values using the MMT results of section 9.6.3. For the Antarctic spring, the models roughly scatter evenly about a similar date for the return of ozone and chlorine to 1980 values (given by the black line), indicating that halogen chemistry is the dominant driver in determining ozone recovery. Several models (CCSRNIES, UMUKCA-UCAM) fall significantly above the line, implying ozone returns faster than Cl_y, and several others fall significantly below the line, implying that ozone returns more slowly than Cl_y. The reason for these differences has not been identified, but may reflect, in part, the fact that in most models ozone recovers slowly in the middle 21st century, and a small change in the reference date (for example 1980 to 1985)

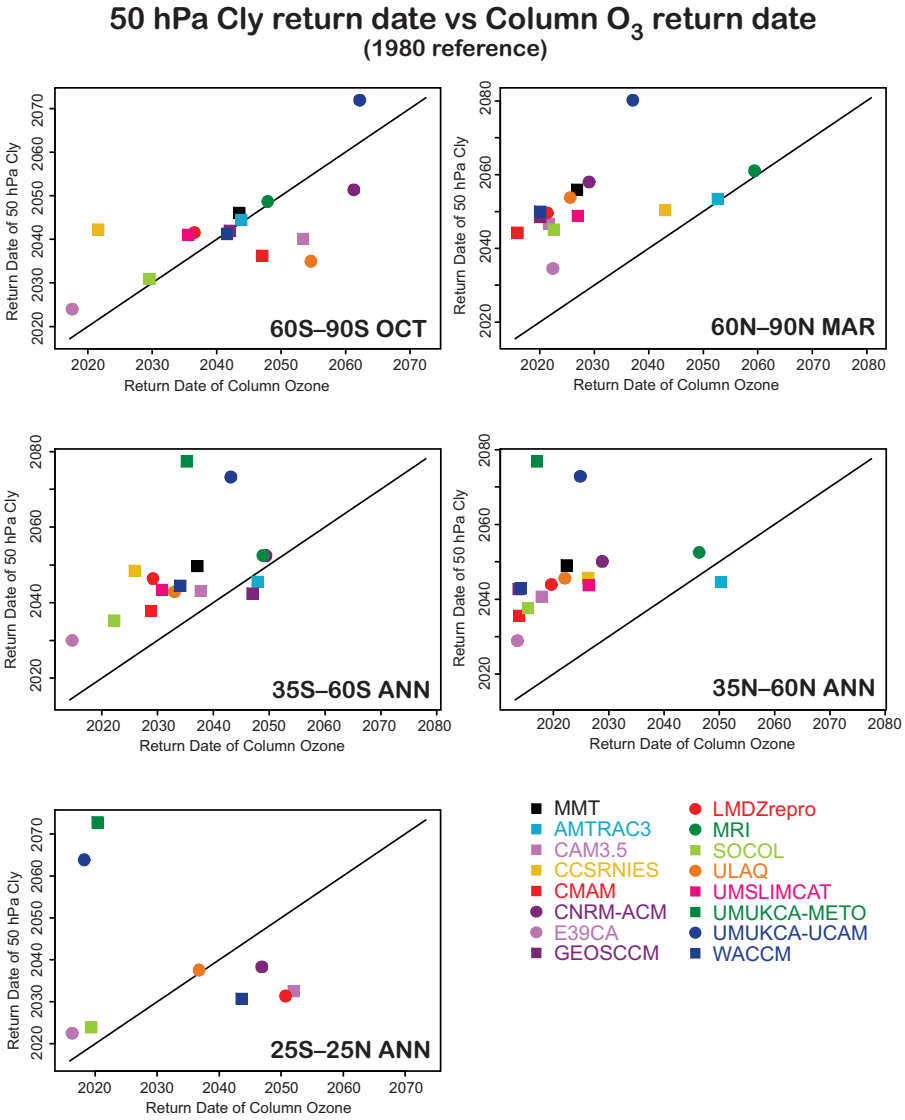

Figure 9.24: Relationship between the date of return of Cl_y to the1980 value compared with the date of return of column ozone for the selected latitude ranges in Figure 9.20. Results are taken from the IMT and MMT fits.

can cause a large change in ozone return date. A different picture is seen for the Arctic spring, and annual mean mid-latitudes where most models return to 1980 column ozone values before Cl_y returns to 1980 values. As indicated in Section 9.6.3, only about half of the models indicate a return of tropical ozone to the 1980 values.

9.6.5 Ozone recovery as a function of latitude and reference year

A complementary view of ozone recovery is shown in **Figure 9.25**, which indicates the return date for the annual mean column ozone appropriate to the reference date given on the abscissa. The column has been separated into two regions, above and below 20 hPa, and the analysis excludes the atmosphere below 500 hPa. For each year in the analysis, the first date after the year 2005 that the ozone partial column returned to the value on the reference date was determined for the mean model results. Above 20 hPa (Figure 9.25, upper panel), ozone recovery is simulated to occur steadily. In this region, the temperature and halogen effects on ozone dominate, as shown by the MLR analysis for the different regions described in the earlier sections. As suggested by this analysis, ozone change is approximately linearly dependent on $Cl_y + \alpha Br_y$. Taking approximate values for $Cl_y + \alpha Br_y$ of 3, 1.5 and 0.75 for 2000, 1980 and 1960 implies that the ozone recovery to 1960 levels should take about 50% longer than the recovery to 1980 levels. This is confirmed by Figure 9.25 (upper panel).

In the lower stratosphere (Figure 9.25, middle panel) a return date could not be established for the tropics due to the strengthening BD circulation which systematically

decreases tropical ozone as the simulations proceed (*e.g.*, Waugh *et al.*, 2009). The results also show a strong hemispheric asymmetry discussed above, with Antarctic ozone recovering much more slowly than Arctic ozone. Again, this is largely due to the increased BD circulation, which for the models as a whole has much more influence in the northern than the southern hemisphere (Austin and Wilson, 2006; Eyring *et al.*, 2007; Shepherd *et al.*, 2008). In high southern latitudes, the simulations on average do not return to the pre-1970 ozone levels before the end of the simulations.

The results for the total column (Figure 9.25, lower panel) combine the results for the two regions. In the tropics, the total ozone column recovers until about 2050 (Figure 9.2) due to decreasing halogen amounts and stratospheric cooling, but thereafter ozone decreases due to the increasing BD circulation. This implies that in the tropics, the total ozone column does not return to pre-1985 values before the end of the simulations. Over Antarctica, recovery to 1960s levels of total ozone does not occur in the mean model until shortly before the end of the simulations.

9.6.6 The Role of transport in mid-latitude ozone recovery

Given the important effects that changes in the BD circulation can have on projected ozone recovery, changes in the seasonal cycle in the different CCMVal models have been analysed with an emphasis on how the spring buildup of ozone relates to ozone recovery. An eight-term harmonic function (plus an extra term for the annual average) was fitted to the zonally and monthly averaged ozone column over mid-latitude bands in each hemisphere for the periods 1960-1979 and 2040-2059. The annual cycle derived from the fitting, with the annual mean for each model and time period removed, and the change in the seasonal cycle is shown in **Figure 9.26**. These results are outside the ozone hole period and show in both hemispheres a maximum in spring and a minimum in autumn. Several models (notably ULAQ, GEOSCCM, CMAM and, to a lesser extent, WACCM) show an increased build-up of ozone through the boreal spring between the 1960-1979 and 2040-2059 periods (panel c). In contrast, other models (AMTRAC3, MRI and UMUKCA-METO) show little change in the amplitude of the seasonal cycle between these periods.

As shown in **Figure 9.27**, changes in the seasonal cycle, as measured here by the change in the amplitude of the seasonal cycle averaged over January-April, show some correlation with the MMT estimate of 1980 recovery date for annual ozone derived from the TSAM analysis (Figure 9.20). The models showing an increased build-up of ozone through the spring have ozone recovery dates for the 35°N-60°N region before 2020. While the models showing little change in the amplitude of the seasonal cycle have

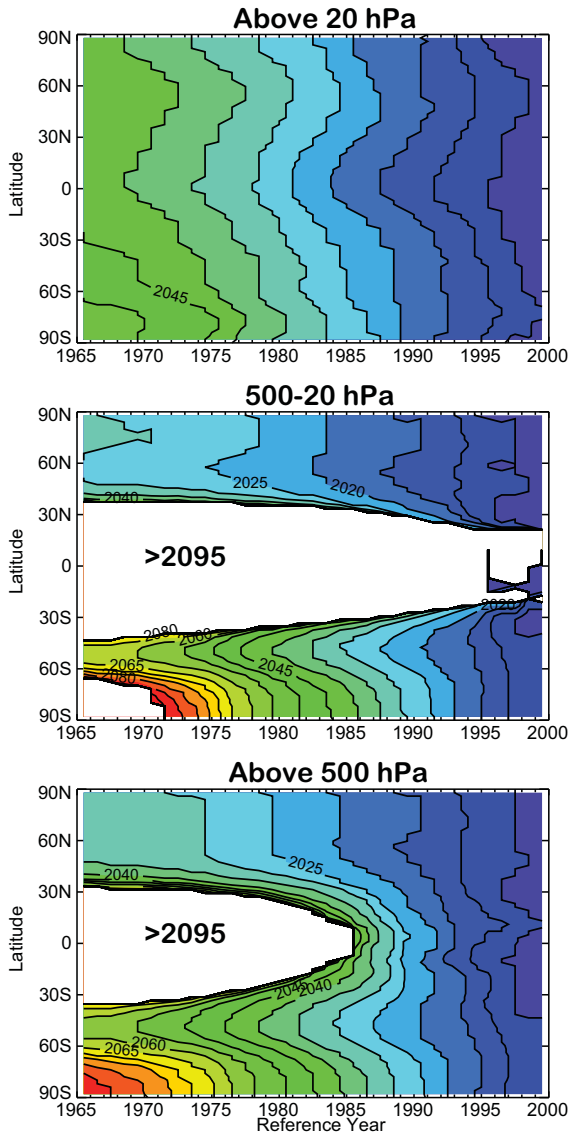

Figure 9.25: Date of return of the annual mean ozone to the value appropriate to the reference year indicated on the abscissa. Results were taken from the models AMTRAC3, CAM3.5, CCSRNIES, CMAM, CNRM-ACM, GEOSCCM, LMDZrepro, MRI, SOCOL, ULAQ, UMSLIMCAT, UMUKCA-UCAM, UMUKCA-METO and WACCM, which were first interpolated to a common latitudinal grid (AMTRAC3). The mean model result was then smoothed with an 11-year running mean filter. Data prior to 1965 (which limits the definition of the reference year data) or after 2094 (which limits the data for the return year) do not exist because of the need for an accurate time-smoothed field. The white region in the figure indicates where the mean model ozone has not recovered by the end of the simulations (nominally 2094). Results are shown for the total column above 500 hPa, for the range 500-20 hPa and for the column above 20 hPa.

recovery dates between 2040 and 2050. The UMUKCA-METO model is an exception, showing little change in the amplitude of the seasonal cycle yet having a recovery date before 2020.

Several models (CNRM-ACM, MRI and UMSLIMCAT) show an increased buildup of ozone during SH late-fall and winter (May, June and July) in the 2040-2059 period (Figure 9.26f), but no coherent changes persist into the spring. The seasonal cycle is further perturbed with the breakup of the Antarctic vortex in October and November, mixing ozone depleted air from within the Antarctic vortex into mid-latitudes. As shown in Figure 9.27, no clear relationship can be found between changes in the spring-time buildup of ozone and the recovery date. The lack of a clear signal in the amplitude of the seasonal cycle of column ozone is further evidence of a weaker change in the SH branch of the BD circulation.

Although chemistry is always a factor affecting the distribution of ozone, the spring-time build-up of ozone is a feature in the annual cycle driven by the transport of ozone from tropical to mid-latitudes by the BD circulation (*e.g.*, Fusco and Salby, 1999; Fioletov and Shepherd, 2003). Analysing the spring-time buildup should, therefore, highlight the role of dynamics over chemistry. Further, we analyse changes in the seasonal cycle over 1960-1979 to 2040-2059 to avoid the period of time when halogens are expected to have the largest effects on column ozone. For these reasons we believe that changes in the spring-time ozone column analysed here are indicative of changes in transport by the BD circulation in the models.

9.6.7 Brief Summary

The main processes influencing total ozone recovery are the increasing strength of the BD circulation, the GHG induced stratospheric cooling and the halogen loading. Because of the lesser importance of the BD circulation in the SH, recovery approximately follows that of Cl_y, while in the NH, the BD circulation and cooling play important roles in speeding up recovery. CCMVal-2 results suggest in general an earlier recovery than the CCMVal-1 results. However, in the tropics, the impact of the BD circulation is such that column ozone does not recover to the values present prior to about 1985 regardless of the reduction in halogen amounts. Nonetheless, the model results continue to show a very wide range of results for the ozone recovery time scale. Finally, because ozone approximately follows Cl_y over the Antarctic, the disappearance of the ozone hole does not occur by the end of the simulation in some models.

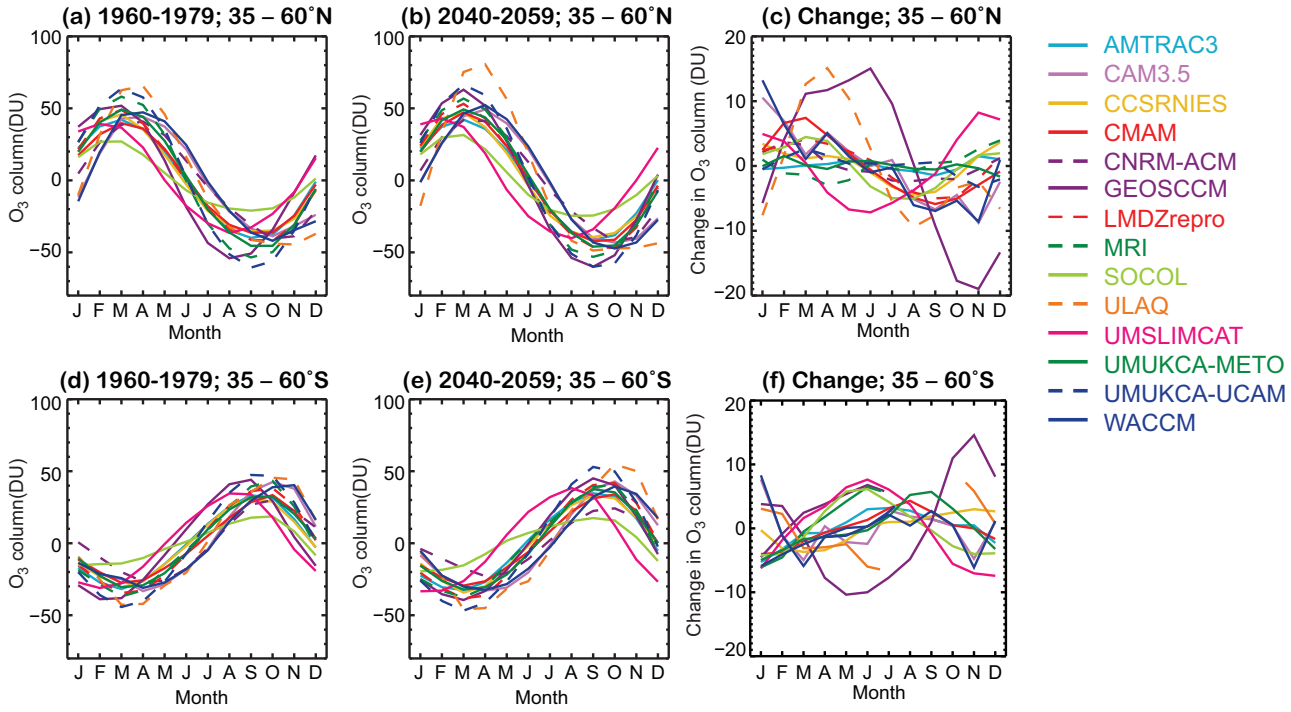

Figure 9.26: The average seasonal cycle of total column ozone over NH and SH mid-latitudes for two periods and its change. (a) 1960-1979, 35°N-60°N, (b) 2040-2059, 35°N-60°N, (c) Change from 1960-1979 to 2050-2059. (d)-(f), as(a)-(c), but for the southern mid-latitudes. Note that the annual mean for each model and each time period is removed from the annual cycle before plotting and before taking the difference.

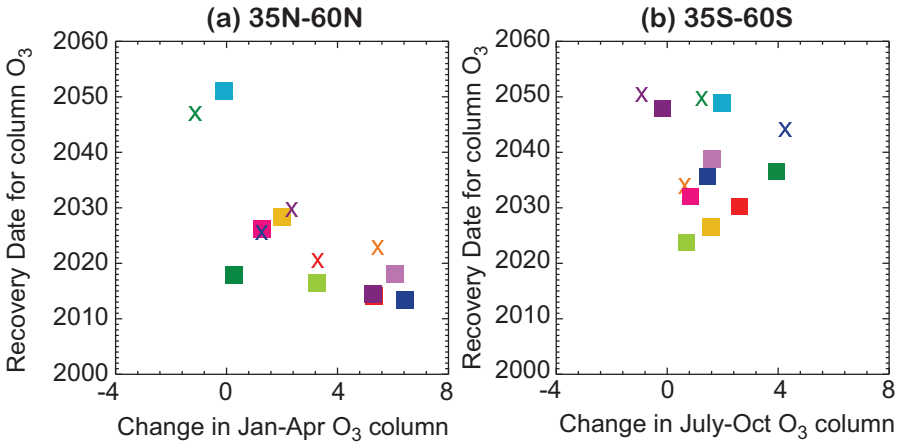

Figure 9.27: The relationship between the recovery date of mid-latitude (35°-60°) annual average ozone from the MMT analysis and the change in amplitude of the seasonal cycle of ozone averaged over the spring in each hemisphere. The change in the seasonal cycle is defined as the difference between 1960-1979 and 2040-2059 and is shown in panels (b) and (d) of Fig. 9.26. The averages are calculated for January-April and July-October for the NH and SH, respectively.

9.7 Summary

9.7.1 Summary by Model

Here, we provide a brief summary of the mean model ozone results. Summaries for each model are also provided, which identify differences from the multi-model mean, emphasizing where each model performs particularly well with respect to observations, or particularly poorly. For ozone recovery, comparisons are made with the multi-model mean.

Multi-model mean: In the tropics, the total ozone column for the multi-model mean agrees reasonably well with observations whereas in mid-latitudes, models are generally biased high by 10-20 DU. In the polar regions although the depth of the ozone hole is well reproduced in the multi-model mean, there is a wide spread in results and most models simulate an ozone hole that is too small in area. Arctic ozone in the multi-model mean is close to that observed, but there is a wide spread in results due to interannual variability in the polar vortex. The recovery properties of the multi-model mean have been discussed at length in Section 9.6.

AMTRAC3 has one of the smallest ozone depletions for the upper stratosphere due to low Cl_y. In the column amount, the model is only slightly lower than observed in the tropics and mid-latitudes, but has one of the largest losses in mid-latitudes. The model simulates the ozone hole reasonably well, but in the Arctic, the model column ozone is biased low. Ozone recovery is consistent with the multi-model mean in the SH, but tends to be late in the NH. AMTRAC3 O_3 is much more sensitive to NOy change in the tropics than most models.

CAM3.5 has a large high bias in ozone in the tropical upper stratosphere and one of the smallest depletions. In the column amount, the model is only slightly lower than observed in the tropics and mid-latitudes, but has one of the smallest depletions for the lower stratosphere and column ozone. This is likely due to the model Cl_y, which is one of the smallest. Polar ozone is biased high and the ozone hole is much smaller than observed due to a combination of high ozone bias and small area of PSCs (Chapter 4). Ozone recovery is consistent with the multi-model mean.

CCSRNIES has one of the largest cooling rates in the upper stratosphere, leading to a faster ozone recovery. The model has a high bias in the cold areas in the Antarctic late winter and spring, but the ozone hole is under-predicted in size and depth.

CMAM has a column ozone which is lower than observed in the tropics and northern mid-latitudes. The model has one of the largest tropical vertical ascent rates and corresponding change in lower stratospheric tropical ozone. The model has generally less ozone reduction than the multi-model mean, due to lower Cl_y levels. Ozone recovery in northern mid-latitudes is similar to the multi-model mean, but is early in the Arctic and in southern mid-latitudes. The simulated Antarctic ozone hole agrees reasonably well with observations, and the return to 1980 levels occurs at a similar year as the multi-model mean.

CNRM-ACM has a larger tropical and mid-latitude ozone reduction than observations due to chlorine and a corre-

sponding larger recovery than most models. The ozone change is particularly notable in the SH. In polar regions, past ozone loss and Cl_y are similar to that observed (Chapter 5). The Antarctic ozone hole, using a 220 DU theshold, is large in area, because of a low bias in the lower atmosphere.

EMAC has a small and shallow ozone hole, due in part to the region of low temperatures (T < 195 K) being smaller than observed.

E39CA has a high bias in ozone in the tropical upper stratosphere. In the column amount, the model has a high bias at all latitudes with the largest bias of all models in the tropics. The model has a small ozone hole area, based on a 220 DU threshold, due to an overall ozone bias. For both ozone and Cl_y, E39CA generally has the earliest recovery dates, which are roughly one decade prior to those of the multi-model mean.

GEOSCCM is similar to observations in the tropics, but the total ozone column is higher than observed in middle and high latitudes. Cl_y is similar to the multi-model mean but reduces faster in the future. The ozone hole is smaller and more shallow than observed because of the ozone bias. The model has one of the earliest returns to 1980 polar ozone values.

LMDZrepro has the deepest ozone hole of CCMVal-2, which give rise to the steepest gradients in ozone column at the edge of the southern polar vortex. However, the ozone depletion due to chlorine is at the low end of the model range and the model cooling rate is the largest in the upper stratosphere.

MRI is biased high at all latitudes compared with measurements of the total column ozone. The model has a large ozone column reduction due to chlorine increase, which is larger than most models. The model has a corresponding slower ozone recovery in the NH, but is near the model average for the SH. The depth of the ozone hole agrees well with observations, but the area of the ozone hole is much smaller than observed primarily because of the ozone high bias.

NiwaSOCOL is the same as SOCOL with a difference in the model lower boundary. Results are similar to SOCOL — no significant differences in the ozone hole diagnostics were seen.

SOCOL agrees with observations and the multi-model mean for tropical ozone for the first part of the simulation, but after about 2050, column ozone decreases substantially due to the large change in the BD circulation (Chapter 4). The circulation change gives rise to a strong cooling in the tropical lower stratosphere and a reduction of ozone. The model has a large reduction in Cl_y during the 21st century compared with the model mean, leading to a faster recovery. The simulated Antarctic ozone hole is in good agreement with observations for the current atmosphere, although low column ozone values are simulated early in the REF-B1 simulation due to dynamical influences.

ULAQ has an ozone column that is higher than observed for the past due to low Cl_y. The model ozone return to 1980 levels is near the multi-model mean in mid- and high latitudes of the NH, but is later than the mean in southern polar regions. After about 2040 ozone recovers faster than in most models. The simulated Antarctic ozone hole agrees reasonably well with observations, although low column ozone values are also simulated early in the REF-B1 simulation.

UMETRAC did not supply data in time to be evaluated.

UMSLIMCAT has an ozone column in all latitudes that is biased low, possibly because of a low bias in tropospheric ozone. Ozone recovers faster than in most models, particularly in the SH, due in part to Cl_y values being lower than the multi-model mean. The simulated Antarctic ozone hole is in reasonable agreement with observations.

UMUKCA-METO generally agrees with observations of the tropical and mid-latitude mean column ozone. In the tropical upper stratosphere, the model ozone change is similar to the multi-model mean, but the model is biased low due to very high chlorine. In southern mid-latitudes, the ozone column reduces unexpectedly after 2070. In the Arctic the simulated ozone column is reasonably consistent with observations, but in the Antarctic the model is biased high. The Antarctic ozone hole is small and shallow due to insufficient PSCs.

UMUKCA-UCAM is higher than observed for the total column ozone at all latitudes and is lower than most models in the upper stratosphere, due to higher Cl_y. Ozone recovery to 1980 levels is similar to the multi-model mean in the NH, and southern mid-latitudes, but is late over Antarctica. Due to a combination of the ozone bias, and low PSCs, the Antarctic ozone hole is small and shallow.

WACCM simulates a tropical total column ozone which is lower than observed. Tropical upper stratospheric ozone is higher than most models. In mid-latitudes and polar regions, the model agrees reasonably well with observation of the total column ozone. Column ozone recovers to 1980 values at about the same time as the multi-model mean in the SH, but earlier than the mean in the NH. The Antarctic

ozone hole is well simulated by the model, but disappears faster than in other models which simulate the ozone hole well.

9.7.2 Overall Summary

In this Chapter we have introduced a time series additive model (TSAM) analysis to make individual- and multi-model trend estimates, which may be used to make formal inference. One of the primary goals of this analysis was to produce more quantitative multi-model ozone projections with associated uncertainty estimates. Another goal was the careful comparison of ozone projections between the CCMVal-1 and CCMVal-2 data sets to identify areas where models have improved and areas that continue to require modelling effort. In the application of the TSAM analysis it is clear that a number of practical issues can influence this comparison (*e.g.*, longer, more complete time series of the period of interest were submitted to CCMVal-2 compared to CCMVal-1). Our findings are summarized below.

Most of the conclusions of the last WMO assessment remain unchanged. Ozone recovery time scales are very similar to those previously deduced, and several models in particular have undergone several major changes that have tended to reduce the overall spread of results. This provides more confidence in model trends. One important change from WMO (2007) is that some models now indicate that a small, residual ozone hole may still be present from 2060 until 2100 or later.

The results from CCMVal-2 have been analysed over broad latitudinal ranges. In the tropics, ozone does not change substantially in the simulations, and transport *i.e.*, upward motion is likely to be the largest driver. As a result, ozone decreases in the past, and recovers slightly due to chlorine decreases. In the second half of the 21st century, column ozone is expected to reduce once more, primarily due to the transport effect dominating chlorine reduction, which is essentially complete.

In mid-latitudes, chlorine and bromine are likely playing the most important role and consequently the narrower spread in simulated halogen amounts has led to a reduced spread in ozone simulations. In addition ozone transport is important in northern mid-latitudes.

In the Arctic ozone is very variable and difficult to simulate, due at least in part to the chaotic nature of dynamical processes. In addition there is no clear consensus on the trends in downwelling, and hence the amount of ozone transport is not clear compared with other impacts. In some cases models do not simulate well the Antarctic ozone hole, even when some allowance is made for the vortex edge or for the PSC areas, at least as defined in Chapter 4 by temperature threshold. No significant progress has been made on this since CCMVal-1 by most models. The large differences between the models could be due to differences in model chemistry. Another possibility is that the cloud microphysics may be being treated inadequately by some models (Chapter 6). For example if particle fall rates are too large during June and July, there would be no material surfaces in the warmer spring period for PSCs to form. While this would suggest that estimates of the date of disappearance of the ozone hole are unreliable, there is some consistency in the group of models which reproduce best the current ozone hole. These models suggest that a small, residual ozone hole will still be present from 2060 until the end of the simulations in 2100.

There is a need for a range of simulations looking at all aspects of the atmosphere-ocean system to try to address some of these issues. Uncertainties in net temperature changes, which arise from uncertainties in the increase of the strength of the BD circulation *versus* radiative changes, need to be reduced. Realistic bromine amounts need to be included in model simulations to allow for the short lifetime species known to be present (WMO, 2007, Chapter 2). Finally, simulations with fixed halogens or fixed GHGs need to be completed to complement the realistic simulations that have been completed to establish more rigorously the impact of climate and chemistry changes.

References

Austin, J. and F. Li, 2006. On the relationship between the strength of the Brewer-Dobson circulation and the age of stratospheric air, *Geophys. Res. Lett.*, **33**, doi:10.1029/2006GL026867.

Austin, J. and T. J. Reichler, 2008. Long term evolution of the cold point tropical tropopause: Simulation results and attribution analysis, *J. Geophys. Res.*, **113**, doi:10.1029/ 2007JD009768.

Austin, J. and R. J. Wilson, 2006. Ensemble simulations of the decline and recovery of stratospheric ozone, *J. Geophys. Res.*, **111**, doi:10.1029/2005JD006907.

Austin, J., K. Toupali, E. Rozanov, H. Akiyoshi, S. Bekki, G. Bodeker, C. Brühl, N. Butchart, M. Chipperfield, M. Deushi, V. I. Fomichev, M. A. Giorgetta, L. Gray, K. Kodera, F. Lott, E. Manzini, D. Marsh, K. Matthes, T. Nagashima, K. Shibata, R. S. Stolarski, H. Struthers, and W. Tian, 2008. Coupled chemistry climate model simulations of the solar cycle in ozone and temperature, *J. Geophys. Res.*, **113**, doi:10.1029/2007JD009391.

Bodeker, G. E., H. A. Struthers, and B. J. Connor, 2002. Dynamical containment of Antarctic ozone depletion, *Geophys. Res. Lett.*, **29**, doi:10.1029/2001GL014206.

Bodeker, G. E., H. Shiona, and H. Eskes, 2005. Indicators of Antarctic ozone depletion, *Atmos. Chem. Phys.*, **5**, 2603-2615.

Butchart, N., and A. A. Scaife, 2001. Removal of chlorofluorocarbons by increased mass exchange between the stratosphere and troposphere in a changing climate, *Nature*, **410**, 799-802.

N. Butchart, A. A. Scaife, M. Bourqui, J. de Grandpré, S. H. E. Hare, J. Kettleborough, U. Langematz, E. Manzini, F. Sassi, K. Shibata, D. Shindell and M. Sigmond, 2006. Simulations of anthropogenic change in the strength of the Brewer-Dobson circulation. *Clim. Dyn.*, **27**, 727-741.

Charlton-Perez, A., L. M. Polvani, J. Austin, and F. Li, 2008. The frequency and dynamics of stratospheric sudden warmings in the 21st century, *J. Geophys. Res.*, **113**, doi:10.1029/2007JD009571.

Daniel, J. S., S. Solomon, R. W. Portmann, and R. R. Garcia, 1999. Stratospheric ozone destruction: The importance of bromine relative to chlorine, *J. Geophys. Res.*, **104**, 23,871-23,880.

Deckert, R. and M. Dameris, 2008. Higher tropical SSTs strengthen the tropical upwelling via deep convection, *Geophys. Res. Lett.*, **35**, doi: 10.1029/2008GL033719.

Douglass, A. R., R. S. Stolarski, M. R. Schoeberl, C. H. Jackman, M. Gupta, P. A. Newman, J. E. Nielsen, E. L. Fleming, 2008. Relationship of loss, mean age of air and the distribution of CFCs to stratospheric circulation and implications for atmospheric lifetimes, *J. Geophys. Res.*, **113**, doi: 10.1029/2007JD09575.

Engel, A., T. Mobius, H. Bonisch, U. Schmidt, R. Heinz, I. Levin, E. Atlas, S. Aoki, T. Nakazawa, S. Sugawara, F. Moore, D. Hurst, J. Elkins, S. Schauer, A. Andrews, and K. Boering, 2009. Age of stratospheric air unchanged within uncertainties over the past 30 years, *Nature Geosci.*, **2**, 28-31.

Eyring, V., N. Butchart, D. W. Waugh, H. Akiyoshi, J. Austin, S. Bekki, G. E. Bodeker, B. A. Boville, C. Brhl, M. P. Chippereld, E. Cordero, M. Dameris, M. Deushi, V. E. Fioletov, S. M. Frith, R. R. Garcia, A. Gettelman, M. A. Giorgetta, V. Grewe, L. Jourdain, D. E. Kinnison, E. Mancini, E. Manzini, M. Marchand, D. R. Marsh, T. Nagashima, P. A. Newman, J. E. Nielsen, S. Pawson, G. Pitari, D. A. Plummer, E. Rozanov, M. Schraner, T. G. Shepherd, K. Shibata, R. S. Stolaarski, H. Struthers, W. Tian, and M. Yoshiki, 2006. Assessment of temperature, trace species, and ozone in chemistry-climate model simulations of the recent past, *J. Geophys. Res.*, **111**, doi:10.1029/2006JD007327.

Eyring, V., D. W. Waugh, G. E. Bodecker, E. Cordero, H. Akiyoshi, J. Austin, S. R. Beagley, B. A. Boville, P. Braesicke, C. Brhl, N. Butchart, M. P. Chippereld, M. Dameris, R. Deckert, M. Deushi, S. M. Frith, R. R. Garcia, A. Gettelman, M. A. Giorgetta, D. E. Kinnison, E. Mancini, E. Manzini, D. R. Marsh, S. Matthes, T. Nagashima, P. A. Newman, J. E. Nielsen, S. Pawson, G. Pitari, D. A. Plummer, E. Rozanov, M. Schraner, J. F. Scinocca, K. Semeniuk, T. G. Shepherd, K. Shibata, B. Steil, R. S. Stolaarski, W. Tian, and M. Yoshiki, 2007. Multi-model projections of ozone recovery in the 21st century, *J. Geophys. Res.*, **112**, doi:10.1029/2006JD008332.

Fioletov, V. E., G. E. Bodeker, A. J. Miller, R. D. McPeters, and R. Stolarski, 2002. Global ozone and zonal total ozone variations estimated from ground-based and satellite measurements: 1964-2000, *J. Geophys. Res.*, **107**, doi:10.1029/2001JD001350.

Fioletov, V. E. and T. G. Shepherd, 2003. Seasonal persistence of midlatitude total ozone anomalies, *Geophys. Res. Lett.*, **30**, doi:10.1029/2002GL016739.

Fomichev, V. I., A. I. Jonsson, J. de Grandpre, S. R. Beagley, C. McLandress, K. Semeniuk and T. G. Shepherd, 2007. Response of the middle atmosphere to CO2 doubling: Results from the Canadian Middle Atmosphere Model, *J. Clim.*, **20**, 1121-1144.

Forster, P. M., G. Bodeker, R. Schoeld, S. Solomon, and D. Thompson, 2007. Effects of ozone cooling in the tropical lower stratosphere and upper troposphere, *Geophys. Res. Lett.*, **34**, doi:10.1029/2007GL081994.

Fusco, A. C. and M. L. Salby, 1999. Interannual variations of total ozone and their relationship to variations of planetary wave activity, *J. Clim.*, **12**, 1619-1629.

Garcia, R. R., D. R. Marsh, D. E. Kinnison, B. A. Boville, and F. Sassi, 2007. Simulation of secular trends in the middle atmosphere, 1950-2003, *J. Geophys. Res.*, **112**, doi:10.1029/2006JD007485.

Garcia, R. R. and W. J. Randel, 2008. Acceleration of the Brewer-Dobson circulation due to increases in greenhouse gases, *J. Atmos. Sci.*, **65**, 2731-2739.

Garnkel, C. I. and D. L. Hartmann, 2007. Effects of El

Nino-Southern Oscillation and the Quasi-Biennial Oscillation on polar temperatures inthe stratosphere, *J. Geophys. Res.*, **112**, doi:10.1029/2007JD008481.

Gettelman, A., T. Birner, V. Eyring, H. Akiyoshi, S. Bekki, C. Bruhl, M. Dameris, D. E. Kinnison, F. Lefevre, F. Lott, E. Mancini, G. Pitari, D. A. Plummer, E. Rozanov, A. Stenke, H. Struthers, and W. Tian, 2009. The tropical tropopause layer, 1960-2100, *Atmos. Chem. Phys.*, **9**, 1621-1637.

Hitchcock, P., T. G. Shepherd, and C. McLandress, 2009. Past and future conditions for polar stratospheric cloud formation simulated by the Canadian Middle Atmosphere Model, *Atmos. Chem. Phys.*, **9**, 483-495.

Holton, J. R., and H.-C. Tan, 1980. The influence of the equatorial quasi-biennial oscillation on the global circulation at 50mb. *J. Atmos. Sci.*, **37**, 2200-2208.

Huck, P. E., S. Tilmes, G. E. Bodeker, W. J. Randel, A. J. McDonald, and H. Nakajima, 2007. An improved measure of ozone depletion in the Antarctic stratosphere, *J. Geophys. Res.*, **112**, doi: 11110.11029/12006JD007860.

Li, F., J. Austin, and J. Wilson, 2008. The strength of the Brewer-Dobson circulation in a changing climate: coupled chemistry-climate model simulations, *J. Clim.*, **23**, 40-57.

Li, F., R. S. Stolarski, and P. A. Newman, 2009. Stratospheric ozone in the post-CFC era, *Atmos. Chem. Phys.*, **9**, 2207-2213.

McLandress, C. and T. G. Shepherd, 2009a. Simulated anthropogenic changes in the Brewer-Dobson circulation, including its extension to high latitudes, *J. Clim.*, **22**, 1516-1540.

McLandress, C. and T. G. Shepherd, 2009b. Impact of climate change on stratospheric sudden warmings as simulated by the Canadian Middle Atmosphere Model, *J. Clim.*, **22**, 5449-5463.

Manzini, E., M.A. Giorgetta, M. Esch, L. Kornbluh, and E. Roeckner, 2006. The influence of sea surface temperatures on the northern winter stratosphere: Ensemble simulations with the MAECHAM5 model, *J. Clim.*, **19**, 3863-3881.

Miller, A. J., R. M. Nagatani, L. E. Flynn, S. Kondragunta, E. Beach, R. Stolarski, R. D. McPeters, P. K. Bhartia, M. T. DeLand, C. H. Jackman, D. J. Wuebbles, K. O. Patten, R. P. Cebula, 2002. A cohesive total ozone data set from SBUV(/2) satellite system, *J. Geophys. Res.*, **107**, doi:10.1029/2001JD000853.

Newman, P. A., J. S. Daniel, D. W. Waugh, and E. R. Nash, 2007. A new formulation of equivalent effective stratospheric chlorine (EESC), *Atmos. Chem. Phys.*, **7**, 4537-4552.

Oman, L., D. W. Waugh, S. Pawson, R. S. Stolarski, and P. A. Newman, 2009. On the influence of anthropogenic forcings on changes in the stratospheric mean age, *J. Geophys. Res.*, **114**, doi:10.1029/2009JD010378.

Oman, L., D. W. Waugh, S. R. Kawa, R. S. Stolarski, A. R. Douglass, and P. A. Newman, 2010. Mechanisms and feedbacks causing changes in upper stratospheric ozone in the 21st century, *J. Geophys. Res.*, **115**, doi:10.1029/2009JD012397, In press.

Portmann R. W., and S. Solomon, 2007. Indirect radiative forcing of the ozone layer during the 21st century, *Geophys. Res. Lett.*, **34**, doi:10.1029/2006GL028252.

Pawson, S., R. S. Stolarski, A. R. Douglass, P. A. Newman, J. E. Nielsen, S. M. Frith, and M. L. Gupta, 2008. Goddard Earth Observing System chemistry-climate model simulations of stratospheric ozone-temperature coupling between 1950 and 2005, *J. Geophys. Res.*, **113**, doi:10.1029/2007JD009511.

Plumb, R.A., 1996. A "tropical" pipe model of stratospheric transport, *J. Geophys. Res.*, **101**, 3957-3972.

Randel, W. J. and F. Wu, 2007. A stratospheric ozone prole data set for 1979-2005: Variability, trends and comparisons with column ozone data, *J. Geophys. Res.*, **112**, doi:10.1029/2006JD007339.

Shepherd, T. G., 2008. Dynamics, stratospheric ozone and climate change, *Atmos.-Ocean*, **46**, 117-138.

Shine, K. P., M. S. Bourqui, P. M. de F. Forster, S. H. E. Hare, U. Langematz, P. Braesicke, V. Grewe, M. Ponater, C. Schnadt, C. A. Smith, J. D. Haigh, J. Austin, N. Butchart, D. T. Shindell, W. J. Randel, T. Nagashima, R. W. Portmann, S. Solomon, D. J. Seidel, J. Lanzante, S. Klein, V. Ramaswamy, and M. D. Schwarzkopf, 2003. A comparison of model-simulated trends in stratospheric temperatures, *Quart. J. Roy. Meteorol. Soc.*, **129**, 1565-1588.

Son, S.-W., L. M. Polvani, D. W. Waugh.,T. Birner, H. Akiyoshi, R.R. Garcia, A. Gettelman, D. A. Plummer and E. Rozanov, 2008. The impact of stratospheric ozone recovery on tropopause height, *J. Clim.*, **22**, 429-445.

Stolarski, R. S., and S. Frith, 2006. Search for evidence of

trend slowdown in the long-term TOMS/SBUV total ozone data record: The importance of instrument drift uncertainty, *Atmos. Chem. Phys.*, **6**, 4057-4065.

Struthers H., G. E. Bodeker, J. Austin, S. Bekki, I. Cionni, M. Dameris, M.A. Giorgetta, V. Grewe, F. Lefevre, F. Lott, E. Manzini, T. Peter, E. Rozanov, and M. Schraner, 2009. The simulation of the Antarctic ozone hole by chemistry-climate models, *Atmos. Chem. Phys.*, **9**, 6363-6376.

Takahashi, M., 1996. Simulation of the stratospheric quasi-biennial oscillation using a general circulation model, *Geophys. Res. Lett.*, **23**, 661-664.

Tie, X., and G. Brasseur, 1995. The response of stratospheric ozone to volcanic eruptions: Sensitivity to atmospheric chlorine loading, *Geophys. Res. Lett.*, **22**, 3035-3038.

Tilmes, S., D. E. Kinnison, R. R. Garcia, R. Müller, F. Sassi, D. R. Marsh, and B. A. Boville, 2007. Evaluation of heterogeneous processes in the polar lower stratosphere in the Whole Atmosphere Community Climate Model, *J. Geophys. Res.*, **112**, doi:10.1029/2006JD008334.

Waugh, D. W., 2009. The age of stratospheric air, *Nature Geosci.*, **2**, 14-16.

Waugh, D. W., L. Oman, S. R. Kawa, R. S. Stolarski, S. Pawson, A. R. Douglass, P. A. Newman, and J. E. Nielsen, 2009. Impact of climate change on stratospheric ozone recovery, *Geophys. Res. Lett.*, **36**, doi:10.1029/2008GL036223.

World Meteorological Organization (WMO)/United Nations Environment Programme (UNEP), 2007. *Scientific Assessment of Ozone Depletion: 2006*, World Meteorological Organization, Global Ozone Research and Monitoring Project, Report No. 50, Geneva, Switzerland.

Yang, Q., Q. Fu, J. Austin, A. Gettelman, F. Li, H. Vömel, 2008. Observationally Derived and GCM Simulated Tropical Stratospheric Upward Mass Fluxes, *J. Geophys. Res.*, **113**, 2008JD009945.

Supplement to Chapter 9

This document contains material that is ancillary to Chapter 9 of the CCMVal ozone report. The material is divided into three sections. The first section provides a more complete set of TSAM diagnostics for the five latitude bands discussed in Chapter 9. The second section investigates the sensitivity of the TSAM analysis, and its prediction of return dates, to the elimination of an outlying model. The final section investigates the application of 1:2:1 smoothing to individual model ensemble time series in the definition of a multi-model ensemble mean and performs a direct comparison with the results of the TSAM analysis.

9S.1 TSAM Latitude-Band Diagnostics

In this section we present a more complete set of figures associated with the application of the TSAM analysis to the time series of total column ozone and 50hPa inorganic Cly in the 5 latitude bands discussed in Chapter 9. For each of these two types of time series, and in each latitude band, a set of 4 figures is presented.

The first and second figures in the set provide a comparison of CCMVal-1 vs CCMVal-2 (e.g. Fig. 9S.1 and 9S.2). The first shows four panels in which the two panels on the left display raw time series data with their initial individual model trend (IMT) estimates and the two panels on the right display 1980 baseline-adjusted time series data with their 1980 baseline-adjusted IMT estimates. The second figure provides a comparison of 1980 baseline adjusted IMT and multi-model trend (MMT) estimates with 95% confidence and 95% prediction intervals.

The third and fourth figures in the set focus on CCMVal-2 and investigate the use of the earlier reference dates of 1970 and 1960 for the baseline adjustment in the TSAM analysis. The third figure shows the 1970 and 1960 baseline-adjusted time series data and baseline-adjusted IMT estimates for the TSAM analysis (e.g. Fig. 9S.3). The fourth figure displays the 1970 and 1960 baseline-adjusted IMT and MMT estimates along with 95% confidence and 95% prediction intervals (e.g. Fig. 9S.4).

In the first figure of this set, the range along the vertical axis has been forced to be identical in each of the four panels (e.g. Fig. 9S.1). In this way the collapse of the data arising from the application of the baseline adjustment (left to right) and differences between CCMVal-1 and CCMVal-2 (top to bottom) can be visually identified. In nearly all latitude bands, it is seen that there exists a large inter-model spread in the raw time series that is not apparent in the baseline adjusted time series, which form the primary diagnostic considered in Chapter 9. In at least one instance, the baseline adjusted time series would seem to show CCMVal-2 to have less model-spread than CCMVal-1 while the raw time series indicates the opposite behaviour (i.e. Fig. 9S.17). For this reason it is important to have plots of this nature for all of the latitude bands discussed in Chapter 9.

9S.2 Sensitivity to Outliers

As described in the Appendix to Chapter 9, the TSAM analysis allows the specification of prior weights for individual models based on quantitative performance metrics. The expectation was that such performance based weighting might reduce the sensitivity of the final multi-model average to the presence of outliers. For this report, however, it was decide that quantitative performance metrics were not as yet sufficiently robust to be useful for prior weighting of the models. Even so, it is of interest to investigate the sensitivity of the TSAM analysis to outlying models. In this section, we employ an extreme limit of performance-based weighting by arbitrarily removing one model from the TSAM analysis. For this sensitivity experiment, we have selected the UMUKCA-METO model which displayed anomalously large 50hPa Cly in all latitude bands.

The impact of removing the UMUKCA-METO model on the evolution of total column O_3 is considered first. While the UMUKCA-METO model is an outlier with respect to 50hPa Cly, its column O_3 is within the main spread of models. Consequently, for column O_3, the removal of UMUKCA-METO tests the sensitivity of the TSAM analysis to the removal of a model that is not an outlier. In Fig. 9S.41 MMT estimates for total Column O_3 in the 5 latitude bands considered in Chapter 9 are presented for the two cases of the TSAM analyses applied to all models (right column) and the TSAM applied to all models except UMUKCA.METO (left column). Inspection of Fig. 9S.41 shows the MMT estimates and 95% confidence and prediction intervals for all latitude bands to be very similar in both cases. This is verified in Fig. 9S.42 where the MMT estimate with UMUKCA-METO removed (blue) is overlayed on the MMT estimate derived from all models (dark grey). For total column O_3 the two cases are essentially indistinguishable. A test of the impact on 1980 return dates, Fig. 9S.43, shows no difference between the two cases. From this we may conclude that, for the CCMVal-2 model set, the TSAM analysis is insensitive to the removal of a model that is not an outlier.

The sensitivity of the TSAM analysis of 50hPa Cly to the removal of UMUKCA-METO is a more severe test as the 50hPa Cly of UMUKCA-METO is a significant outlier in all latitude bands. In Fig. 9S.44 MMT estimates for 50hPa Cly in the 5 latitude bands are presented for the two cases of the TSAM analyses applied to all models (right column) and to all models except UMUKCA.METO (left column). Again, the MMT estimates and the 95% confidence and prediction intervals, for all latitude bands, appears very similar in both cases. It is only when the MMT estimates in both cases are overlain, Fig. 9S.45, that differences become apparent. The largest difference is found in the Arctic (60°N-90°N) where the removal of UMUKCA-METO causes a reduction in the MMT estimate of 50hPa Cly. While this seems significant, the impact on return dates remains within the confidence intervals of the original TSAM analysis (Fig. 9S.46). This suggests that, for the CCMVal-2 model set, predictions based on the TSAM analysis are robust to the removal of one of the largest model outliers.

The sensitivity experiments in this section suggest that, for the CCMVal-2 model set, the application of prior weights based on quantitative performance metrics would not significantly alter predictions based on the TSAM analysis.

9S.3 1:2:1 Smoothing vs the TSAM Analysis

Previous studies of CCMVal-1 time series determined smooth trends in the data by employing a simple 1:2:1 filter [WMO 2007, Eyring et al. 2007]. As described in Chapter 9, the TSAM

analysis is based on a statistical framework employing a nonparametric additive model to determine smooth IMT and MMT estimates from the time series. In addition to the ability to make formal inference (e.g. calculation of confidence and prediction intervals), it was suggested that the TSAM analysis was also advantageous because it allowed the formulation of MMT estimates for the full REF2 period from model time series data that sampled only portions of this period. While this is critical for the analysis of the CCMVal-1 time series data, it is less critical for the CCMVal-2 time series data as nearly all models in CCMVal-2 provided time series than spanned the full range of 1960-2099. Given a sufficient number of models, the expectation is that a straight multi-model average of the time series should produce a MMT estimate that is very close to the TSAM MMT estimate. Here we investigate this question for the CCMVal-2 model set employing 1:2:1 filtering of individual model time series in the derivation of the multi-model average.

There were two issues which complicated the application of a straight multi-model average of the CCMVal-2 REF-B2 time series. Two of the thirteen models did not provide time series for the full REF-B2 period of 1960-2099. GEOSCCM provided only 2000-2099 and UMUKCA-METO provided 1960-2084. For the case of the GEOSCCM, in Chapter 9, the data from the REF-B1 experiment spanning 1960-2004 was included in the TSAM analysis to have GEOSCCM data cover the complete REF-B2 period. The GEOSCCM REF-B1 and REF-B2 time series are not really ensemble members as they overlap only over the range 2000-2004. Here it was decided to average the two over the this range to produce one time series which spanned 1960-2099. While this produced small kinks in the GEOSCCM time series at 2000 and 2004, it was found not to cause kinks in the multi-model average time series.

For the case of UMUKCA-METO, its sudden termination at 2084 causes a kink in a straight multi-model average as the equal weights of 1/13 for each model switch suddenly to 1/12 at this point. In the end it was decided to use the prior weighting that produced quadratic tapering towards the ends of the time series that was introduced in Section 9A.4 of the appendix to Chapter 9 (equations 9.20 and 9.21). A multi-model average of time series which span the entire period would not be affected by the introduction of the quadratic tapering. Only models that do not span the entire period would see their contribution to the multi-model mean diminish towards the ends of their time series. As in the TSAM analysis, this proved to be very effective at eliminating discontinuities in the multi-model trend estimate.

In Fig. 9S.47 the IMT estimates of column ozone in 5 latitude bands derived from a 1:2:1 filter applied 30 times to each model time series (left) is compared to the IMT estimates derived from the TSAM analysis (right). The MMT estimates for each approach is displayed in this figure and Fig. 9S.48. While the IMT estimates derived from the TSAM approach are much smoother than those derived using 1:2:1 filtering, the MMT estimates appear nearly identical for each approach. This is further verified in Fig. 9S.49 where a comparison of total column ozone 1980 return dates for each method is presented. The MMT return dates derived from 1:2:1 filtered model time series are essentially identical to those derived from the TSAM approach. The IMT return dates generally display a larger spread for the 1:2:1 filtering since these are less smooth than the IMT estimates produced by the TSAM approach (Fig. 9S.47). Similar conclusions apply to the analysis of 50hPa Cly which is presented in Figs. 9S.50-9S.52.

The conclusion here is that, for the CCMVal-2 data set, multi-model averaged time series

produced from 1:2:1 filtered individual model time series are consistent with the MMT estimate of the more sophisticated TSAM analysis. However, the use of 1:2:1 filtering does not provide confidence and prediction intervals for the multi-model average as it is not based on a statistical model. The use of 1:2:1 filtering to investigate IMT estimates is less robust as the 1:2:1 filter leaves significant structure in the individual model time series compared to the IMT estimates of the TSAM approach.

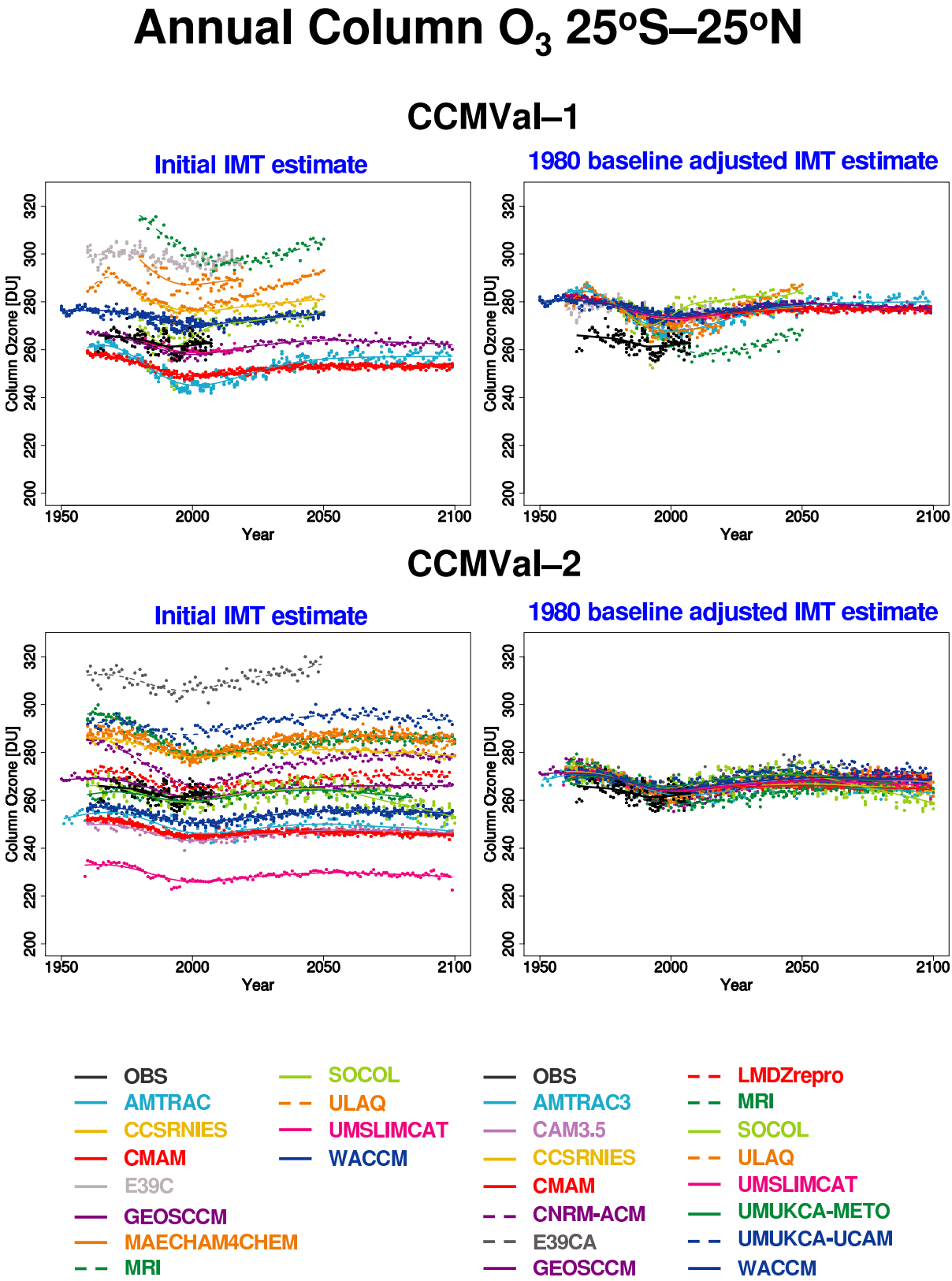

Figure 9S.1: Raw time series data of annually averaged Column O_3 (25°S-25°N) and initial individual model trend (IMT) estimates (left-hand panels), and 1980 baseline-adjusted time series data and IMT estimates (right-hand panels) for the TSAM analysis of CCMVal-1 (top) and CCMVal-2 (bottom). Observation data (black) and lowess fit (with smoother span f=0.4) to the observations appears as a black line in all panels.

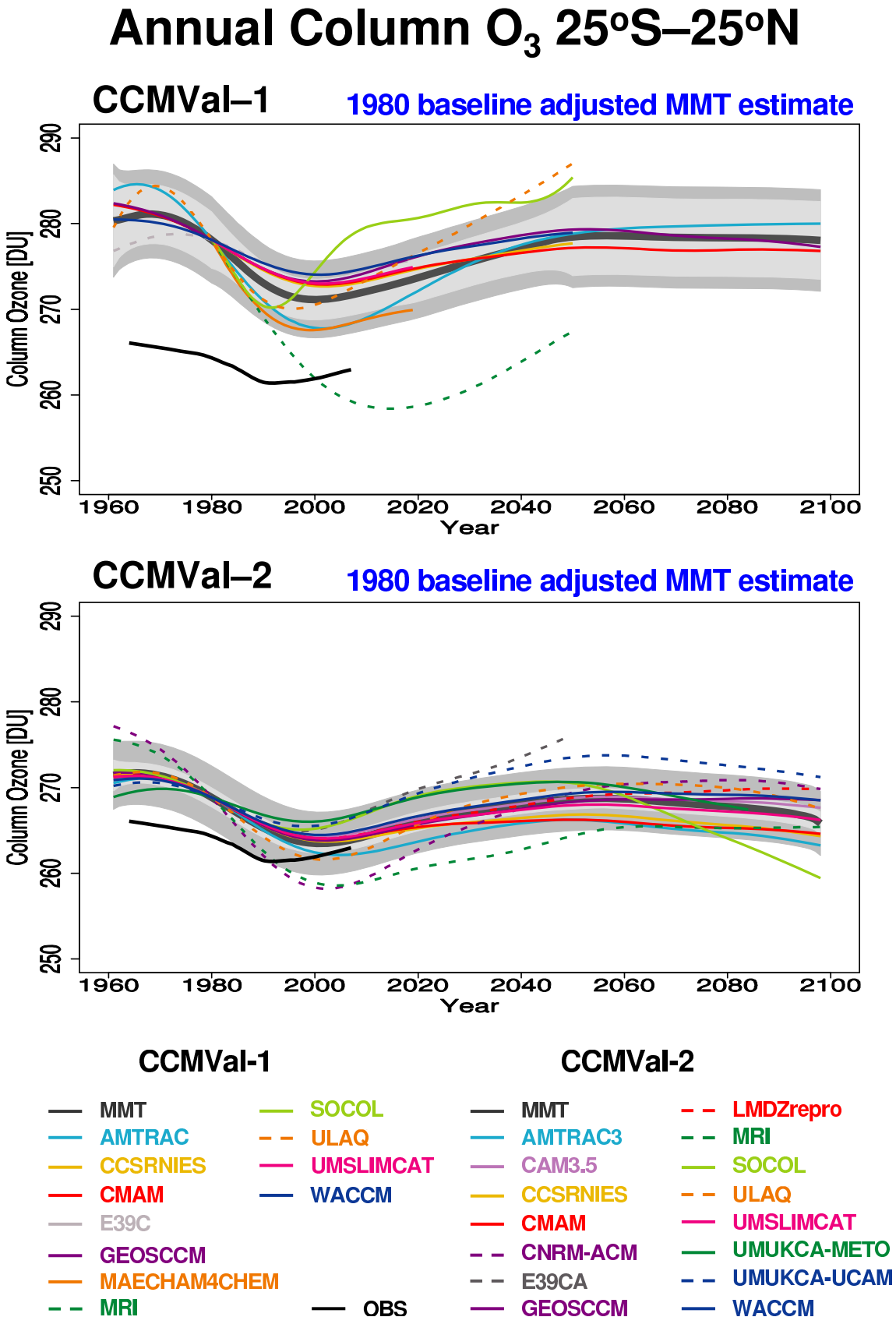

Figure 9S.2: 1980 baseline-adjusted multi-model trend (MMT) estimates of annually averaged Column O_3 (25°S-25°N) (heavy dark grey line) with 95% confidence and 95% prediction intervals appearing as light- and dark-grey shaded regions about the trend. The 1980 baseline-adjusted IMT estimates, and unadjusted lowess fit to the observations are additionally plotted. CCMVal-1 results appear in the upper panel and CCMVal-2 results appear in the lower panel.

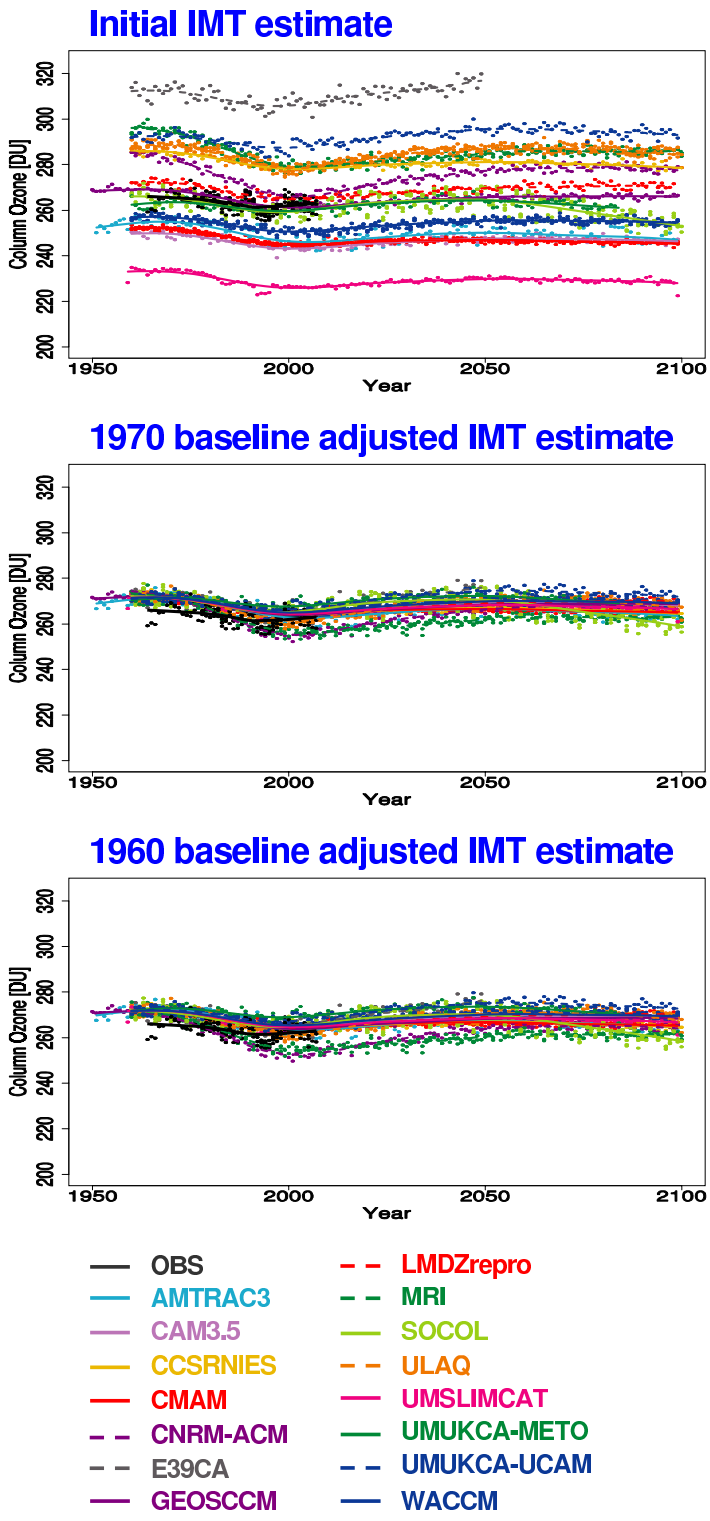

Figure 9S.3: Raw time series data of annually averaged Column O_3 (25°S-25°N) and initial IMT estimates (top panel), and 1970 (middle panel) and 1960 (bottom panel) baseline-adjusted time series data and baseline-adjusted IMT estimates for the TSAM analysis of CCMVal-2. Following Fig. 9S.1 a lowess fit to the observations appears as a black line in all panels and the observations are not baseline-adjusted.

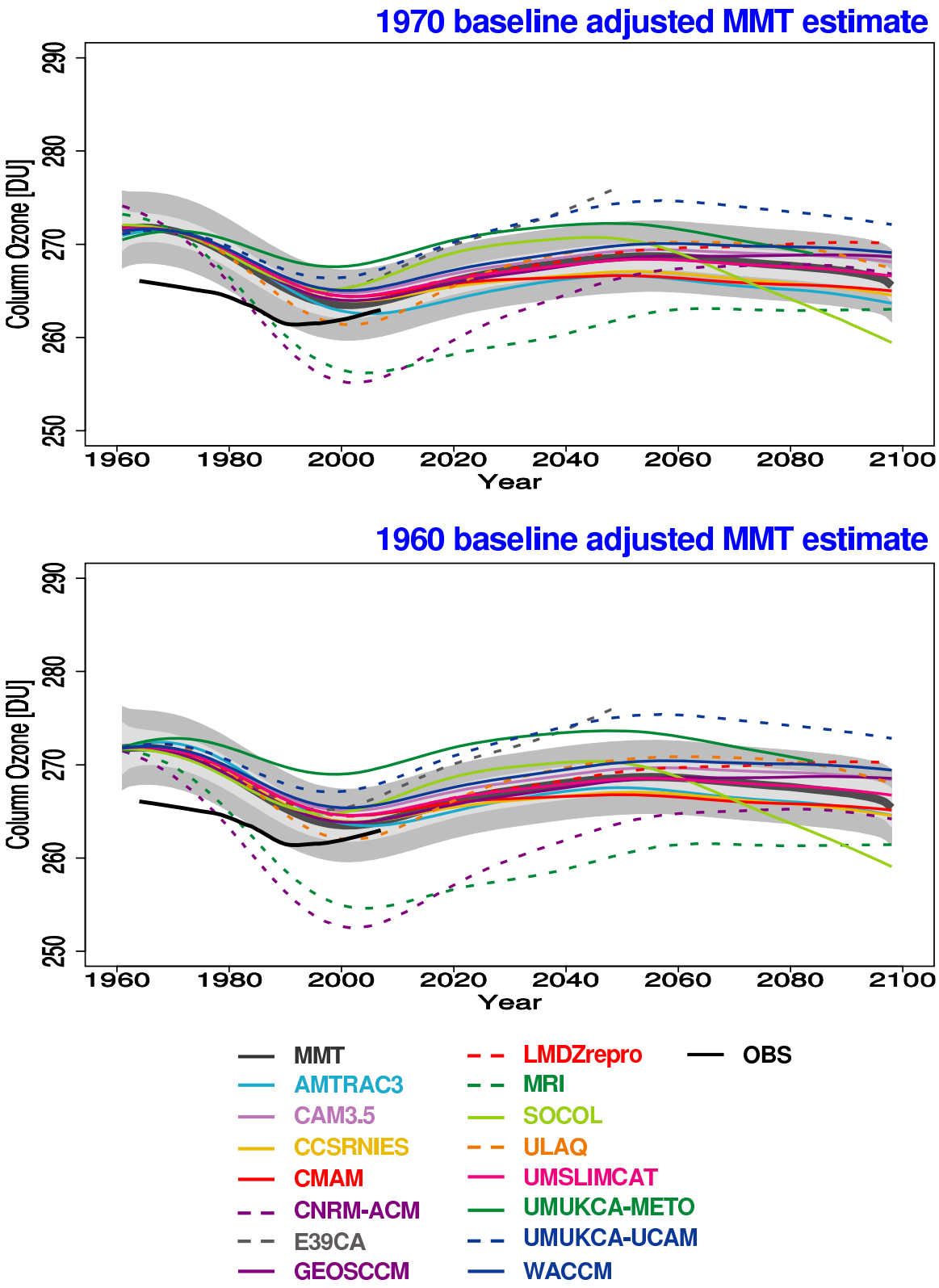

Figure 9S.4: CCMVal-2 1970 (top) and 1960 (bottom) baseline-adjusted IMT and MMT estimates of annually averaged Column O_3 (25°S-25°N) following Fig. 9S.2.

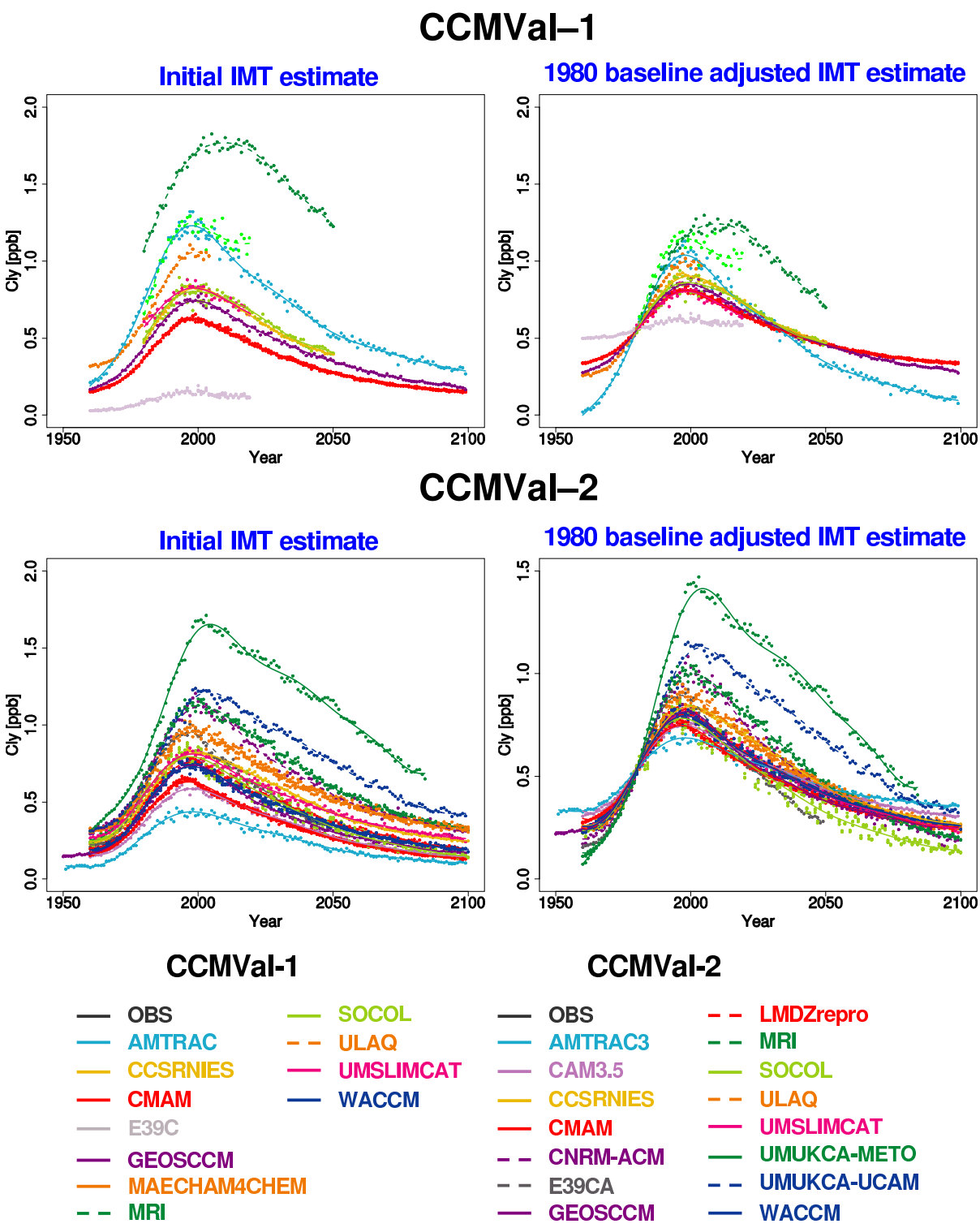

Figure 9S.5: As in Fig. 9S.1 but for 50hPa total inorganic chlorine (Cl_y) simulated by the models for the latitude range 25°S-25°N.

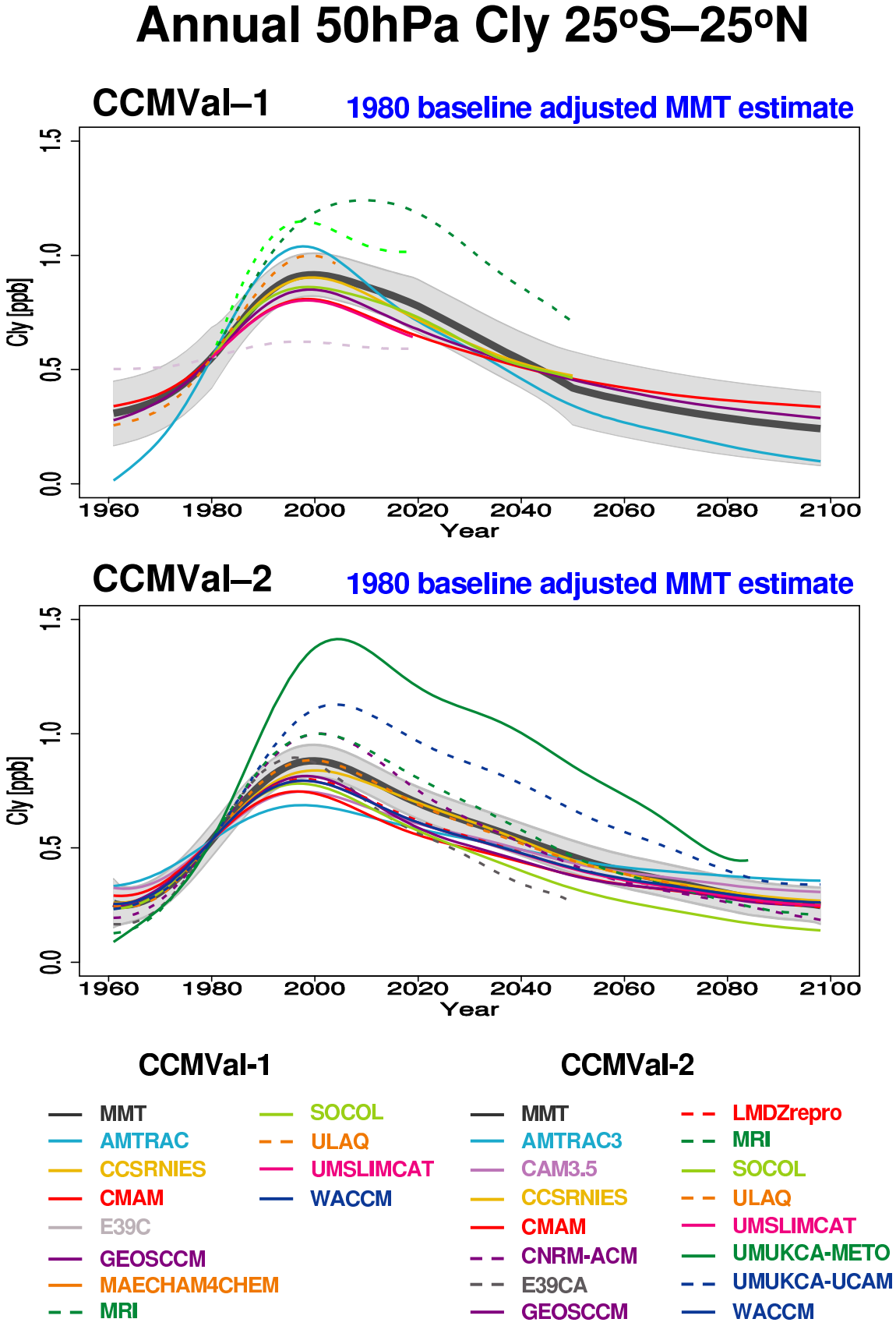

Figure 9S.6: As in Fig. 9S.2 but for 50hPa total inorganic chlorine (Cl_y) simulated by the models for the latitude range 25°S-25°N.

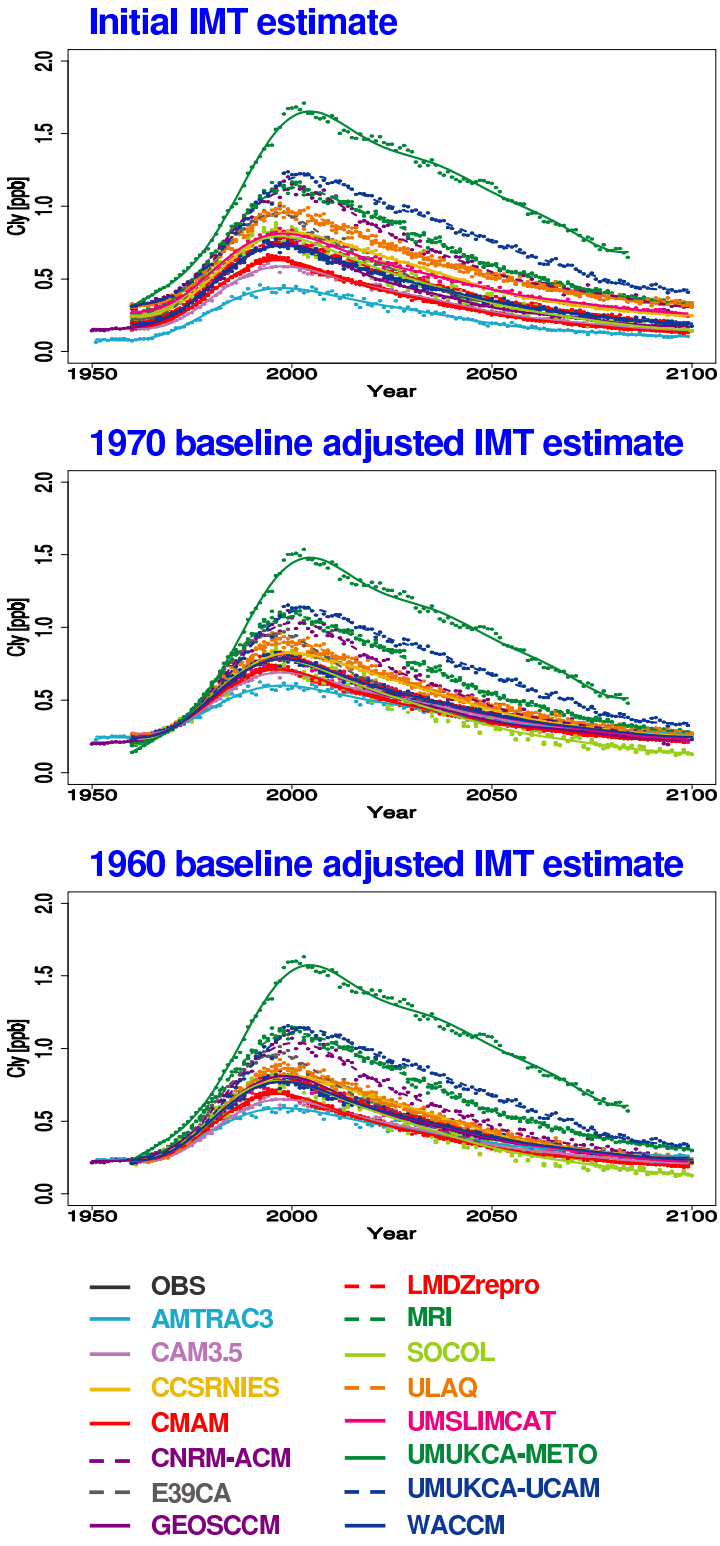

Figure 9S.7: As in Fig. 9S.3 but for 50hPa total inorganic chlorine (Cl_y) simulated by the models for the latitude range 25°S-25°N.

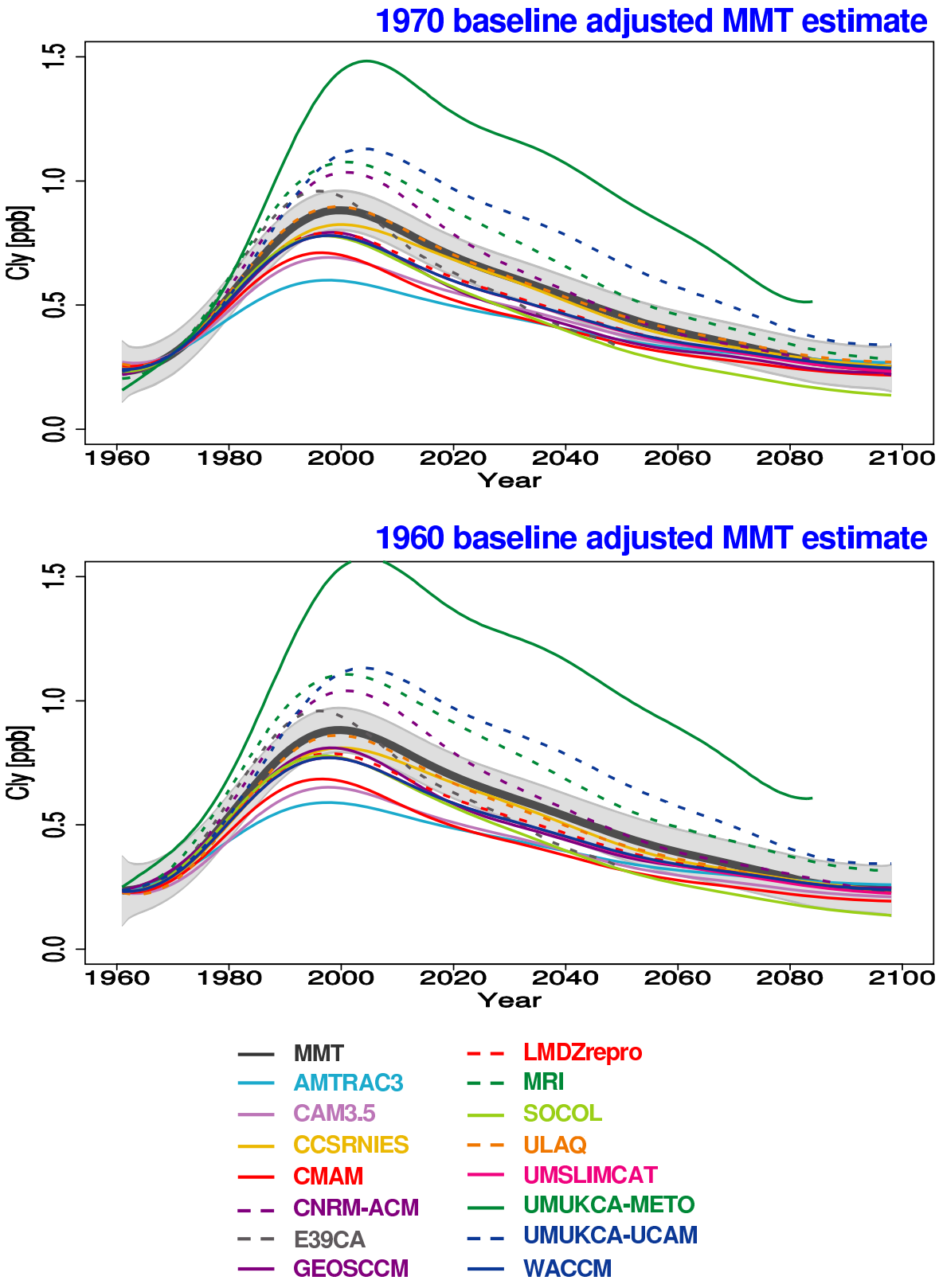

Figure 9S.8: As in Fig. 9S.4 but for 50hPa total inorganic chlorine (Cl_y) simulated by the models for the latitude range 25°S-25°N.

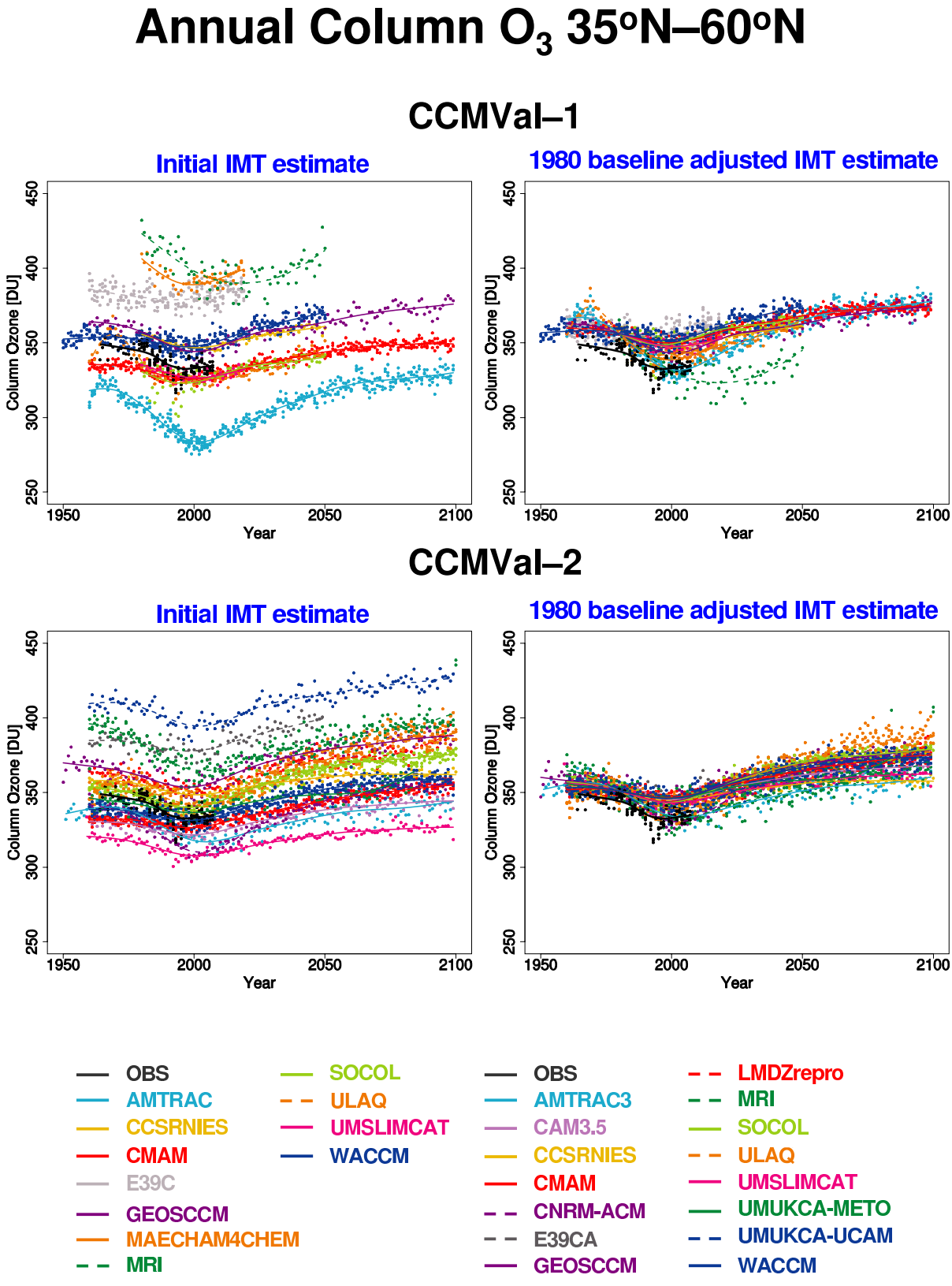

Figure 9S.9: As in Fig. 9S.1 but for the latitude range 35°N-60°N.

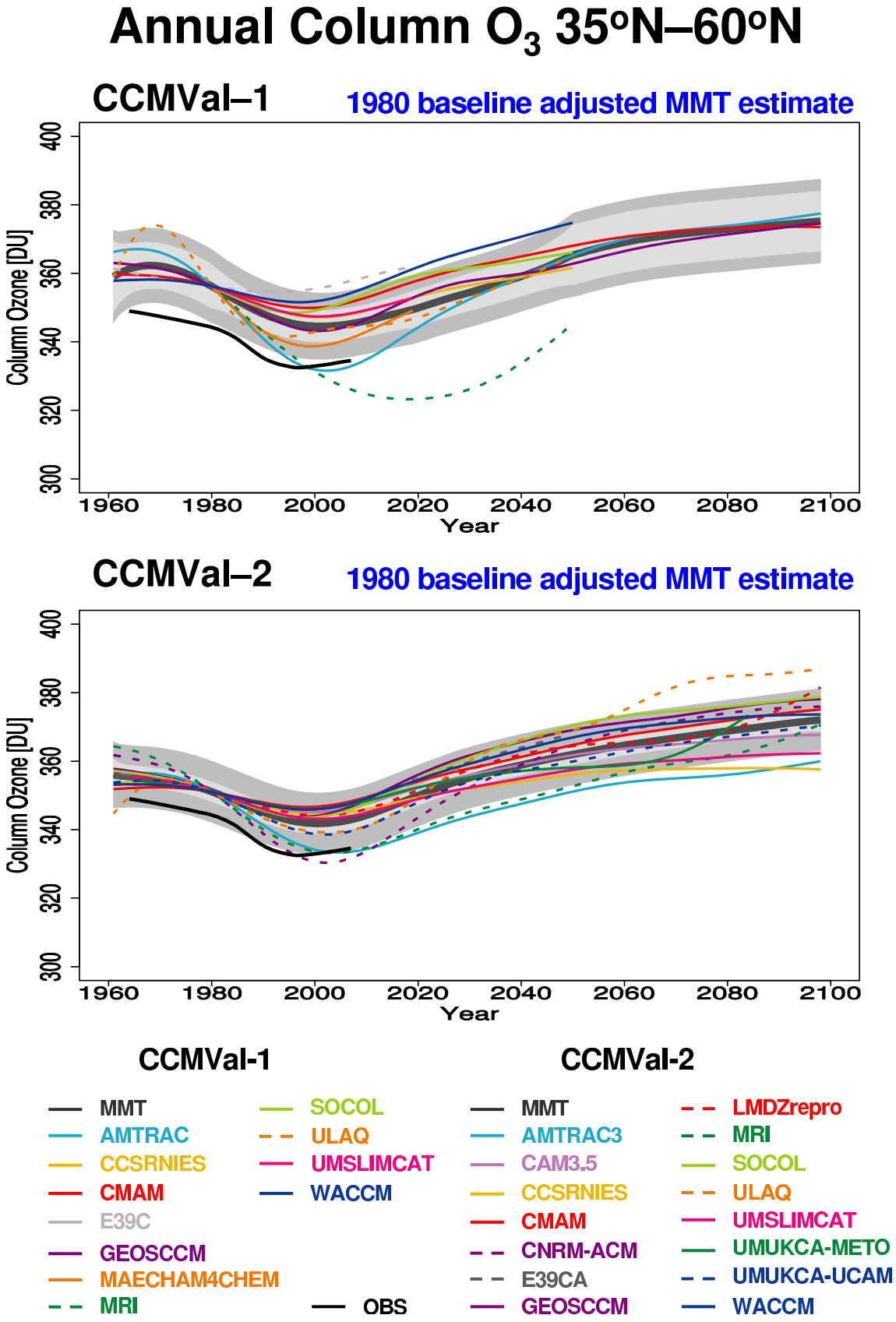

Figure 9S.10: As in Fig. 9S.2 but for the latitude range 35°N-60°N.

CCMVal-2 Annual Column O_3 35°N–60°N

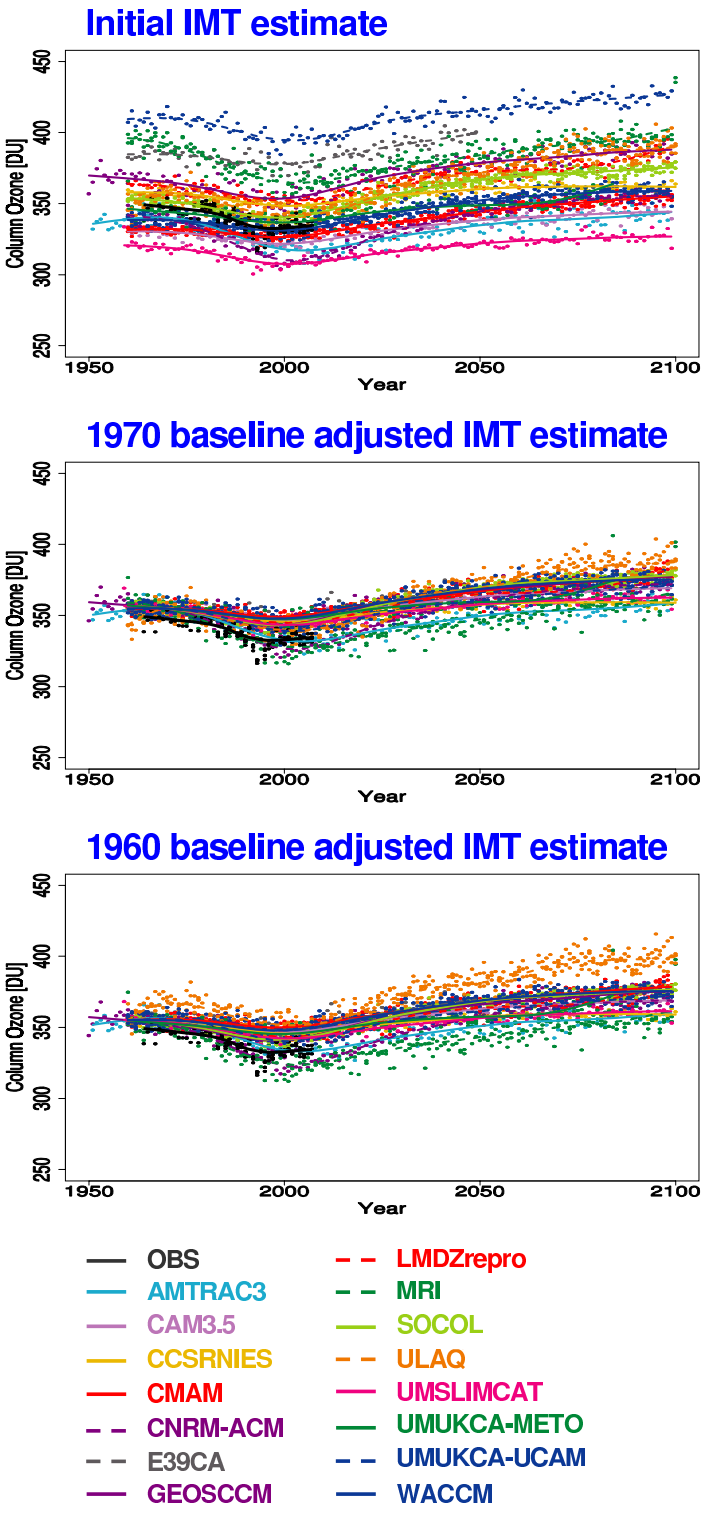

Figure 9S.11: As in Fig. 9S.3 but for the latitude range 35°N-60°N.

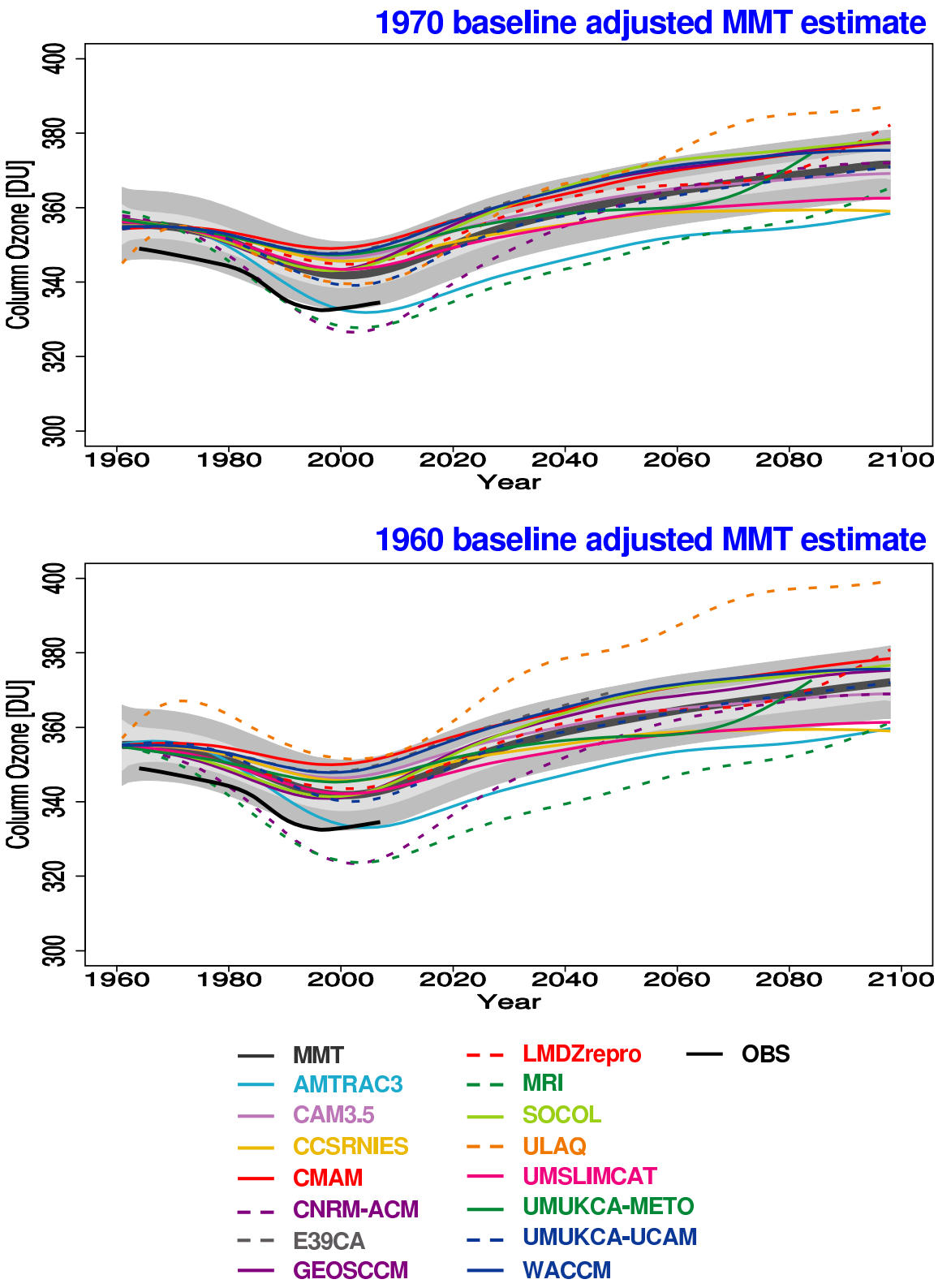

Figure 9S.12: As in Fig. 9S.4 but for the latitude range 35°N-60°N.

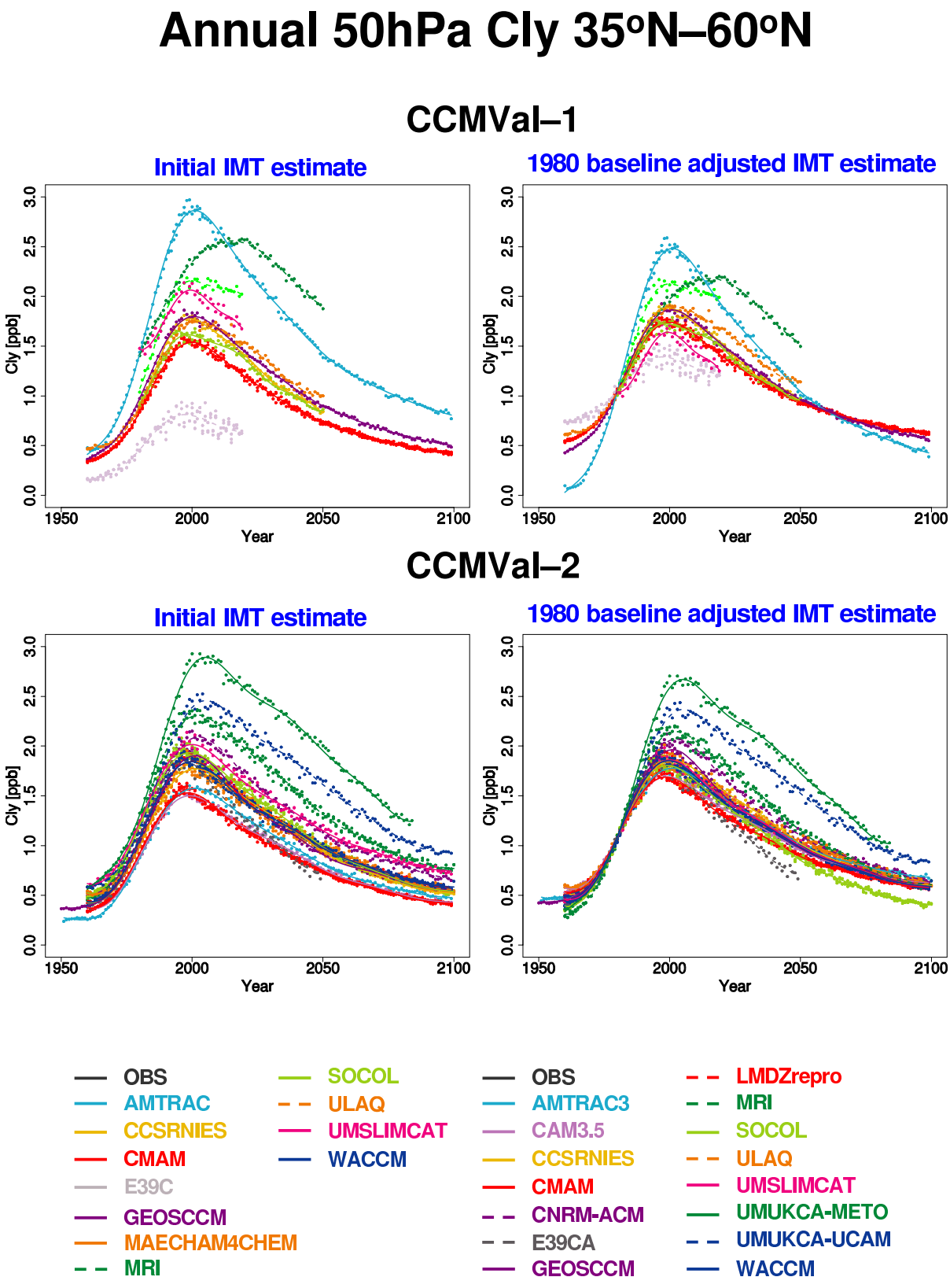

Figure 9S.13: As in Fig. 9S.5 but for the latitude range 35°N-60°N.

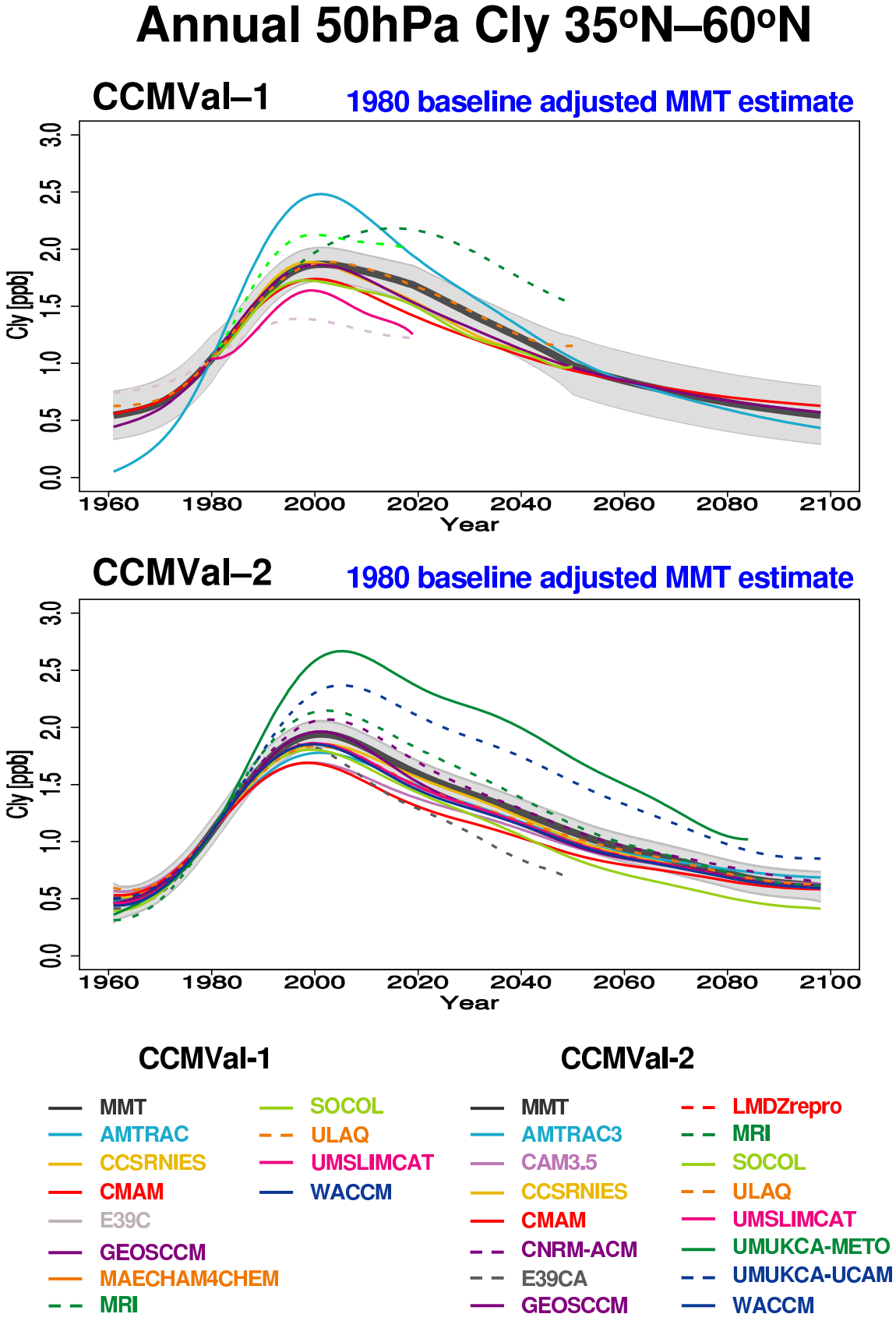

Figure 9S.14: As in Fig. 9S.6 but for the latitude range 35°N-60°N.

CCMVal-2 Annual 50hPa Cly 35°N–60°N

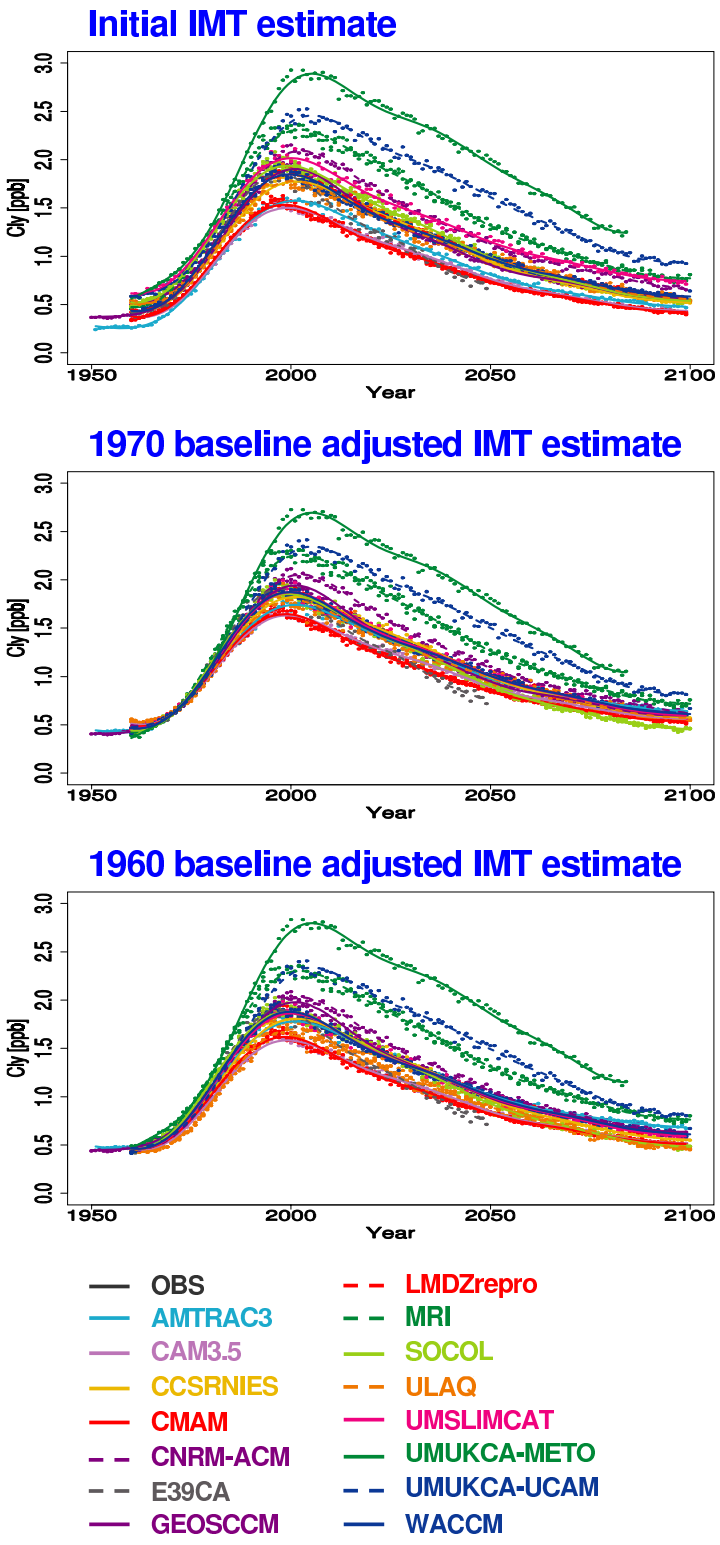

Figure 9S.15: As in Fig. 9S.7 but for the latitude range 35°N-60°N.

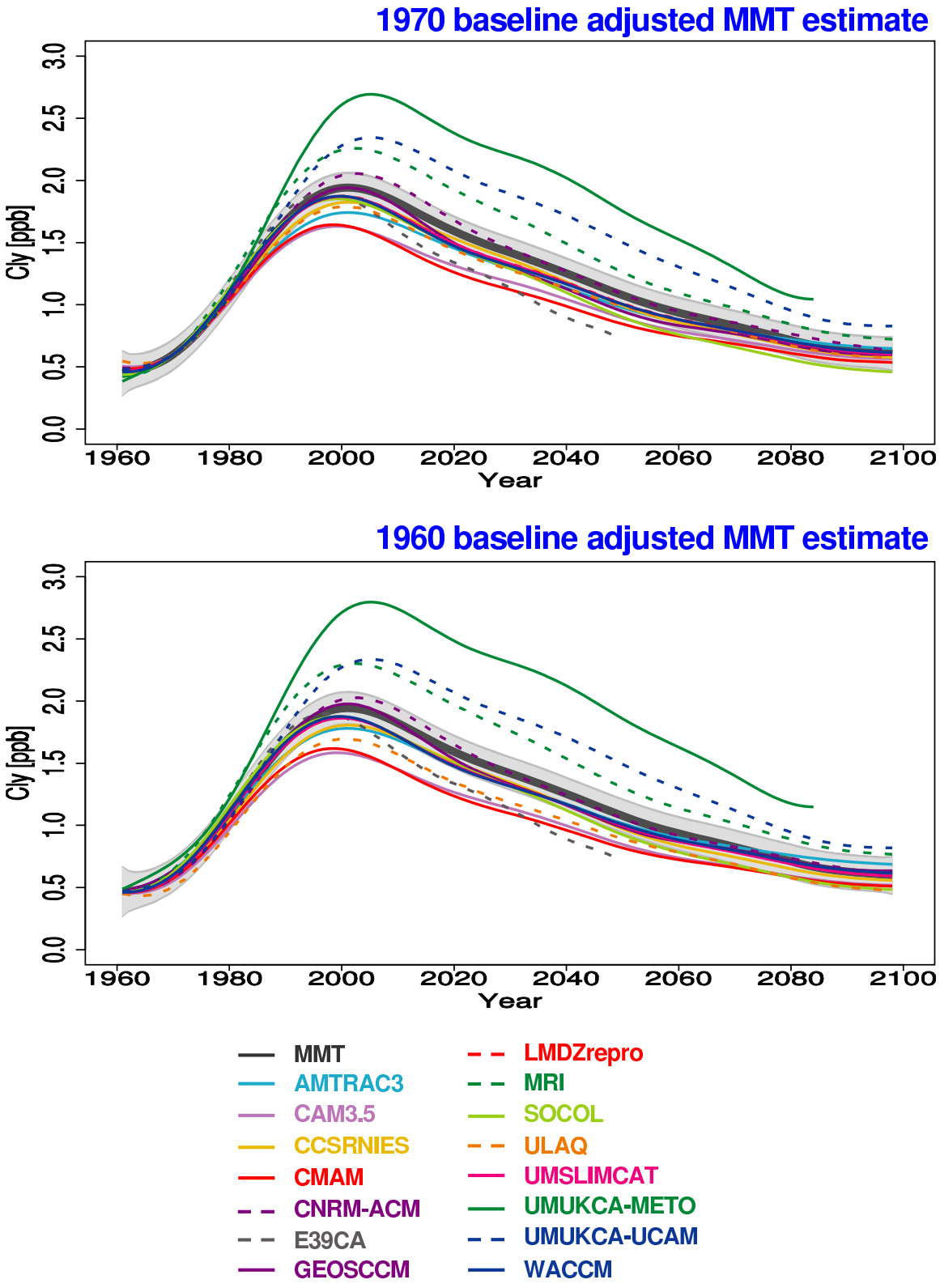

Figure 9S.16: As in Fig. 9S.8 but for the latitude range 35°N-60°N.

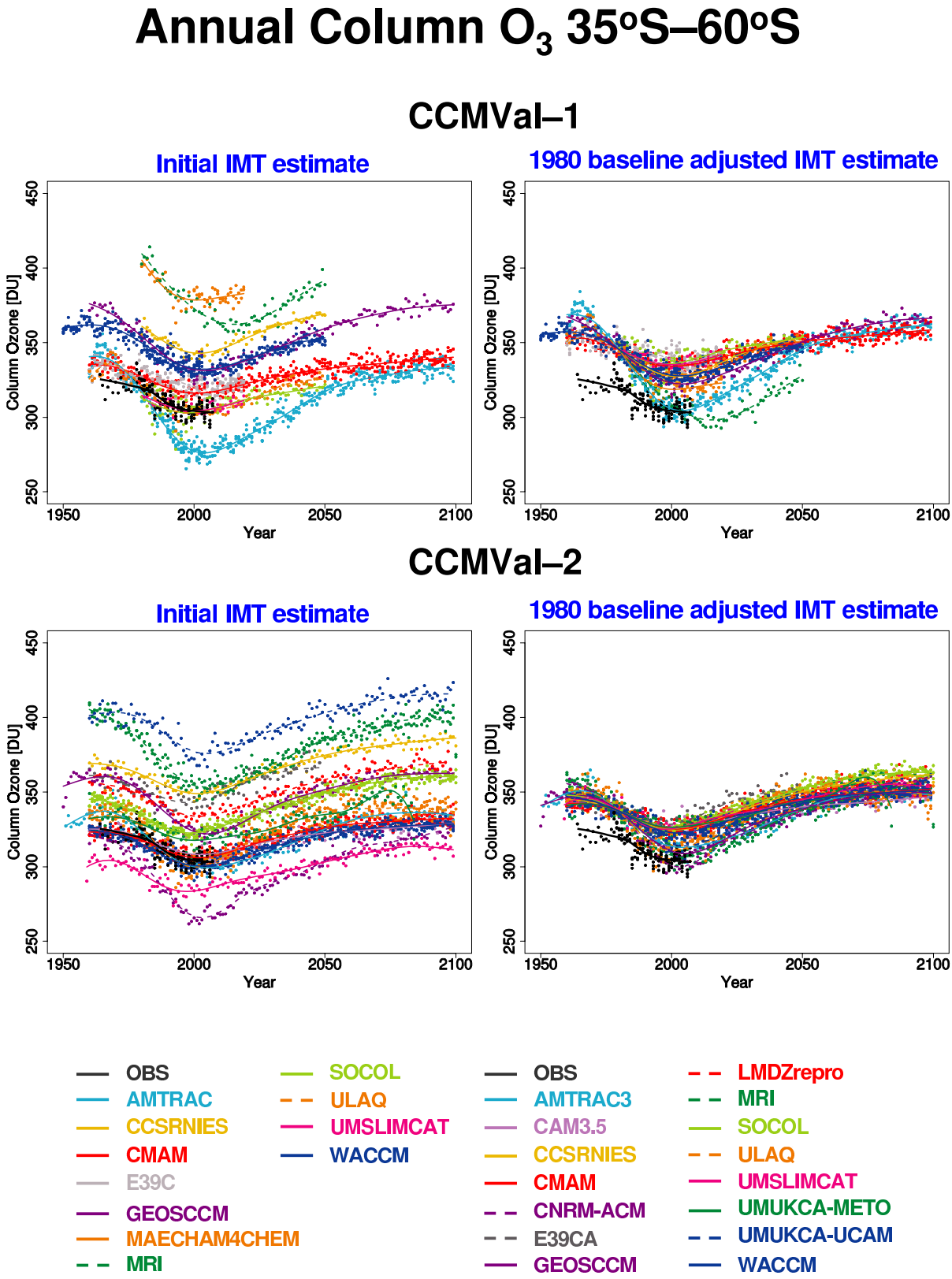

Figure 9S.17: As in Fig. 9S.1 but for the latitude range 35°S-60°S.

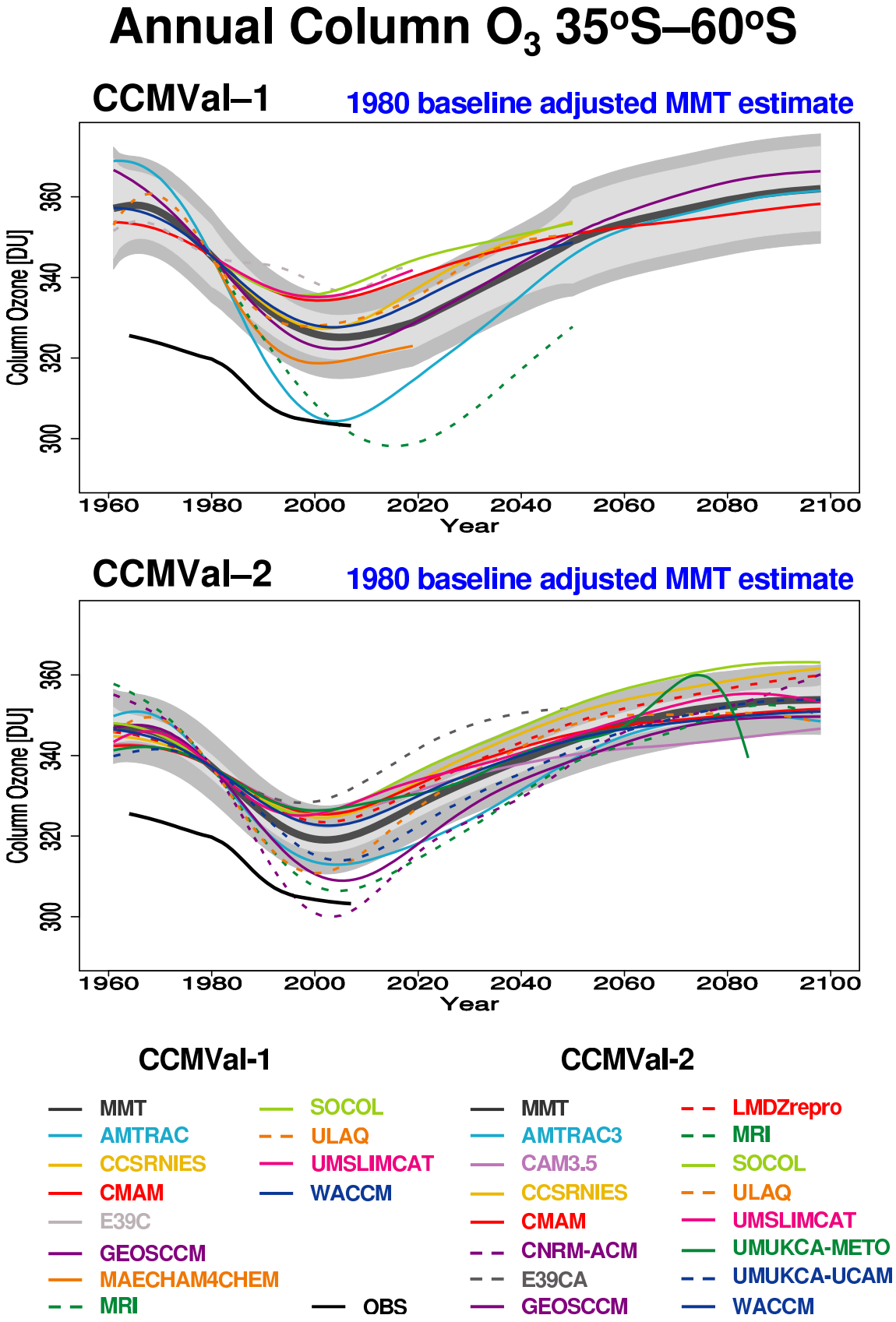

Figure 9S.18: As in Fig. 9S.2 but for the latitude range 35°S-60°S.

CCMVal-2 Annual Column O_3 35°S–60°S

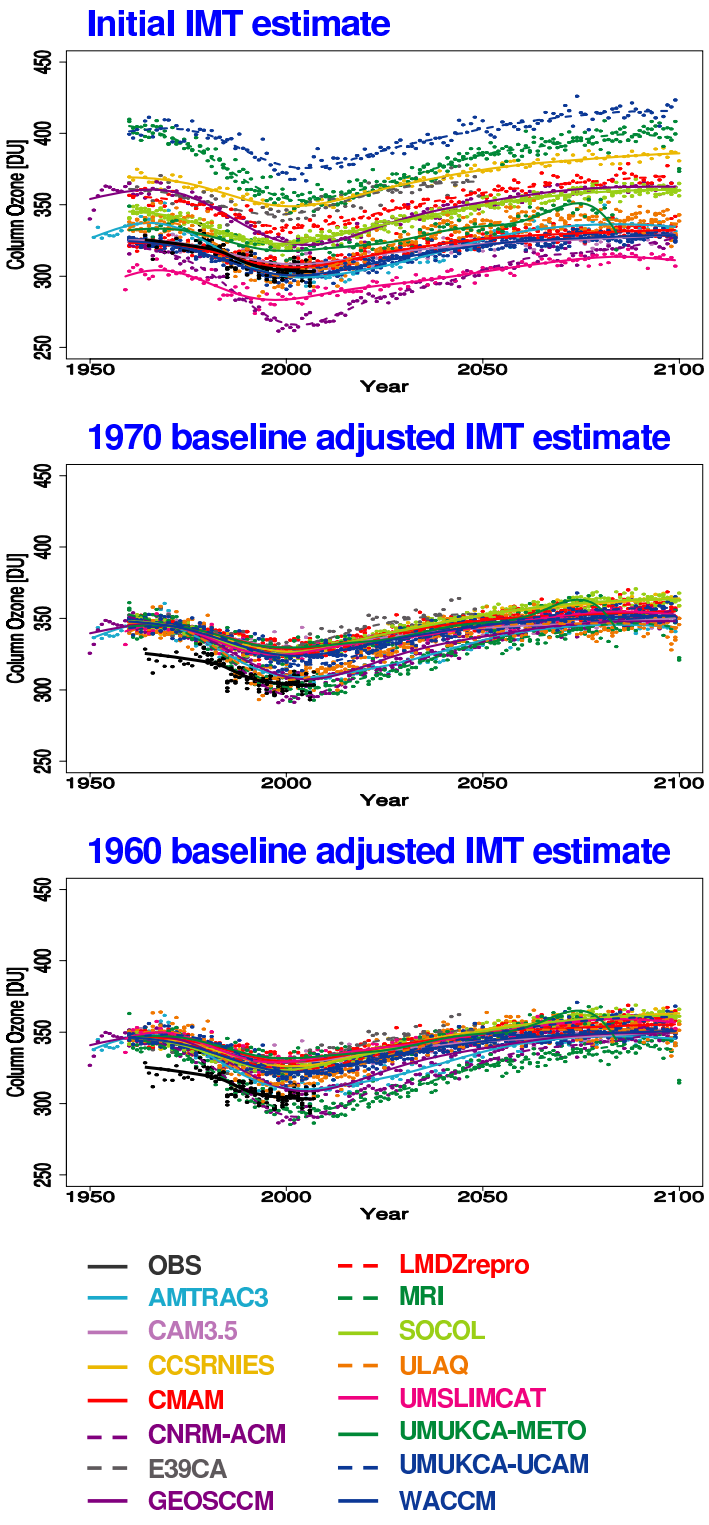

Figure 9S.19: As in Fig. 9S.3 but for the latitude range 35°S-60°S.

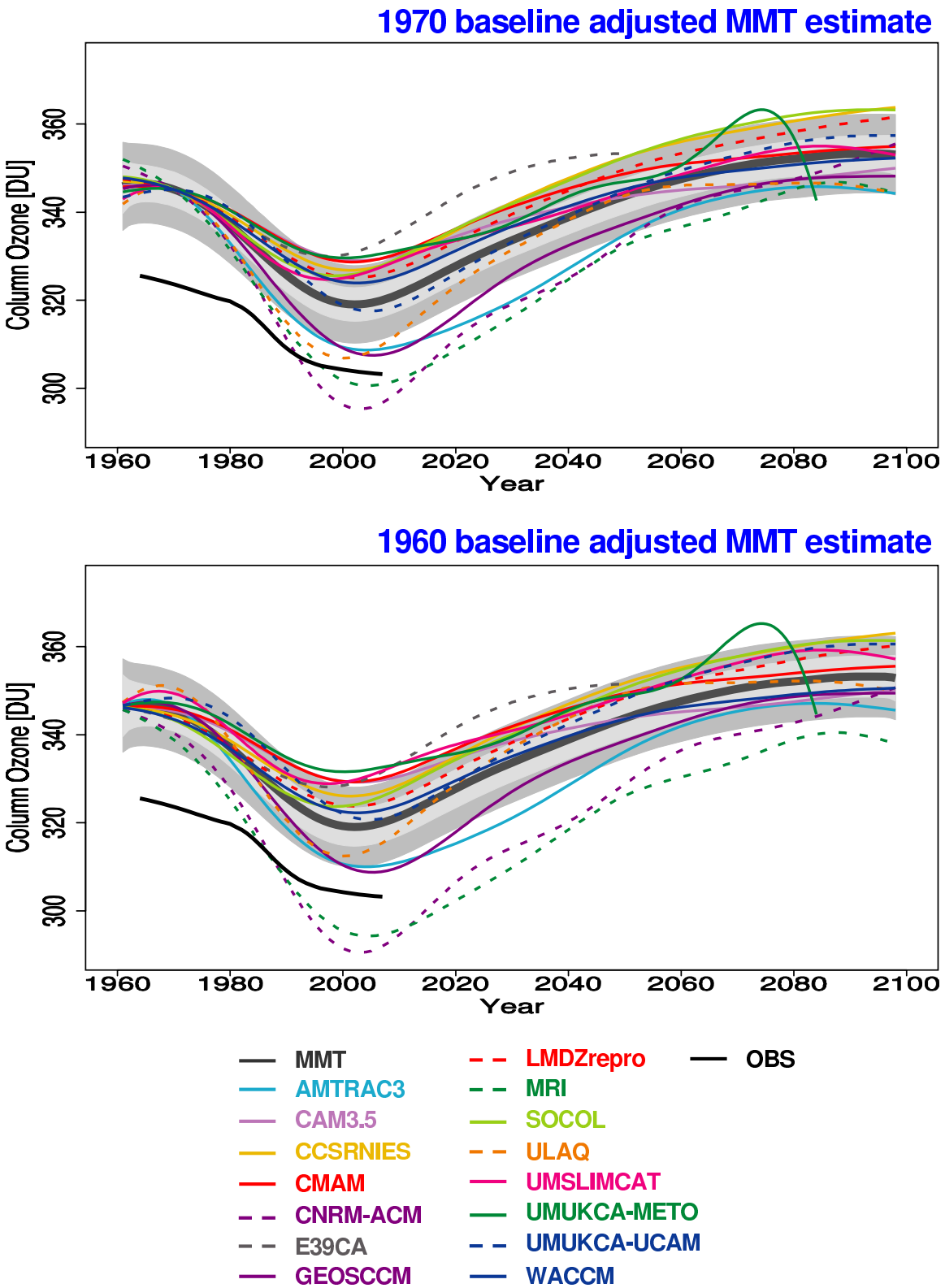

Figure 9S.20: As in Fig. 9S.4 but for the latitude range 35°S-60°S.

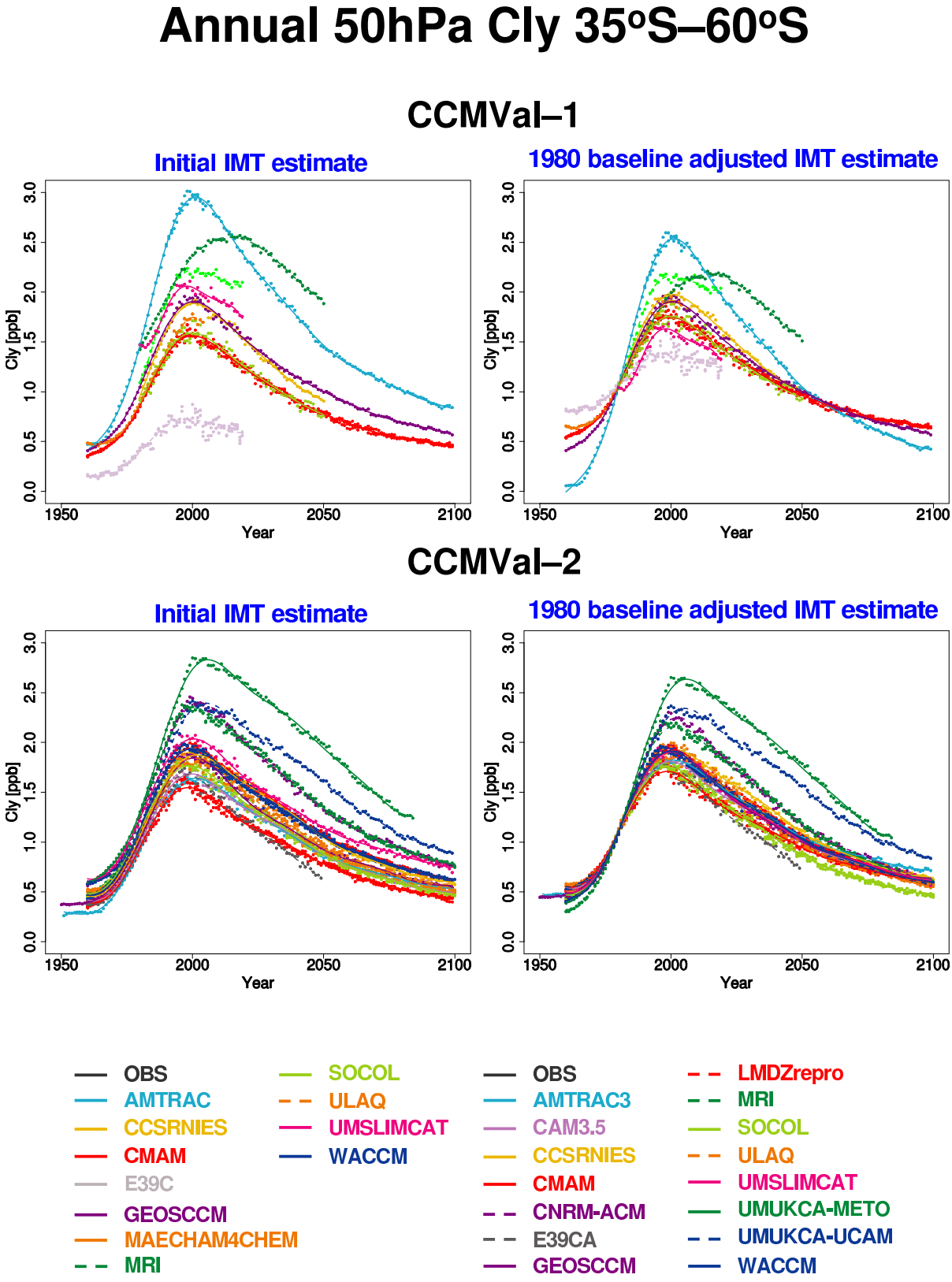

Figure 9S.21: As in Fig. 9S.5 but for the latitude range 35°S-60°S.

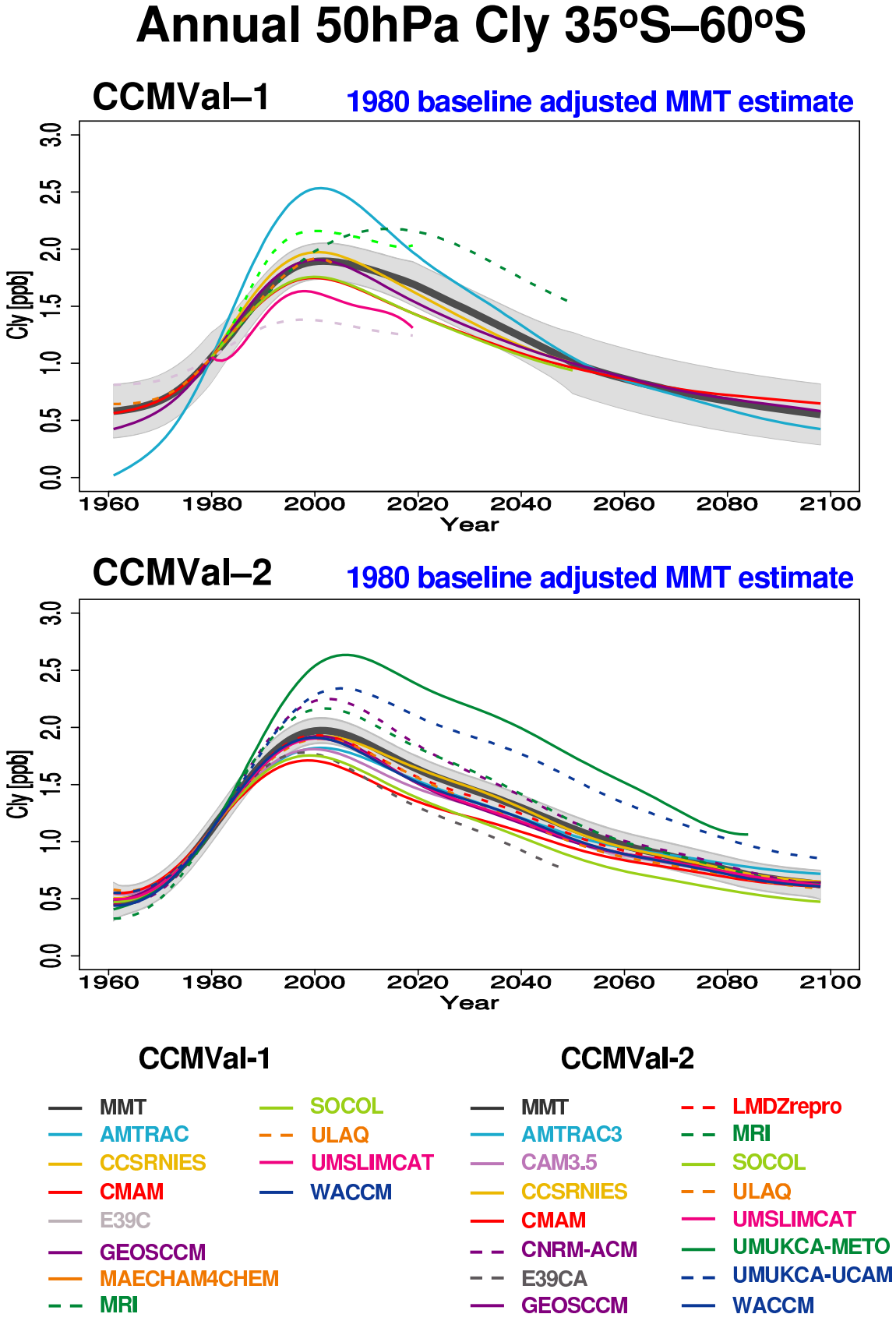

Figure 9S.22: As in Fig. 9S.6 but for the latitude range 35°S-60°S.

CCMVal-2 Annual 50hPa Cly 35°S–60°S

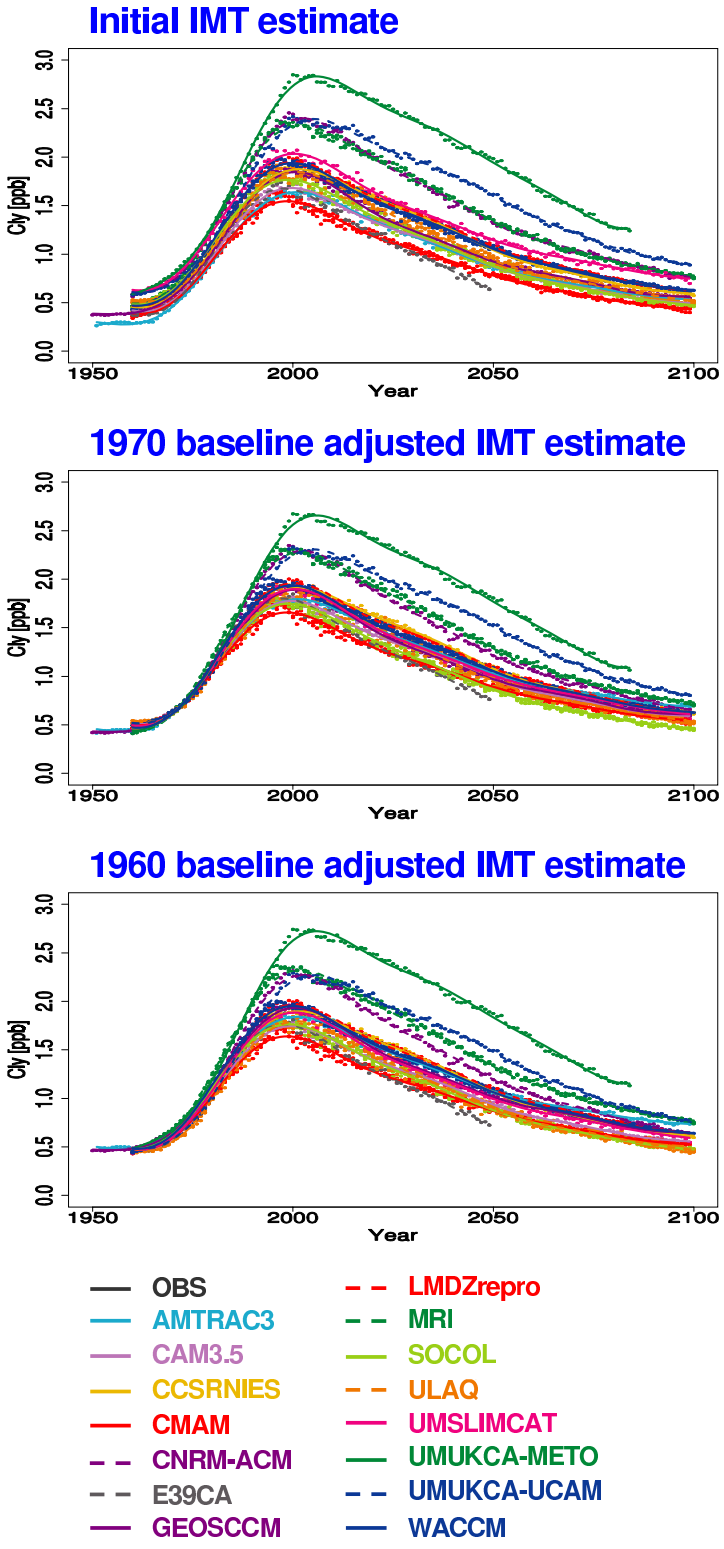

Figure 9S.23: As in Fig. 9S.7 but for the latitude range 35°S-60°S.

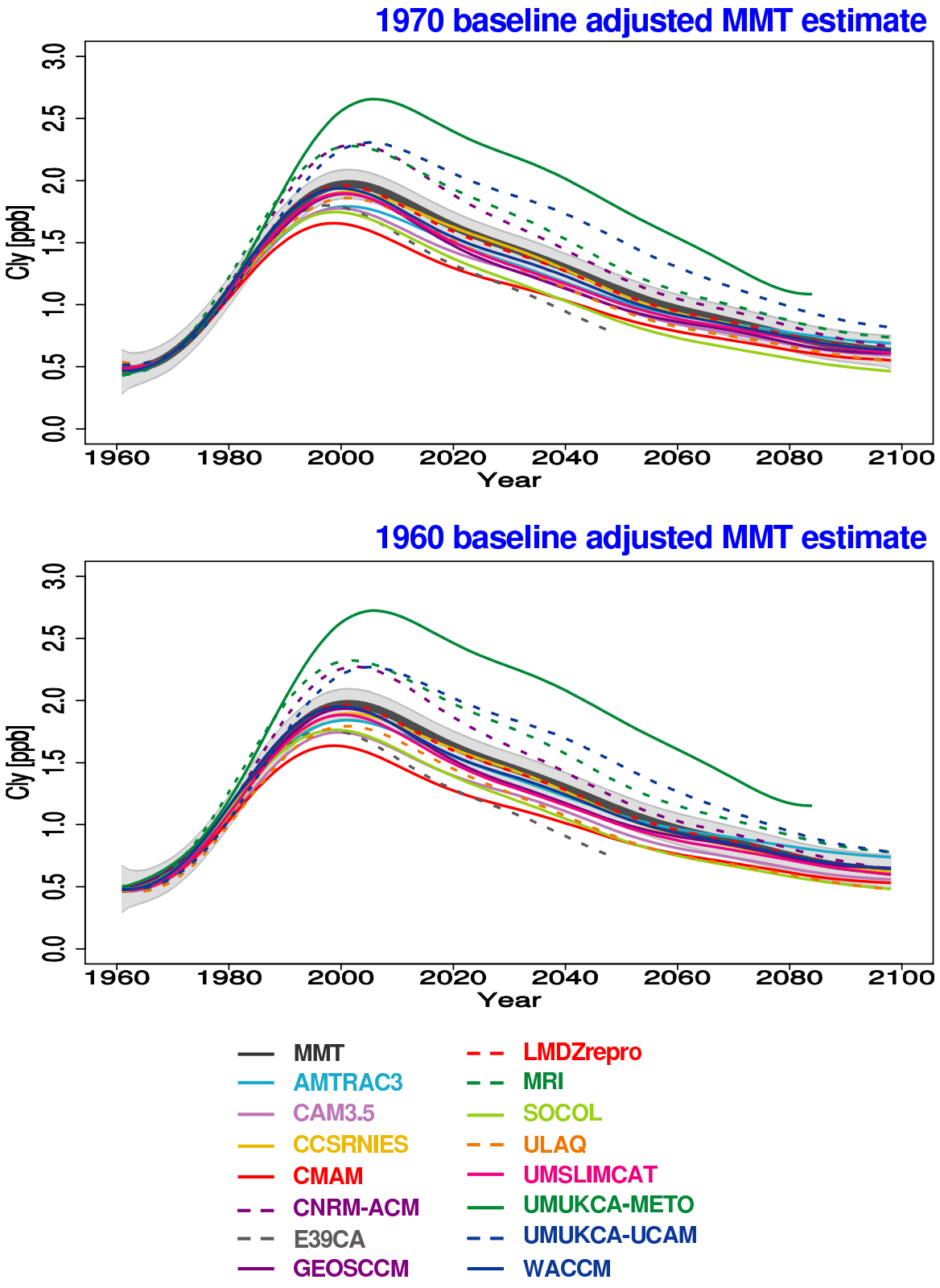

Figure 9S.24: As in Fig. 9S.8 but for the latitude range 35°S-60°S.

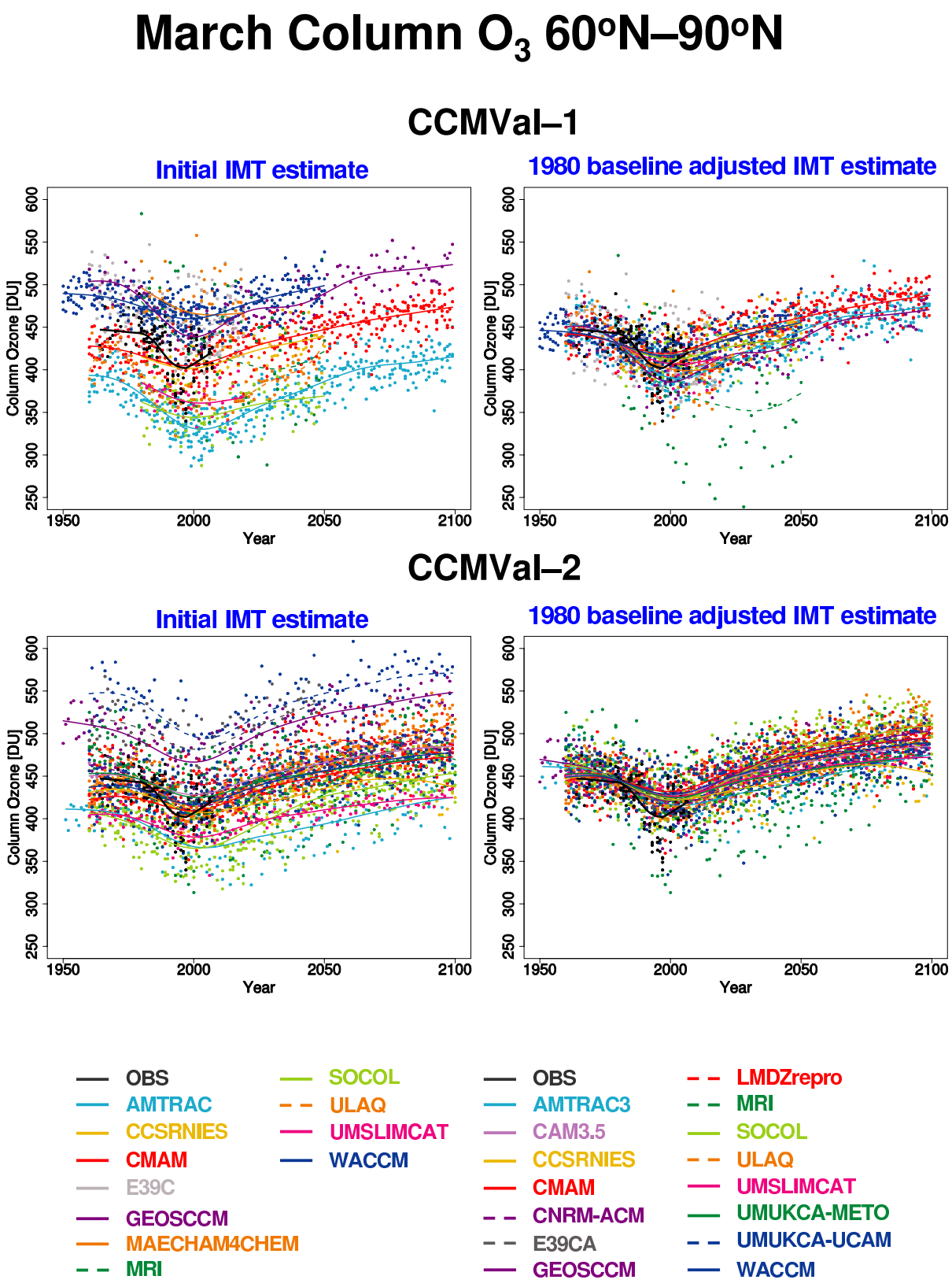

Figure 9S.25: As in Fig. 9S.1 but for the month of March and the latitude range 60°N-90°N.

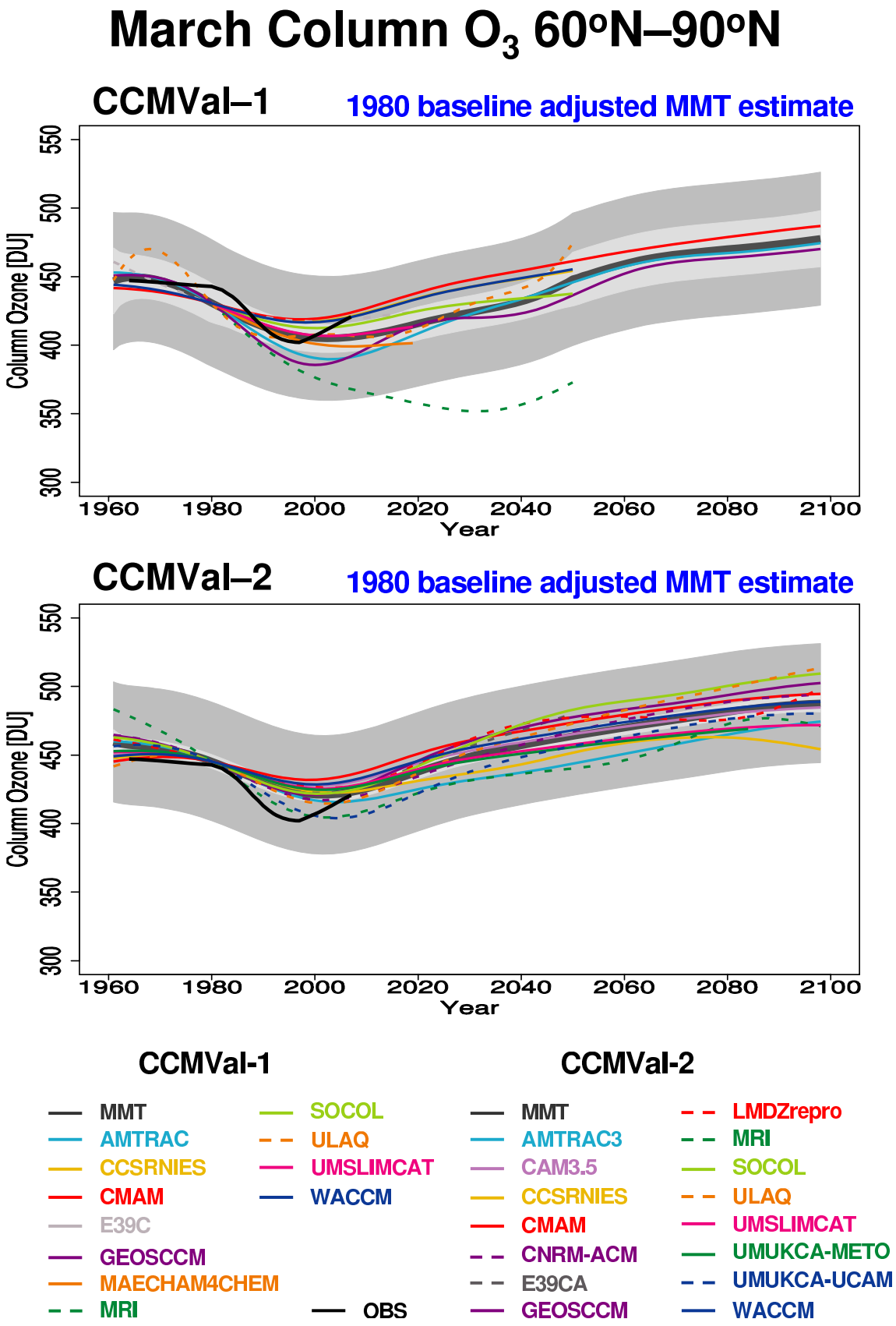

Figure 9S.26: As in Fig. 9S.2 but for the month of March and the latitude range 60°N-90°N.

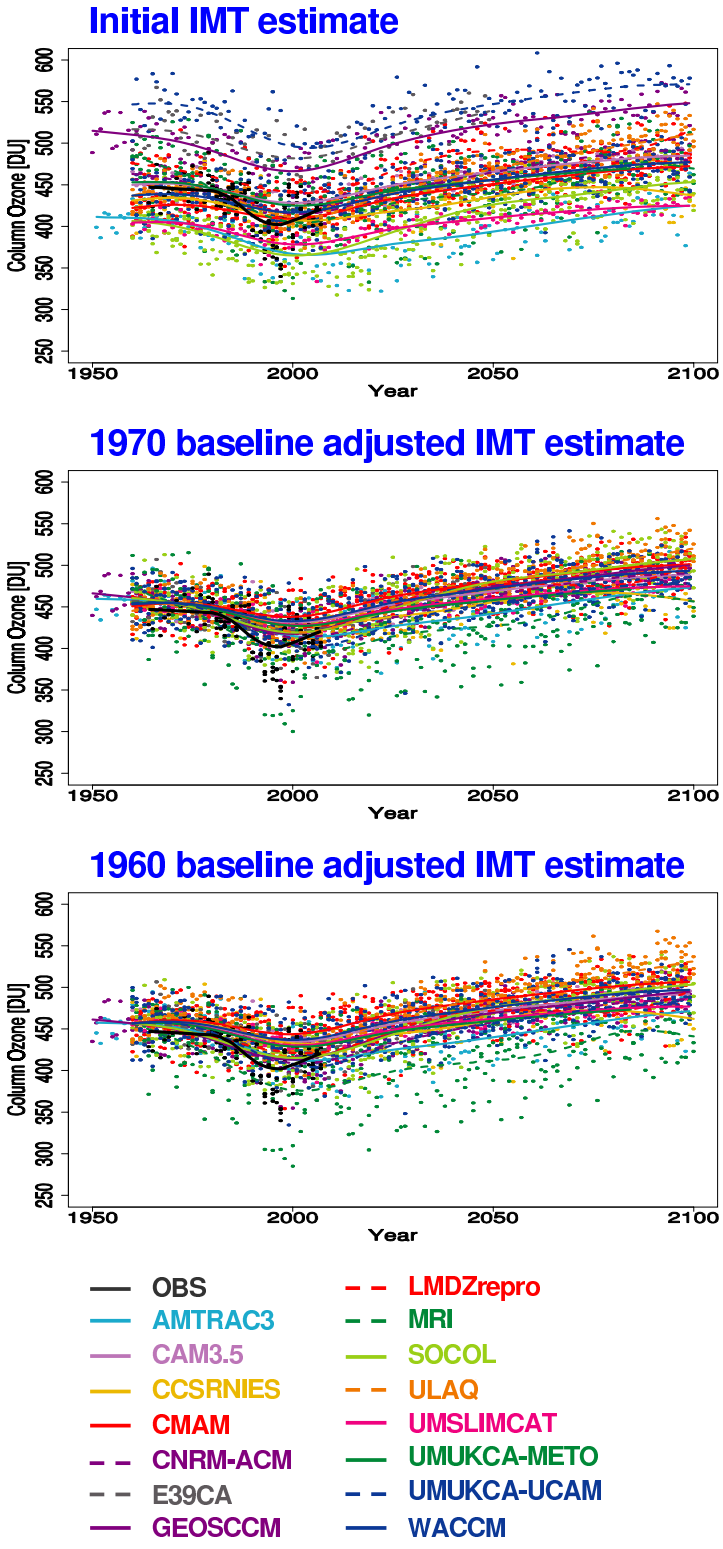

Figure 9S.27: As in Fig. 9S.3 but for the month of March and the latitude range 60°N-90°N.

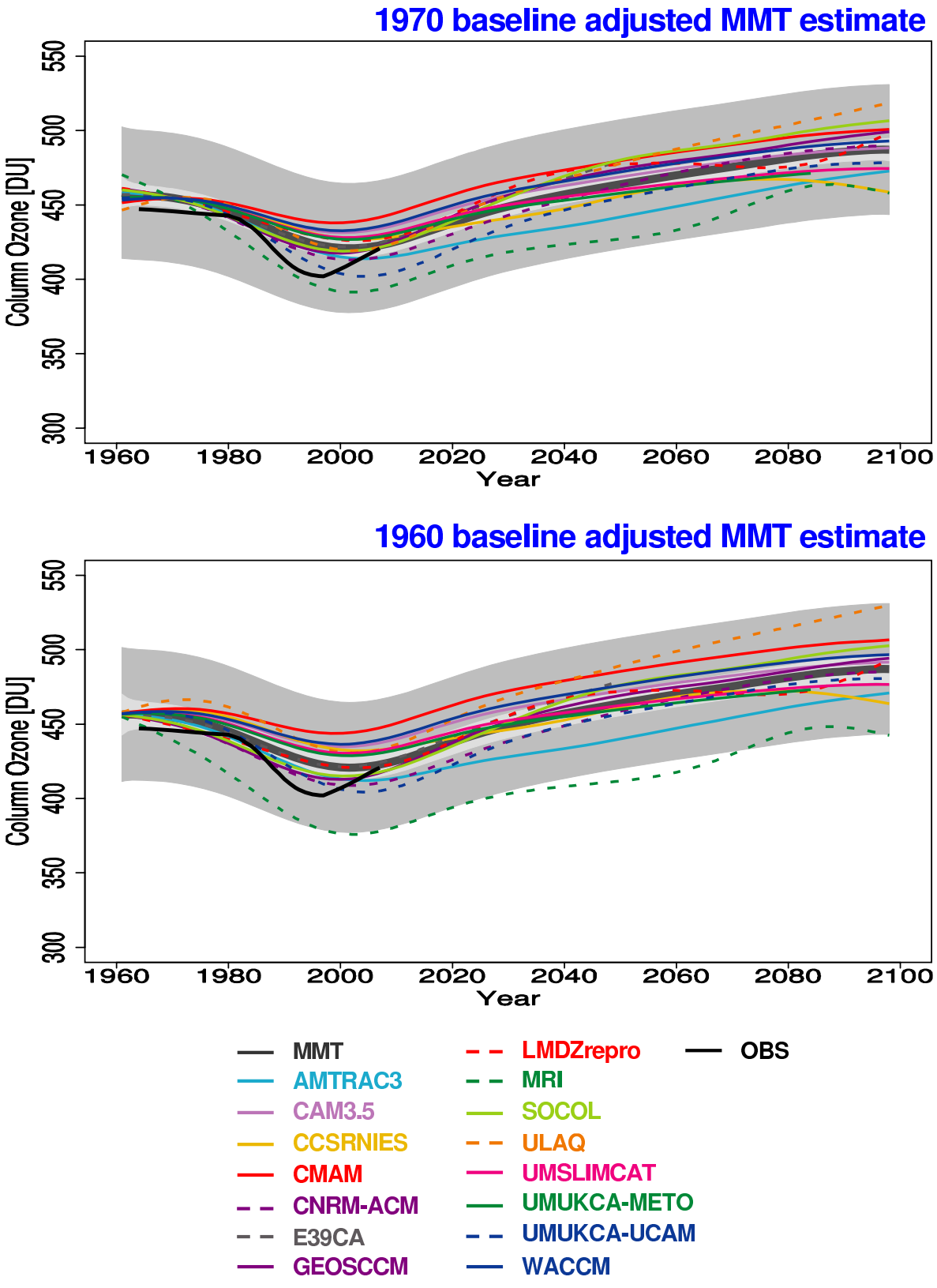

Figure 9S.28: As in Fig. 9S.4 but for the month of March and the latitude range 60°N-90°N.

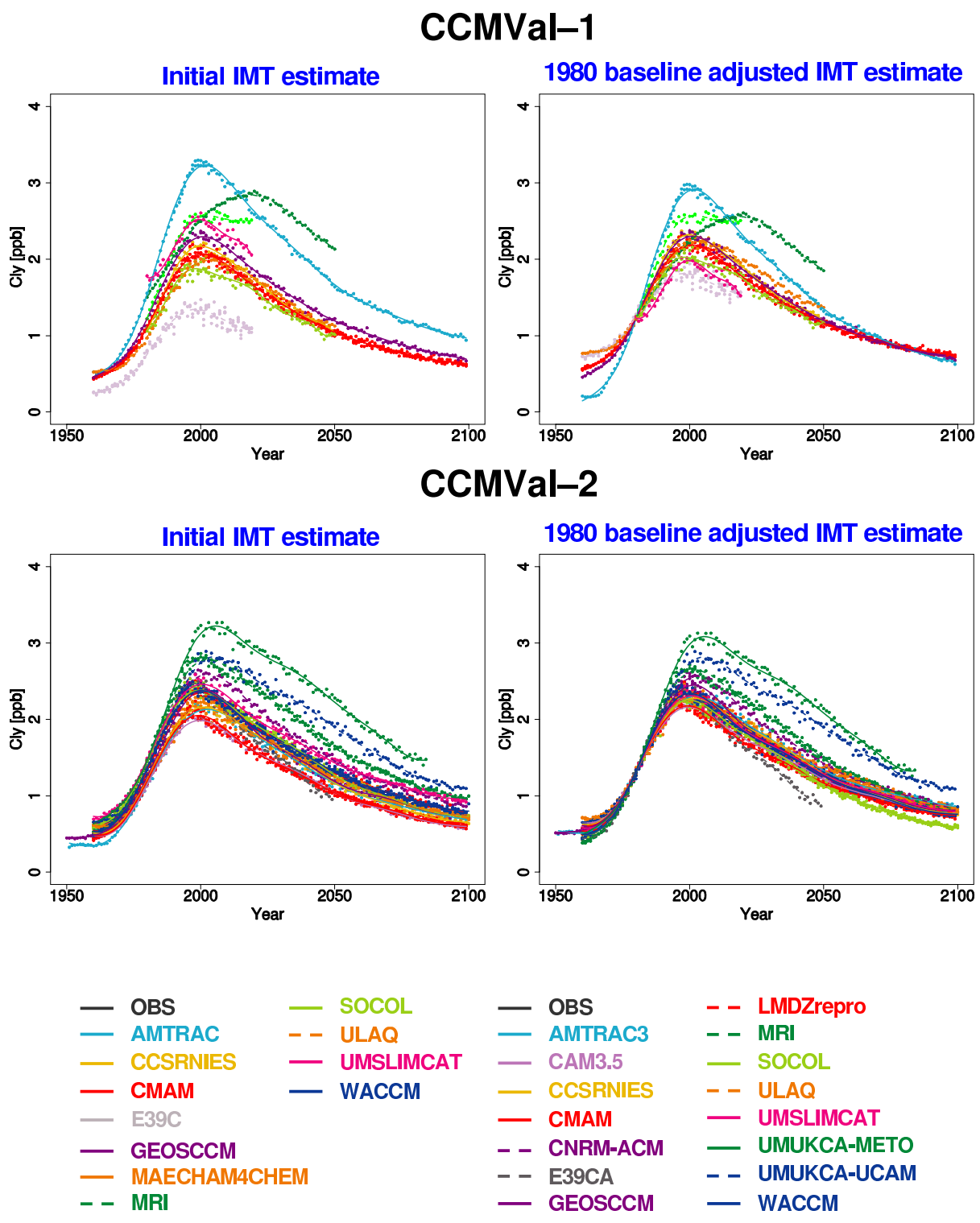

Figure 9S.29: As in Fig. 9S.5 but for the latitude range 60°N-90°N.

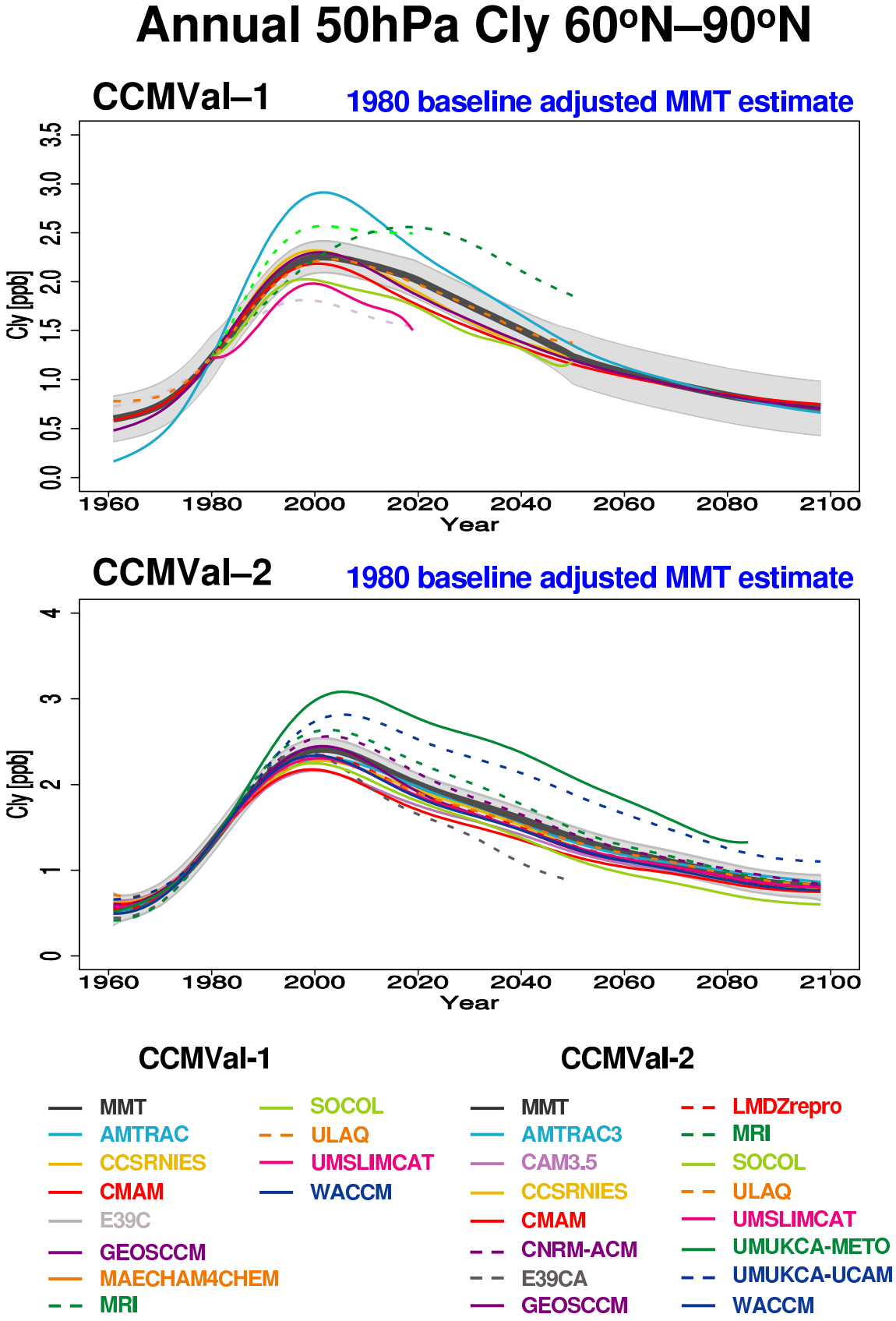

Figure 9S.30: As in Fig. 9S.6 but for the latitude range 60°N-90°N.

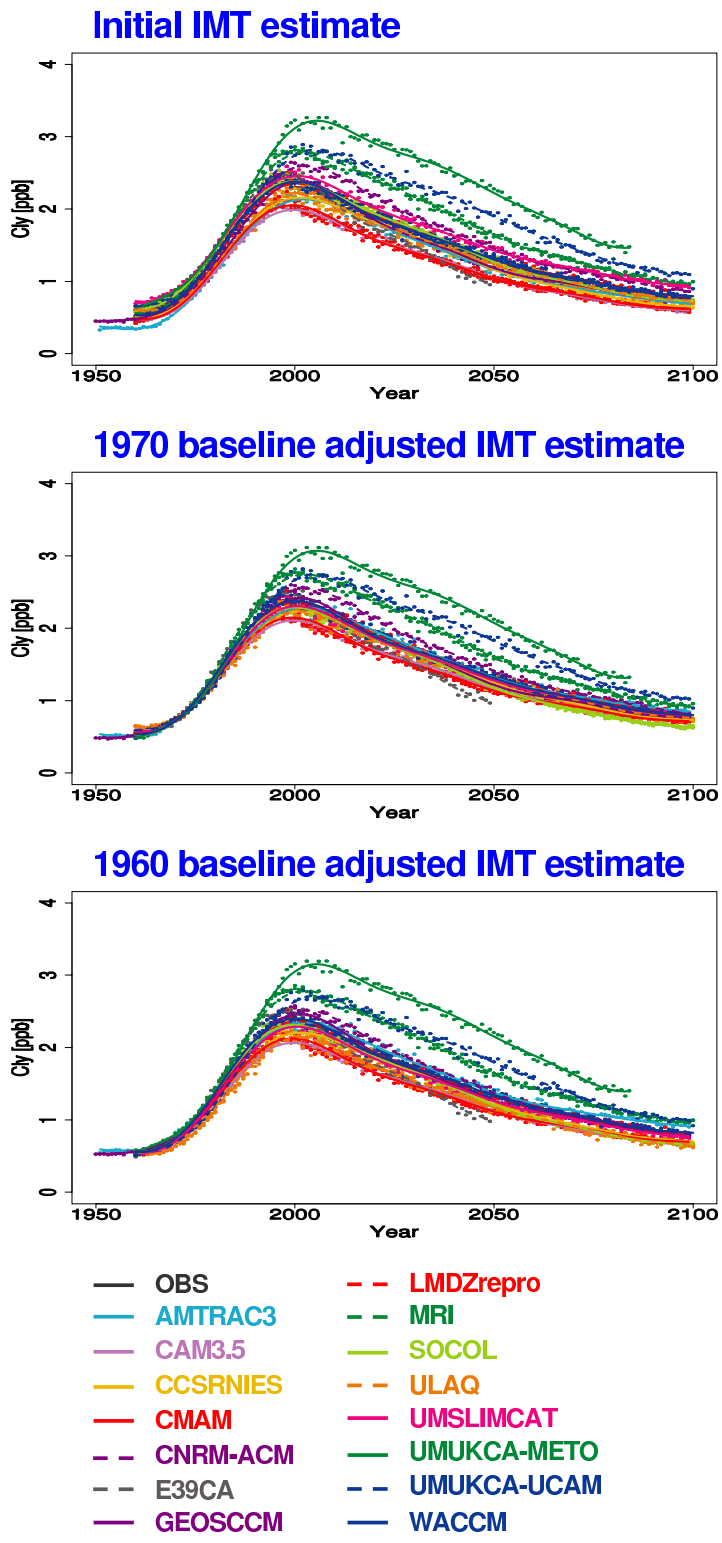

Figure 9S.31: As in Fig. 9S.7 but for the latitude range 60°N-90°N.

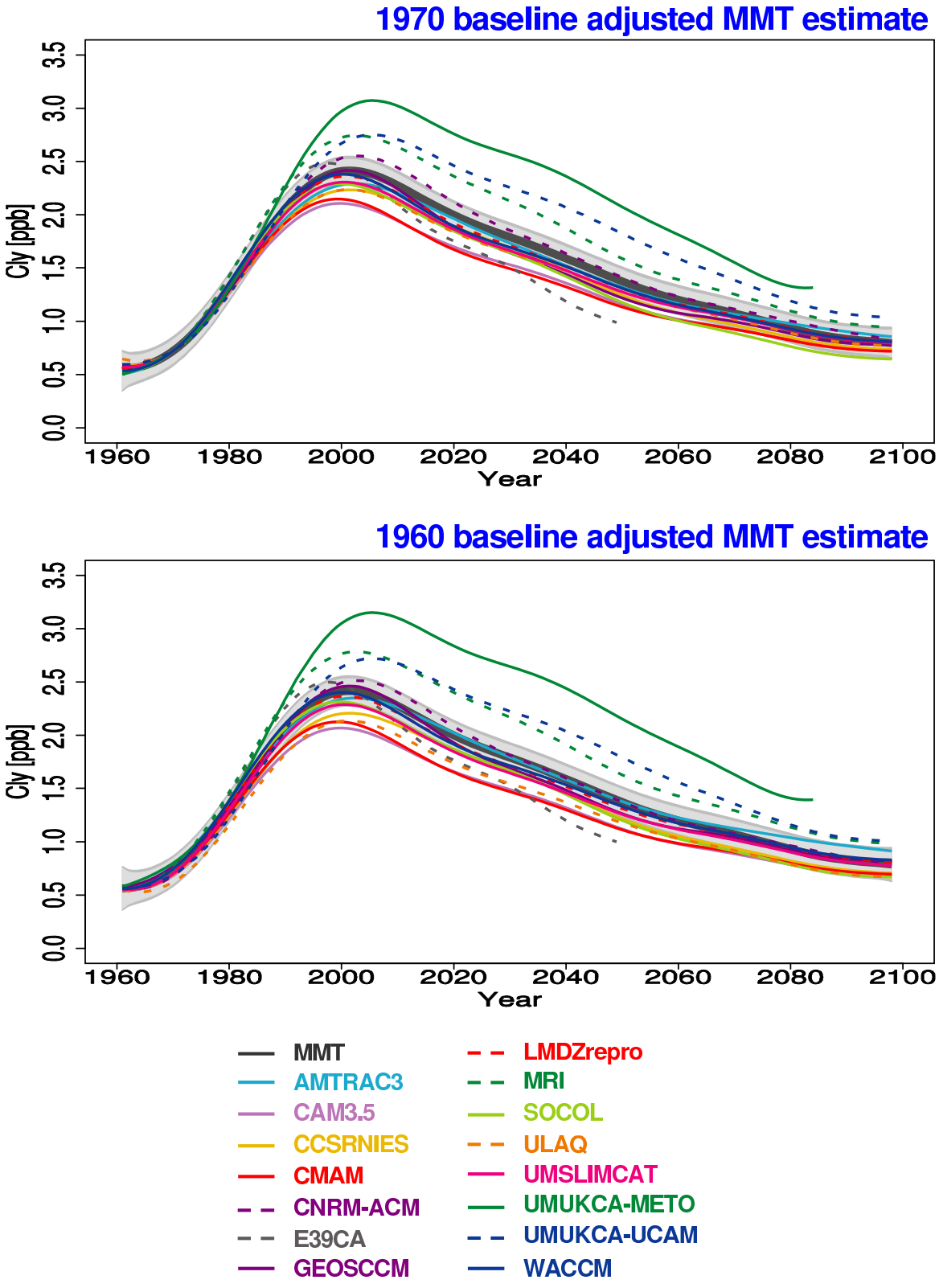

Figure 9S.32: As in Fig. 9S.8 but for the latitude range 60°N-90°N.

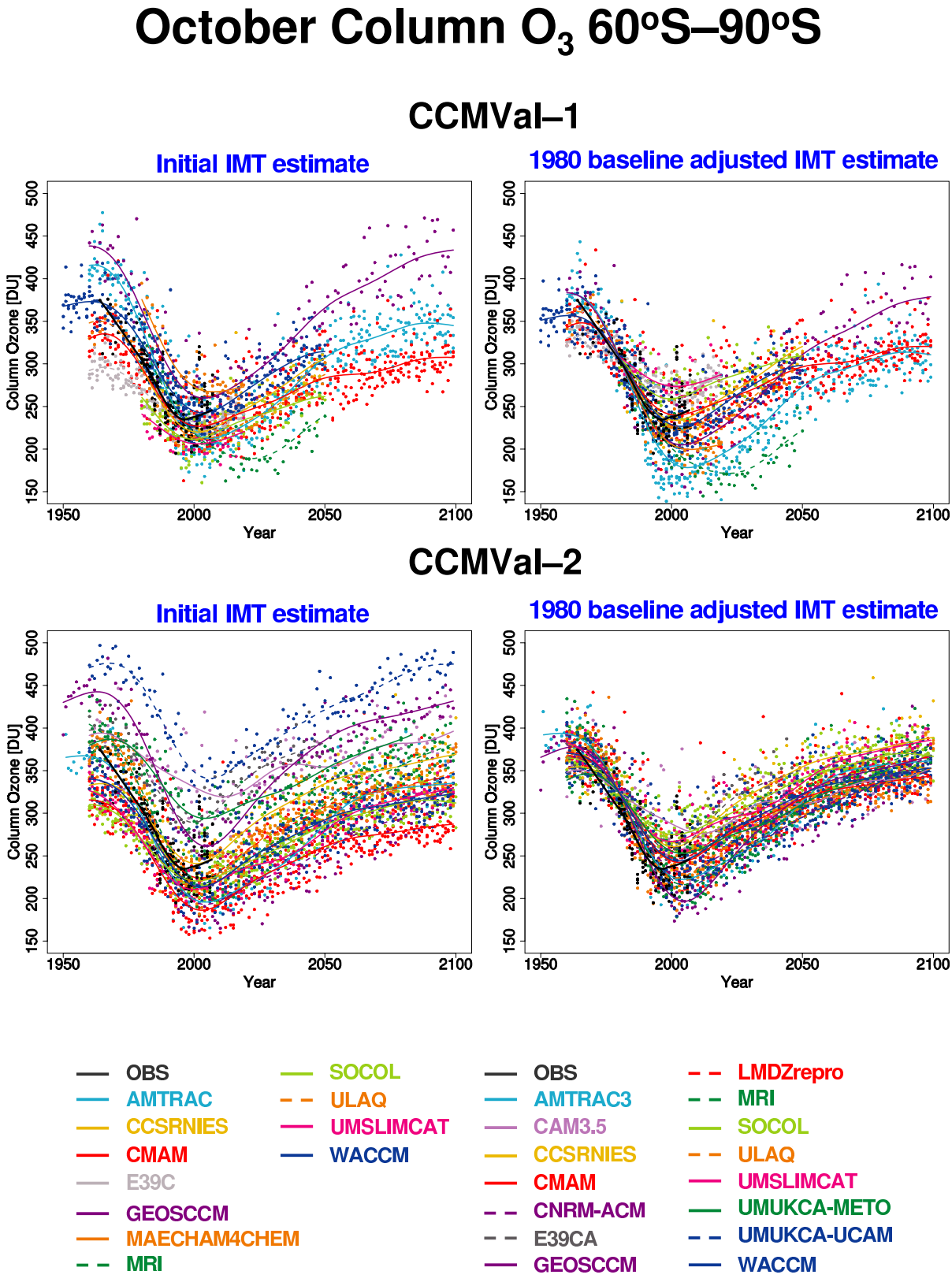

Figure 9S.33: As in Fig. 9S.1 but for the month of October and the latitude range 60°S-90°S.

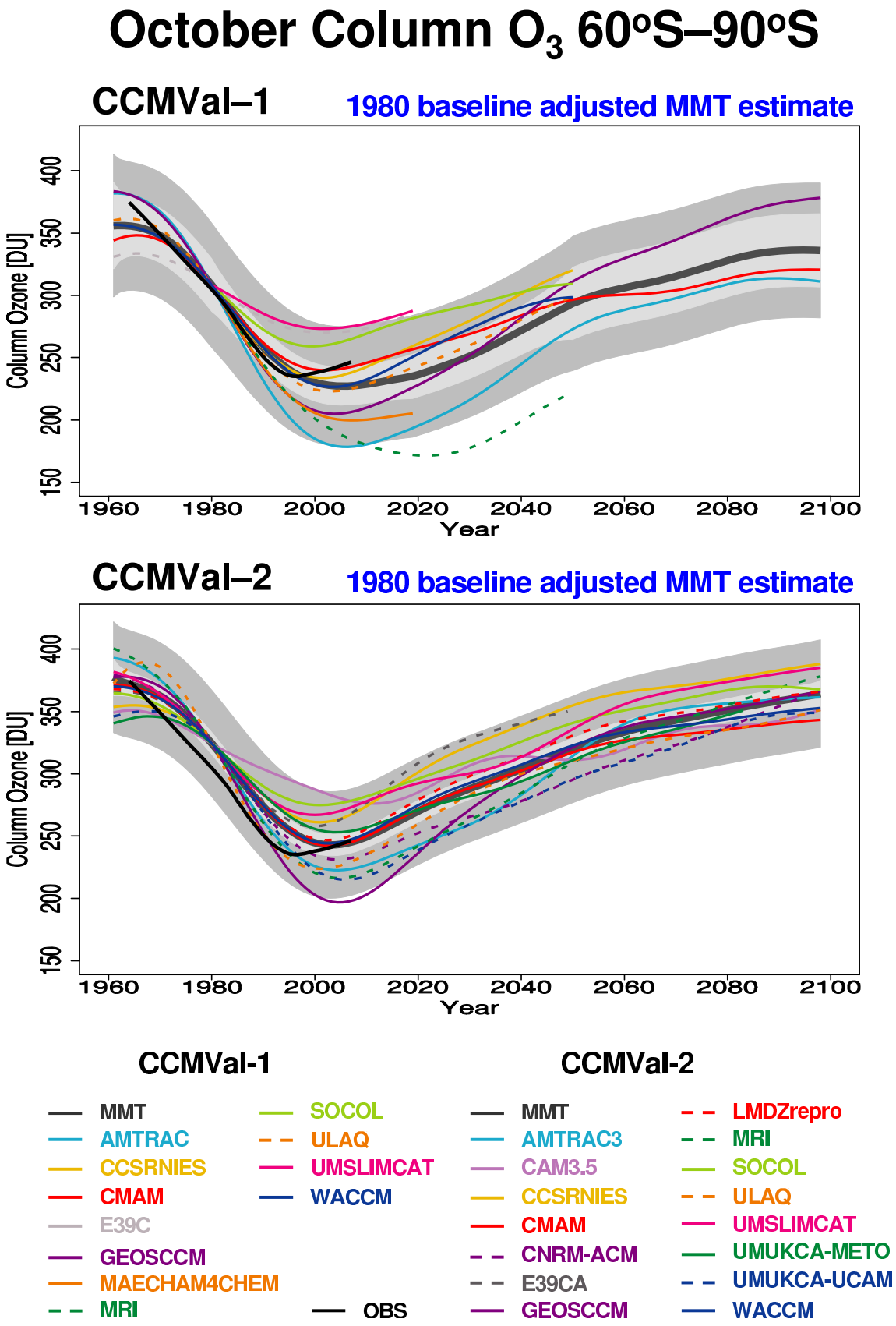

Figure 9S.34: As in Fig. 9S.2 but for the month of October and the latitude range 60°S-90°S.

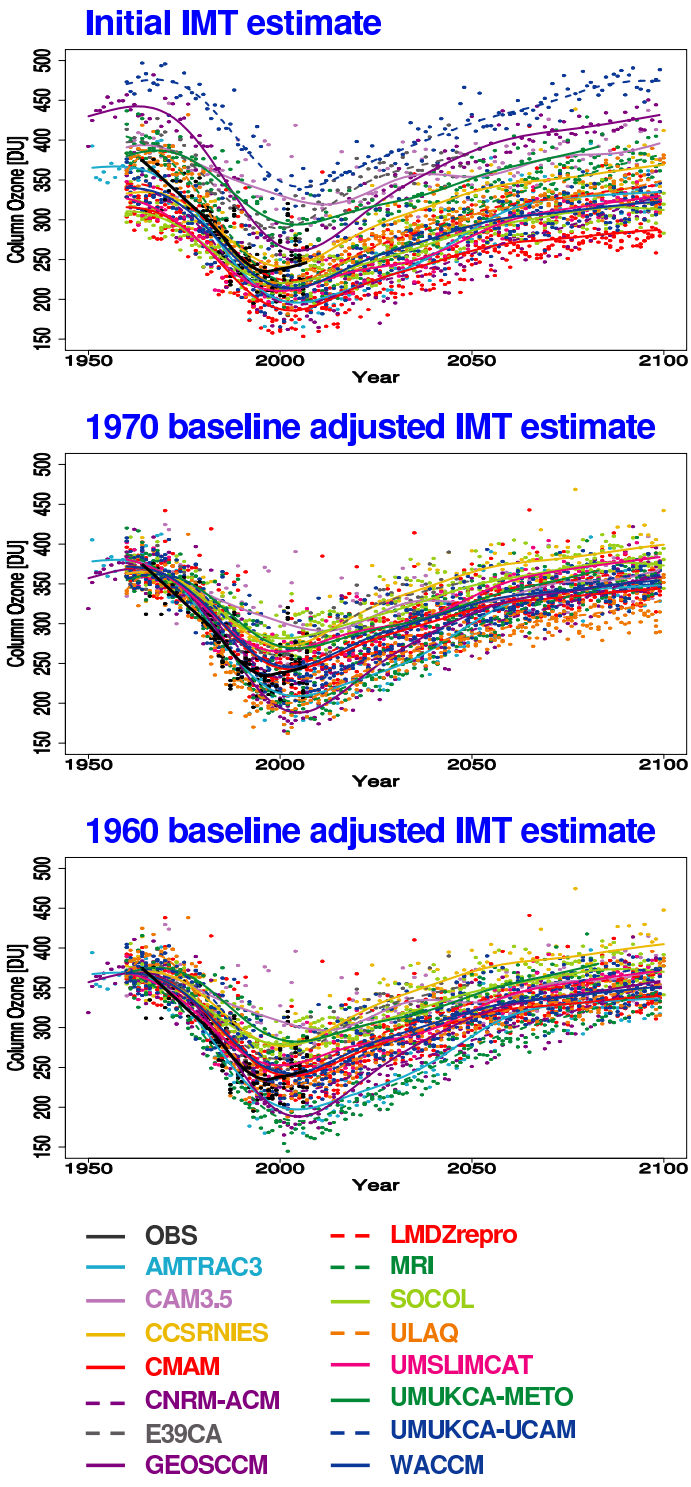

Figure 9S.35: As in Fig. 9S.3 but for the month of October and the latitude range 60°S-90°S.

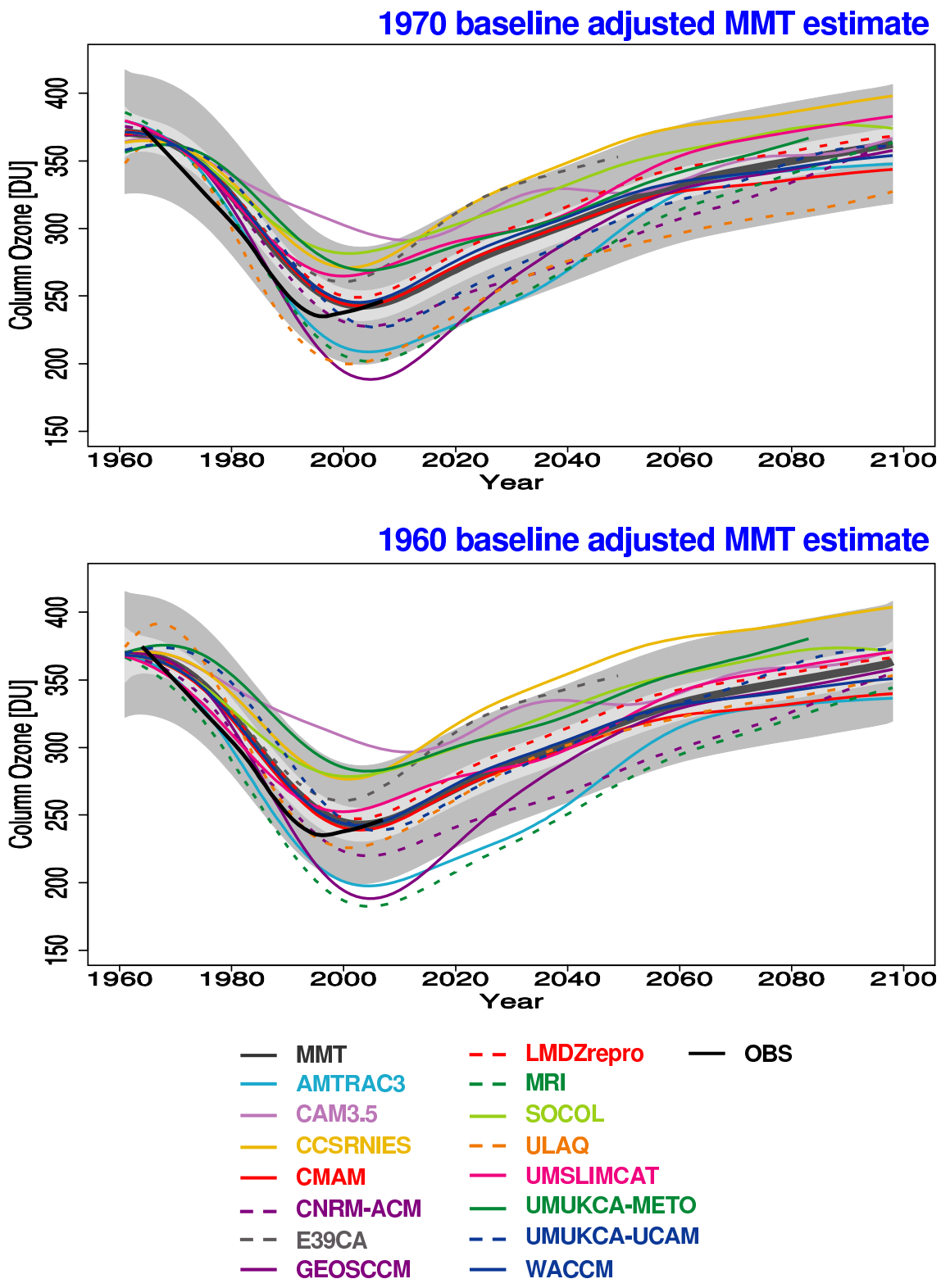

Figure 9S.36: As in Fig. 9S.4 but for the month of October and the latitude range 60°S-90°S.

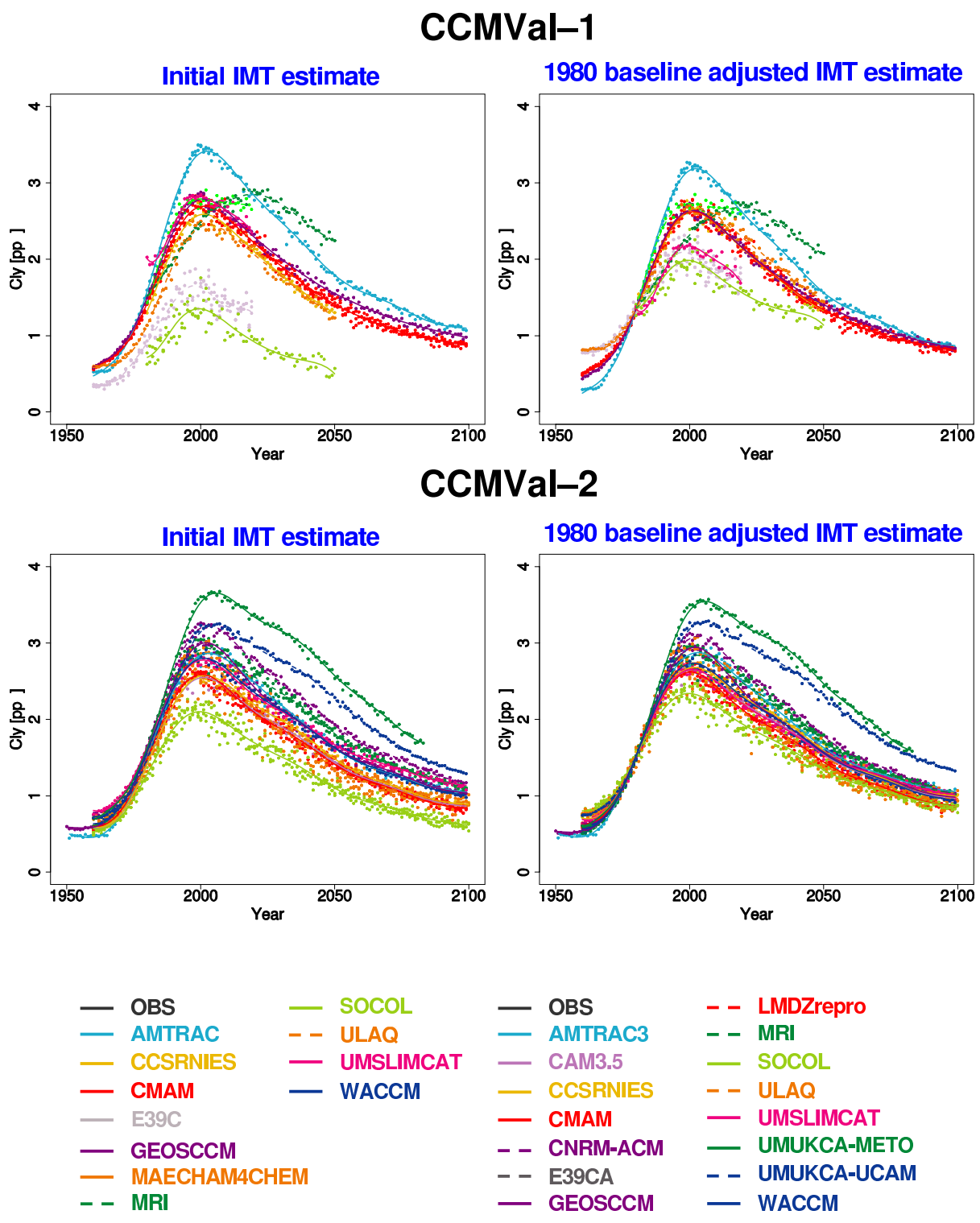

Figure 9S.37: As in Fig. 9S.5 but for the latitude range 60°S-90°S.

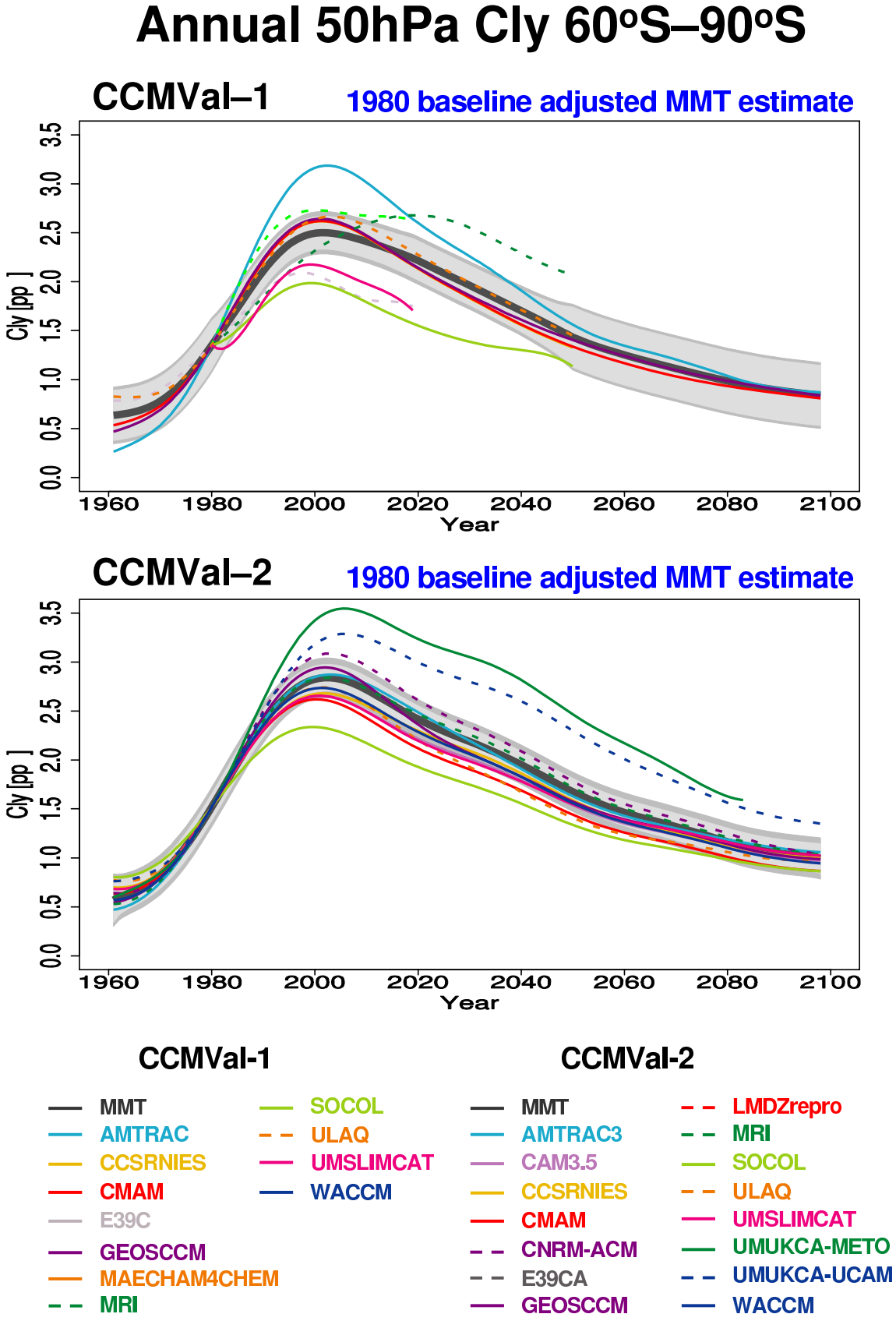

Figure 9S.38: As in Fig. 9S.6 but for the latitude range 60°S-90°S.

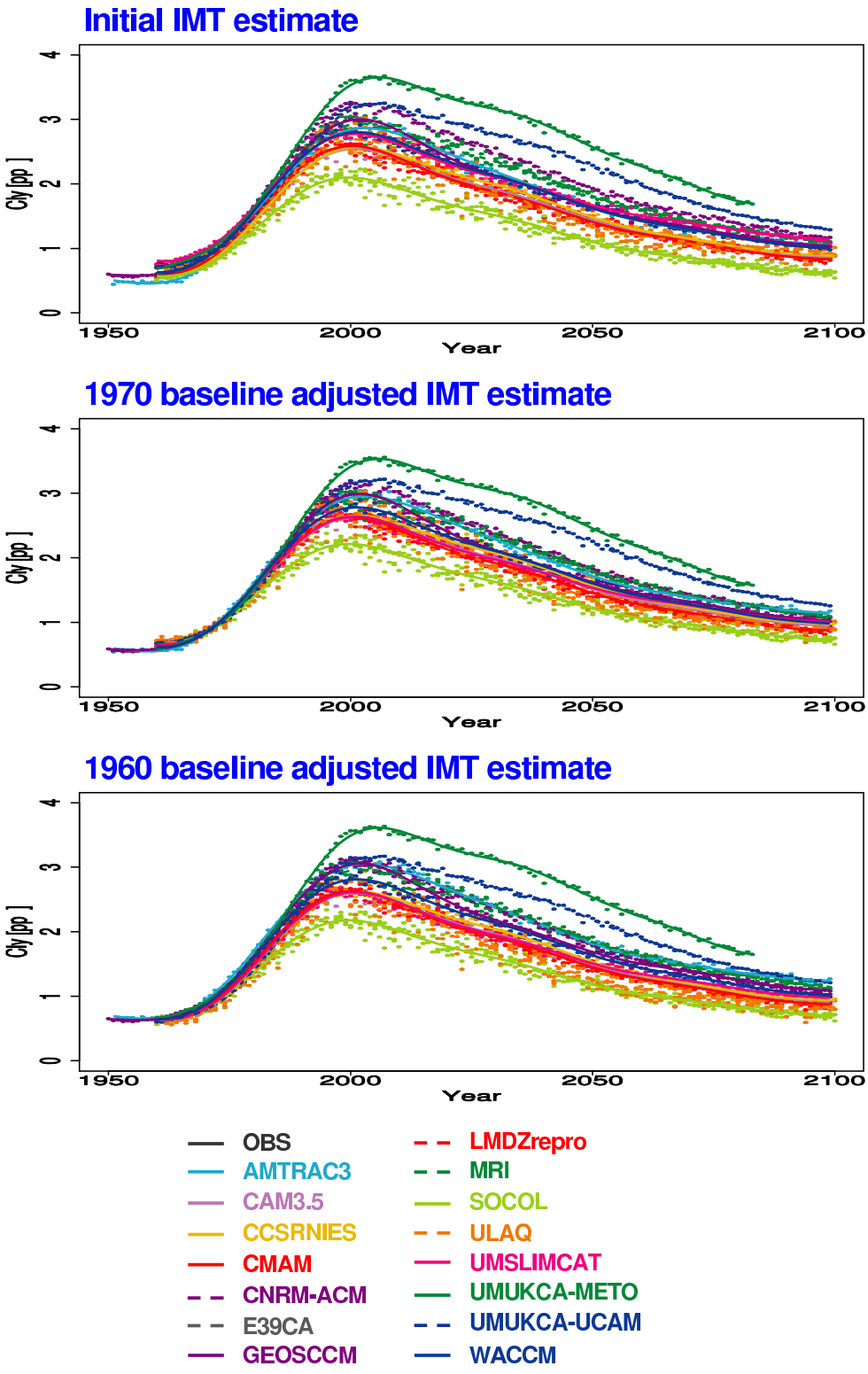

Figure 9S.39: As in Fig. 9S.7 but for the latitude range 60°S-90°S.

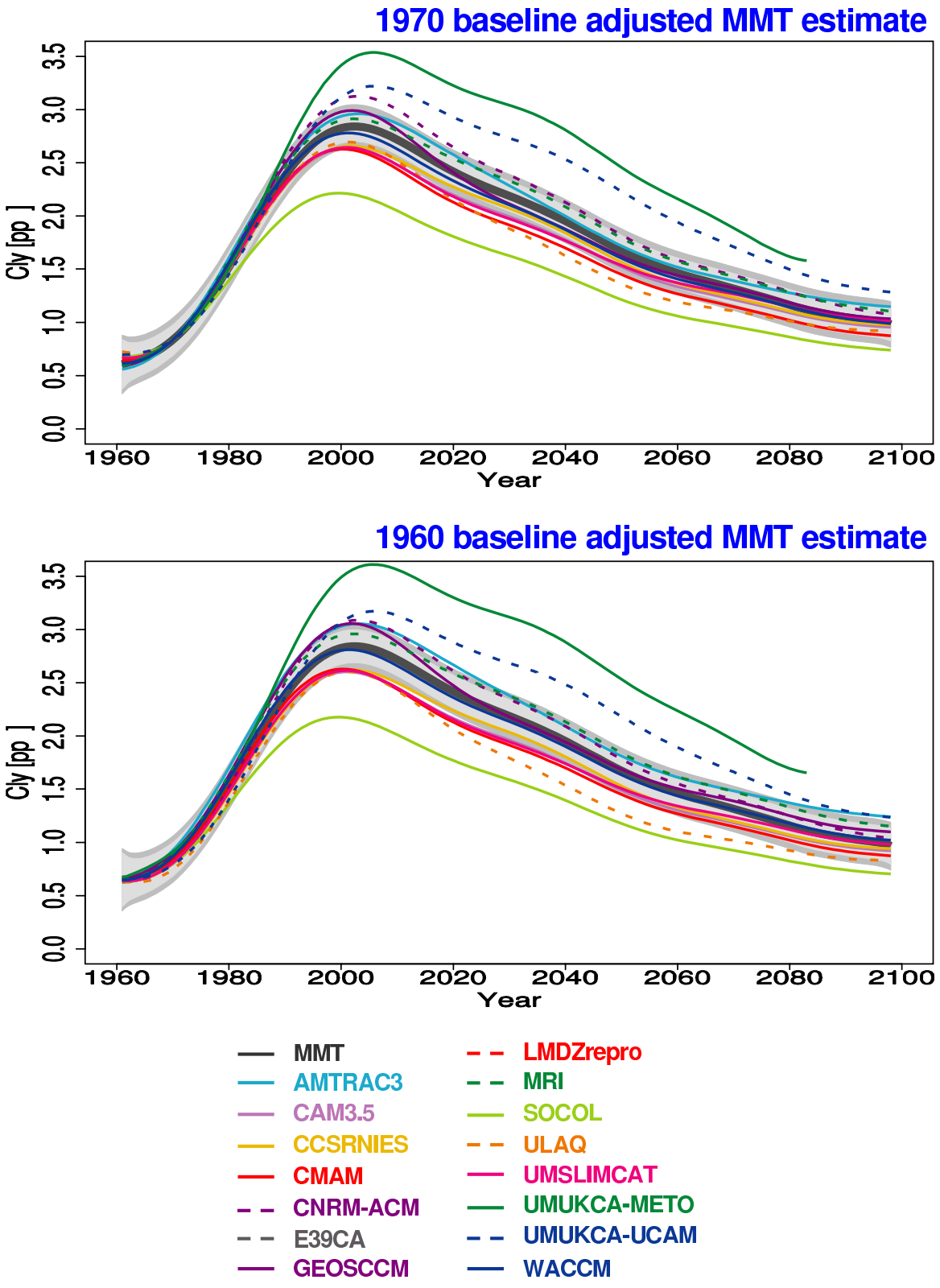

Figure 9S.40: As in Fig. 9S.8 but for the latitude range 60°S-90°S.

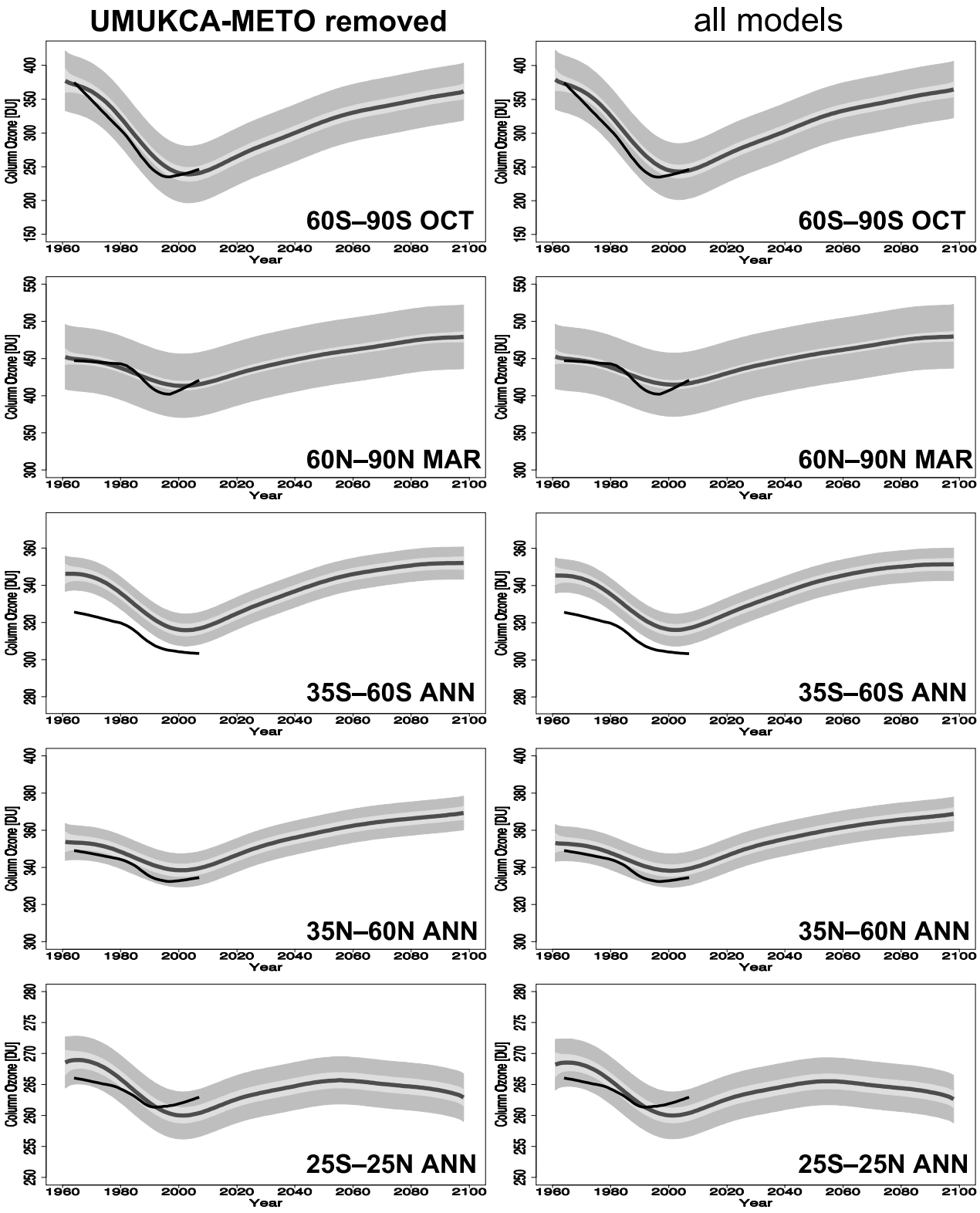

Figure 9S.41: MMT estimates and their 95% confidence and 95% prediction intervals for total Column O_3 in the 5 latitude bands considered in Chapter 9. The right-hand column shows the TSAM analysis applied to all models while the left hand column shows the same analysis but with the UMUKCA-METO model removed.

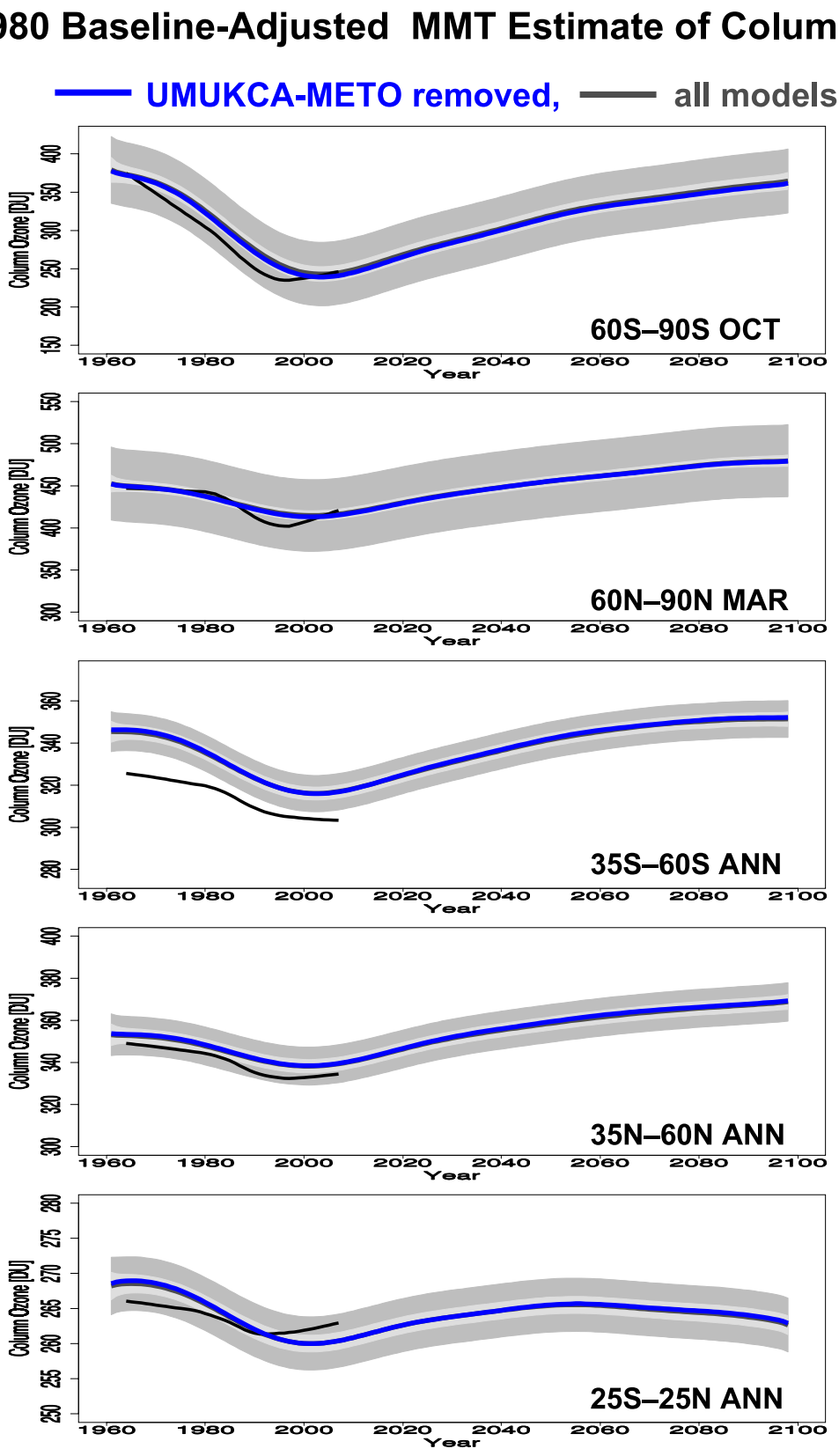

Figure 9S.42: MMT estimates of total column O_3 from the TSAM analysis applied to all models (dark grey lines) and their 95% confidence and 95% prediction intervals overlaid by the MMT estimate from the same TSAM analysis applied to all models except UMUKCA-METO (blue lines).

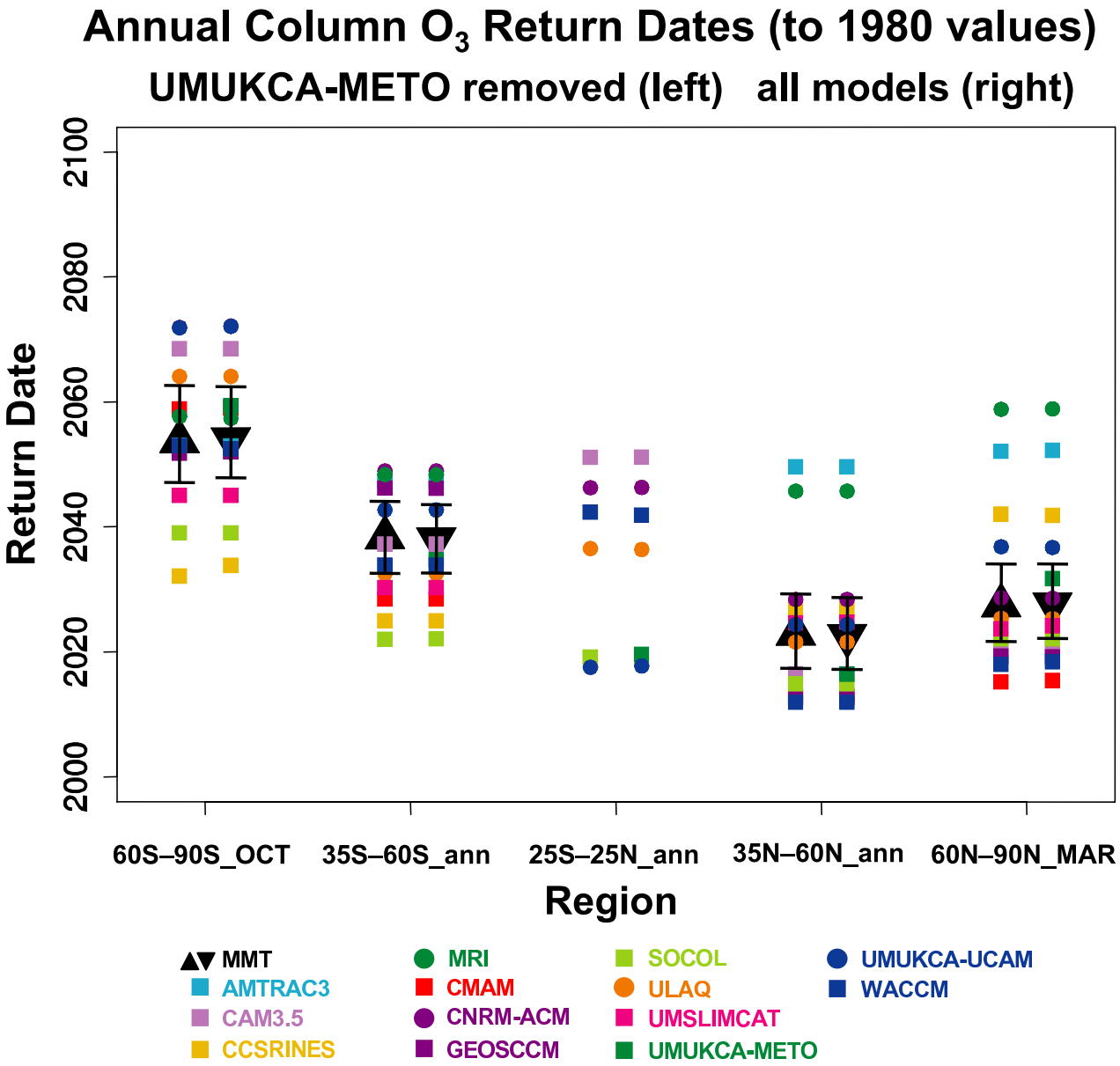

Figure 9S.43: Date of return to 1980 values for the annual average (tropical and midlatitude) and spring (polar) total ozone column derived from the IMT (coloured symbols) and MMT (large black triangles) estimates for all CCMVal-2 models (right) and all models except UMUKCA-METO (left). The error bars on the MMT estimates of recovery date are derived from the 95% confidence interval of the MMT estimates to the 1980 baseline-adjusted time series data.

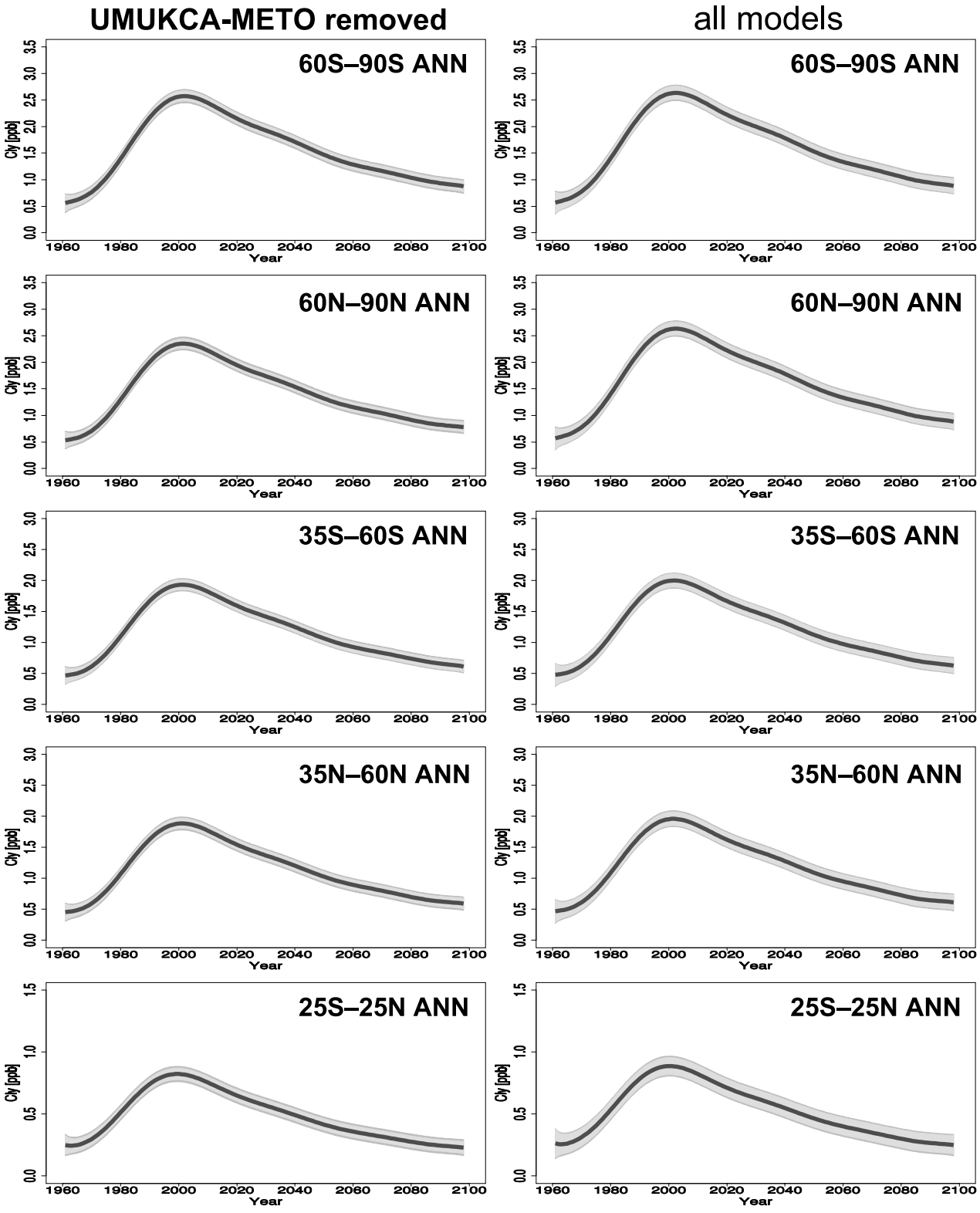

Figure 9S.44: MMT estimates and their 95% confidence and 95% prediction intervals for 50hPa Cly in the 5 latitude bands considered in Chapter 9. The right-hand column shows the TSAM analysis applied to all models while the left hand column shows the same analysis but with the UMUKCA-METO model removed.

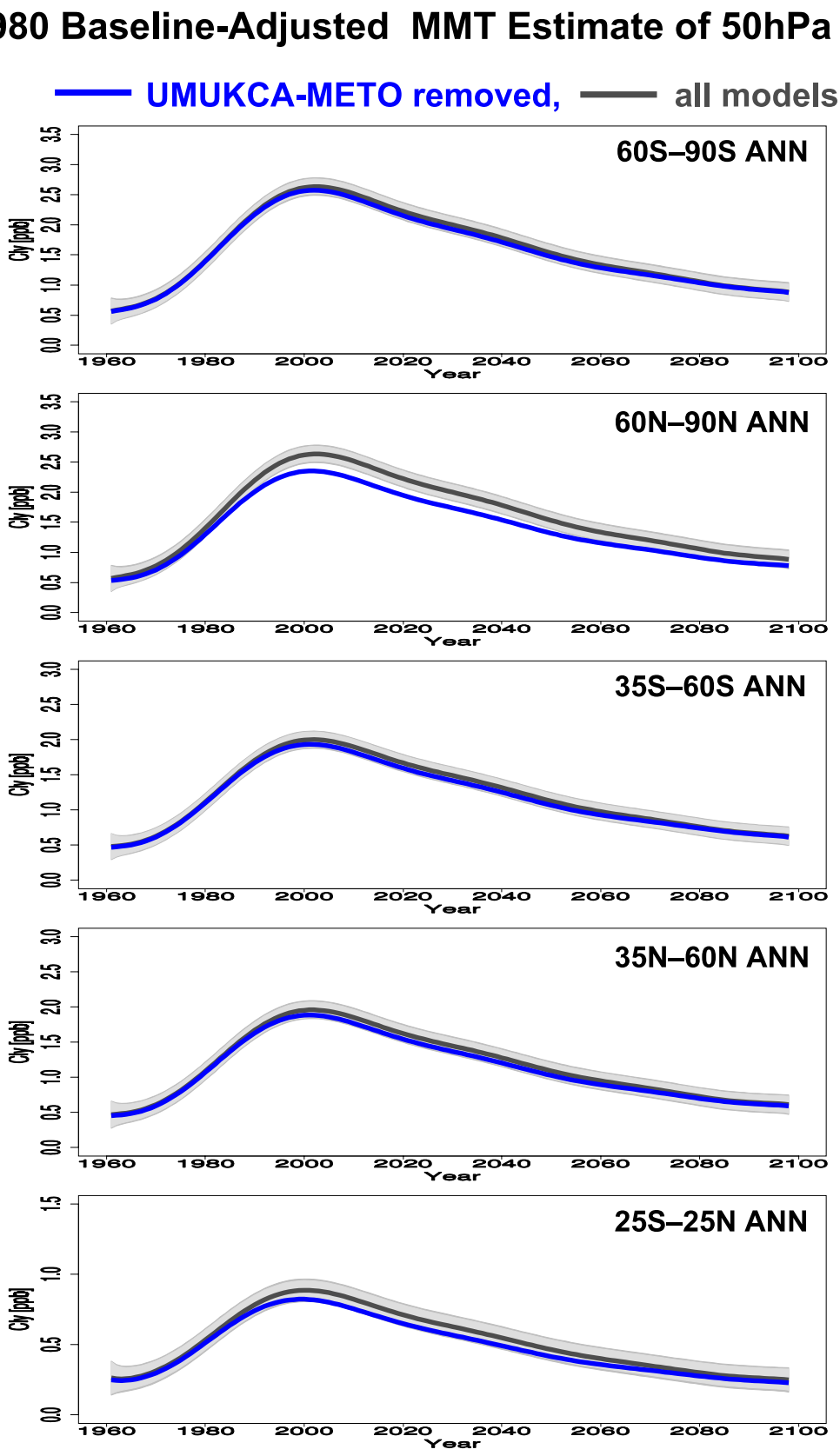

Figure 9S.45: MMT estimates of 50hPa Cly from the TSAM analysis applied to all models (dark grey lines) and their 95% confidence and 95% prediction intervals overlaid by the MMT estimate from the same TSAM analysis applied to all models except UMUKCA-METO (blue lines).

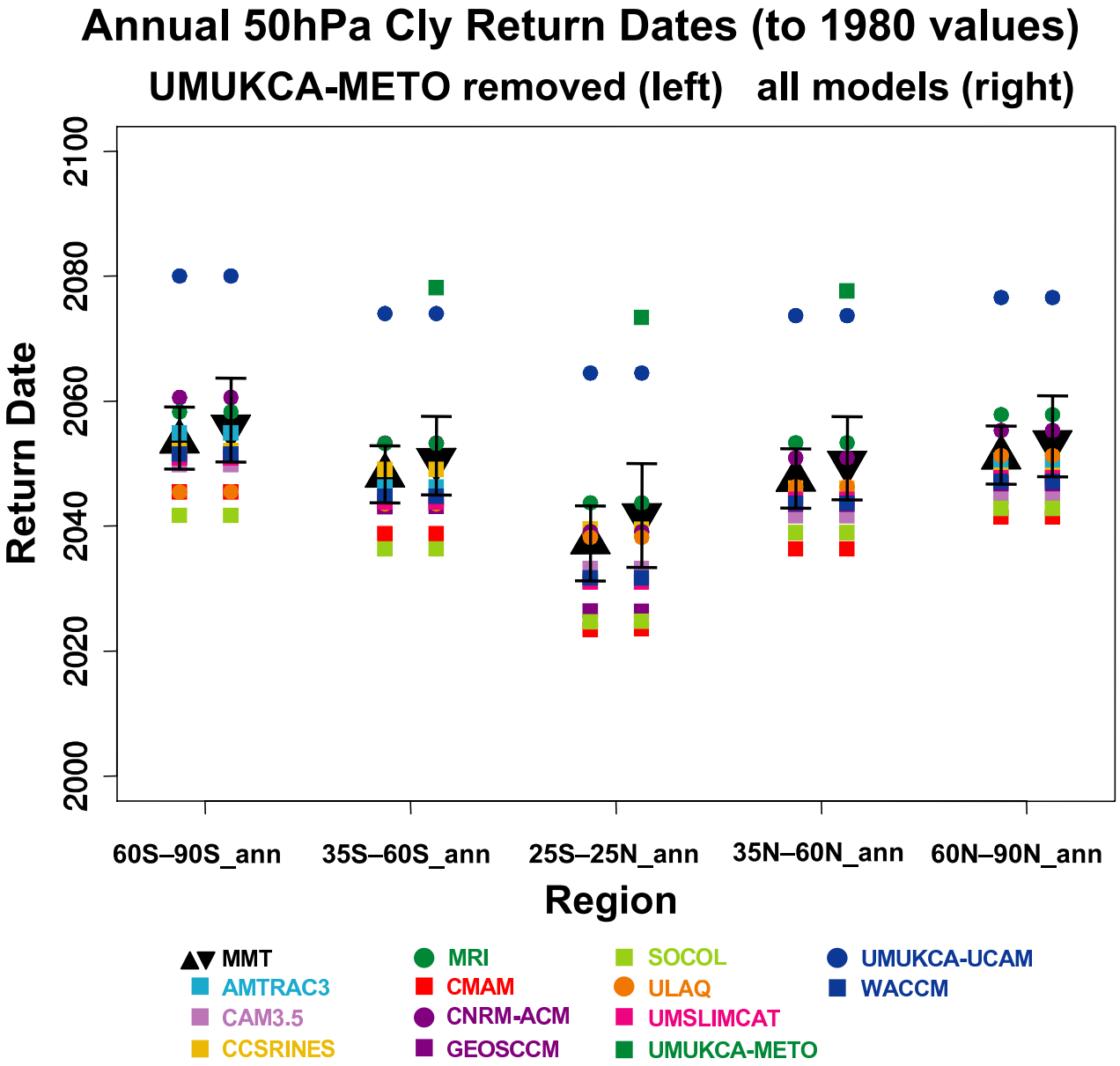

Figure 9S.46: Date of return to 1980 values for the annual average 50hPa Cly derived from the IMT (coloured symbols) and MMT (large black triangles) estimates for all CCMVal-2 models (right) and all models except UMUKCA-METO (left). The error bars on the MMT estimates of recovery date are derived from the 95% confidence interval of the MMT estimates to the 1980 baseline-adjusted time series data.

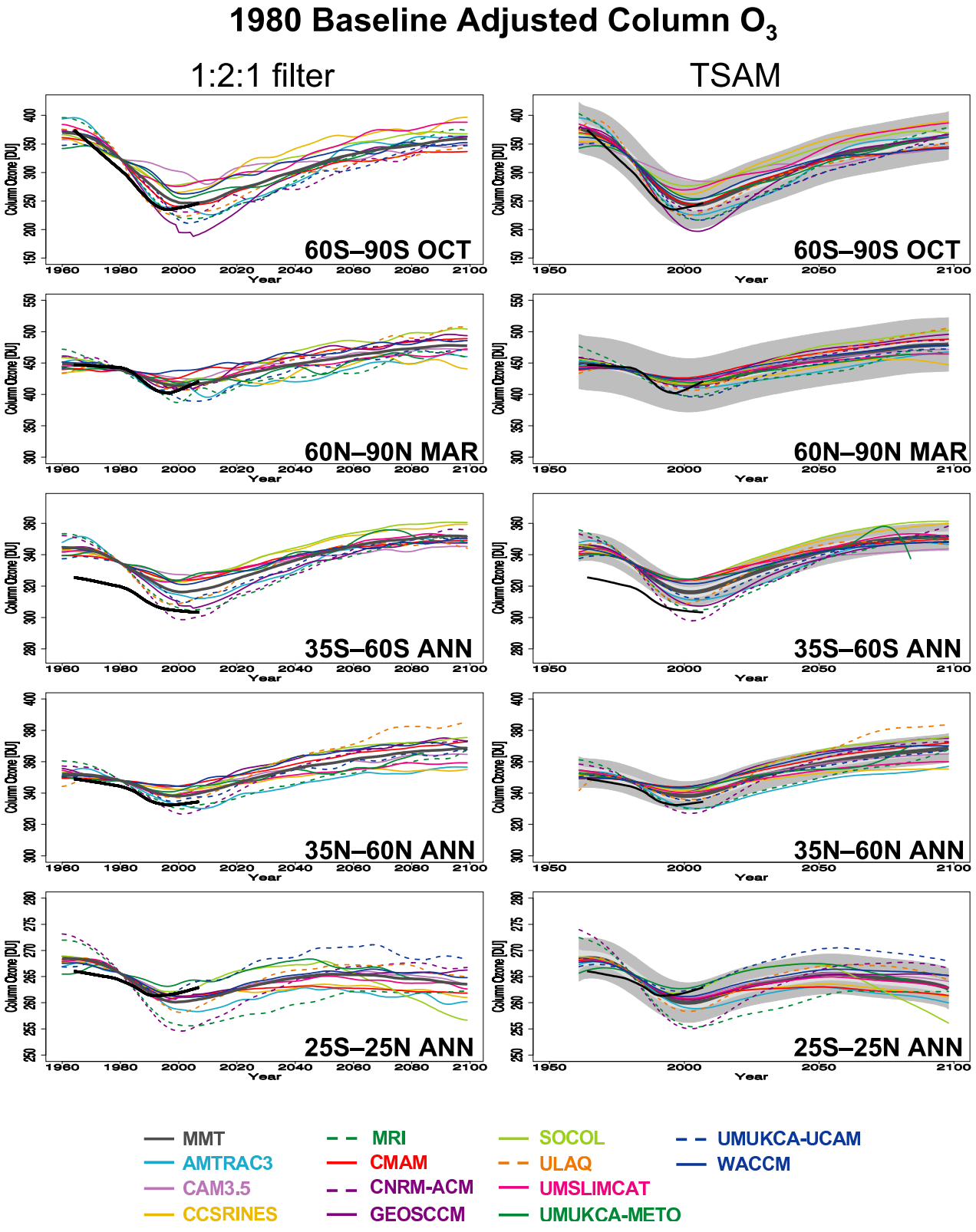

Figure 9S.47: Comparison of IMT estimates derived from a 1:2:1 filter applied 30 times (left) and the TSAM analysis (right) for total Column O_3 in the 5 latitude bands considered in Chapter 9. The multi-model trend derived from an average over the smooth IMT estimates (left) and TSAM procedure (right) are plotted as dark grey lines. 95% confidence and 95% prediction intervals have been included for the TSAM analysis (right).

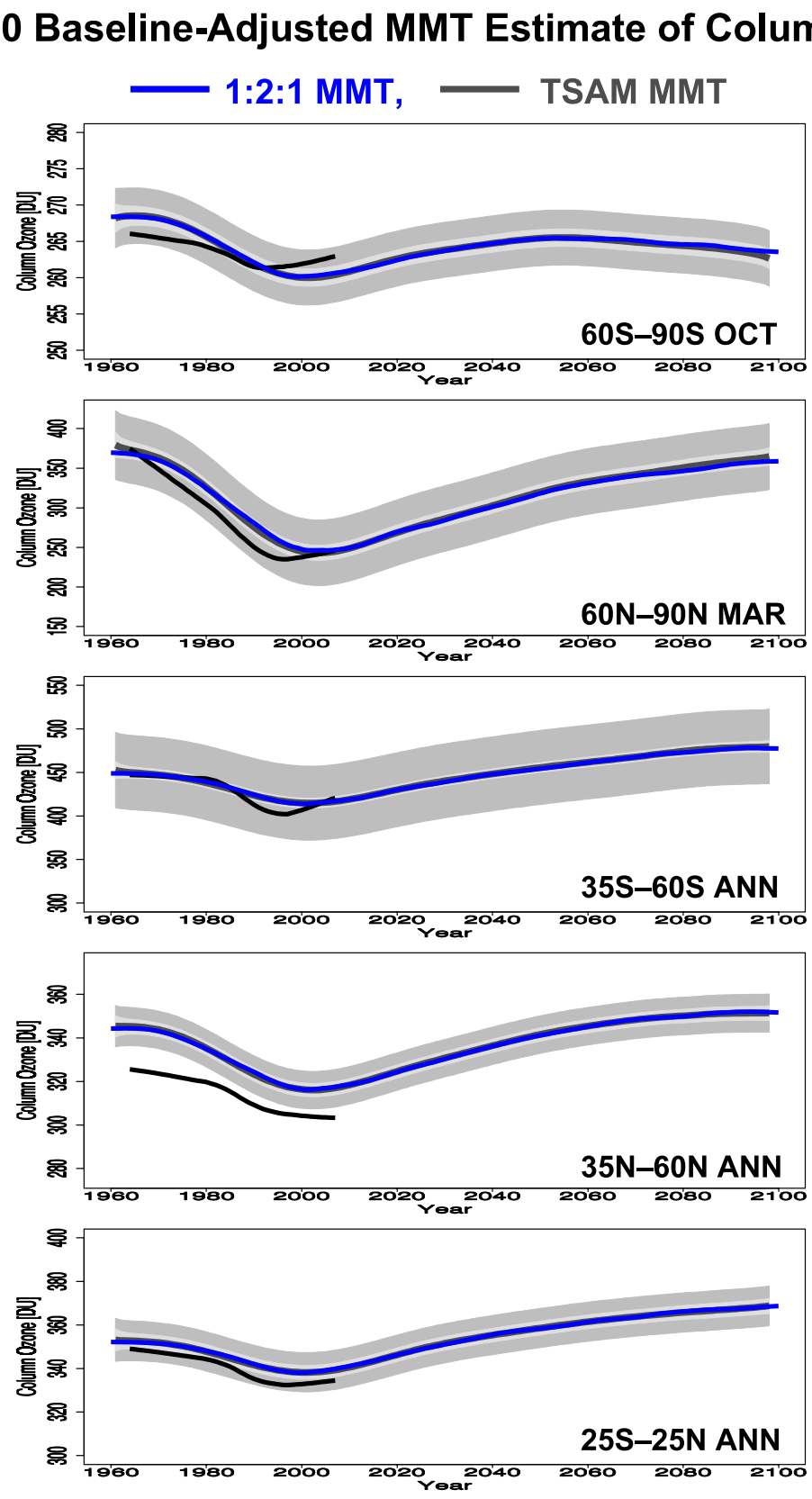

Figure 9S.48: MMT estimates of total column O_3 from the TSAM analysis (dark grey lines) and their 95% confidence and 95% prediction intervals overlaid by the MMT estimate derived from 1:2:1 smoothing presented Fig. 9S.47 (blue lines).

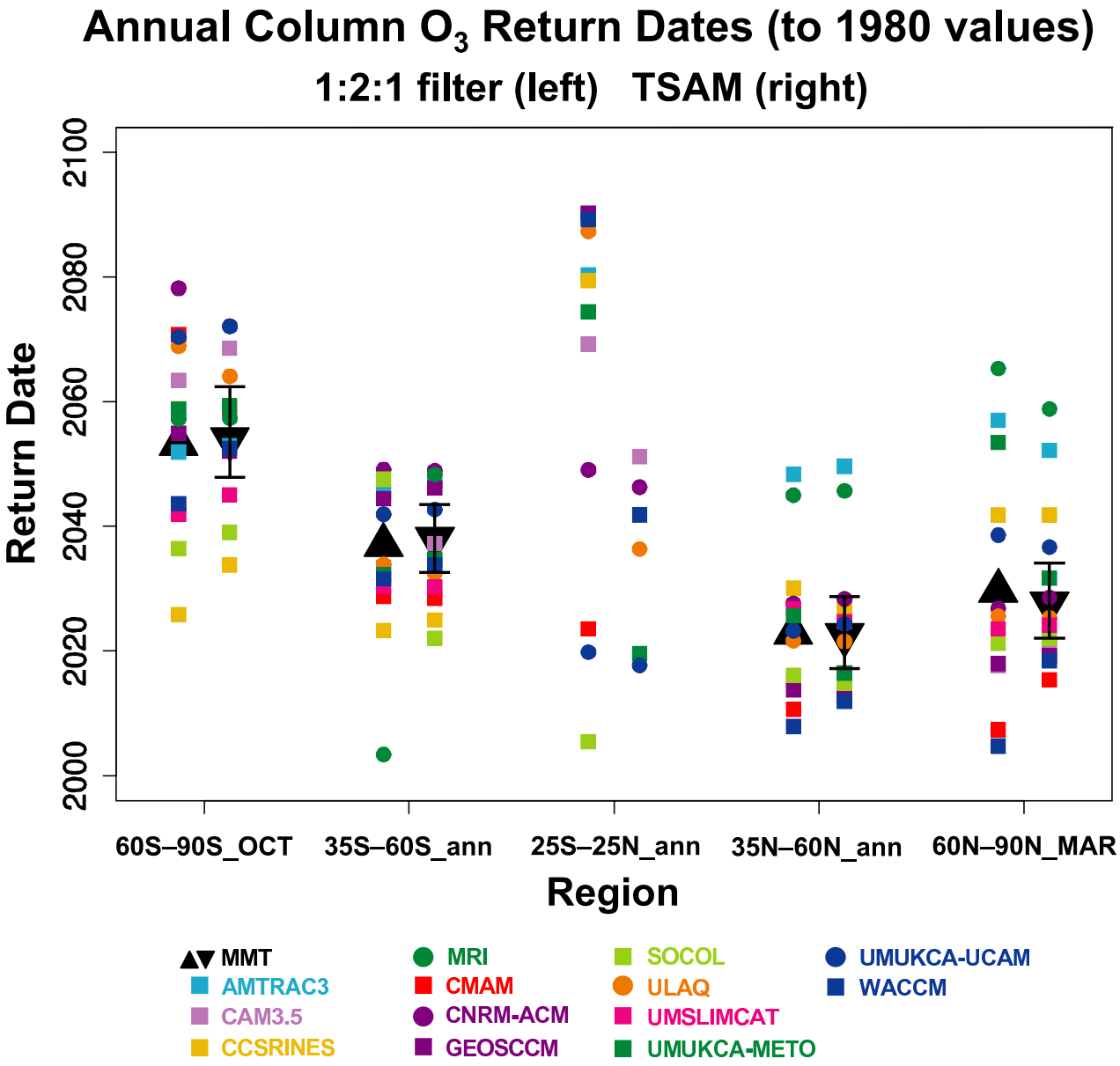

Figure 9S.49: Date of return to 1980 values for the annual average (tropical and midlatitude) and spring (polar) total ozone column derived from the IMT (coloured symbols) and MMT (large black triangles) estimates using 1:2:1 smoothing (left) and the TSAM analysis (right). The error bars on the MMT estimates of recovery date are derived from the TSAM 95% confidence interval of the MMT estimates to the 1980 baseline-adjusted time series data.

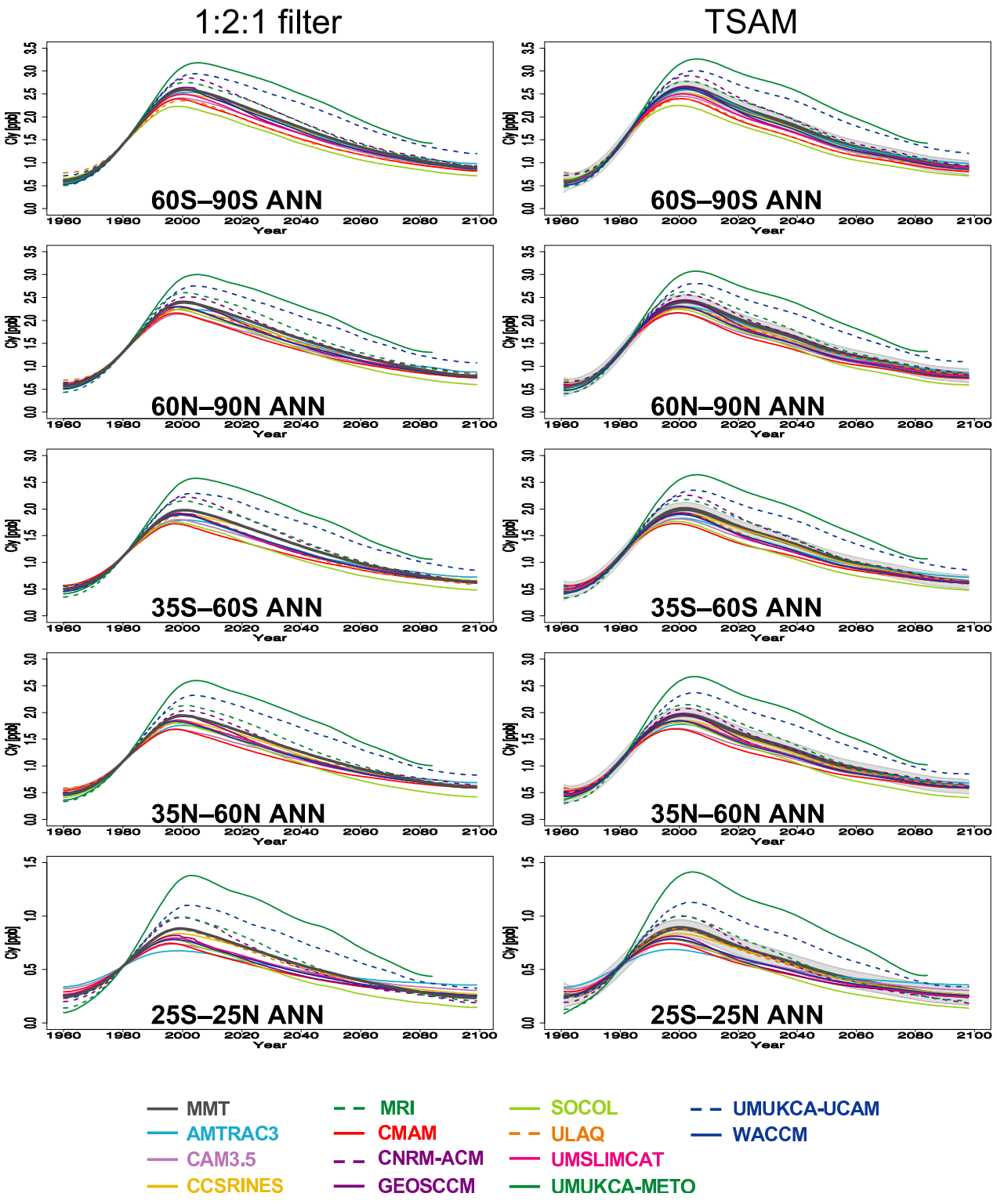

Figure 9S.50: Comparison of IMT estimates derived from a 1:2:1 filter applied 30 times (left) and the TSAM analysis (right) for 50hPa Cly in the 5 latitude bands considered in Chapter 9. The multi-model trend derived from an average over the smooth IMT estimates (left) and TSAM procedure (right) are plotted as dark grey lines. 95% confidence and 95% prediction intervals have been included for the TSAM analysis (right).

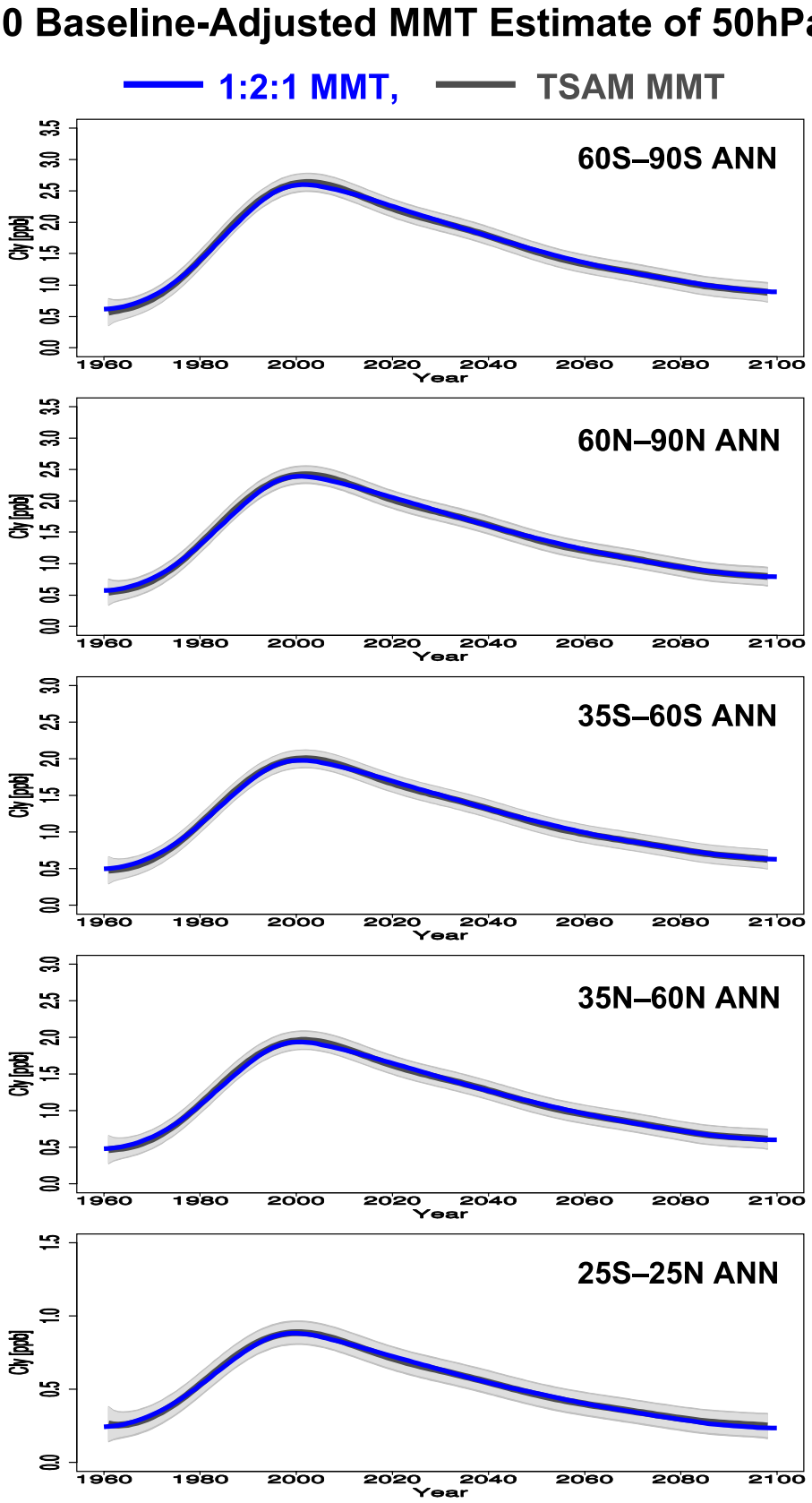

Figure 9S.51: MMT estimates of 50hPa Cly from the TSAM analysis (dark grey lines) and their 95% confidence and 95% prediction intervals overlaid by the MMT estimate derived from 1:2:1 smoothing presented Fig. 9S.50 (blue lines).

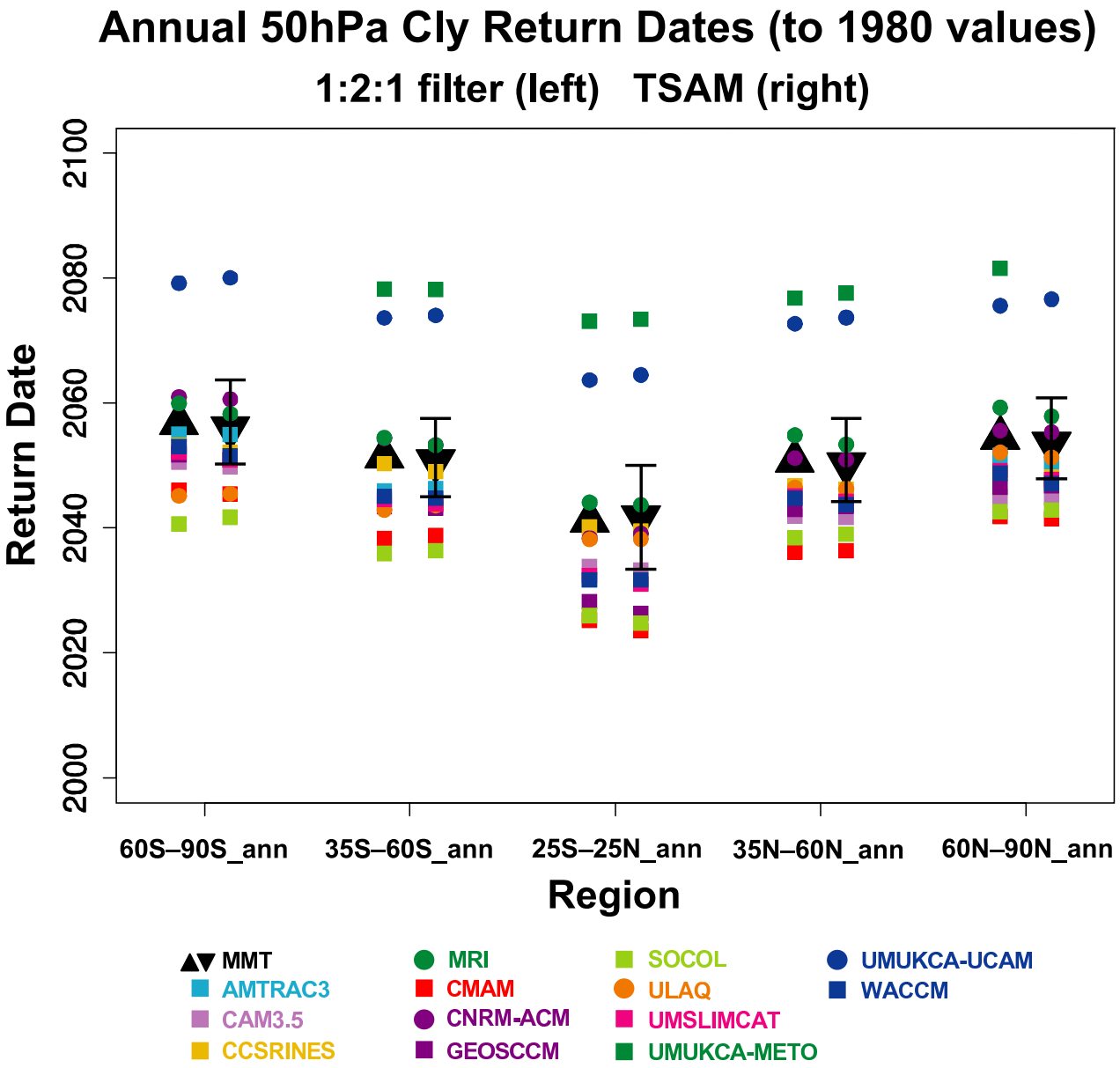

Figure 9S.52: Date of return to 1980 values for the annual average 50hPa Cly derived from the IMT (coloured symbols) and MMT (large black triangles) estimates using 1:2:1 smoothing (left) and the TSAM analysis (right). The error bars on the MMT estimates of recovery date are derived from the TSAM 95% confidence interval of the MMT estimates to the 1980 baseline-adjusted time series data.

Chapter 10

Effects of the stratosphere on the troposphere

Lead Authors: Mark P. Baldwin & Nathan P. Gillett

Co-Authors: Piers V. Forster
Edwin P. Gerber
Michaela I. Hegglin
Alexey Yu. Karpechko
Junsu Kim
Paul J. Kushner
Olaf H. Morgenstern
Thomas Reichler
Seok-Woo Son
Kleareti Tourpali

10.1 Introduction

While the focus of this report is on an evaluation of the stratospheric climate and composition of the CCMVal models, public attention is invariably focused more closely on tropospheric climate and climate change. This chapter therefore investigates how the stratospheric variability and changes simulated by the CCMVal models influence tropospheric climate. The simulation of stratosphere-troposphere coupling by the CCMVal models is validated by comparison with observations, and compared with that of the CMIP3 models, whose simulations of future climate formed the basis of the climate projections of the Intergovernmental Panel on Climate Change (IPCC) (Meehl *et al*., 2007b).

As well as reviewing the influences of past and future stratospheric changes on the troposphere in the CCMVal simulations in this chapter, we also review diagnostic studies of dynamical, radiative and chemical processes coupling the stratosphere and troposphere in an attempt to shed light on these issues.

Increasing observational evidence (*e.g*., Kodera *et al*., 1990) suggests stratospheric processes play an important role in tropospheric climate variability across a wide range of time scales. For example:

- On intraseasonal time scales, observations show that

large amplitude anomalies in the strength of the Northern Hemisphere wintertime stratospheric polar vortex frequently precede long-lived (up to ~two months) changes to the tropospheric circulation (Baldwin and Dunkerton 1999, 2001; Polvani and Waugh, 2004). These changes modulate not only average weather, but also the likelihood of extreme events on time scales longer than the limit of deterministic weather prediction (Thompson *et al*., 2002).

- On interannual time scales, the stratospheric QBO has been found to exhibit a signature in surface climate (Coughlin and Tung, 2001; Thompson *et al*., 2002). A stratospheric role has also been suggested in modulating the tropospheric response to solar forcing (*e.g*., Rind *et al*., 2008) and the El Niño/Southern Oscillation (ENSO) variations (Ineson and Scaife, 2009).
- On time scales of several years, volcanic eruptions that inject sulphate aerosols into the stratosphere also noticeably influence tropospheric climate both radiatively and dynamically (Robock and Mao, 1992; Graf *et al*., 1994; Kodera and Yamazaki, 1994; Stenchikov *et al*., 1998; 2004; Hamilton, 2007).
- On decadal time scales, Antarctic ozone depletion appears to have had a demonstrable impact not only on stratospheric temperatures and circulation, but on surface climate as well (Thompson and Solomon, 2002; Gillett and Thompson, 2003; Keeley *et al*., 2007).

To first order, the coupling between the stratosphere and troposphere is mediated by wave dynamics. Planetary-scale Rossby waves, gravity waves, and equatorial Kelvin and mixed Rossby-gravity waves typically originate in the troposphere, propagate upward into the stratosphere, and then dissipate causing variability of the stratospheric flow. The conventional view up to the late 1990s was that the resulting interactions are principally one way, *i.e*., that tropospheric waves influence the stratospheric circulation, but that stratospheric circulation anomalies do not have significant effects on tropospheric weather and climate. However, in the past ~5-10 years, the prevailing view has changed, and variability in the extra-tropical atmospheric flow is now recognised to reflect "two-way" interactions between the stratospheric and tropospheric circulations.

The relationship between the stratospheric and tropospheric circulations is most clearly evident as deep vertical coupling in the "annular modes" of extra-tropical climate variability (Thompson and Wallace, 1998; Thompson and Wallace, 2000). The annular modes extend from the surface through the stratosphere in both hemispheres, and are characterized by meridional vacillations in the geopotential height field between the polar regions and surrounding middle latitudes. Fluctuations in the annular mode index at a given pressure level are nearly equivalent to fluctuations in the geopotential anomaly averaged over the polar cap (Baldwin and Thompson, 2009). During the cold season in the stratosphere, the annular modes correspond to fluctuations in the strength of the polar vortex, while at the surface the annular modes correspond to meridional shifts in the extra-tropical storm tracks. The stratospheric and tropospheric components of the annular modes are coupled in both hemispheres, particularly in winter in the Northern Hemisphere (NH), and in spring in the Southern Hemisphere (SH), but the reasons for this coupling are still not understood.

Stratosphere-troposphere coupling is also an important process in the context of climate change. Any long-term changes in stratospheric winds and temperatures are likely to affect surface climate and climate variability. During the past ~25 years, the composition of the stratosphere has changed substantially. Abundances of anthropogenic greenhouse gases (GHGs) and ozone-depleting substances (ODSs) have risen, while stratospheric ozone has been depleted, particularly in the Antarctic vortex. Following the successful implementation of the Montreal Protocol and its ammendments, the concentrations of ozone-depleting substances in the stratosphere have stabilized, and the severity of the ozone hole is expected to decrease over the coming decades. However, concentrations of most greenhouse gases will continue to rise. It is therefore necessary to view stratosphere-troposphere coupling in the context of a changing atmosphere.

It has long been known that radiative processes are important for stratosphere-troposphere coupling in the context of climate change. For example, stratospheric cooling induced by CO_2 increases has long been known to offset part of the induced tropospheric warming, and radiative forcing at the tropopause is routinely reported after allowing for the radiative influence of altered stratospheric temperatures (WMO, 1992; Forster *et al*., 2007). Similarly, stratospheric ozone depletion is thought to exert a small cooling influence on the troposphere in the global mean, while increases in stratospheric water vapour have caused a warming effect at the surface (Forster *et al*., 2007). Moreover the effect of stratospheric volcanic aerosol on tropospheric climate is primarily radiative, and exerts a substantial influence on the global radiative budget on a time scale of ~2 years. The radiative forcing immediately following Pinatubo is estimated to be -3 W m^{-2} in the global mean (Forster *et al*., 2007). Recently, interest in the radiative response to stratospheric forcings has moved beyond the global mean, and several recent studies have examined the role of radiation in driving the regional pattern of temperature to response to stratospheric ozone depletion. Early work using radiative-convective models already suggested that Antarctic ozone depletion could force substantial local surface cooling, as observed (Lal *et al*., 1987). More recent work confirms that cooling of the Antarctic troposphere in late spring and summer is likely largely a radiative re-

Table 10.1: Key diagnostics

Process	Diagnostic	Variables	Data, Models	References[a]
Climate				
Mean Climate	*u* mean, variability	*u*	NCEP, ERA-40	
	Combined Performance metrics	*u, v, T*	NCEP, ERA-40, CMIP3, CCMVal-1	*Reichler and Kim (2008)*
Climate Trends	Linear trends, 20th Century	*T, Z*, O_3	CMIP3	*Thompson and Solomon (2002)*
	Long-term change REF-B2	*u, T*, O_3, jet, Hadley cell	CMIP3	*Thompson and Solomon (2002)*
Dynamical Coupling[b]				
NAM, SAM	Annular Modes	*Z*, REF-B1	ERA-40, NCEP	*Thompson and Baldwin (2009)*
	AM RMS amplitude	*Z*, REF-B1	ERA-40, NCEP	*Gerber et al. (2010)*
	Latitude of AM node	*Z*, REF-B1	ERA-40, NCEP	*Gerber et al. (2010)*
	Seasonal AM variance	*Z*	ERA-40	*Baldwin et al. (2003)*
	Tropospheric AM predictability	*Z*	ERA-40	*Baldwin et al. (2003)*
	AM e-folding time scale	*Z*	ERA-40	*Baldwin et al. (2003)*
Radiation				
Radiative Forcing	Ozone-induced radiative forcing	O_3, REF-B1		*Forster et al. (2007)*
Erythemal Irradiance	Surface erythemal irradiance	O_3, *T* in REF-B1, REF-B2		*Mayer and Kylling (2005)*
Ozone Fluxes				
	Ozone flux from stratosphere	O_3, $\overline{w}^*$	ERA-Interim	*Hegglin and Shepherd (2009)*

[a] *Listed references only provide examples*

[b] *Abbreviations: NAM=Northern Annular Mode; SAM=Southern Annular Mode;*

sponse to ozone-induced stratospheric cooling (Keeley *et al.*, 2007; Grise *et al.*, 2009). Radiative processes may also play a role in intra-seasonal coupling between the stratosphere and troposphere (Ramanathan, 1977; Grise *et al.*, 2009).

The stratosphere also influences the troposphere through the exchange of radiatively active gases across the tropopause. The most important such influence is on tropospheric ozone, the third largest contributor to greenhouse-gas-induced radiative forcing after CO_2 and methane. While the flux of ozone from the stratosphere is only about 10% as large as the tropospheric chemical production source, it delivers ozone directly to the upper troposphere, where its effect on radiative forcing is largest (Denman *et al.*, 2007, Table 7.8; Stevenson *et al.*, 2006). Climate change simulations with models including tropospheric chemistry indicate that an increase in stratosphere-troposphere exchange is a dominant driver of changes in tropospheric ozone (Stevenson *et al.*, 2006).

The recent projections of climate change considered by the IPCC (IPCC, 2007), which focus on the troposphere, are mainly based on the Coupled Model Intercomparison Project phase 3 (CMIP3) climate models, which have varying vertical resolution in the stratosphere. These models generally do not have substantial interactive chemistry, and they are not designed to predict changes to the ozone layer or the dynamics of stratosphere/troposphere coupling. Further many of the models contain constant ozone concentrations, and those which do represent ozone depletion generally specify zonal-mean ozone concentrations, which may make the climate response to specified ozone changes unrealistic (Crook *et al.*, 2008; Waugh *et al.*, 2009). The CCMVal models include good representations of the stratosphere and interactive ozone chemistry, and can therefore simulate changes to the ozone layer and coupling to climate change, though SSTs are in general specified, thereby constraining the surface climate response. In this chapter we use the CMIP3 models as a baseline against which to

Table 10.2: Model used for model validation.

	monthly (mean and interannual variability)	daily (synoptic variability)
CMIP3 (20C3M, AMIP)	CNRM_CM3, GFDL_CM2_1, GISS_MODEL_E_R, INMCM3_0, IPSL_CM4, MIROC3_2_HIRES, MIROC3_2_MEDRES, MPI_ECHAM5, MRI_CGCM2_3_2A, NCAR_CCSM3_0, NCAR_PCM1, UKMO_HADGEM1	CNRM_CM3, GFDL_CM2_1, GISS_MODEL_E_R, INMCM3_0, MIROC3_2_HIRES, MIROC3_ 2_MEDRES, MPI_ECHAM5, MRI_CGCM2_3_2A
CCMVal-1 (REF-1)	AMTRAC, CCSRNIES, CMAM, E39C, GEOSCCM, LMDZREPRO, MAECHAM4CHEM, MRI, SOCOL, ULAQ, UMETRAC, UMSLIMCAT, WACCM	
CCMVal-2 (REF-B1)	AMTRAC3, CAM3.5, CCSRNIES, CMAM, CNRM-ACM, E39CA, EMAC, GEOSCCM, LMDZrepro, MRI, NiwaSOCOL, SOCOL, ULAQ, UMSLIMCAT, UMUKCA-METO, UMUKCA-UCAM, WACCM	AMTRAC3, CCSRNIES, GEOSCCM, LMDZrepro, SOCOL, UMUKCA-METO, WACCM
CCMVal-2 QBO	CAM3.5, CCSRNIES, E39CA, EMAC, MRI, NiwaSOCOL, SOCOL, ULAQ, UMSLIMCAT, UMUKCA-METO, UMUKCA-UCAM, WACCM	CCSRNIES, SOCOL, UMUKCA-METO, WACCM

compare the CCMVal models: This allows us to assess the impacts on stratosphere-troposphere coupling of a better-resolved stratosphere and stratospheric processes.

In this chapter we will review stratosphere-troposphere coupling in the CCMVal models, and compare CCMVal simulations with observations and other models, such as the CMIP3 models. We will investigate what is required to realistically simulate stratosphere-troposphere coupling in climate models.

10.2 Validation of tropospheric and stratospheric climate

In this section we compare measures of mean climate and variability in the stratosphere and troposphere of the CCMVal-2 models with observations. Coupled chemistry-climate models generally have higher stratospheric resolution and more realistic stratospheric processes than conventional climate models, suggesting that their representation of stratospheric climate may be better. Given the notion that the stratosphere and the troposphere form a two-way interacting system, one might even argue that an improved stratosphere should lead to a superior troposphere. On the other hand, less attention is typically devoted to a realistic simulation of the troposphere when developing coupled chemistry-climate models (CCMs). In order to assess which of these different view-points is most appropriate, this subsection will use broad aspects of mean climate and climate variability to evaluate CCMVal-2 and other classes of climate models. The performance metric used here is based on zonal mean quantities describing the large-scale circulation and the temperature structure of the atmosphere.

Table 10.2 gives an overview of model output considered in this comparison. All available model output from the CCMVal-2 simulations is employed. In addition, results from CMIP3 (Meehl *et al*., 2007a) and the "First Chemistry-Climate Model Validation (CCMVal-1) (Eyring *et al*., 2007) are included. The CMIP3 data set contains simulations from all the major coupled ocean-atmosphere models around the world, compiled around 2005. The corresponding models were not specifically designed to resolve the stratosphere, and their stratospheric resolution, which varies greatly from model to model, is generally lower than that of the CCMVal-2 models. Thus, comparing CMIP3 with CCMVal should shed some light on the effects of a well-resolved stratosphere for the simulation of tropospheric climate.

The exact number of models examined depends on the type of analysis. Analysis based on monthly means includes 12 models from CMIP3, 13 models from CCMVal-1 (REF-1 experiment), and 18 models from CCMVal-2 (REF-B1 experiment). Some models provided multiple ensemble members; in this case all available members are used and appropriately combined into a mean outcome. Analysis of daily data is limited to fewer models because the necessary output was not provided by all models. The ERA-40 rean-

alysis (ERA-40, Uppala *et al*., 2005) is used as a reference against which the simulations are validated. The NCEP/NCAR reanalysis (NNR) is also used to provide an indication of uncertainty associated with the reanalysis method.

The performance metric used in this comparison is based on zonal means of zonal wind (u), meridional wind (v), and temperature (T). Clearly, it would have been desirable to include more than three quantities, but this was not possible because of the limited amount of archived model output. The above three quantities are examined from pole-to-pole and from the surface to the mid-stratosphere. In most of the analysis tropospheric (1000 - 200 hPa) and stratospheric (150 - 10 hPa) climate is investigated separately. The common base period for models and observations is 1979-1999, and three different categories of climate are investigated: (1) long-term means, (2) interannual variability, and (3) synoptic variability. Interannual variability is calculated from seasonal mean anomalies over the given number of years. Synoptic variability is calculated from daily high-pass filtered anomalies, derived by removing a low-pass filtered version of the daily data (using a Gaussian weighting with a "full width at half maximum" of 15 days) from the original daily data. Multi-model variability is computed by concatenating the anomaly time series from all participating models (and/or ensemble members) and then calculating variability. Before errors are calculated all model data are interpolated to the common grid of the validating ERA-40 reanalysis.

For each climate category and climate quantity two different measures of error are considered: First, the pattern correlation (r) between the simulated and observed spatial fields, and second, the normalised error variance (E^2) or root mean square error (E). E^2 is defined by

$$E^2 = \sum_{n=1}^{N} w_n d_n^2 \,, \qquad (10.1)$$

where w_n indicates appropriate weighting by the cosine of latitude, the layer thickness in log pressure (corresponding approximately to weighting each grid cell by its volume), and the number N of grid points, and d_n represents a (normalised) difference between simulated and observed fields at grid point n. For the analysis of mean climate, d_n is taken to be the difference between model and observation, normalised by the observed local interannual standard deviation. This can be written as

$$d_n = \frac{m_n - o_n}{\sigma_{n,o,\mathrm{inter}}} \,, \qquad (10.2)$$

where m and o represent the mean climate of model and observation, and σ denotes the observed interannual standard deviation (Reichler and Kim, 2008). For the analysis of climate variability, d_n represents the $\log_2$ variability ratio between model and observation, or

$$d_n = \log_2 \frac{m_n}{o_n} \,. \qquad (10.3)$$

Here, m and o are the standard deviations on interannual or synoptic time scales. With this definition, a perfect simulation has a variability ratio of zero, and positive or negative values indicate the factor by which a model over- or underestimates the observed variability. The above two definitions for d result in normalised and non-dimensional error estimates that can be compared across quantities.

In some of the analysis, the individual r and E^2 values for the different quantities and/or models are combined into an overall error estimate. This is accomplished by taking simple averages from the E^2 values. The correlations r, however, are combined by averaging their Fisher-z-transformed values and by applying the inverse Fisher-z-transform to the average.

The error calculations are carried out separately by quantity (u, v, T), season (January-March, JFM; October-December, OND), model, and also for the multi-model mean. The analysis is focused on the northern extra-tropics (30°N-90°N) during JFM and the southern extra-tropics (30°S-90°S) during OND. These two cases were chosen because they represent the time when and the region where the dynamical coupling between the stratosphere and troposphere is expected to be strongest (Baldwin *et al*., 2003). One should therefore expect that the possibility that the simulations of the stratosphere and the troposphere are related is maximised.

10.2.1 Multi-model mean comparison

The zonal mean cross sections in **Figure 10.1** present multi-model mean errors for zonal wind during JFM for mean climate and its interannual variability (results for individual CCMVal-2 models can be found in the electronic supplement). The errors shown are simple differences (*i.e*., $\bar{m}_k - o_k$ or $\log_2(\bar{m}_k/o_k)$) between the multi-model means ($\bar{m}$) and ERA-40.

Overall, the outcomes from the two CMIP3 experiments (20C3M and AMIP) are very similar, indicating that specifying observed SSTs has only a limited impact on the simulation of zonal winds. For mean climate, both CMIP3 experiments exhibit a pronounced positive wind bias extending down from the stratosphere into the troposphere. This leads to tropospheric jets that are too strong over the NH and equator-ward and upward shifted over the SH. The error patterns in interannual variability show large negative biases in the tropical stratosphere. This lack of variability is because most CMIP3 models do not simulate the Quasi-Biennial Oscillation (QBO). The CMIP3 models as a group also have a tendency toward too much variability over the SH extra-tropics.

The multi-model mean simulations of CCMVal-1 and CCMVal-2 are also quite similar, although biases tend to be somewhat smaller in the more recent CCMVal-2 models. Comparing CCMVal models against CMIP3 models

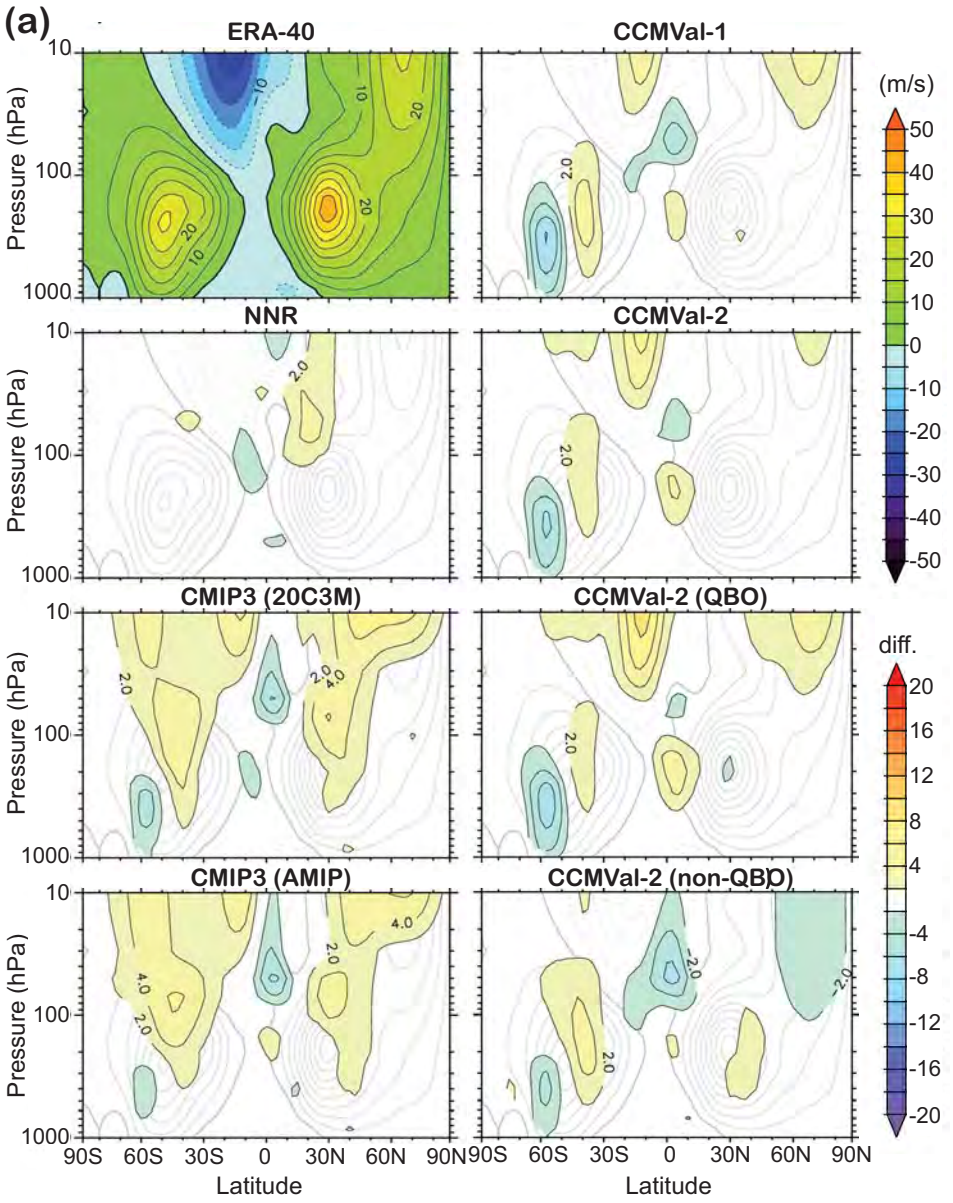

Figure 10.1: JFM multi-model errors in zonal-mean zonal wind. Errors are based on (a) mean climate and (b) interannual variability. The first panels show full fields (in m/s) from the validating ERA-40 reanalysis. The remaining panels show errors for the NCEP/NCAR reanalysis and for the various multi-model groups. Yellowish (bluish) colours indicate positive (negative) errors. Errors in (a) mean climate are differences drawn at 2 m/s intervals. Errors in (b) variability are $\log_2$-variability ratios drawn at 0.5 contour intervals. Grey contour lines indicate full fields from the validating ERA-40, shown in the first panels.

gives clear evidence that, overall, the stratosphere-resolving CCMVal models perform better in their simulations of mean stratospheric circulation. The CCMVal models also exhibit more realistic variability in the tropical stratosphere, even in those models without a QBO, although the CCMVal-2 models tend to exhibit a larger high bias in JFM SH stratosphere variability than the CMIP3 models, very likely associated with the delayed SH final warming seen in these models (Section 4.4.4). In the troposphere, the general problem of a shifted southern hemispheric jet is even more pronounced in the CCMVal models. In addition, the CCMVal models exhibit an even larger bias in interannual variability in the SH troposphere than the CMIP3 models. It also seems that the tropospheric wind simulations are somewhat more realistic in CMIP3, but the differences are quite subtle. This could be because more attention is focused on tuning the CMIP3 models to reproduce a realistic tropospheric climate than for the CCMVal-2 models.

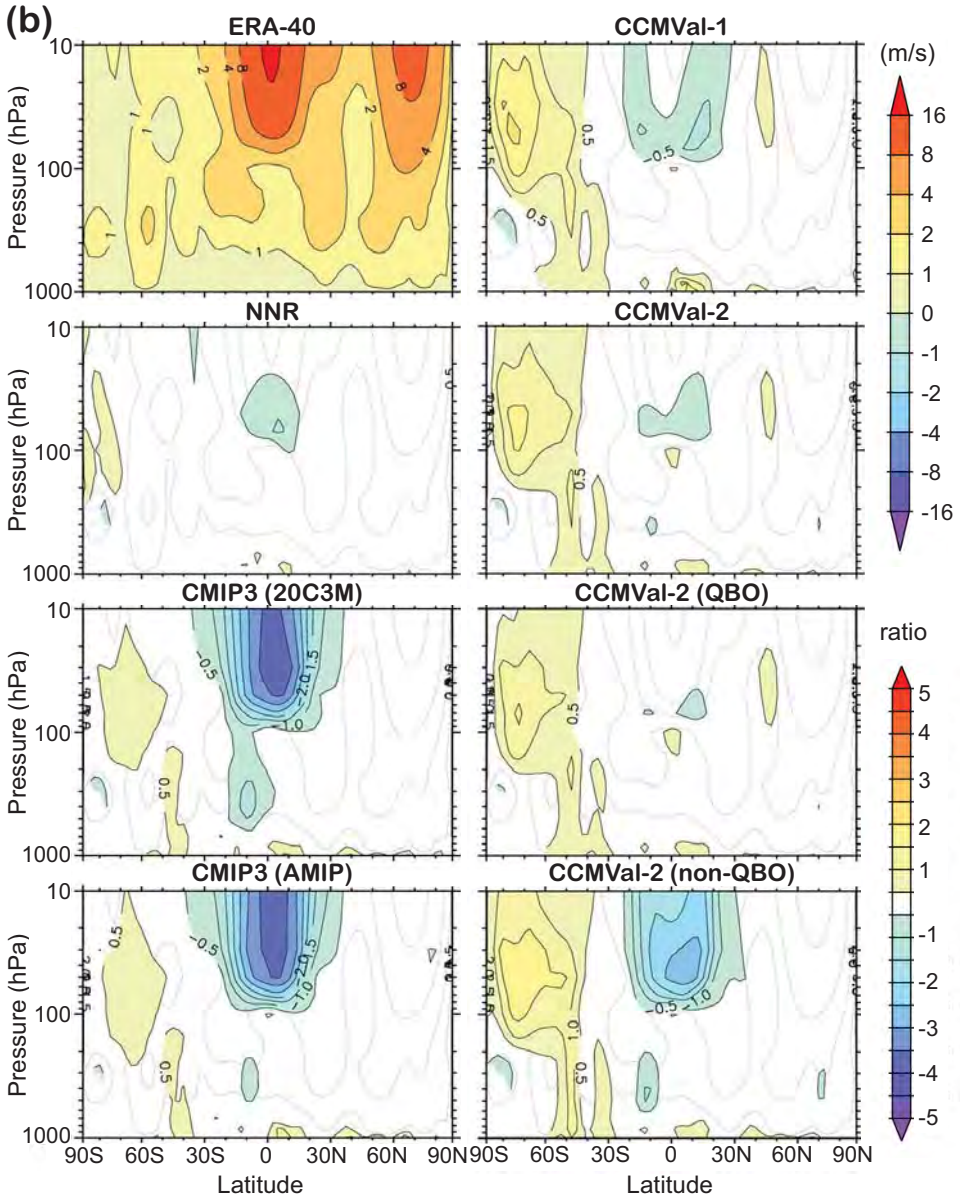

Figure 10.1 continued.

Stratifying CCMVal-2 into QBO-producing and non-QBO-producing models shows the expected impact on the interannual variability in the tropical stratosphere. This, however, does not seem to affect the extra-tropical interannual variability much, and the problem of a positive bias in variability over the SH exists in both model groups.

10.2.2 CCMVal-2 performance

The diagrams in **Figure 10.2** summarize the combined errors in zonal and meridional wind and temperature for the individual CCMVal-2 models. The *x* and *y* axes show the normalised root mean square errors *E*, and the pattern correlations *r*, such that the best performing models are located in the lower left corner. The grey contour lines combine *r* and *E* into a single skill index *S* according to

$$S = \frac{r^2}{1 + bE^2},$$

where the parameter *b* assigns a relative weight to the two error components *r* and *E*. Here, *b* is chosen such that *S* = 1% if *r* = 1 and *E* = 30.

Individual models are identified by the first two letters of their official model names (Table 10.2). The larger filled "2" symbols indicate the median of all models. Colour is used to discriminate six different aspects of model performance, hue indicates tropospheric (reddish) and stratospheric (bluish) performance, and colour intensity

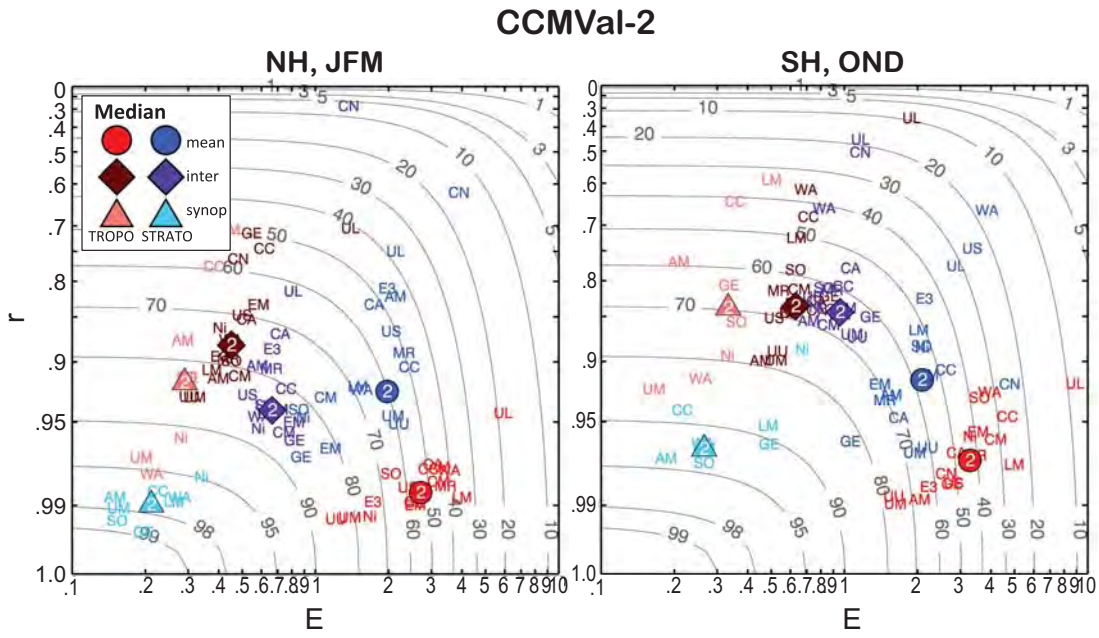

Figure 10.2: CCMVal-2 seasonal mean combined performance for u, v, and T. Performance is shown in terms of (y-axis) pattern correlation, (x-axis) nrms-error, and (gray contours) skill S (in %). Lower left (upper right) corner corresponds to best (worst) performance. Left panel is for NH (30°N-90°N) (January-March) and right panel is for SH (30°S-90°S) (October-December) extra-tropics. Blue (red) colours indicate stratospheric (tropospheric) performance. Colour intensity indicates: (light) synoptic variability; (dark) interannual variability; (medium) mean climate. Individual models are identified by first two letters of their official model names. US, UM, and UU denote UMSLIMCAT, UMUKCA-METO, and UMUKCA-UCAM, respectively. Large filled symbols denote median outcome of all models in one group.

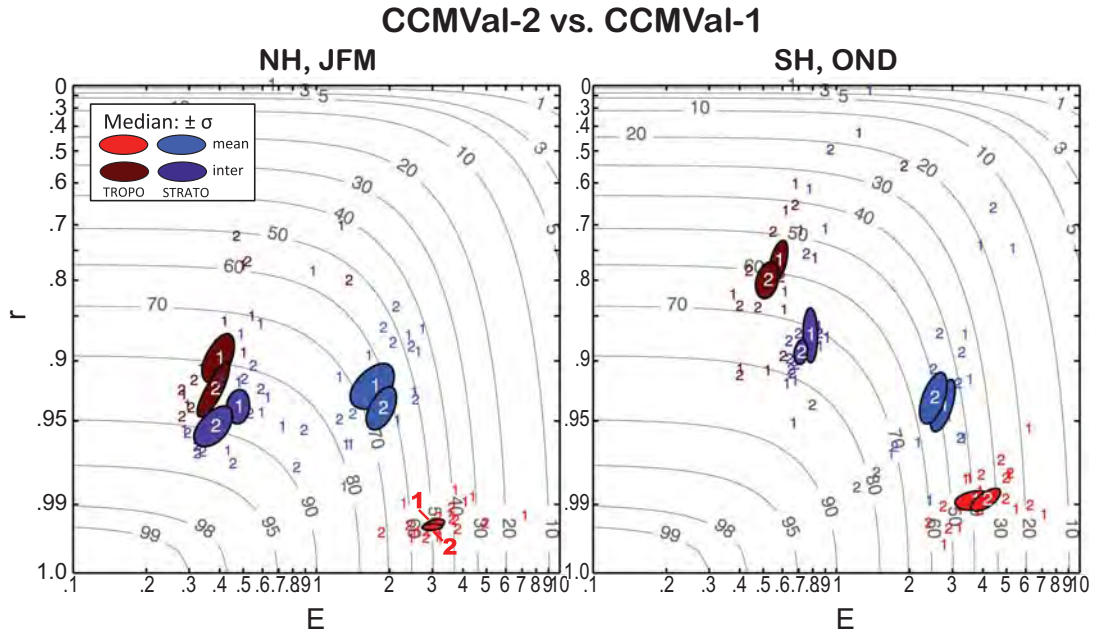

Figure 10.3: Comparison between CCMVal-2 and CCMVal-1 for u and T. Individual models are indicated by "1"s (CCMVal-1) and "2"s (CCMVal-2). Oval shapes indicate ±1σ uncertainty range of median performance for one model group. The shapes are ellipses that are distorted by the logarithmic scale of the axis. See the caption to Figure 10.2 for more details.

indicates performance for the three climate categories, *i.e.*, mean (medium), interannual variability (dark), and synoptic variability (light). Thus, each model's performance, and the multi-model means appear six times on each diagram.

The outcomes for the different climate categories tend to be well separated from each other. For example, stratospheric skill is generally higher than tropospheric skill, mean climate is usually associated with larger r and E values and interannual variability with smaller ones. Within each performance category, the variation of E and r leads to elongated structures of individual model outcomes. Models also tend to perform better over the NH during JFM (left) than over the SH during OND (right), which is in part related to the fact that the two diagrams represent different seasons (boreal winter and austral spring). However, taking all seasons together skill values are still generally higher over the NH than over the SH (not shown),

As indicated by the median outcomes ("2" symbols), overall the models match the observations quite well. In most cases, the pattern correlations exceed 70% and the root mean square errors amount to less than four standard deviations. This leads to skill scores of 50-70%. However, there are also some noticeable outliers. ULAQ underperforms in all categories of climate: in stratosphere and troposphere, over both hemispheres, and in mean climate as well as in interannual variability. CNRM-ACM performs well in the troposphere but underperforms in the stratosphere, which is likely related to the strongly equator-ward displaced jet in this model (Figure 4.3). WACCM performs poorly in the SH, which is likely related to a strong late bias in the final warming date for this model (Figure 4.27). In summary, these results suggest that there is a wide range of performances amongst the individual CCMVal-2 models, with some models clearly being identifiable as outliers.

As explained before, the model results represent means of all available ensemble members. However, outcomes for individual realizations for models that provide multiple members are very similar ($\Delta S < 5\%$, not shown), indicating that the results are robust. For clarity, the outcomes of validating NNR against ERA-40 are also omitted. However, the skill of NNR generally ranges between 80 and 99% and thus exceeds that of any individual model.

10.2.3 CCMVal-2 vs. CCMVal-1

CCMVal-2 is a continuation of the former CCMVal-1 project, and it is natural to ask whether the new features and improvements implemented in CCMVal-2 models also translate into better climate simulations. This issue is addressed in **Figure 10.3**. The diagrams here are similar to Figure 10.2 except that synoptic variability is omitted and that errors in meridional wind are not considered (both because of limited data from CCMVal-1). Another difference is that median outcomes are replaced by median uncertainty estimates. These estimates were derived by bootstrapping, *i.e.*, by randomly selecting the models included in the calculation of the median and by repeating this procedure many (1000) times. The resulting probability distributions were used to determine the $\pm 1\sigma$ median intervals, which are shown by the filled oval structures.

Figure 10.3 only includes models that participated in both the CCMVal-1 and the CCMVal-2 activity. Individual model outcomes are indicated by "1" and "2" for CCMVal-1 and CCMVal-2, respectively. In most cases there is overlap between the median uncertainty estimates of the two model groups, indicating that the performance differences between CCMVal-1 and CCMVal-2 are small. In particular, CCMVal-1 and CCMVal-2 produce tropospheric mean climate simulations (medium red) that are almost identical. In the other climate categories, however, CCMVal-2 tends to have somewhat higher skill, indicating slight, but non-significant, improvements of CCMVal-2 over its first generation predecessor.

10.2.4 CCMVal-2 vs. CMIP3

Figure 10.4 presents a comparison between CCMVal-2 and CMIP3. The average over all three climate quantities is displayed. In order to make the comparison fair, CMIP3 model output was derived from the AMIP-type experiment, meaning that both CCMVal-2 and CMIP3 models were forced with prescribed sea surface temperatures (SSTs) and sea ice.

From the median uncertainty estimates one can see that tropospheric mean climate and tropospheric synoptic variability are simulated quite similarly by the two model groups. In the other categories, however, CCMVal-2 generally outperforms CMIP3. This is perhaps to be expected in the stratosphere, but interannual variability in the troposphere over both hemispheres is also better simulated in CCMVal-2. We investigated whether this result is related to the simulation of a more realistic QBO by many CCMVal-2 models. However, stratifying CCMVal-2 into QBO and non-QBO producing models (not shown) does not support this hypothesis. These results provide clear evidence that the improved representation of stratospheric processes in the CCMVal-2 models gives an improved stratospheric climate relative to the CMIP3 models. Moreover, this improvement is not realized at the expense of tropospheric simulation quality.

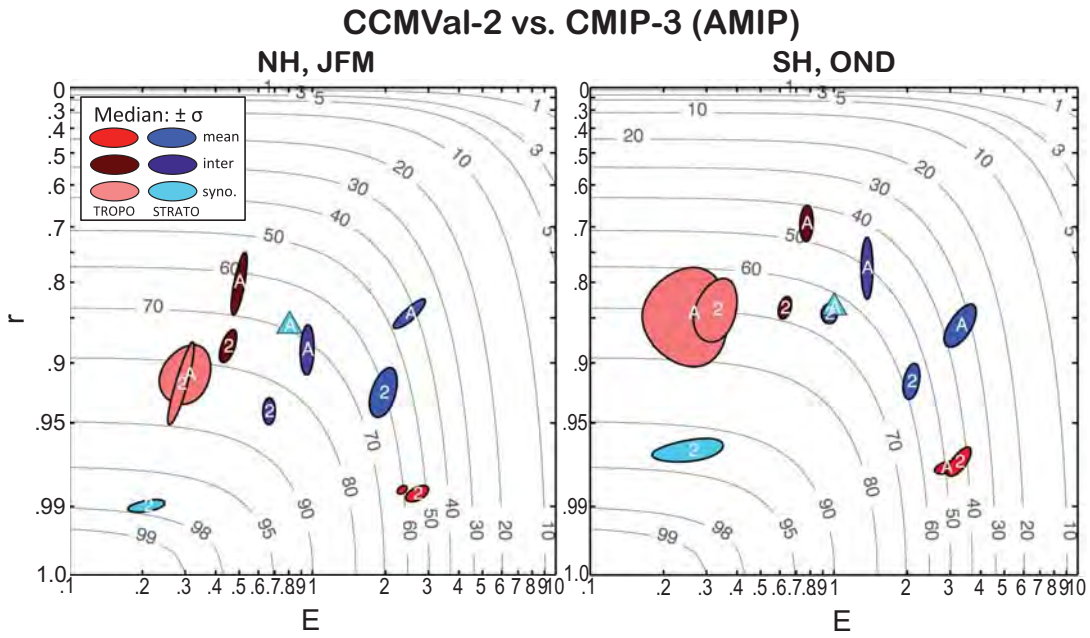

Figure 10.4: Median uncertainty comparison between CCMVal-2 (REF-B1) ("2") and CMIP3 (AMIP experiment) ("A") for u, v, and T combined. For clarity, individual model outcomes are not shown. For CMIP3, daily variability in the stratosphere is only based on the GFDL_CM2.1 model and thus the median estimate is replaced by a light blue triangle. See caption Figure 10.3 for additional information.

10.3 Evaluation of Stratosphere-Troposphere Coupling in Models

10.3.1 Downward propagation of Annular Mode anomalies

Baldwin and Dunkerton (1999, 2001) demonstrated that circulation anomalies originating in the stratosphere propagate downward and influence the tropospheric circulation for up to two months. In this subsection the downward propagation of circulation anomalies in the CCMVal-2 models is examined using time series of the annular mode indices. The Northern Annular Mode (NAM) and Southern Annular Mode (SAM) at each pressure level are defined here as the first Empirical Orthogonal Functions (EOFs) of the daily zonal-mean geopotential height between the equator and the respective pole, weighted by the square root of the cosine of latitude. Before the analysis, the global-mean geopotential height is removed each day and a slowly-varying seasonal climatology is also removed (Gerber *et al*., 2010). The seasonal cycle (smoothed by a 30 day running mean) and linear trends are removed from the height fields before the analysis. The annular mode indices are computed by projecting the area-weighted daily geopotential height anomalies onto the EOF patterns, and are normalised to have unit variance. For the model integrations, the annular modes were calculated from one realization of the REF-B1 scenario. The indices from all integrations of a given model were then computed by projecting the de-trended geopotential height anomalies onto this pattern. As the annular mode statistics appear to be relatively insensitive to climate trends, we use all REF-B0, -B1, and -B2 scenario integrations available to maximise the sample size. ECMWF and NCEP-NCAR reanalyses were analysed from 1958–2008 in the NH and 1979–2008 in the SH, due to the poor quality of the reanalyses prior to the advent of satellite observations in the SH.

Daily mean (or instantaneous) fields are provided by nine CCMVal-2 models (REF-B1 simulations). For those models which provided multiple realizations the time series were constructed by concatenation of all available realisations. We also use output from BCCR-BCM2.0, GFDL CM2.0 and GFDL CM2.1, the only CMIP3 models that provide daily geopotential height data. These are low top models with upper layers at 10 hPa, 3 hPa and 3 hPa respectively. Following Baldwin and Dunkerton (2001) and Thompson *et al*. (2005), we show composite differences of strong and weak stratospheric annular mode events. The strong (weak) events are determined by the dates on which the 10-hPa NAM index cross the ±2 standard deviation threshold. Only one event per year (the one with the largest magnitude) is chosen because the time scale of the events is comparable to the length of the dynamically active season.

Figure 10.5 shows a comparison of composite differ-

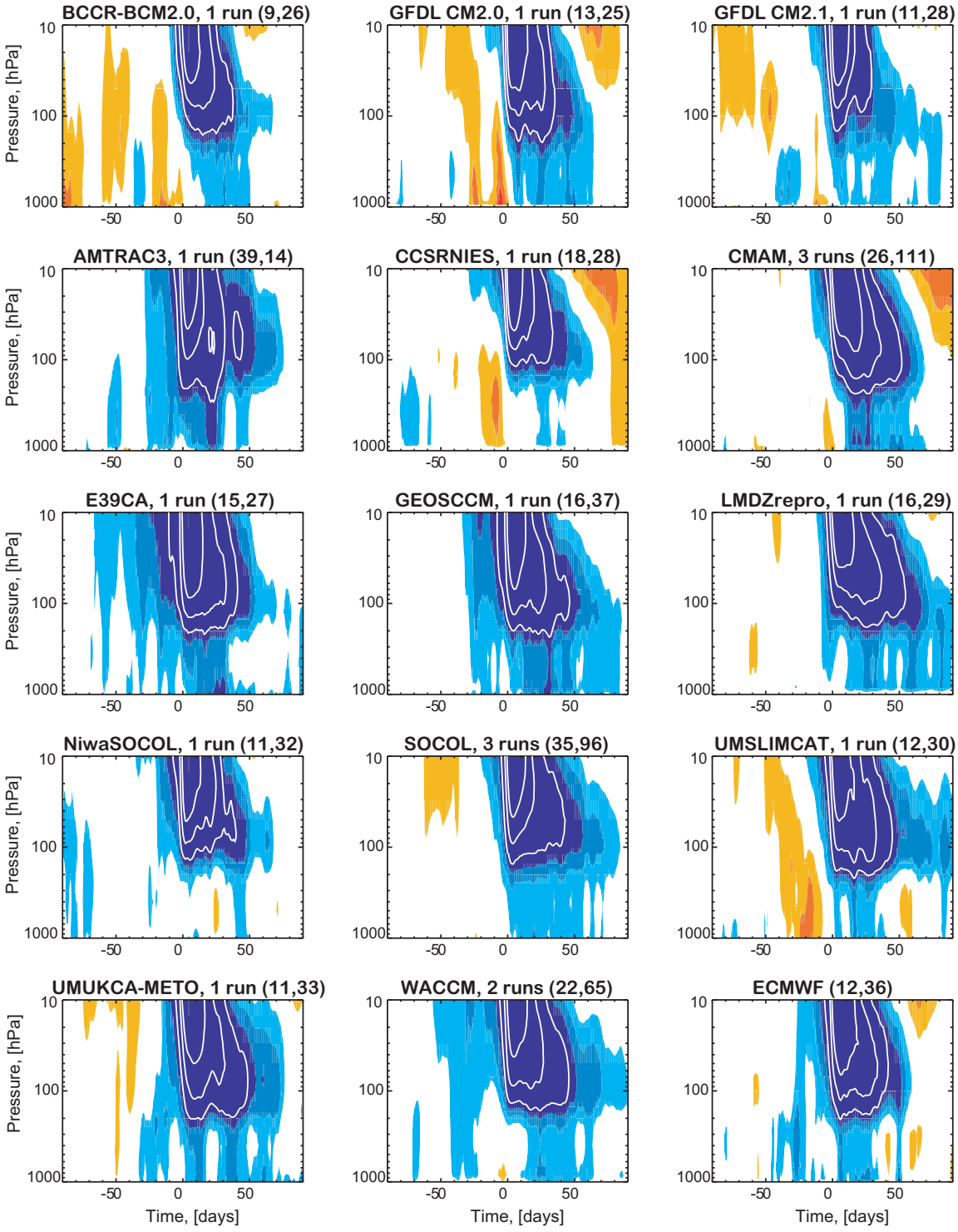

Figure 10.5: Composite differences of the standardized NAM index between strong and weak stratospheric events. Results are shown for three CMIP3 models for which suitable daily data were available (top row), eleven CCMVal-2 models (REF-B1 simulations) with daily data available, and the ERA-40 reanalysis. Day 0 corresponds to the onset of the stratospheric event at 10 hPa. Shading interval is at 0.5 standard deviations and contour interval is at 1 standard deviation. Shading is drawn for values exceeding 0.5 standard deviations. Blue shading denotes positive values in the NAM index. Numbers above each panel indicate numbers of strong and weak events included in the composite.

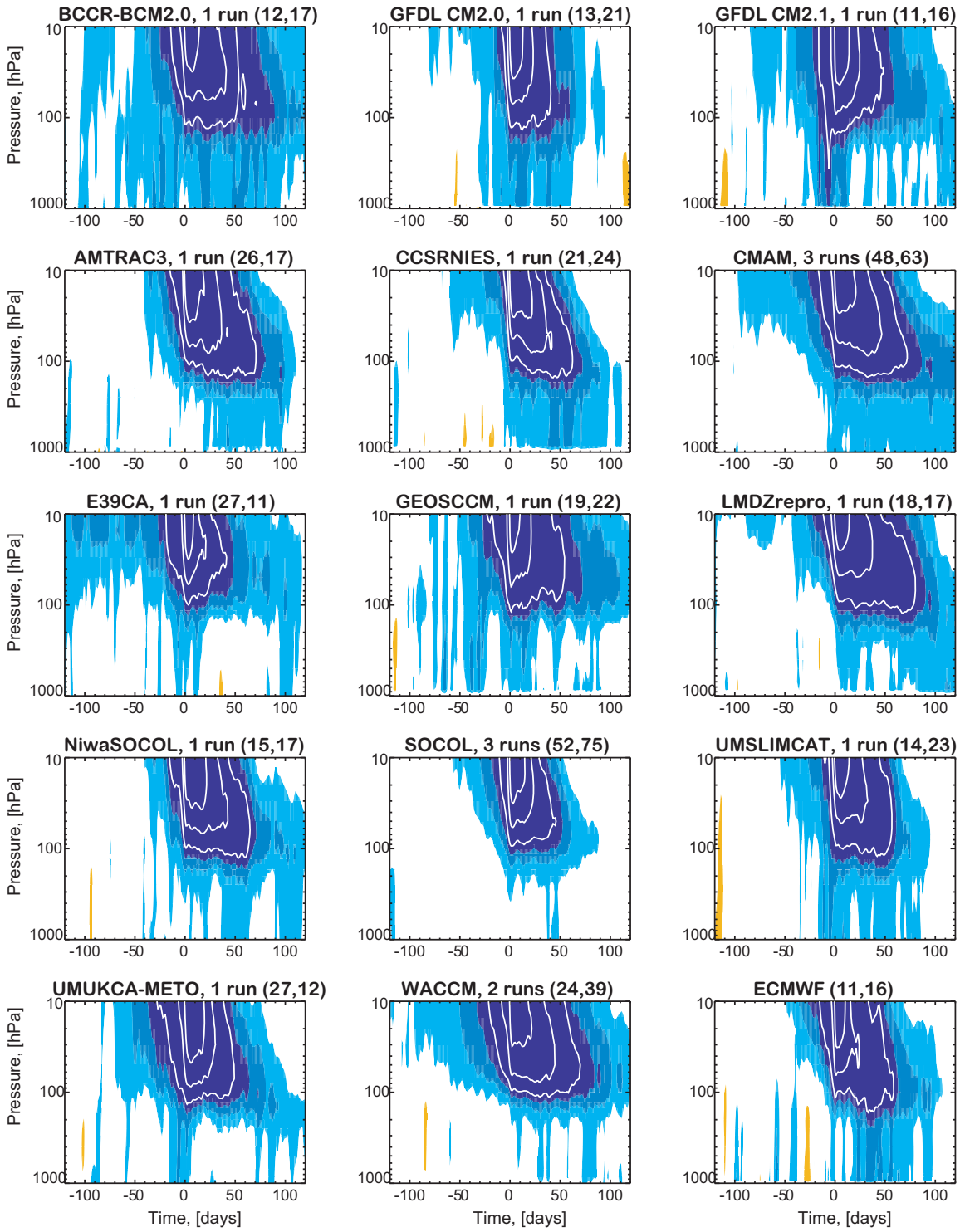

Figure 10.6: Composite differences of the standardized SAM index between strong and weak stratospheric events. Results are shown for three CMIP3 models for which suitable daily data were available (top row), eleven CCMVal-2 models (REF-B1 simulations) with daily data available, and the ERA-40 reanlaysis. Day 0 corresponds to the onset of the stratospheric event at 10 hPa. The shading interval is 0.5 standard deviations and contour interval is 1 standard deviation. Shading is drawn for values exceeding 0.5 standard deviations. Blue shading denotes positive values in the SAM index. Numbers above each panel indicate numbers of strong and weak events included into the composite, and are lower for ERA-40 because observations were taken solely from the period 1979-2008.

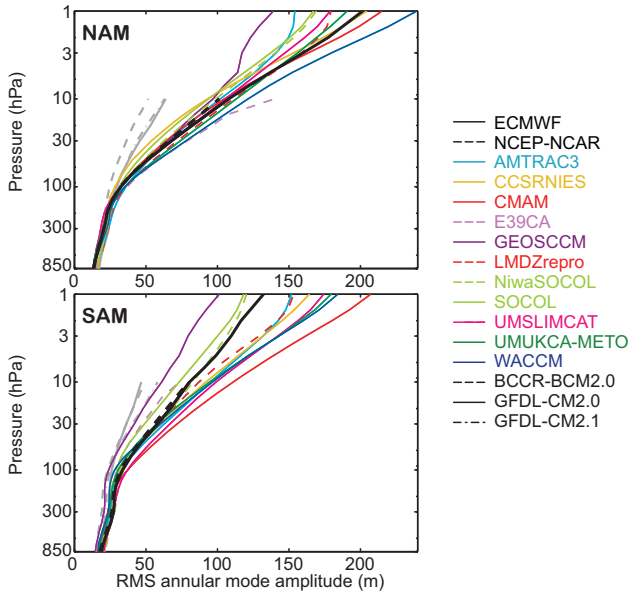

Figure 10.7: The RMS amplitude of the annular mode pattern of variability as a function of pressure in the (top) NH and (bottom) SH. Analysis of three CMIP3 models (gray lines) are included for reference.

ences of the NAM index for ERA-40 data and ten models. The models capture the downward propagation of NAM anomalies, including the low-top CMIP3 models. Given the relatively short (50 year) observational period and model runs, there is a lot of sampling noise in the troposphere, and no significance can be attached to the short-period variations in the troposphere. However, a comparison of similar plots based on multiple ensemble members from one model (not shown) indicates that inter-model differences are in most cases larger than differences between ensemble members from the same model. All models show that large anomalies tend to extend downward to near the tropopause, as in the observations. In some models (most clearly in GEOSCCM and LMDZrepro), the anomalies in the lower stratosphere and troposphere tend to last too long compared with observations (see also Section 10.3.2). **Figure 10.6** shows composite differences of the SAM index between strong and weak SAM events. After the peak at 10 hPa, the anomalies descend to the lower stratosphere in both ERA-40 and the models. In ERA-40, the tropospheric anomalies peak 30-40 days after the onset of the event at 10 hPa, with values exceeding 1.5 standard deviations, and persist for at least three months after the onset. All the models reproduce tropospheric anomalies following the stratospheric events. As in the NH, some models (BCCR-BCM2.0, CMAM, GEOSCCM, and LMDZrepro) show noticeably longer persistence of the anomalies in the lower stratosphere compared with the observations.

10.3.2 Annular mode time scales and predictability

We first quantify the amplitude of the annular mode (AM) variability as a function of height in **Figure 10.7**. All CCMVal-2 models simulate the amplitude of the annular modes in the stratosphere more accurately than the three CMIP3 models for which upper atmospheric output is available. The improvements are particularly evident in the NH. Nearly all CCMVal-2 models correctly capture the increased variance of the NAM relative to the SAM, while the CMIP3 models incorrectly have larger AM amplitudes in the SH. There is substantially more spread between the models and reanalyses in the SH, suggesting less agreement between models in representing SH dynamics. This is consistent with differences in the temporal variability, as documented below.

Figure 10.8 compares the seasonal and vertical structure of the annular mode variance in the ECMWF reanalysis and the multi-model ensemble mean. The models, both as a group and individually (not shown), simulate the structure quite well, capturing the marked asymmetry of the AM seasonal cycle between the two hemispheres. The seasonal cycle in models, however, is slightly delayed in both hemispheres, particular in the lower stratosphere. This is likely a consequence of a delayed break down of the vortex, and, in the NH, of limited variability in the early winter (see Figure 4.27).

The models capture the qualitative structure of the annular mode temporal variability, as seen in the seasonal and vertical evolution of the AM *e*-folding time scale in **Figure 10.9**. This time scale is found by computing a seasonally localized autocorrelation function at each pressure level and calendar date, which is then fit to an exponential function (Baldwin *et al.*, 2003). It thus provides a rough estimate of the persistence of AM anomalies. It is important to interpret these time scales in the context of the variance structure shown in Figure 10.8. The time scales are most meaningful when the AM is active; the extreme persistence in the NH summer, for instance, occurs during a period when there is almost no variability of the NAM, and could be due to very small variations in total column ozone left over from the previous winter (Fioletov and Shepherd, 2003). The models simulate the NH-SH asymmetry in the seasonal cycle of the AM *e*-folding time scale, both in the troposphere and lower stratosphere, and the tendency towards longer time scales in the SH. The models, however, overestimate the time scales, particular in the SH (note the nonlinearity of the colour scale). The biases in the troposphere are similar to those found in the CMIP3 models (Gerber *et al.*, 2008). In addition, the seasonal cycle of the time scales is delayed and broadened in both hemispheres.

Comparison between Figures 10.8 and 10.9 suggests a close relationship between increased *variance* of the AM

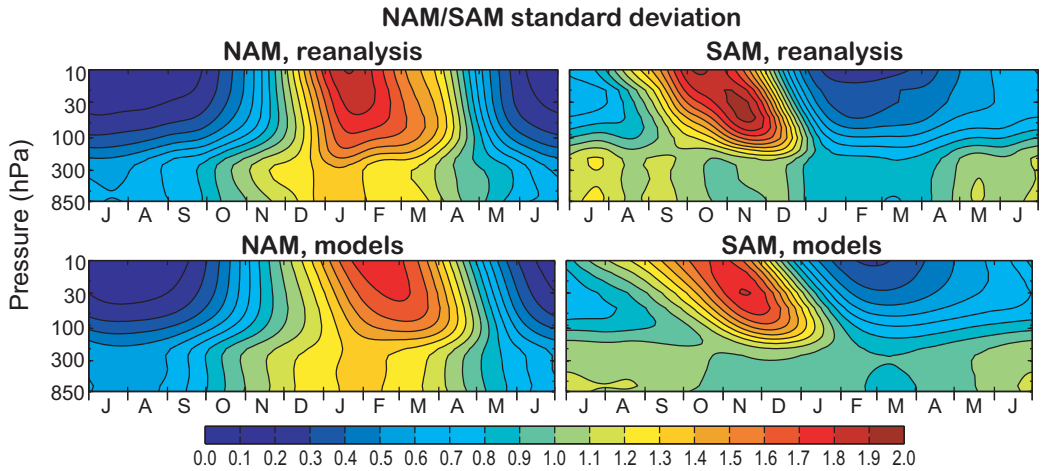

Figure 10.8: The variance of the NAM and SAM indices as a function of seasonal and height: (top) ECMWF reanalysis and (bottom) the multi-model ensemble mean. Note that the indices have been normalised to have unit variance at all levels, removing the systematic increase in variance with height shown in Figure 10.7.

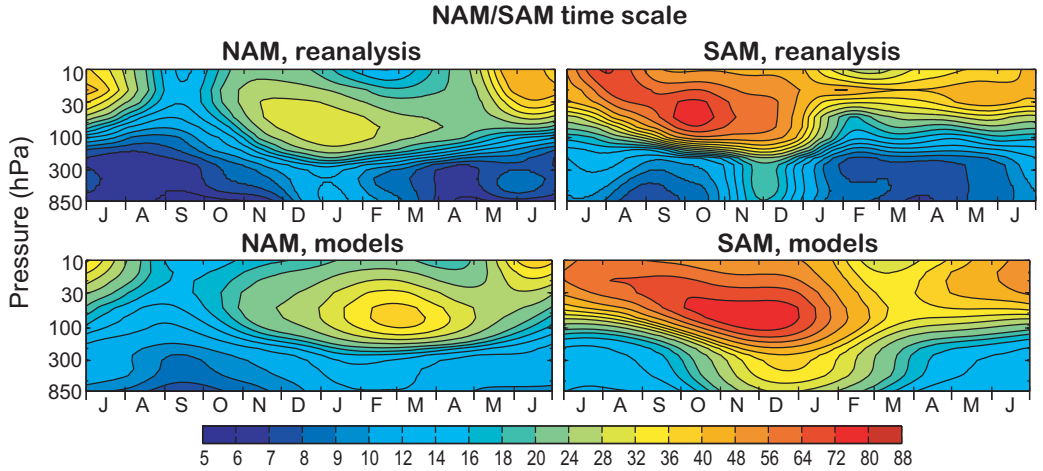

Figure 10.9: The e-folding time scale of the NAM and SAM indices as a function of seasonal and height: (top) ECMWF reanalysis and (bottom) the multi-model ensemble mean.

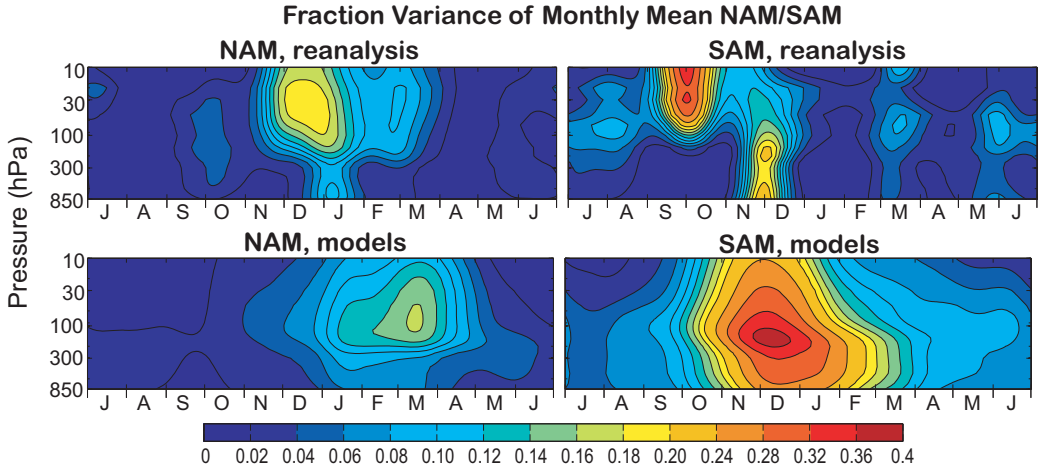

Figure 10.10: The fraction of the variance of the monthly mean 850 hPa AM index, lagged by 10 days, that is linearly correlated with the instantaneous AM index as a function of season and height: (top) ECMWF reanalysis and (bottom) the multi-model ensemble mean.

in the lower stratosphere and increased *persistence* of the AM in the troposphere in both the reanalysis (as observed by Baldwin *et al*. (2003)) and in the models. One does not find this connection between variance and persistence of the AM in the troposphere alone. This suggests that the tropospheric AM becomes more persistent when there is stronger variability in the stratosphere; at these times, the longer time scales of the lower stratosphere can impact tropospheric persistence.

To confirm this connection between the lower stratosphere and troposphere, we repeat the analysis of Baldwin *et al*. (2003, *c.f*. Figure 2). **Figure 10.10** plots, as a function of height and season, the fraction of the variance of the next month's mean 850 hPa AM index, lagged by 10 days, that can be "predicted" from a persistence forecast based on today's instantaneous AM index. For example, the bullet of increased variance in the NH winter stratosphere suggests that information about the state of the NAM between 30 and 100 hPa is more useful for making forecast of next month's near surface NAM than knowledge of the near surface NAM itself. The consistency of the model biases toward a later seasonal cycle – in variance, time scales, and predictability – is particularly striking in the NH, and suggests that these phenomena are closely related. The predictability relationship in the SH is less clear. With the reanalysis, we have restricted analysis to the satellite era, which is a relatively short period leading to more uncertain correlations. With the models, the bias towards very long time scales leads to spurious predictability. Nonetheless, there is evidence of delayed and downward coupling between the lower stratosphere and the near surface, likely associated with the final warming of the vortex.

Gerber *et al*. (2008) found that the AM time scales in the CMIP3 models were relatively insensitive to climate trends. To assess the stability of the annular mode statistics in the CCMVal-2 models, we compared the late 20th century AM statistics (variance, time scales, and correlation structure) of the REF-B1 integrations with those based on the last five decades of the 21st century in the REF-B2 integrations (not shown). In general, we find that the statistics do not change much. The most significant exception is found in the variance structure of the SH stratosphere, where the period of peak variance shifts earlier in the season and weakens slightly. This is most likely due to the recovery of the ozone hole, which warms the spring/summer stratosphere, producing an earlier and more regular transition from westerlies to easterlies. In the NH, there is evidence that the peak AM time scales and the correlation structure shift earlier in the seasonal cycle, which could indicate increased variability in the winter and an earlier breakdown of the vortex. We note that the models have trouble getting the timing of the seasonal cycle correct in the observed period, so we must be cautious of over-interpreting these trends. In both hemispheres, however, these trends make the late 21st century simulations less biased compared to 20th century observations than the 20th century simulations themselves.

Up to this point we have focused on similarities in the model results. There is, however, significant spread between models. The AM *e*-folding time scales of each model at 100 and 500 hPa are shown in **Figure 10.11**. Individual models robustly capture the seasonal cycle of variability in both hemispheres, with the possible exception of the NH troposphere; the seasonal cycle of the tropo-

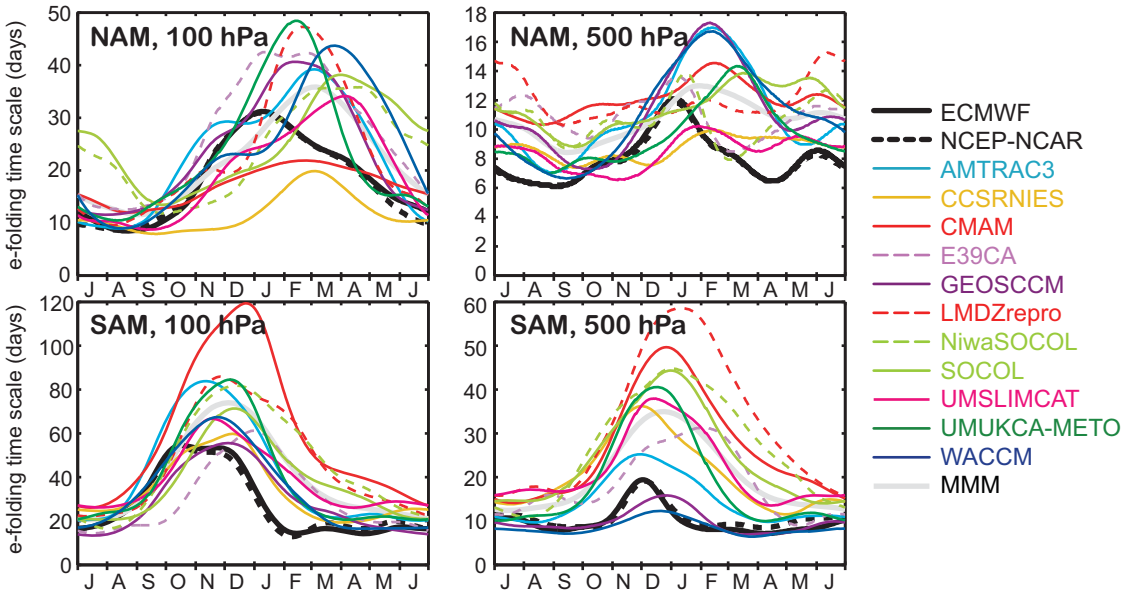

Figure 10.11: The annular mode e-folding time scale (left) in the lower stratosphere and (right) mid-troposphere as a function of season for the CCMVal-2 models: (top) NH, (bottom) SH.

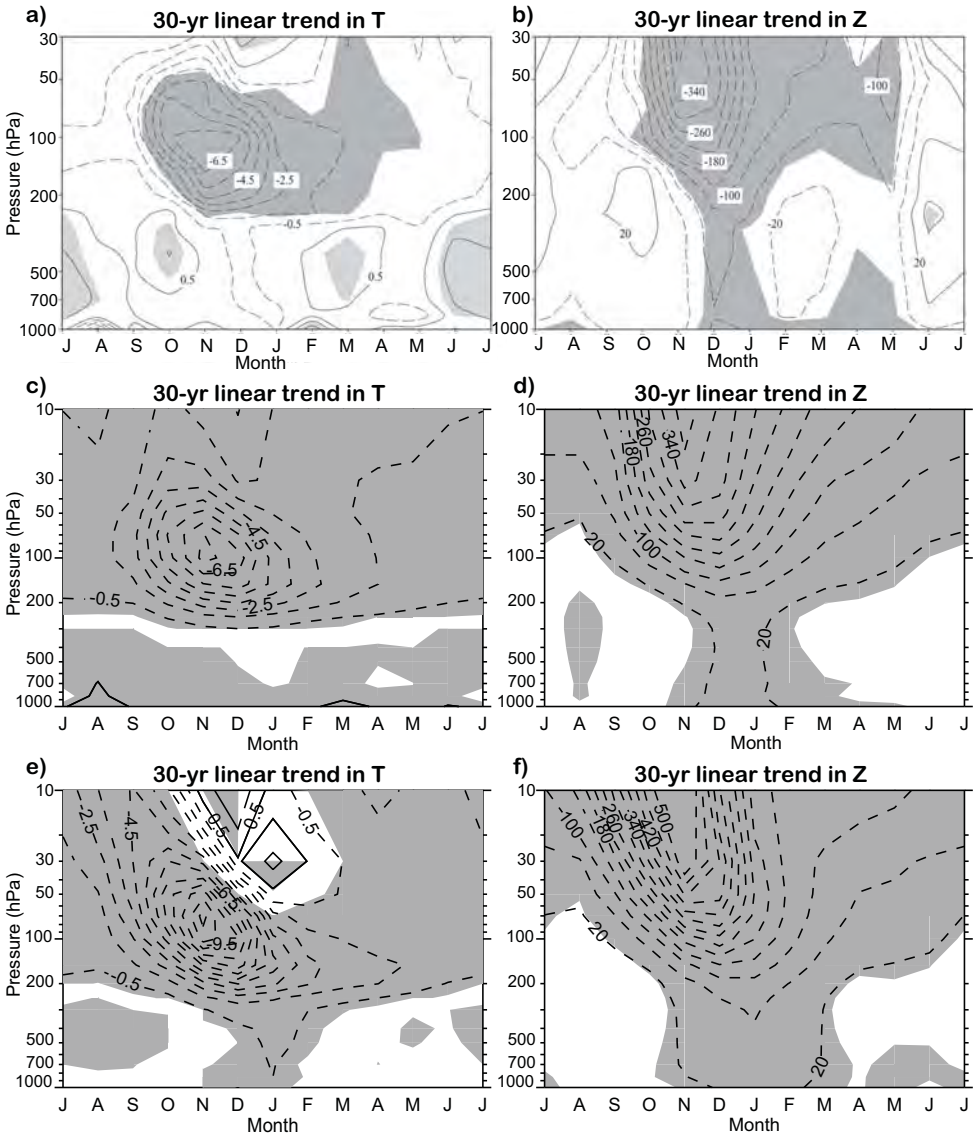

Figure 10.12: Seasonal cycle of linear trends (1969-1998) in (a,c,e) temperature (K per 30 years) and (b,d,f) geopotential height (m per 30 years) over the Antarctic. (a,b) observations (c,d) CMIP3 ozone ensemble average (e,f) CCMVal-2 (REF-B1) ensemble mean. Shading denotes trends that exceed one standard deviation of the respective monthly time series. The models used here are those listed in Figure 10.13 except HadCM3, whose simulations were driven by erroneously prescribed ozone forcing.

spheric NAM, and evidence of downward coupling, are less clear in some models. It is also evident that the delay in the seasonal cycle and overestimation of time scales is a common bias. The SAM time scales vary by a factor of 2 in the stratosphere and a factor of 4 in the troposphere. It should be noted that GEOSCCM and WACCM, however, appear to match observations well. The vertical structure of their temporal variability (and that of many models) however differs slightly from observations. As seen in Figure 10.9, the SAM time scales in the reanalysis are relatively barotropic in the troposphere, while models tend to exhibit weaker persistence in the lower troposphere. We also note that their appears to be little correlation between model biases in the NH and SH. For example, GEOSCCM and WACCM, noted above for their short SAM time scales, exhibit among the longest tropospheric NAM time scales.

The overestimation of time scales in the SH may influence the sensitivity of the models to external forcing, as suggested by the Fluctuation-Dissipation theorem (Gerber *et al*., 2008). In particular, the tropospheric jets in models with long time scales may be more sensitive to external forcing. The biases and spread between the models suggest errors in model dynamics, especially in the SH, where coupling between the stratosphere and troposphere and/

or between eddies and the mean flow may be too strong. Lastly, the unrealistic SAM time scales in the troposphere of many models may have implications for their representation of regional climate variability, particularly in the mid-latitudes.

10.4 Simulations of stratospheric influence on the troposphere in the past and future

10.4.1 Dynamical effects

10.4.1.1 Southern Hemisphere

The most often discussed and perhaps most important mode of influence of long-term stratospheric changes on the troposphere are the effects of changes in the stratospheric circulation on the tropospheric circulation, or dynamical effects. The last decades of the 20th century were marked by a significant change in the Antarctic tropospheric circumpolar circulation, with strengthening westerly winds and decreases in Antarctic geopotential height (Thompson and Solomon, 2002). The trends were largest in summer, lagging by 1-2 months similar trends in the stratosphere, which suggests a possible stratosphere-to-troposphere influence.

Figure 10.12 shows ensemble-averaged 1969-1998 temperature and geopotential height trends in the Antarctic in observations (Thompson and Solomon, 2002), in 13 CMIP3 models that include stratospheric ozone depletion, and in 17 CCMVal-2 models (REF-B1 simulations). Here and elsewhere in this chapter, trends shown are linear least squares trends. See **Figure 10.13** for the models and the number of realizations used. Consistent with the observations and CMIP3 simulations, the CCMVal-2 simulations show a maximum cooling at close to 100 hPa in November. However, the magnitude of the cooling is rather larger in the CCMVal-2 model mean, reaching 11 K, as opposed to ~7 K in the observations and the CMIP3 models. This discrepancy between models and observations is reduced by ~1 K if each model (rather than each simulation) is given equal weight, it is further reduced if the cooling is averaged over October-January at 100 hPa, and it is further reduced if the cooling is averaged over the whole of the Antarctic rather than at the locations of the radiosonde stations (see below). There is a large spread in this simulated cooling across the model ensemble, and no consistent bias in total ozone trend across the ensemble, but there is some indication that the CCMVal-2 models tend to simulate a larger stratospheric cooling for a given September-December total ozone trend compared to observations or the CMIP3 simulations (Figure 10.13). Note however, that the observed ozone trend used here is based on data from a single station (Halley), and therefore is relatively uncertain, and likely different to the Antarctic mean trend. EMAC,

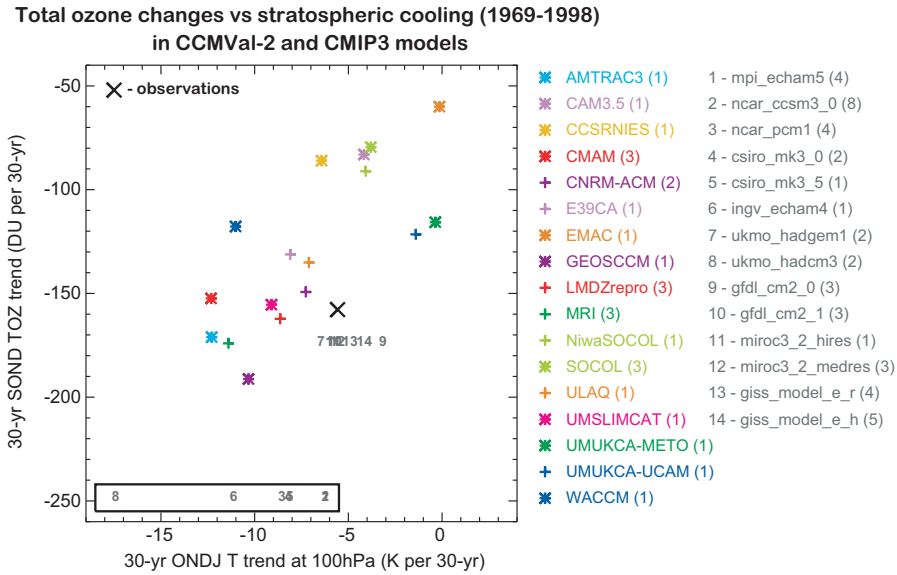

Figure 10.13: 30-yr trends (1969-1998) in Antarctic September-December total ozone versus the October-January temperature trend at 100-hPa in 17 CCMVal-2 (REF-B1) models, 14 CMIP3 models including stratospheric ozone depletion, and observations. Observed temperature trends are based on Thompson and Solomon (2002) and ozone trends are based on measurements at Halley. CMIP3 ozone trends are shown for those models using Randel and Wu (1999) ozone. The temperature trends for CMIP3 models whose driving ozone trends were not reported or not available are shown in the black box in the lower part of the plot.

UMUKCA-METO, and UMUKCA-UCAM simulate too weak a stratospheric cooling and EMAC also simulates a total ozone trend that is too weak. The CCMVal-2 models also simulate a warming overlying the ozone-induced cooling, which is likely dynamical in nature (*e.g.*, Manzini *et al.*, 2003), and is just visible in the radiosonde observations, while being absent in the CMIP3 simulations, perhaps because of their limited stratospheric resolution.

The focus of this chapter is on coupling to the troposphere, and the second column of panels in Figure 10.12 shows that the simulated decrease in geopotential height is not limited to the stratosphere, but is also simulated in the troposphere, reaching a maximum in January in the CCMVal-2 models, two months after the maximum stratospheric cooling, and three months after the maximum stratospheric ozone depletion. Thus, consistent with earlier modelling studies (Gillett and Thompson, 2003; Arblaster and Meehl, 2006; Shindell and Schmidt, 2004; Karpechko *et al.*, 2008), the CCMVal-2 simulations simulate a clear downward propagation of the response to ozone depletion from the stratosphere to the troposphere. The tropospheric geopotential height response is somewhat weaker than that observed, but somewhat stronger than that simulated by the CMIP3 models. Concurrent with the tropospheric geopotential height response, and despite the prescribed SSTs in all but one model, the CCMVal-2 models simulate a tropospheric cooling over the Antarctic, consistent with the observed non-significant tropospheric cooling trend. The ensemble-mean cooling trend is larger than that simulated by the CMIP3 models, perhaps because of the larger cooling in the stratosphere.

Figure 10.14a shows ensemble mean zonal wind changes in the CCMVal-2 ensemble, and demonstrates that the historical simulated wind changes correspond to a poleward shift of the SH tropospheric jet in DJF. The ensemble mean simulated trends in the satellite era are remarkably similar to those estimated from reanalysis data, although the magnitude of the tropospheric trends is somewhat under-estimated (reanalysis data not shown).

Figure 10.16a shows that the simulated Antarctic cooling at 100 hPa in the CCMVal-2 models and CMIP3 models with ozone depletion agrees well with the observations, when averaged over October-January and with equal weight given to each model. Observations of October Antarctic column ozone depletion lie within the spread of CCMVal simulations (Chapter 9). A close correlation is seen between SOND ozone depletion and the ONDJ 100-hPa Antarctic temperature trend (**Figure 10.15a**), and a similarly high correlation is seen with the DJF tropopause pressure trend (Figure 10.15b). Cooling in the lower stratosphere increases the temperature lapse rate near the tropopause, pushing the height of 2 K/km temperature lapse rate upward (this lapse rate is used to define the tropopause here) (Santer *et al.*, 2003; Son *et al.*, 2009a).

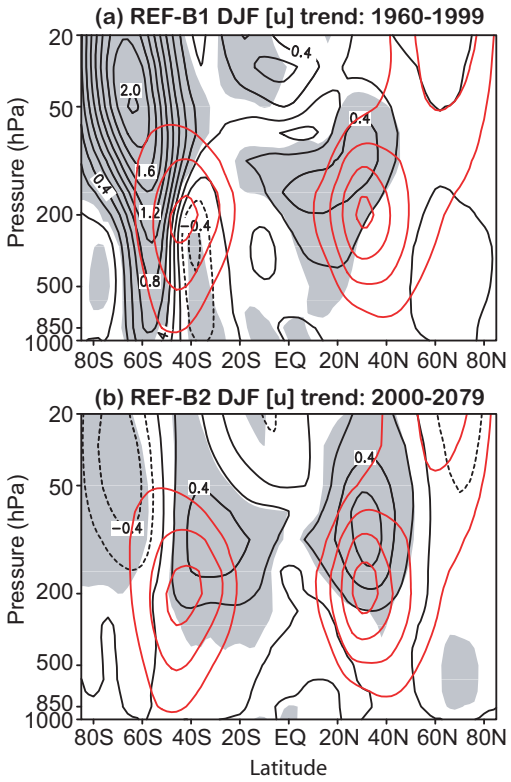

Figure 10.14: Long-term mean (orange) and linear trend (black contour) of the DJF-mean zonal-mean zonal wind (a) for the time period of 1960-1999 in REF-B1 runs, and (b) for the time period of 2000-2079 in REF-B2 runs. Contour intervals are 10 m/s starting from 10 m/s for climatology and 0.2 m/s/decade for trend. Zero lines are omitted and values greater than one standard deviation are shaded.

Figure 10.15c shows the latitudinal shift of the wind maximum in DJF at 850 hPa in each of the CCMVal-2 models and demonstrates that this is correlated with the SOND ozone depletion simulated in the same model, indicating that the amount of stratospheric ozone depletion is the dominant factor controlling the size of the tropospheric circulation change in each model. Past trends in the DJF tropospheric circulation have clearly been forced in part by ozone, though part of the trend has also been attributed to increasing greenhouse gases (Marshall *et al.*, 2004; Arblaster and Meehl, 2006). While increasing greenhouse gases in the future are expected to lead to a further poleward intensification of SH tropospheric winds in DJF, future ozone recovery is expected to act in the opposite sense (*e.g.*, Son *et al.*, 2008). Figure 10.15a demonstrates that at 100 hPa in the future, stratospheric ozone recovery exerts the dominant influence on stratospheric temperature, with a simulated warming which is approximately proportional to the amount of ozone recovery simulated in the first half of the 21st century (Son *et al.*, 2008). However in the troposphere the effect of ozone recovery on the circulation is

likely to be largely cancelled out by the effect of greenhouse gas increases in DJF, and no significant shift in the jet location at 850 hPa is seen (Figure 10.14b and 10.15c). Figure 10.16b contrasts the shift in the tropospheric jet in the 21st century simulated in the CCMVal-2 models with that simulated in the CMIP3 models with and without changes in stratospheric ozone. Those CMIP3 models with no future ozone changes, but continued greenhouse gas increases simulate a southward shift in the DJF jet location, in contrast to little change in the jet location in those CMIP3 models with specified ozone recovery and in the CCMVal-2 simulations. Note that, in contrast to CCMVal-1 (Son *et al.*, 2008), there is only a small and non-significant northward shift in DJF jet location in the 21st century in the CCMVal-2 ensemble mean. The reason for this difference in behaviour between the CCMVal-1 and CCMVal-2 simulations remains to be determined. The jet location trends simulated in the 21st century in the CCMVal-2 models are consistent with those simulated in the CMIP3 models with stratospheric ozone recovery (Figure 10.16).

Figure 10.16c demonstrates that both CCMVal-2 models and CMIP3 models simulate a poleward expansion of the SH Hadley cell in the last decades of the 20th century (Lu *et al.*, 2007; Seidel *et al.*, 2008). Changes in the width of the Hadley Cell are of particular interest because of their potential impacts on precipitation patterns (Seidel *et al.*, 2008). Previous research has mainly focused on the role of greenhouse gases in forcing this trend, but the results presented here both for the CMIP3 models with and without ozone depletion (Figure 10.16c), and for the CCMVal-2 simulations (Figure 10.15d and Figure 10.16c), demonstrate an important role for stratospheric ozone depletion in driving the broadening of the Hadley Cell in DJF (see also Son *et al.*, 2009b). Observed broadening of the Hadley Cell is larger than that simulated by the CMIP3 models (Seidel *et al.*, 2008): These results suggest that stratospheric ozone depletion, not included in many of the CMIP3 models, may help to explain this discrepancy. In JJA, when stratospheric ozone depletion is small, the CCMVal-2 simulations and the CMIP3 simulations all exhibit similar broadening

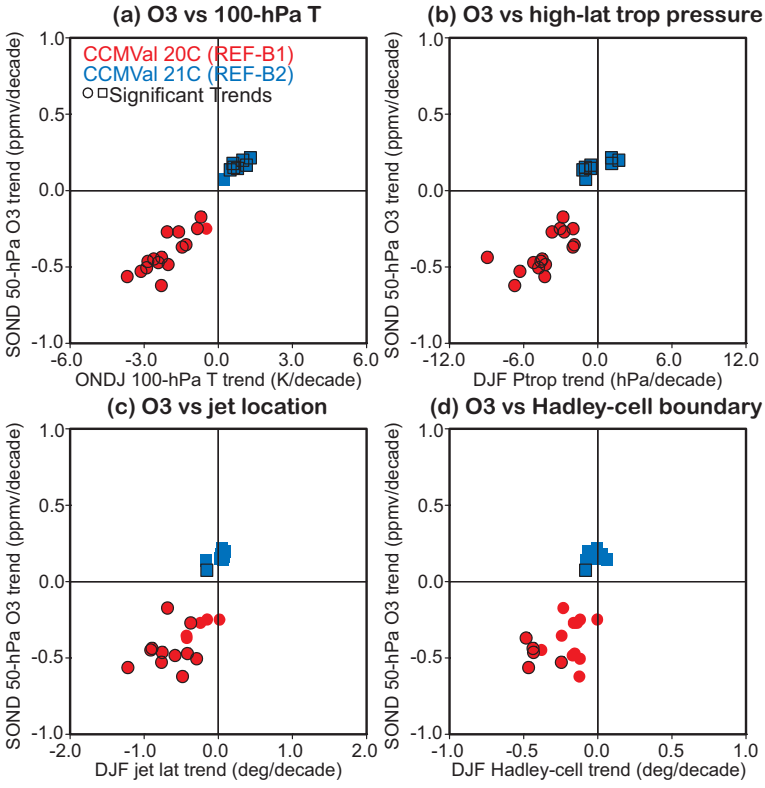

Figure 10.15: Trend relationship between SOND-mean ozone at 50 hPa integrated south of 64°S and variables of interest: (a) ONDJ-mean temperature at 100 hPa integrated south of 64°S, (b) DJF-mean extra-tropical tropopause pressure integrated south of 50°S, (c) location of the DJF-mean zonal wind maximum at 850 hPa, and (d) location of the SH Hadley cell boundary at 500 hPa. Linear trends are computed for the time period of 1960-1999 in the REF-B1 runs (red circles) and for the time period of 2000-2079 in the REF-B2 runs (blue squares). Trends which are statistically significant at the 95% confidence level are bounded in black. Significance is tested with the method used in Santer et al. (2000). Note that the 20th century trends are calculated over a 40-yr period compared to an 80-yr period for the 21st century trends, likely explaining their larger variability.

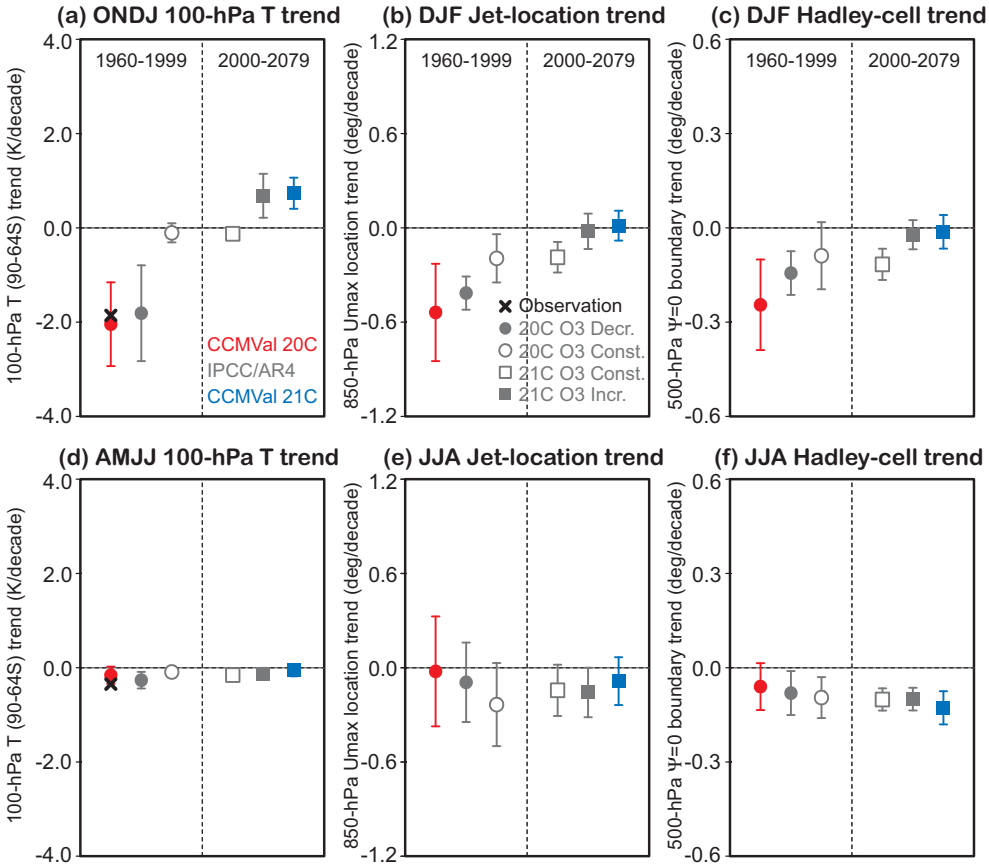

Figure 10.16: SH circulation changes as simulated by the SPARC/CCMVal-2 models and four sets of the IPCC/AR4 models. The multi-model mean trends are shown with one standard deviation for (a) ONDJ-mean temperature at 100 hPa integrated south of 64°S, (b) location of the DJF-mean zonal-mean zonal wind maximum at 850 hPa, (c) location of the DJF-mean SH Hadley-cell boundary at 500 hPa, (d-f) same as (a-c) but for AMJJ, JJA, and JJA, respectively. In (a,d), observed temperature trends between 1969 and 1998 (Thompson and Solomon, 2002) are shown in crosses. The negative values in (b-c, e-f) denote a poleward shift of the westerly jet or a poleward expansion of the Hadley cell. Uncertainty bars show one standard deviation for each set of models.

trends (Figure 10.16f). Future greenhouse gas increases are expected to drive a continuing poleward expansion of the Hadley Cell (Seidel *et al*., 2008), but the results presented here indicate that this effect may be offset by the effects of stratospheric ozone recovery in DJF in the SH, with the CCMVal-2 models simulating little change in the width of the SH Hadley Cell in this season (Figure 10.15d and Figure 10.16c).

10.4.1.2 Northern Hemisphere

Figure 10.14a shows very few regions of significant trends in zonal-mean zonal wind in DJF in the NH in the CCMVal-2 model mean for the 1979-1999 period. In the 2000-2079 period (Figure 10.14b) a strengthening of the subtropical jet is seen in the upper troposphere and lower stratosphere, but with few regions of significant zonal wind change in the lower troposphere. Arctic average geopotential and temperature trends in the CCMVal-2 simulations of the past do not show a clear downward propagating trend signal of the type shown in the SH in Figure 10.12 (not shown). However, a regression analysis of the NAM index onto hemispheric mean total column ozone and CO_2 indicated significant co-variability between ozone variations and the near-surface NAM index in winter and spring, and also significant covariability between Cl_y at 50 hPa and the near-surface NAM, taking the ensemble of models together (Morgenstern *et al*., 2010). Results are therefore suggestive of a role for ozone depletion in forcing long-term changes in the NAM in the CCMVal-2 models.

10.4.2 Radiative effects

Stratospheric changes in temperature and composi-

tion influence the troposphere and surface not only through dynamical mechanisms, but also more directly through changes in the radiative fluxes between the stratosphere and troposphere. Stratospheric ozone depletion has contributed to an increase in surface UV radiation (WMO/UNEP, 2007), it is a contributor to global radiative forcing (*e.g.*, Forster *et al.*, 2007), and the radiative influence of ozone depletion on the troposphere has been proposed as a mechanism to explain tropospheric cooling over Antarctica (Grise *et al.*, 2008; Keeley *et al.*, 2007). Some of these effects are investigated in the CCMVal-2 models here.

10.4.2.1 The response of surface UV radiation to stratospheric ozone changes

Total column ozone and vertical profiles of ozone and temperature from the REF-B1 and REF-B2 runs of the CCMVal-2 models were used to calculate solar ultraviolet radiation levels at the surface in the second half of the 20th and through the 21st century using the UVSPEC model (Mayer and Kylling, 2005; Tourpali *et al.*, 2009). While column ozone is the dominant driver of erythemal UV variations, ozone profile, and to a lesser extent temperature changes, also contribute to the changes in erythemal UV, especially in the polar regions. Surface UV reflectivity was set to a climatological mean, calculated from the Total Ozone Mapping Spectrometer (TOMS) surface UV reflectivity (Herman *et al.*, 1997). For the tropospheric aerosol optical depth, we used the AeroCom climatology (Kinne *et al.*, 2006), and a fixed cloud distribution was assumed. All results are presented here as departures (in %) from the corresponding monthly means of the 15-year average of the period 1965 through 1979.

Figure 10.17 shows changes in UV radiation calculated from the REF-B1 runs, representing past changes in ozone. Starting in the early 1980s, surface erythemal irradiance is found to increase globally (earlier at high south-

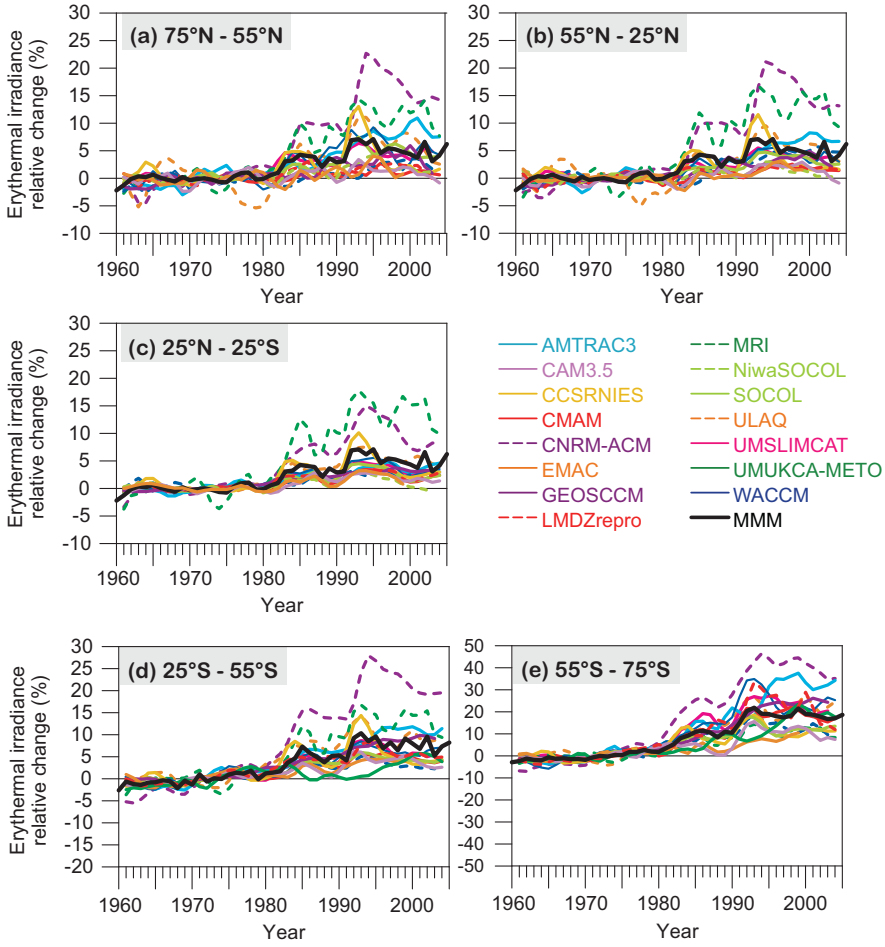

Figure 10.17: REF-B1 Runs: Annual means of surface clear-sky erythemal irradiance changes (in %, relative to 1965-1979) for five latitude belts. From top left to bottom (a)75°N-55°N, (b)55°N-25°N, (c)25°N-25°S, (d)25°S-55°S and (e) 55°S-75°S. The model names are indicated in the centre panel. The black line represents the multi-model average.

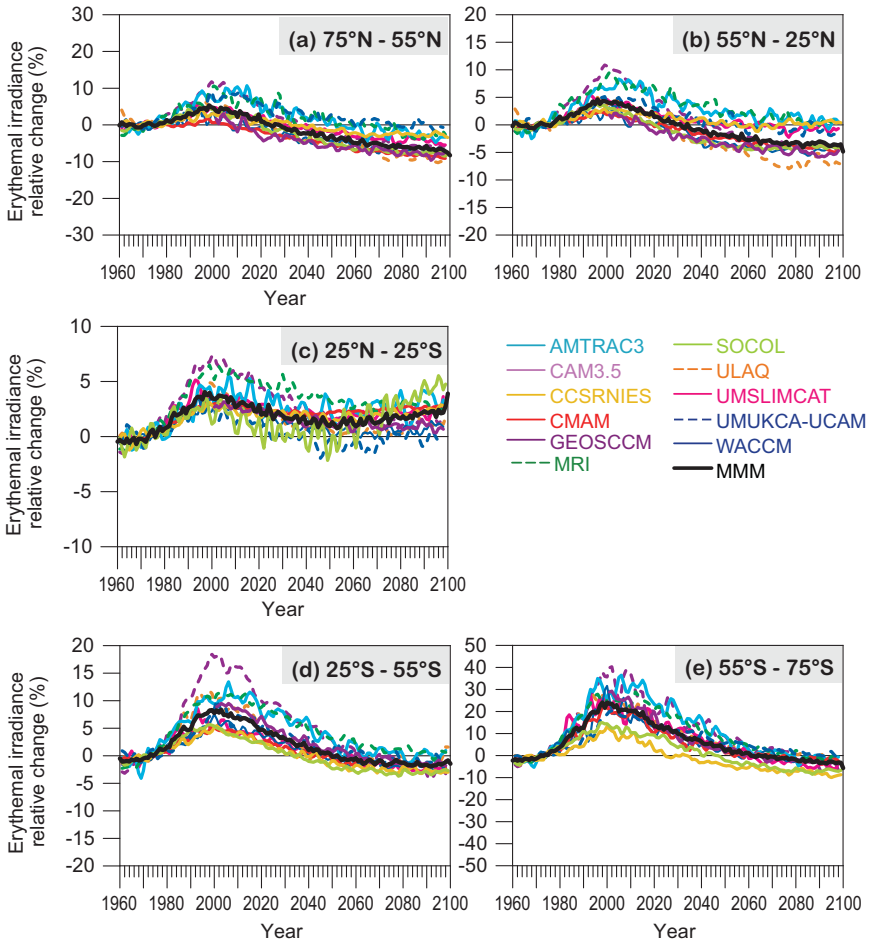

Figure 10.18: REF-B2 runs. Annual means of surface clear-sky erythemal irradiance changes (in %, relative to 1965-1979) for five latitude belts. From top left to bottom (a)75°N-55°N, (b)55°N-25°N, (c)25°N-25°S, (d)25°S-55°S and (e) 55°S-75°S. The model names are indicated in the centre panel. The black line represents the multi-model average.

ern latitudes), as a result of the ozone decline. These results are related to variations in column ozone shown in Chapter 9: For example, MRI and CNRM-ACM have larger than average tropical ozone losses (Section 9.3.4), and hence a larger increase in tropical UV. The ozone-induced effect of the El Chichón and Pinatubo eruptions on surface UV radiation is clearly seen at all latitudes, including the tropical regions.

Figure 10.18 presents the changes in UV radiation calculated from the REF-B2 runs, representing projected future changes in ozone. Starting around 2005, the surface erythemal irradiance is projected to decrease globally as a result of ozone recovery. The magnitude of these decreases varies with latitude and is more pronounced in areas where the most ozone depletion currently occurs, such as the Antarctic. In the tropics, erythemal UV is projected to increase towards the end of the 21st century, a trend related to a decrease in column ozone associated with an acceleration of the Brewer-Dobson circulation (Hegglin and Shepherd, 2009).

Figure 10.19 presents the evolution of the zonal-mean erythemal irradiance in the polar regions (75° - 90°) of both hemispheres. The top panel (a) presents the changes in surface erythemal irradiance in the southern polar latitudes and for the months October – November, the time when the Antarctic ozone hole reaches its maximum in area and intensity. All models show large interannual variability in this latitude belt and months, larger than at all other latitude belts, with surface erythemal irradiance reaching pre-1980 levels only after 2070. The bottom panel (b) presents the evolution of surface erythemal irradiance in the northern polar region during late winter-early spring (March-April). The interannual variability is large as well, but smaller than in the SH. The magnitude of the changes is much smaller than in the south (note the different scales used), and pre-1980 levels are reached earlier (~ 2050): this is consistent with the earlier return to pre-1980 ozone levels in the Arctic (Figure 9.20). The changes described here reflect

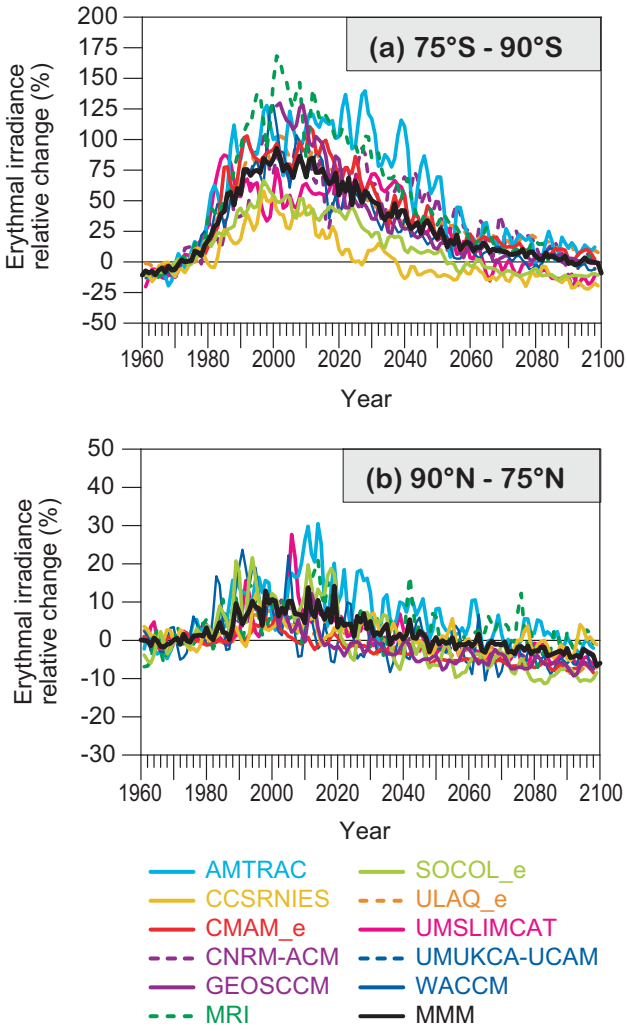

Figure 10.19: (a) Average of surface erythemal irradiance for October - November at 75°S-90°S. (b) same as in (a) but for March –April at 90°N-75°N.

the corresponding changes in the simulated ozone fields (Section 9.5.3), and are strongly influenced by changes in stratospheric circulation (Hegglin and Shepherd, 2009).

As climate change is likely to affect future cloudiness, the change in cloud transmittance (or cloud modification factor) was calculated as the change in the ratio of surface shortwave flux under all skies over the flux under clear skies. Here data provided by 8 runs of 5 CCMs were used. The cloud transmittance derived from the models was compared to results from a similar analysis performed using data from 11 CMIP3 models, and good agreement was found over the 2001-2100 period. The shortwave cloud transmittance was converted to erythemal UV cloud transmittance, and our analysis was extended to the calculation of changes in surface erythemal solar irradiance under all-sky conditions.

Figure 10.20, top panels, presents the changes in surface erythemal solar irradiance for the months of January (left panels) and July (right panels) under clear-sky conditions. The 20-year period 2080-2099 is shown, relative to the base-period of 1965-1979, before total ozone started its continuous decline. The bottom panels present the changes for the same months, but for all – sky conditions (*i.e.*, taking into account changes in cloudiness in the troposphere). While ozone is mainly responsible for the latitudinal changes of erythemal irradiance, cloud effects result in a more complex pattern with alternating regional positive and negative changes during the 21st century.

Generally, as is also seen in the clear-sky conditions case (top panels), erythemal irradiance is projected to increase in the tropics, and to decrease in the mid- and high latitudes of both hemispheres. The positive response in the tropics becomes larger when the effect of clouds is taken into account. Large reductions in surface irradiance (-10 to -15 %) are calculated for the second half of the 21st century in specific regions of the high northern latitudes, as well as over Antarctica. Large increases in erythemal irradiance (10-15%) appear in tropical regions of south-east Asia and Central America, with more moderate increases over southern Europe in summer.

During the late 20th century (not shown) the effects of ozone depletion on erythemal solar irradiance are apparent with a more uniform pattern of small to moderate increases in irradiance across the globe. Particularly in Antarctica, the strong ozone depletion dominates surface erythemal irradiance changes over the cloud effects leading to strong increases of up to 15%.

10.4.2.2 Radiative forcing due to stratospheric ozone changes

CCMs predict concentrations of chemically active species and model their radiative effects on atmospheric temperatures, yet they do not allow the effects of changes in individual species on tropopause radiative forcing to be evaluated directly. Stratospheric ozone changes since the 1970s are believed to have led to a small negative radiative forcing of around -0.05 Wm^{-2} with a 0.1 Wm^{-2} uncertainty range (Forster *et al.*, 2007). Stratospheric water vapour and methane changes can also be a significant source of forcing. The Forster *et al.* (2007) estimate is based on relatively few radiative calculations and ozone data sets.

Here we use an offline version of a single radiation code (Edwards and Slingo, 1996) to evaluate the radiative forcing from ozone changes predicted by the models' REF-B1 integration using their monthly averaged ozone fields. We assume clear skies and evaluate the radiative forcing using the Seasonally Evolving Fixed Dynamical Heating (SEFDH) approximation (Forster *et al.*, 1997). We fix the dynamical heating at the models' 1960 values and time-step the stratospheric temperatures forward using dai-

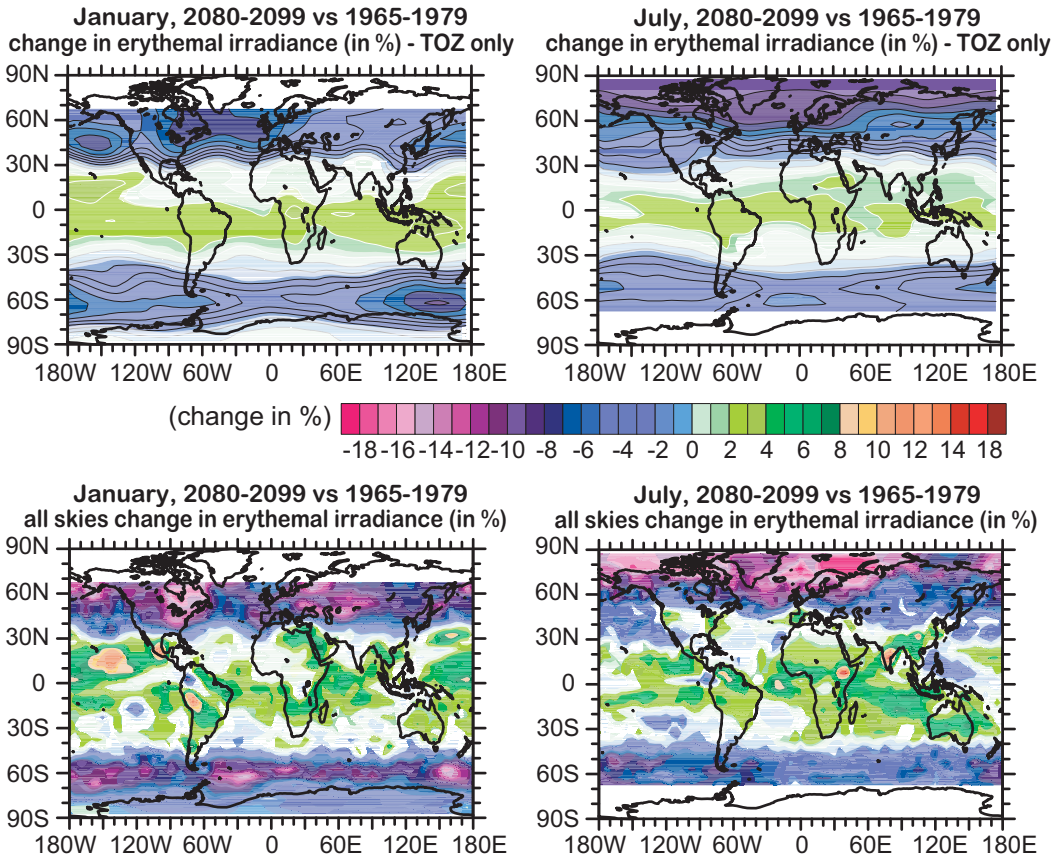

Figure 10.20: REF-B2 Runs. 20-year averages of clear-sky (top) and all-sky (bottom) erythemal irradiance changes (%) for January (left panels) and July (right panels) with respect to the 1965-1979 average. Calculations refer to local noon values and changes reflect the predicted changes in total ozone (11 CCMs provided 18 runs in total) and cloud transmittance (8 runs by 5 CCMs). In the top panels, small but positive changes appear in the tropics, and are statistically significant (95% level) over the equator. In the bottom panels, coloured areas denote statistically significant changes. Areas with insignificant changes are left blank.

ly time steps, updating the ozone or other trace gas values each day by interpolating between monthly average values.

Figure 10.21 shows global mean shortwave, longwave and total radiative forcing anomalies relative to 1960-1969 due to ozone changes based on 17 CCMVal-2 REF-B1 simulations. Over this period there is a clear upward trend in SW forcing, associated with decreased absorption of UV in the stratosphere, and a downward trend in LW forcing, associated primarily with stratospheric cooling (Grise *et al*., 2009). The ensemble mean trend in total radiative forcing due to ozone is small but positive, and individual simulations show a large range of trends, including some simulations that show positive trends. This spread is much larger than the uncertainty range on the radiative forcing trend due to observed ozone changes given by Forster *et al*. (2007). It remains to be determined whether this is because some models have unrealistic ozone changes, or whether this is because Forster *et al*. (2007) under-estimated the uncertainty in ozone-induced radiative forcing. The radiative forcing of volcanically-induced ozone changes is also apparent, particularly the decrease in total ozone-induced radiative forcing following the eruption of Mt Pinatubo in 1991 (the radiative effects of the aerosols themselves are not accounted for here).

10.4.3 Chemical effects

Lastly, the stratosphere may influence the composition of the troposphere through changes in the fluxes of chemical constituents across the tropopause. The most important such flux is the ozone flux associated with stratosphere-troposphere exchange (STE).

10.4.3.1 Stratosphere-to-troposphere ozone fluxes

While the contribution of stratospheric ozone to the total tropospheric ozone budget is only about 10%, it strongly affects ozone concentrations in the upper troposphere (Stevenson *et al*., 2006; Denman *et al*., 2007),

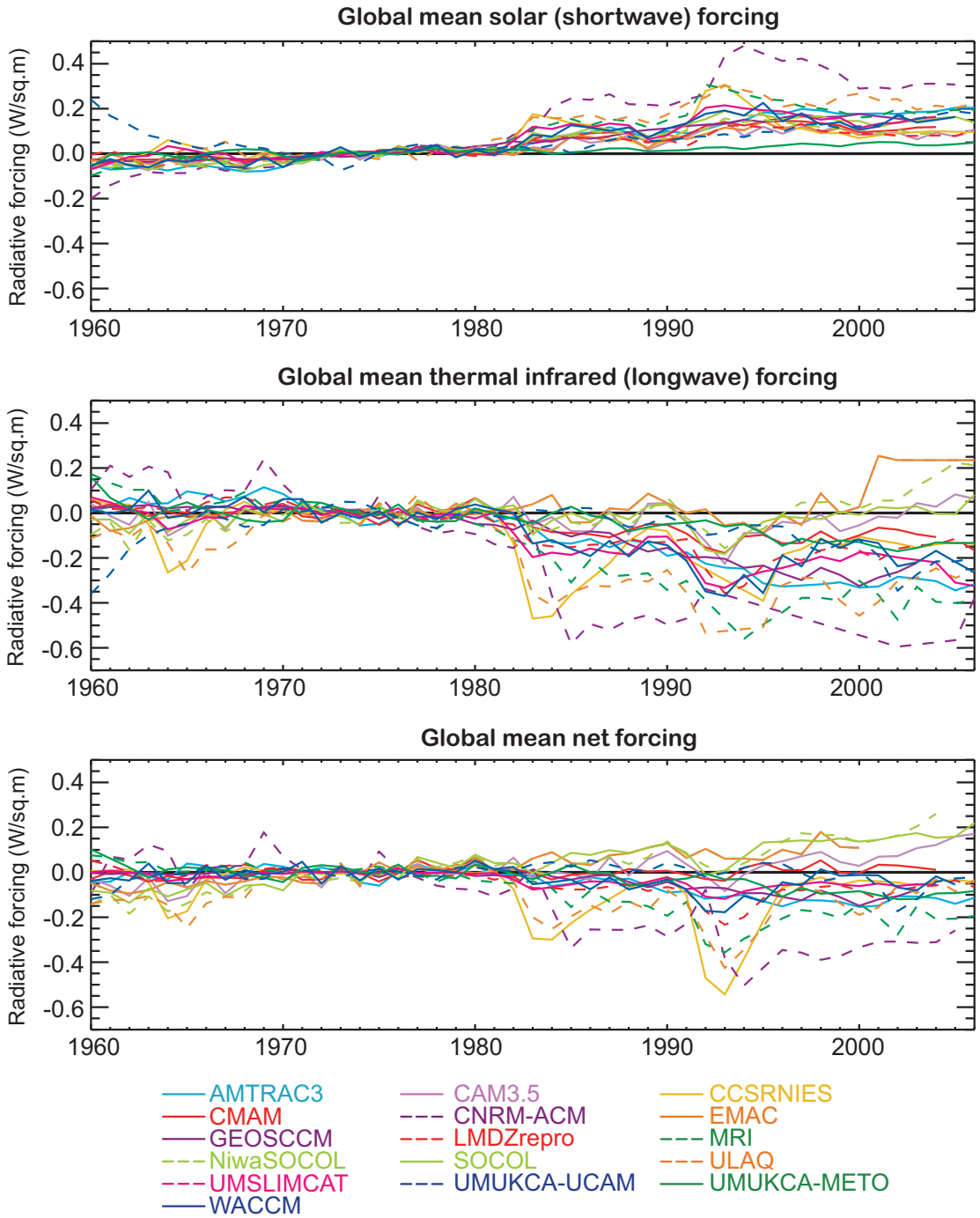

Figure 10.21: Calculated changes in global mean ozone-induced radiative forcing evaluated at the tropopause based on simulated ozone in 17 REF-B1 simulations and a fixed dynamical heating model. (a) SW forcing, (b) LW forcing, and (c) total forcing. Anomalies with respect to the period 1970-1979 are shown.

where ozone has a relatively long lifetime of about one month and also the greatest impact on the radiative forcing of surface temperatures (Forster and Shine, 1997).

CCMs consistently predict an increase in the strength of the Brewer-Dobson circulation due to climate change (Butchart *et al*., 2006; McLandress and Shepherd, 2009; see also Chapter 4). It has also been shown that this increase strongly affects the distribution of stratospheric ozone, especially in the mid-latitude lower stratosphere (Shepherd 2008; Li *et al*., 2009). These changes in the ozone distribution will affect the amount of ozone transported from the stratosphere into the troposphere, which

is why it is important to use stratosphere-resolving, fully interactive CCMs to quantify the impact of climate change on STE ozone fluxes, and to separate its effect from that of ozone depletion and recovery (Hegglin and Shepherd, 2009). Note that most of the tropospheric CCMs used for the IPCC AR4 to examine future changes in STE ozone fluxes had poor vertical resolution within the stratosphere and generally relaxed stratospheric ozone to prescribed values (Denman *et al*., 2007).

STE ozone fluxes are generally calculated in one of two ways. The first and most direct method is to calculate the STE ozone flux across the tropopause using instantaneous model fields with high temporal resolution. However, these calculations have been shown to be very sensitive to the particular tropopause definition used (Stevenson *et al*., 2004). This is presumably because the net ozone flux is a small difference of large terms, as a result of the small-scale two-way (*i.e*., reversible) transport into and out of the lowermost stratosphere. It is moreover an impractical calculation for a multi-model comparison with restricted data availability such as CCMVal-2. The second method is to infer the STE ozone flux as a residual in the tropospheric ozone budget. That calculation, too, involves a small difference of large terms, and it is also not possible with the fields saved in CCMVal-2. However, Holton *et al*. (1995) argued that the stratosphere-to-troposphere flux of any long-lived tracer (including ozone) is controlled by the Brewer-Dobson circulation, since any material that descends across a particular control surface (*e.g*., 100 hPa) must, in the absence of sources and sinks within the lowermost stratosphere, eventually make it into the troposphere.

The STE ozone fluxes (F_{STE}) are therefore calculated for each hemisphere on a monthly mean basis using a simple box-model approach previously used for mass flux calculations (Appenzeller *et al*., 1996), but applied instead to ozone (Hegglin and Shepherd, 2009):

$$F_{STE} = F_{100hPa} - dM_{LMS}/dt \qquad (10.4)$$

Here F_{100hPa} is the downward flux of ozone across the 100-hPa surface, estimated as the area-weighted integral within each hemisphere of the zonal-mean ozone concentration multiplied by the residual vertical velocity $\overline{w}^*$, and M_{LMS} is the total mass of ozone contained in the lowermost stratosphere (defined as the region between the 100-hPa surface and the thermal tropopause). The STE ozone flux, F_{STE}, is then calculated as a residual. The advantage of this method (as with the Appenzeller *et al*. (1996) method for mass flux) is that the terms contributing substantially to F_{100hPa} are mainly of the same sign. In this calculation, chemical processes between the tropopause and 100 hPa are assumed to have a negligible impact on F_{STE}. This is a reasonable assumption for global fluxes because the photochemical lifetime of ozone is generally much longer than its residence time in this region (Olsen *et al*., 2004). The largest error would come from the effect of the ozone hole, which would lead to an overestimation of the STE ozone fluxes, but only during the period of ozone depletion/recovery. In any case, so long as the calculation is done the same way for all models and for observations, it serves as a consistent and readily calculated diagnostic.

Figure 10.22 shows the long-term evolution of the STE ozone fluxes for all the CCMVal-2 models which provided the necessary data. In total, data from nine REF-B2 and two REF-B1 model simulations were available. For CMAM, CCMVal-1 results were used instead of CCMVal-2, as they are believed to be more realistic[1]. An observational estimate from 1991-2002 is also provided (black dots) using the ERA-Interim reanalysis together with the monthly resolved ozone climatology of McPeters *et al*. (2007).

Figure 10.22a shows that the calculated global STE ozone fluxes during the 1990s for the different models are generally somewhat larger, by up to 30%, than those based on the observations. The latter are seen to be in the middle of the (rather uncertain) observational range given by Denman *et al*. (2007), shown by the black vertical bar, which was obtained using different calculation methods. This provides confidence in our diagnostic method. Note that apart from ULAQ, which is well below the observational range, the STE ozone fluxes in the CCMVal models tend to lie in the upper half of the range provided by the tropospheric models (Stevenson *et al*., 2006). The consistently larger ozone fluxes obtained in most of the models may stem from a high bias of around 10-20% in ozone at 100 hPa as can be seen in Chapter 7, Figures 7.22 and 7.23.

SOCOL, MRI, and CCSRNIES are, aside from ULAQ, the models with the largest differences in the global fluxes when compared to the observations (using this method). The best agreement is found for GEOSCCM, with only a small under-estimation of the STE ozone fluxes in the SH when compared to the observations, also reflected in the global mean. Note that in order to cover the period between 1960 and 2100, the REF-B2 run of GEOSCCM did have to be extended into the past using the REF-B1 run. These two runs do not merge exactly into each other, which will have a slight impact on the trend estimation between the future and the past.

In both the NH and the SH, the model fluxes are generally larger than the observations as reflected in the global flux. The spread between the different models is higher in the NH than in the SH. In the NH, the largest differences are seen between the observations and SOCOL, MRI, and CCSRNIES. In the SH, these models are close to the rest of

[1] *For CCMVal-2, CMAM was coupled to an ocean model. Changes to the model made to enforce energy balance for coupling led to a degradation of the stratospheric dynamics, for reasons that are not fully understood (see also Chapter 4).*

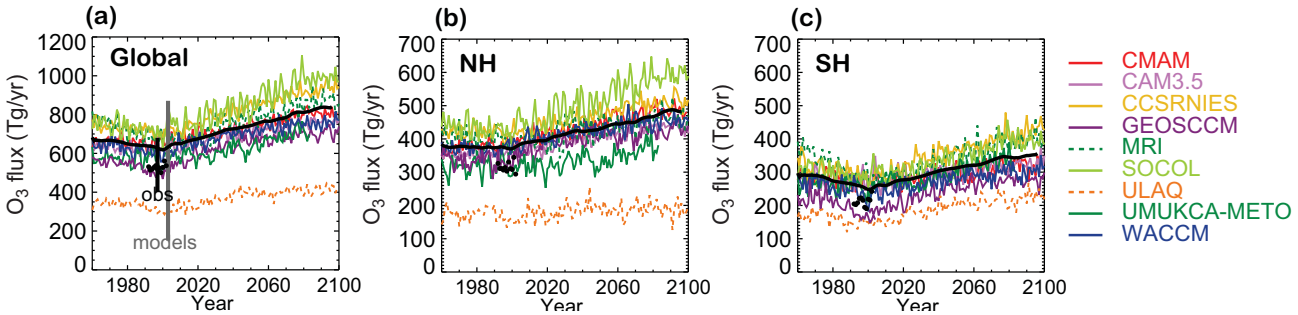

Figure 10.22: Multi-model comparison of the time evolution of (A) global, (B) northern hemispheric, (C) southern hemispheric stratospheric ozone flux into the troposphere between 1960 and 2100 derived from CCMVal-2 models. Coloured lines denote different models as given in the colour code, and the black line denotes the multi-model mean. The black uncertainty bar indicates the observational range given in the IPCC AR4 report (Denman et al., 2007), the grey uncertainty bar the tropospheric model range given in Stevenson et al. (2006). Black dots indicate observations calculated from ERA-Interim data together with the ozone climatology of McPeters et al. (2007) using the same method as used for the CCMs.

the models during the past, but exhibit anomalously strong fluxes towards the end of the current century. The NH flux is about 30% larger than the SH flux in both observations and models, except for ULAQ. The multi-model mean (thick solid black line) is calculated excluding ULAQ, since this model obtained the lowest scores in the metrics of Chapter 7 relevant for a good performance in simulating STE ozone fluxes. The multi-model mean is biased high in both hemispheres and also in the global mean, relecting the single model behaviour.

Simulated past and future STE ozone flux changes are influenced both by changes in stratospheric dynamics due to climate change and by ozone depletion and recovery, though to different degrees in the different models and in the two hemispheres. The changes over three time periods are given in **Table 10.3**. The multi-model mean of the change in the STE ozone flux attributable to climate change (1965-2095) is slightly larger in the NH (26%) than in the SH (21%). The multi-model mean change in global STE ozone flux between 1965 and 2095 is consistent in terms of percentage changes with the CMAM result shown in Hegglin and Shepherd (2009), however, its changes calculated for the NH and SH are smaller and larger, respectively. Over the period 2000-2030, the CCMVal-2 models show increases in the global ozone flux of 73.3 (±3.6) Tg/year or 11.7 (±0.6) %, which is toward the upper end of the range from tropospheric models of 41 (± 31) Tg/year or 7.6 (± 5.7) % reported by Stevenson *et al*. (2006). The results are expected to be dependent on the choice of the models that are included in the calculation of the mean.

10.5 Summary

10.5.1 Summary by Model

Multi-model mean: On average, the CCMVal-2 models simulated the mean climate and variability of the zonal mean *u*, *v*, and *T* fields well. CCMVal-2 models were only slightly better than CCMVal-1 models overall. However, the stratospheric simulations using CCMVal-2 models were much better than CMIP3 models. There was no clear improvement in the simulation of the mean or variability in the extra-tropics in models which included a simulated or nudged QBO. The performance skill (based on *u*, *v*, and *T*) was better in the NH than the SH, with a fairly large spread among models.

The NAM and the SAM were very well simulated by nearly all the CCMVal-2 models, especially in the troposphere. Both the latitudinal pattern and the amplitude of the patterns tended to be similar to the observations. In the stratosphere, the multi-model mean annular modes, as well as their variability, were close to the observations. However, there was a large inter-model spread. The CMIP3 models were inferior to all the CCMVal-2 models in the stratosphere.

Downward propagation of NAM and SAM signals was observed in all models, with the average tropospheric effect being slightly stronger than in the observations. However, there is uncertainty in the observations due to the short observational record.

On average, the CCMVal-2 simulation of the seasonal cycle of the variance of the NAM and SAM was realistic, except that the models tend to have a cold-season maximum that is delayed by roughly one month. There is large variability in how well the CCMVal models simulate the persistence (*e*-folding time scale) of the NAM and SAM.

Table 10.3: Multi-model mean of the relative changes in global, northern, and southern hemispheric ozone fluxes for different time periods (corresponding to ozone depletion (1965-2000), ozone recovery (2000-2035), and climate change (1965-2095). For the calculation of the mean, only REF-B2 simulations have been used. For models providing more than one simulation, the ensemble means have been used.

	Time period (yr)	O_3-flux change (Tg yr-1)	O_3-flux change (%)
Global	1965-2000	-40.8 (±2.7)	-6.1 (±0.4)
	2000-2035	73.3 (±3.6)	11.7 (±0.6)
	1965-2095	169.0 (±5.4)	24.1 (±0.8)
NH (0°N-90°N)	1965-2000	-2.8 (±1.6)	-0.7 (±0.4)
	2000-2035	39.8 (±1.9)	10.6 (±0.5)
	1965-2095	108.4 (±3.8)	26.2 (±1.0)
SH (0°S-90°S)	1965-2000	-38.0 (±1.6)	-13.0 (±0.5)
	2000-2035	33.5 (±1.9)	13.2 (±0.8)
	1965-2095	60.7 (±3.5)	21.1 (±1.2)

The models tend to have time scales that are too long, in both the troposphere and lower stratosphere. Some models had SH time scales up to four times that observed.

In the SH, the 1969-1998 trends in *Z* (geopotential height) and *T* capture the observed cooling that extends to the surface. Although the average modelled ozone trend was less than that observed at 100 hPa, the *T* trend at 100 hPa was, on average, somewhat larger than that observed.

The multi-model mean ozone-induced erythemal radiation shows an increase over all regions, maximising in around 2000 in Antarctica, and followed by a reduction through the 21st century. In the NH extra-tropics, erythemal radiation recovers to 1960 levels by 2020 – 2040, while in the Antarctic it does not recover to these levels until the end of the century, and in the tropics, erythemal radiation begins to increase again in the latter part of the century.

The CCMVal-2 REF-B2 simulations show a fairly large spread in stratospheric ozone flux into the troposphere. The observations do little to constrain the range, and it is difficult to discern which models are better.

Below are model-by-model results that emphasize mainly the instances in which each model is significantly different from the multi-model mean.

AMTRAC3 performs better than average in the SH and worse than average in the NH based on the *u*, *v*, *T* metrics. It exhibits anomalously strong cooling of the Antarctic vortex in spring compared to observations.

CAM3.5 performs worse than average in the NH and about average in the SH based on the *u*, *v*, *T* metrics.

CCSRNIES performs worse than average in the stratosphere and troposphere of both hemispheres based on the *u*, *v*, *T* metrics. Its simulated decrease in Antarctic ozone is smaller than observations, and hence its simulated increase in SH erythemal radiation is smaller than in other models. Global stratosphere-troposphere ozone fluxes are overestimated in this model.

CMAM performs better than average in the NH and about average in the SH based on the *u*, *v*, *T* metrics. CMAM was the only model coupled to an ocean model, but this did not have a noticeable effect on the diagnostics examined here. All the models reproduce tropospheric anomalies following the stratospheric events, but in the NH, CMAM (along with some other models) showed noticeably longer persistence of the anomalies compared with the observations. Its SAM index is too persistent compared to observations in both the troposphere and the stratosphere. It exhibits anomalously strong cooling of the Antarctic vortex in spring compared to observations.

E39CA performs worse than average in the stratosphere and about average in the troposphere, based on the *u*, *v*, *T* metrics. This model has realistic global mean stratosphere-troposphere ozone fluxes, but this is due to compensating errors, with a too high flux in the SH and too low a flux in the NH.

CNRM-ACM performs very poorly in the stratosphere, and about average in the troposphere, based on the *u*, *v*, *T* metrics. Its stratospheric jets are displaced too far equator-ward. CNRM-ACRM has larger than average tropical ozone losses (Section 9.3.4), and hence a larger increase in tropical UV. It is also the model with the largest negative radiative forcing due to ozone changes.

EMAC performs about average overall based on the *u*, *v*, *T* metrics. EMAC simulates too weak a stratospheric cool-

ing in the Antarctic vortex in spring and also simulates an Antarctic total ozone trend that is too weak. It exhibits positive tropopause radiative forcing in ~2000 associated with stratospheric ozone changes.

GEOSCCM performs very well in the stratosphere based on the *u*, *v*, *T* metrics. Tropospheric skill was generally close to average, except that NH tropospheric variability was simulated somewhat poorly. This model exhibits realistic SAM time scales in the troposphere and the stratosphere, but its NAM time scales are somewhat too long. Moreover, in both hemispheres lower stratospheric annular mode anomalies exhibit too much persistence in their coupling with annular mode anomalies at 10 hPa. Stratosphere-troposphere ozone fluxes in this model exhibit particularly good agreement with observations.

LMDZrepro performs poorly in its simulation of synoptic variability in both hemispheres, it is about average in its simulation of other aspects of NH climate and below average in its simulation of other aspects of SH climate, based on *u*, *v*, *T* metrics. In both hemispheres, lower stratospheric annular mode anomalies exhibit too much persistence in their coupling with annular mode anomalies at 10 hPa in this model, and its annular mode indices are themselves too persistent in both hemispheres, in both the troposphere and stratosphere.

MRI exhibits about average performance based on the *u*, *v*, *T* metrics. MRI simulates larger than average increases in erythemal radiative associated with ozone depletion, and it also simulates a larger than average negative radiative forcing. It exhibits anomalously large stratosphere-troposphere ozone fluxes, particularly in the NH.

NiwaSOCOL simulates mean climate in the NH better than average, and realistic synoptic variability in the troposphere, but poor synoptic variability in the stratosphere, based on the *u*, *v*, *T* metrics. It exhibits a relatively large negative radiative forcing due to ozone.

SOCOL simulates NH stratosphere mean conditions well, and in other aspects is about average, based on the *u*, *v*, *T* metrics. It exhibits anomalously weak Antarctic ozone depletion, and hence weaker than average ozone-induced increases in SH erythemal radiation. It exhibits positive tropopause radiative forcing in ~2000 associated with stratospheric ozone changes. It exhibits anomalously high stratosphere-troposphere ozone fluxes.

ULAQ underperforms in all categories of climate: in the stratosphere and troposphere, over both hemispheres, and in mean climate as well as in interannual variability based on the *u*, *v*, *T* metrics. ULAQ simulates much lower stratosphere-troposphere ozone fluxes than observed, and has the largest bias in ozone fluxes compared to the observations.

UMSLIMCAT exhibits about average performance in its simulation of mean tropospheric climate, and tropospheric and stratospheric variability, but below average performance in its simulation of stratospheric variability, based on the *u*, *v*, *T* metrics.

UMUKCA-METO is one of the best models at simulating means and variability in the troposphere, and performs better than average in the stratosphere, based on the *u*, *v*, *T* metrics. This model simulates too weak a stratospheric cooling in the Antarctic stratosphere in spring.

UMUKCA-UCAM exhibits among the best simulation of tropospheric mean climate and variability, and is about average in its simulation of stratospheric mean climate and variability, based on the *u*, *v*, *T* metrics. It simulates too weak a stratospheric cooling in the Antarctic stratosphere in spring.

WACCM performs poorly in the *u*, *v*, *T* metrics for the SH, but about average in the NH. Its tropospheric synoptic variability is particularly realistic in both hemispheres. WACCM has among the most realistic (shortest) SAM time scales, but among the least realistic (longest) NAM time scales.

10.5.2 Overall Summary

This chapter has examined the dynamical, radiative and chemical effects of the stratosphere on the troposphere in the CCMVal-2 models. Stratospheric ozone changes will not greatly alter the global-mean surface warming. However, Antarctic climate as well as the global distribution of surface UV radiation are expected to be affected significantly.

An examination of the mean climate and variability in the CCMVal-2 models showed that they exhibit a much more realistic stratospheric climate than the CMIP3 climate models, and more realistic interannual variability in the troposphere. CCMVal-2 models exhibit a slight but non-significant reduction in biases compared to the earlier generation CCMVal-1 models. CCMVal-2 models simulate a downward propagation of annular mode anomalies in both hemispheres similar to that observed, with realistic ensemble-mean annular mode variances through the troposphere and stratosphere. However, the peak in variability associated with the break-down of the vortex consistently occurs too late in the year in both hemispheres in the CCMVal-2 models, and the simulated SAM tends to be

too persistent through the troposphere and stratosphere in summer.

Over the period 1960-2000 the CCMVal-2 models simulate a spring cooling of the Antarctic polar vortex, and a decrease in Antarctic geopotential height which descends to the troposphere in December-February, and is associated with an intensification and southward shift of the mid-latitude jet. The amount of Antarctic ozone depletion in each model is closely correlated with its poleward shift in midlatitude jet location, amount of broadening of the Hadley Cell, and its increase in SH tropopause height. The models indicate that in the 21st century, the effects of ozone recovery and GHG increases largely cancel leading to little change in jet location, tropopause height, or Hadley Cell width in the SH in summer. The effect of stratospheric ozone changes on the NAM in the CCMVal-2 models appears to be weak but significant.

Stratospheric ozone changes in the CCMVal-2 models lead to an increase in SW forcing and a decrease in LW forcing at the tropopause. However, while the ensemble mean net forcing change due to ozone changes between 1960-2000 is negative, consistent with that reported by IPCC (2007), some models show a positive net tropopause radiative forcing due to stratospheric ozone changes over this period. Erythemal ultraviolet irradiance, calculated based on CCMVal-2 ozone changes, exhibits an increase throughout the globe in the last decades of the 20th century. In the 21st century, decreasing chemical depletion is likely to contribute to a decrease in erythemal irradiance globally, while changes in the Brewer-Dobson circulation will tend to enhance the decrease in the Arctic and slow or reverse the decrease in the tropics and Antarctic. Changes in cloudiness and tropospheric ozone and aerosols are uncertain and may also be important drivers of regional surface UV change.

In the CCMVal-2 simulations ozone depletion causes a small global decrease in the stratosphere-troposphere ozone flux in the 20th century, and its recovery contributes to the 21st century increase. However, a strengthening of the Brewer-Dobson circulation is projected to be the dominant driver of an increase in stratosphere-to-troposphere ozone fluxes in the 21st century.

References

Arblaster, J. M., and G. A. Meehl, 2006. Contributions of external forcings to Southern Annular Mode trends, *J. Climate*, **19**, 2896–2905.

Appenzeller, C., J. Holton, and K. Rosenlof, Seasonal variation of mass transport across the tropopause, 1996. *J. Geophys. Res.* **101**, 15,071–15,078.

Baldwin, M. P., and T. J. Dunkerton, 1999. Downward propagation of the Arctic Oscillation from the stratosphere to the troposphere, *J. Geophys. Res.*, **104**, 30,937–30,946.

Baldwin, M. P. and T. J. Dunkerton, 2001. Stratospheric harbingers of anomalous weather regimes, *Science*, **244**, 581–584.

Baldwin, M. P., D. B. Stephenson, D. W. J. Thompson, T. J. Dunkerton, A. J. Charlton, and A. O'Neill, 2003. Stratospheric memory and extended-range weather forecasts, *Science*, **301**, 636–640.

Baldwin, M. P., D. W. J. Thompson, 2009: A critical comparison of stratosphere-troposphere coupling indices, submitted to *Quart. J. Royal. Meteorol. Soc.*, in press.

Butchart, N., A. A. Scaife, M. Bourqui, J. de Grandpre, S. H. E. Hare, J. Kettleborough, U. Langematz, E. Manzini, F. Sassi, K. Shibata, D. Shindell, and M. Sigmond, 2006: Simulations of antropogenic change in the strength of the Brewer-Dobson circulation, *Clim. Dyn.*, **27**, doi: 10.1007/s00382-006-0162-4.

Coughlin, K., and K.-K. Tung, 2001. QBO Signal found at the extratropical surface through Northern Annular Modes. *Geophys. Res. Lett.*, **28**, 4563–4566.

Crook, J. A., N. P. Gillett, S. P. E. Keeley, 2008. Sensitivity of Southern Hemisphere climate to zonal asymmetry in ozone, *Geophys. Res. Lett.*, **35**, doi:10.1029/2007GL032698.

Denman, K. L., G. Brasseur, A. Chidthaisong, P. Ciais, P. M. Cox, R. E. Dickinson, D. Hauglustaine, C. Heinze, E. Holland, D. Jacob, U. Lohmann, S. Ramachandran, P. L. da Silva Dias, S. C. Wofsy and X. Zhang, 2007. Couplings Between Changes in the Climate System and Biogeochemistry. In: *Climate Change 2007: The Physical Science Basis. Contribution of Working Group I to the Fourth Assessment Report of the Intergovernmental Panel on Climate Change,* Cambridge University Press, Cambridge, United Kingdom and New York, NY, USA.

Edwards, J. M. and A. Slingo, 1996. Studies with a flexible new radiation code. I: Choosing a configuration for a large-scale model, *Quart. J. Royal. Meteorol. Soc.*, **122**, 689-719.

Eyring, V., D. W. Waugh, G. E. Bodeker, E. Cordero, H. Akiyoshi, J. Austin, S. R. Beagley, B. A. Boville, P. Braesicke, C. Brühl, N. Butchart, M. P. Chipper_eld, M. Dameris, R. Deckert, M. Deushi, S. M. Frith, R.

R. Garcia, A. Gettelman, M. A. Giorgetta, D. E. Kinnison, E. Mancini, E. Manzini, D. R. Marsh, S. Matthes, T. Nagashima, P. A. Newman, J. E. Nielsen, S. Pawson, G. Pitari, D. A. Plummer, E. Rozanov, M. Schraner, J. F. Scinocca, K. Semeniuk, T. G. Shepherd, K. Shibata, B. Steil, R. S. Stolarski, W. Tian, and M. Yoshiki, 2007. Multi-model projections of ozone recovery in the 21st century, *J. Geophys. Res.*, **112**, doi:10.1029/2006JD008332.

Fioletov, V. E., and T. G. Shepherd, 2003. Seasonal persistence of midlatitude total ozone anomalies, *Geophys. Res. Lett.*, **30**, doi:10.1029/2002GL016739.

Forster, P., V. Ramaswamy, P. Artaxo, T. Berntsen, R. Betts, D. W. Fahey, J. Haywood, J. Lean, D. C. Lowe, G. Myhre, J. Nganga, R. Prinn, G. Raga, M. Schulz and R. Van Dorland, 2007. Changes in Atmospheric Constituents and in Radiative Forcing. In: *Climate Change 2007: The Physical Science Basis. Contribution of Working Group I to the Fourth Assessment Report of the Intergovernmental Panel on Climate Change*. Cambridge University Press, Cambridge, United Kingdom and New York, NY, USA.

Forster, P. M. F., R. S. Freckleton and K. P. Shine, 1997. On aspects of the concept of radiative forcing, *Clim. Dyn.,* **13**, 547-560.

Forster, P. and K. Shine, 1997. Radiative forcing and temperature trends from stratospheric ozone changes. *J. Geophys. Res.* **102**, 1084.

Gerber, E. P., M. P. Baldwin, H. Akiyoshi, J. Austin, S. Bekki, P. Braesicke, N. Butchart, M. Chipperfield, M. Dameris, S. Dhomse,. S. M. Frith, R. R. Garcia, H. Garny, A. Gettelman, S. C. Hardiman, M. Marchand, O. Morgenstern, J. E. Nielsen, S. Pawson, T. Peter, D. A. Plummer, J. A. Pyle, E. Rozanov, J. F. Scinocca, T. G. Shepherd, and D. Smale, 2010. Stratosphere-Troposphere Coupling and Annular Mode Variability in Chemistry-Climate Models. *J. Geophys. Res.*, submitted.

Gerber, E. P., L. M. Polvani, and D. Ancukiewicz, 2008. Annular mode time scales in the Integovernmental Panel on Climate Change Fourth Assessment Report models. *Geophys. Res. Lett.*, **35**, doi:10.1029/2008GL035712.

Gillett, N., and D. W. J. Thompson, 2003. Simulation of recent southern hemisphere climate change. *Science*, **302**, 273–275.

Graf, H.-F., J. Perlwitz and I. Kirchner, 1994. Northern Hemisphere tropospheric mid-latitude circulation after violent volcanic eruptions, *Contr. Atm. Phys.*, **67**, 3–13.

Grise, K. M., D. W. J. Thompson and P. M. Forster, 2009. On the role of radiative processes in stratosphere-troposphere coupling, *J. Clim.*, **22**, 4154-4161.

Hamilton, K. P., 2007. Analyses of IPCC Climate Model Data at IPRC, *IPRC Climate Newsletter*, **7**.

Hegglin, M. I., and T. G. Shepherd, 2009. Large climate-induced changes in ultraviolet index and stratosphere-to-troposphere ozone flux, *Nature Geosci.*, **2**, 687–691.

Herman, J. R., and E. A. Celarier, 1997. Earth surface reflectivity climatology at 340 nm to 380 nm from TOMS data, *J. Geophys. Res.*, **102**, 28,003-28,011.

Holton, J., P. Haynes, M. McIntyre, A. Douglass, R. Rood, and L. Pfister, 1995. Stratosphere-Troposphere Exchange, *Rev. Geophys.*, **33**, 403-439.

IPCC, 2007: Climate Change 2007: The Physical Science Basis. Contribution of Working Group I to the Fourth Assessment Report of the Intergovernmental Panel on Climate Change [Solomon, S., D. Qin, M. Manning, Z. Chen, M. Marquis, K.B. Averyt, M.Tignor and H.L. Miller (eds.)]. Cambridge University Press, Cambridge, United Kingdom and New York, NY, USA.

Ineson, S., and A. A. Scaife, 2009. The role of the stratosphere in the European climate response to El Niño, *Nature Geosci.*, **2**, 32-36.

Keeley, S. P. E., N. P. Gillett, D. W. J. Thompson, S. Solomon, P. M. de F. Forster, 2007. Is Antarctic climate most sensitive to ozone depletion in the mid or lower stratosphere? *Geophys. Res. Lett.*, **34**, doi:10.1029/2007GL031238.

Karpechko, A. Yu., N. P. Gillett, G. J. Marshall, and A. A. Scaife, 2008. Stratospheric influence on circulation changes in the southern hemisphere troposphere in coupled climate models, *Geophys. Res. Lett.*, **35**, doi:10.1029/2008GL035354.

Kinne, S., M. Schulz, C. Textor, S. Guibert, Y. Balkanski, S. E. Bauer, T. Berntsen, T. F. Berglen, O. Boucher, M. Chin, W. Collins, F. Dentener, T. Diehl, R. Easter, J. Feichter, D. Fillmore, S. Ghan, P. Ginoux, S. Gong, A. Grini, J. Hendricks, M. Herzog, L. Horowitz, I. Isaksen, T. Iversen, A. Kirkevåg, S. Kloster,

D. Koch, J. E. Kristjansson, M. Krol, A. Lauer, J. F. Lamarque, G. Lesins, X. Liu, U. Lohmann, V. Montanaro, G. Myhre, J. Penner, G. Pitari, S. Reddy, O. Seland, P. Stier, T. Takemura, and X. Tie, 2006. An AeroCom initial assessment - optical properties in aerosol component modules of global models, *Atmos. Chem. Phys.*, **6**, 1815-1834.

Kodera, K., K. Yamazaki, M. Chiba and K. Shibata, 1990. Downward propagation of upper stratospheric mean zonal wind perturbation to the troposphere, *J. Meteor. Soc. Japan,* **9**, 1263–1266.

Kodera, K., and K. Yamazaki, 1994. A possible influence of recent polar stratospheric coolings on the troposphere in the northern hemisphere winter, *Geophys. Res. Lett.*, **21**, 809–812.

Lu, J., G. A. Vecchi, and T. E. Reichler, 2007. Expansion of the Hadley cell under global warming. *Geophys. Res. Lett.,* **34**, doi:10.1029/2006GL028443.

Lal, M., A. K. Jain, and M. C. Sinha, 1987. Possible climatic implications of depletion of Antarctic ozone, *Tellus,* **39B**, 326-328.

Li, F., Stolarski, R. S., and Newman, P. A., 2009. Stratospheric ozone in the post-CFC era. *Atmos. Chem. Phys.*, **9**, 2207-2213.

Manzini, E., B. Steil, C. Brühl, M. A. Giorgetta, and K. Krüger, 2003. A new interactive chemistry-climate model: 2. Sensitivity of the middle atmosphere to ozone depletion and increase in greenhouse gases and implications for recent stratospheric cooling, *J. Geophys. Res.*, **108**, doi:10.1029/2002JD002977.

Marshall, G. J., P. A. Stott, J. Turner, W. M. Connolley, J. C. King, and T. A. Lachlan-Cope, 2004. Causes of exceptional atmospheric circulation changes in the Southern Hemisphere, *Geophys. Res. Lett.*, **31**, doi:10.1029/2004GL019952.

Mayer, B., and A. Kylling, 2005. Technical note: The libRadtran software package for radiative transfer calculations - description and examples of use, *Atmos. Chem. Phys.*, **5**, 1855-1877.

McLandress, C., and T. G. Shepherd, 2009. Simulated anthropogenic changes in the Brewer-Dobson circulation, including its extension to high latitudes, *J. Clim.*, **22**, 1516-1540.

McPeters, R. D., G. J. Labow, and J. A. Logan, 2007. Ozone climatological profiles for satellite retrieval algorithms, *J. Geophys. Res.*, **112**, doi:10.1029/2005JD006823.

Meehl, G. A., C. Covey, T. Delworth, M. Latif, B. McAvaney, J. F. B. Mitchell, R. J. Stouffer, and K. E. Taylor, 2007a. The WCRP CMIP3 multimodel dataset: A new era in climate change research. *Bull. Amer. Meteor. Soc.*, **88**, 1383-1394.

Meehl, G. A., T. F. Stocker, W. D. Collins, P. Friedlingstein, A. T. Gaye, J. M. Gregory, A. Kitoh, R. Knutti, J. M. Murphy, A. Noda, S. C. B. Raper, I. G. Watterson, A. J. Weaver and Z.-C. Zhao, 2007b. Global Climate Projections. In: *Climate Change 2007: The Physical Science Basis. Contribution of Working Group I to the Fourth Assessment Report of the Intergovernmental Panel on Climate Change*. Cambridge University Press, Cambridge, United Kingdom and New York, NY, USA.

Morgenstern, O., H. Akiyoshi, S. Bekki , P. Braesicke , N. Butchart, M. Chipperfield , A. Gettelman, D. Cugnet, M. Deushi, S. S. Dhomse, R. R. Garcia, N. P. Gillett, S. C. Hardiman , J. Jumelet, D. E. Kinnison, J.-F. Lamarque , F. Lott, M. Marchand, M. Michou, T. Nakamura, D. Olivié, S. Pawson, T. Peter, D. Plummer, J. A. Pyle, E. Rozanov , D. Saint-Martin, J. F. Scinocca, K. Shibata, M. Sigmond, D. Smale, H. Teyssèdre, W. Tian, A. Voldoire, and Y. Yamashita, 2010. Anthropogenic forcing of the Northern Annular Mode in CCMVal-2 models, *J. Geophys. Res.*, submitted.

Olsen, M. A., M. R. Schoeberl, and A. R. Douglass, 2004. Stratosphere-troposphere exchange of mass and ozone. *J. Geophys. Res.*, **109**, doi:10.1029/2004JD005186.

Polvani L. M., and D. W. Waugh, 2004. Upward wave activity flux as precursor to extreme stratospheric events and subsequent anomalous surface weather regimes , *J. Climate*, **17**, 3548–3554.

Ramanathan, V., 1977. Troposphere-stratosphere feedback mechanism: Stratospheric warming and its effect on the polar energy budget and the tropospheric circulation. *J. Atmos. Sci.*, **34**, 439–447.

Randel, W. J., and F. Wu, 1999. Cooling of the Arctic and Antarctic polar stratosphere due to ozone depletion. *J. Climate,* **12**, 1467-1479.

Reichler, T. and J. Kim, 2008. How well do coupled models simulate today's climate? *Bull. Amer. Meteor. Soc.*, **89**, 303-311.

Rind, D., J. Lean, J. Lerner, P. Lonergan, and A. Leboissitier, 2008. Exploring the stratospheric/tropospheric response to solar forcing, *J. Geophys. Res.*, **113**, doi:10.1029/2008JD010114.

Robock, A., and J. Mao, 1992. Winter warming from large volcanic eruptions, *Geophys. Res. Lett.*, **12**, 2405–2408.

Santer, B. D., T. M. L. Wigley, J. S. Boyle, D. J. Gaffen, J. J. Hnilo, D. Nychka, D. E. Parker, and K. E. Taylor, 2000. Statistical significance of trends and trend differences in layer-average atmospheric temperature time series, *J. Geophys. Res.*, **105**, 7337–7356.

Santer, B. D., M. F. Wehner, T. M. L. Wigley, R. Sausen, G. A. Meehl, K. E. Taylor, C. Ammann, J. Arblaster, W. M. Washington, J. S. Boyle, and W. Bruggemann, 2003.Contribution of anthropogenic and natural forcing to recent tropopause height changes, *Science*, **301**, 479483.

Seidel, D. J., Q. Fu, W. J. Randel, and T. J. Reichler, 2008. Widening of the tropical belt in a changing climate, *Nature Geoscience*, **1**, 21-24.

Shepherd, T. G., 2008. Dynamics, stratospheric ozone, and climate change. *Atmos.-Ocean,* **46**, 117-138.

Shindell, D. T., and G. A. Schmidt, 2004. Southern Hemisphere climate response to ozone changes and greenhouse gas increases, *Geophys. Res. Lett.*, **31**, doi:10.1029/2004GL020724.

Son, S.-W., L. M. Polvani, D. W. Waugh, H. Akiyoshi, R. Garcia, D. Kinnison, S. Pawson, E. Rozanov, T. G. Shepherd, and K. Shibata, 2008. The impact of stratospheric ozone recovery on the Southern Hemisphere westerly jet, *Science*, **320**, 1486-1489.

Son, S.-W., L. M. Polvani, D. W. Waugh, T. Birner, H. Akiyoshi, R. R. Garcia, A. Gettelman, D. A. Plummer, and E. Rozanov, 2009a. The impact of stratospheric ozone recovery on tropopause height trends , *J. Clim.*, **22**, 429-445.

Son S.-W., N. F. Tandon, L. M. Polvani, and D. W. Waugh, 2009b. The ozone hole and southern hemisphere climate change, *Geophys. Res. Lett.*, **36**, doi:10.1029/2009GL038671.

Stenchikov, G. L., I. Kirchner, A. Robock, H.-F. Graf, J. C. Artuna, R. G. Grainger, A. Lambert, and L. Thomason, 1998. Radiative forcing from the 1991 Mount Pinatubo volcanic eruption, *J. Geophys. Res.*, **103**, 13,837–13,857.

Stenchikov, G., K. Hamilton, A. Robock, and V. Ramaswamy, and M.D. Schwarzkopf, 2004. Arctic oscillation response to the 1991 Pinatubo eruption in the SKYHI general circulation model with a realistic quasi-biennial oscillation. *J. Geophys. Res.*, **109**, doi: 10.1029/2003JD003699.

Stevenson, D. S., R. M. Doherty, M. G. Sanderson, W. J. Collins, C. E. Johnson, and R. G. Derwent, 2004. Radiative forcing from aircraft NOx emissions: Mechanisms and seasonal dependence, *J. Geophys. Res.*, **109**, doi:10.1029/2004JD004759.

Stevenson, D. S., F. J. Dentener, M. G. Schultz, K. Ellingsen, T. P. C. van Noije, O. Wild, G. Zeng, M. Amann, C. S. Atherton, N. Bell, D. J. Bergmann, I. Bey, T. Butler, J. Cofala, W. J. Collins, R. G. Derwent, R. M. Doherty, J. Drevet, H. J. Eskes, A. M. Fiore, M. Gauss, D. A. Hauglustaine, L. W. Horowitz, I. S. A. Isaksen, M. C. Krol, J.-F. Lamarque, M. G. Lawrence, V. Montanaro, J.-F. Müller, G. Pitari, M. J. Prather, J. A. Pyle, S. Rast, J. M. Rodriguez, M. G. Sanderson, N. H. Savage, D. T. Shindell, S. E. Strahan, K. Sudo, S. Szopa, 2006. Multi-model ensemble of present-day and near-future tropospheric ozone. *J. Geophys. Res.*, **111**, doi:10.1029/2005JD006338.

Thompson, D. W. J, and J. M. Wallace, 1998. The Arctic Oscillation signature in the wintertime geopotential height and temperature fields, *Geophys. Res. Lett.*, **25**, 1297–1300.

Thompson, D. W. J., and J. M. Wallace, 2000. Annular modes in the extratropical circulation. Part I: Month-to-month variability, *J. Clim.*, **13**, 1000–1016.

Thompson, D. W. J., M. P. Baldwin, and J. M. Wallace, 2002. Stratospheric connection to northern hemisphere wintertime weather: Implications for prediction, *J. Climate*, **15**, 1421–1428.

Thompson, D. W. J., and S. Solomon, 2002. Interpretation of recent southern hemisphere climate change. *Science*, **296**, 895–899.

Thompson, D. W. J., M. P. Baldwin, and S. Solomon, 2005. Stratosphere-troposphere coupling in the southern hemisphere. *J. Atmos. Sci.*, **62**, 708–715.

Tourpali, K., A. F. Bais, A. Kazantzidis, C. S. Zerefos, H. Akiyoshi, J. Austin, C. Brühl, N. Butchart, M. P. Chipperfield, M. Dameris, M. Deushi, V. Eyring, M. A. Giorgetta, D. E. Kinnison, E. Mancini, D. R. Marsh, T. Nagashima, G. Pitari, D. A. Plummer, E.

Rozanov, K. Shibata, and W. Tian, 2009. Clear sky UV simulations in the 21st century based on ozone and temperature projections from Chemistry-Climate Models, *Atmos. Chem. Phys.*, **9**, 1165-1172**.**

Uppala, S.M., P.W. Kållberg, A.J. Simmons, U. Andrae, V. Da Costa Bechtold, M. Fiorino, J.K. Gibson, J. Haseler, A. Hernandez, G.A. Kelly, X. Li, K. Onogi, S. Saarinen, N. Sokka, R.P. Allan, E. Andersson, K. Arpe, M.A. Balmaseda, A.C.M. Beljaars, L. Van De Berg, J. Bidlot, N. Bormann, S. Caires, F. Chevallier, A. Dethof, M. Dragosavac, M. Fisher, M. Fuentes, S. Hagemann, E. Hólm, B.J. Hoskins, L. Isaksen, P.A.E.M. Janssen, R. Jenne, A.P. Mcnally, J.-F. Mahfouf, J.-J. Morcrette, N.A. Rayner, R. W. Saunders, P. Simon, A. Sterl, K.E. Trenberth, A. Untch, D. Vasiljevic, P. Viterbo, and J. Woollen, 2005. The ERA-40 reanalysis, *Quart. J. Royal. Meteorol. Soc.*, **131**, 2961–3012.

Waugh, D. W., L. Oman, P. A. Newman, R. S. Stolarski, S. Pawson, J. E. Nielsen, and J. Perlwitz, 2009. Effect of zonal asymmetries in stratospheric ozone on simulated Southern Hemisphere climate trends , *Geophys. Res. Lett.*, **36**, L18701, doi:10.1029/2009GL040419.

World Meteorological Organisation Scientific assessment of ozone depletion, Global Ozone Res. Monit. Rep. 16, Geneva, 1992.

World Meteorological Organization (WMO)/United Nations Environment Programme (UNEP), 2007. *Scientific Assessment of Ozone Depletion: 2006*, World Meteorological Organization, Global Ozone Research and Monitoring Project, Report No. 50, Geneva, Switzerland.

Appendix A

List of Acronyms

AGCM – Atmospheric General Circulation Model

AM2-LM2 – Atmosphere and Land Model 2

AMIP II – Atmospheric Model Intercomparison Project II

AMTRAC3 – Atmospheric Model with Transport and Chemistry 3

AOGCM – atmosphere-ocean general circulation model

ARPEGE -- (French climate model)

AR – Assessment Round (of IPCC)

ASAP – Assessment of Stratospheric Aerosol Properties

ATTILA -- Atmospheric Tracer Transport In a LAgrangian model

BC – black carbon

BDC – Brewer-Dobson Circulation

CAM3.5 – Community Atmosphere Model 3.5

CCM – chemistry-climate model

CCM2 --- Community Climate Model 2

CCCma – Canadian Centre for Climate Modelling and Analysis

CCSRNIES – Center for Climate-Systems Research – National Institute of Environamental Studies

CFC – chloro-fluoro-carbon

CGCM – Coupled General Circulation Model

CGER – Center for Global Environmental Research

CLASS – Canadian Land Surface Scheme

CLM – Community Land Model

CLSM – Catchment Land Surface Model

CMAM – Canadian Middle Atmosphere Model

CNRM-ACM – Centre National de Recherches Météorologiques – ARPEGE Climat coupled MOCAGE

CNRS -- Centre National de la Recherche Scientifique

CTM – chemistry-transport model

DLR – Deutsches Zentrum für Luft- und Raumfahrt / German Aerospace Center

DMS – dimethyl sulfide

DOM – Discrete Ordinate Method

E39CA – ECHAM4.L39(DLR)/CHEM/-ATTILA

ECMWF – European Centre for Medium-range Weather Forecasts

ECHAM – European Centre Hamburg Model

EMAC – ECHAM5 Middle-Atmosphere with Chemistry

ENSO – El Nino / Southern Oscillation

GAME -- Groupe d'étude de l'Atmosphère MEtéorologique

GCM – global circulation model

GWD – gravity-wave drag

GEOSCCM – Goddard Earth Observing System – Chemistry-Climate Model

GFDL – Geophysical Fluid Dynamics Laboratry

GHG – greenhouse gas

GISS – Goddard Institute for Space Studies

GSFC – Goddard Space Flight Center

HadAM3 – Hadley Centre Atmosphere Model 3

HadGEM1 – Hadley Centre Global Environment Model 1

HadISST – Hadley Centre Ice and Sea-Surface Temperature dataset

HCFC – hydro-chloro-fluoro-carbon

IAC – Institute for Atmosphere and Climate

IFS – Integrated Forecast System

IIASA -- International Institute for Applied Systems Analysis

IPCC – Intergovernmental Panel on Climate Change

IUPAC -- International Union of Pure and Applied Chemistry

JPL – Jet Propulsion Laboratory

LBC – lower-boundary condition

LMDZrepro – Laboratoire de Météorologie Dynamique Zoom – REPROBUS

LTE – local thermodynamic equilibrium

MECCA -- Module Efficiently Calculating the Chemistry of the Atmosphere

MESSy – Modular Earth Submodel System

METO – Met Office

MEZON – Model for Evaluation of oZoNe trends

MIROC -- Model for Interdisciplinary Research On Climate

MOCAGE – (CTM developed by MétéoFrance)

MOSES – MetOffice Surface Exchange Scheme

MOZART -- Model for OZone And Related chemical Tracers

MPI-C – Max-Planck-Institute for Chemistry

MRI – Meteorological Research Institute

NASA – National Aeronautics and Space Administration

NAT – nitric acid trihydrate

NCAR – National Center for Atmospheric Research

NCOM – Naval Coastal Ocean Model

NIWA – National Institute of Water and Atmospheric Research

NMHC – non-methane hydrocarbon

ODS – ozone-depleting substance

OGCM – ocean general circulation model

ORCHIDEE – (French Global Land Surface Model)

PBL – planetary boundary layer

PMOD/WRC – Physical-Meteorological Observatory Davos / World Radiation Center

PSC – polar stratospheric cloud

PRM – piecewise rational method

QBO – quasi-biennial oscillation

RETRO – REanalysis of the TROpospheric chemical composition over the past 40 years

RRTM – Rapid Radiative Transfer Model

SAD – surface area density or sulphuric acid dihydrate

SAGE – Stratospheric Aerosol and Gas Experiment

SOCOL – Solar-Climate-Ozone Links

SPARC – Stratospheric Processes and their Role in Climate

SPE – solar proton event

SRES – Special Report on Emission Scenarios

SS – sea salt

SST – sea-surface temperature

SSW – sudden stratospheric warming

STS – supercooled ternary solution

SZA – solar zenith angle

UCAM – University of Cambridge

UIUC – University of Illinois at Urbana-Champaign

ULAQ – Università degli Studi L'Aquila

UMETRAC – Unified Model with Eulerian Transport and Atmospheric Chemistry

UMSLIMCAT – Unified Model – SLIMCAT

UMUKCA – Unified Model / U. K. Chemistry and Aerosols Module

UTLS – Upper Troposphere / Lower Stratosphere

UV – ultra-violet

VOC – volatile organic compound

WACCM – Whole-Atmosphere Chemistry-Climate Model

WCRP – World Climate Research Program

WMGHG – well-mixed greenhouse gas

WMO – World Meteorological Organization

Appendix B

Time Series Additive-Model Analysis

Lead Authors: John Scinocca & John Austin

Co-authors: Trevor Bailey
Luke Oman
David Plummer
David Stephenson
Hamish Struthers

In this appendix we provide a detailed description of the TSAM analysis, focusing on its development and application to CCMVal-1 and CCMVal-2 ozone-related time series in this chapter. This material is complemented by the supplement to Chapter 9 in which a more complete set of TSAM diagnostics is included, along with an analysis of its sensitivity to outliers and a comparison with the simpler 1:2:1 filtering employed by previous studies of CCMVal-1 time series.

B.1 Multi-Model Ensemble Analysis

The REF2 CCMVal-1 experiment (REF-A2) had a specified integration period of 1980-2050, while the current CCMVal-2 experiment (REF-B2) has a specified integration period of 1960-2100. In each inter-comparison project, ensembles of simulations were also requested. Designing a multi-model analysis of REF-A2 (CCMVal-1) and REF-B2 (CCMVal-2) time series for the purpose of making multi-model trend (MMT) estimates represents a significant challenge due to a number of complicating factors. Particularly,

1. The specified periods for the REF-A2 and REF-B2 experiments are not of equal extent. Furthermore, each modelling centre generally provided a subset of the requested data. For example, individual REF-A2 contributions ranged from ensembles of one, extending over the period 2000-2019, to ensembles of three, extending over the expanded period 1960-2100.
2. In general, large inter-model differences in various latitude bands make it difficult to compare directly the model time series of ozone and chlorine indices, as well as to compute multi-model trend estimates.

Here, we introduce a statistical modelling approach that uses nonparametric regression to estimate smooth

trends from the CCMVal raw data. The nonparametric regression uses a set of optimal thin plate splines to represent the trends and can be used to make formal inference (*e.g.,* calculate confidence and prediction intervals). As discussed in Section 9.2, the approach adopted here consists of three distinct steps: estimation of individual model trends (IMT), baseline adjustment of the trends, and the weighted combination of the individual model trends to produce a multi-model trend (MMT) estimate. In this appendix the development and application of this approach will be illustrated using the time series data presented in **Figure B.1**.

This data corresponds to the CCMVal-1 raw time series in Figure 7 of Eyring *et al.* (2007), which includes both REF-A1 and REF-A2 data for several of the models. The top panel (Figure B.1a) presents the March averaged total column ozone in the latitude band 60°N-90°N, while the bottom panel (Figure B.1b) presents the October averaged total column ozone in the latitude band 60°S-90°S.

B.2 Nonparametric estimation of the individual model trends

The time series $y_{jk}(t)$ of an ozone-related index, such as one of those displayed in Figure B.1, is additively modelled as the sum of a smooth unknown model-dependent trend, $h_j(t)$, and irregular normally-distributed noise:

$$y_{jk}(t) = h_j(t) + \varepsilon_{jk}(t), \qquad \text{(B.1)}$$

where the noise field

$$\varepsilon_{jk}(t) \sim N(0, \sigma^2) \qquad \text{(B.2)}$$

is assumed to be an independent normally distributed random variable with zero mean and variance σ^2, and the indices j and k respectively represent model and ensemble-member number. (Here, the ensemble index k extends over both REF-A1 and REF-A2 simulations for some models.) This is a nonparametric regression of the index on time. The regression is nonparametric because the function of time does not have a fixed functional form with explicit parameters. The noise term (Equation B.2), representing natural variability about the trend, is considered to be an independent normally distributed random variable; independent between different times, models, and runs. The variance of the noise is assumed to be constant over all models and runs. By fitting the trend to all the data rather than to each model separately, one can obtain better estimates of the noise variance (referred to as "borrowing strength").

The unknown smooth functions $h_j(t)$ are estimated by fitting the data to a finite set of smooth basis functions having optimal interpolating properties. This was done here by using the **gam()** function in the **mgcv** library of the R language (R Development Core Team, 2008). The default option was used, which fits the data to a set of thin plate regression splines, by maximising penalized likelihood to find the coefficients multiplying the basis functions. The smoothness of the basis functions is controlled by a smoothing parameter, which is chosen using a leave-one-out generalised cross-validation prediction approach (see Woods (2006) for more details). Unlike iterated 1:2:1 smoothing (*e.g.*, see Section 9S.3 of the supplement to

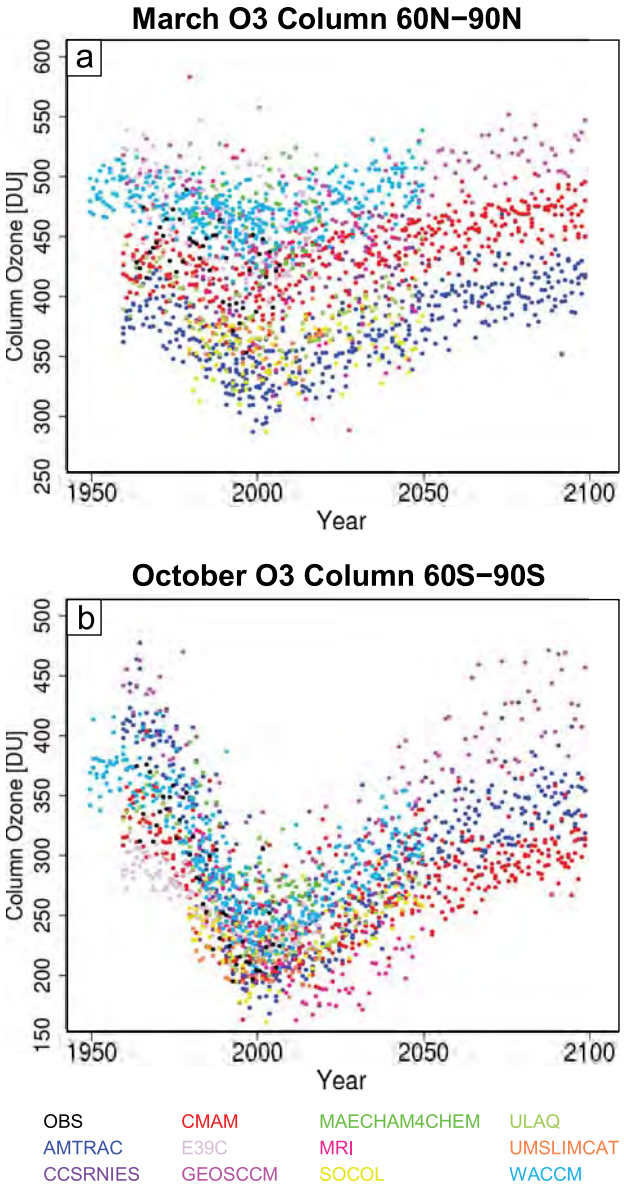

Figure B.1: CCMVal-1 time series of monthly averaged total column ozone in the latitude band 60°N-90°N for March (panel a) and in the latitude band 60°S-90°S for October (panel b). Following Eyring et al. (2007), these time series include REF-A1 data in addition to REF-A2 data for several of the models.

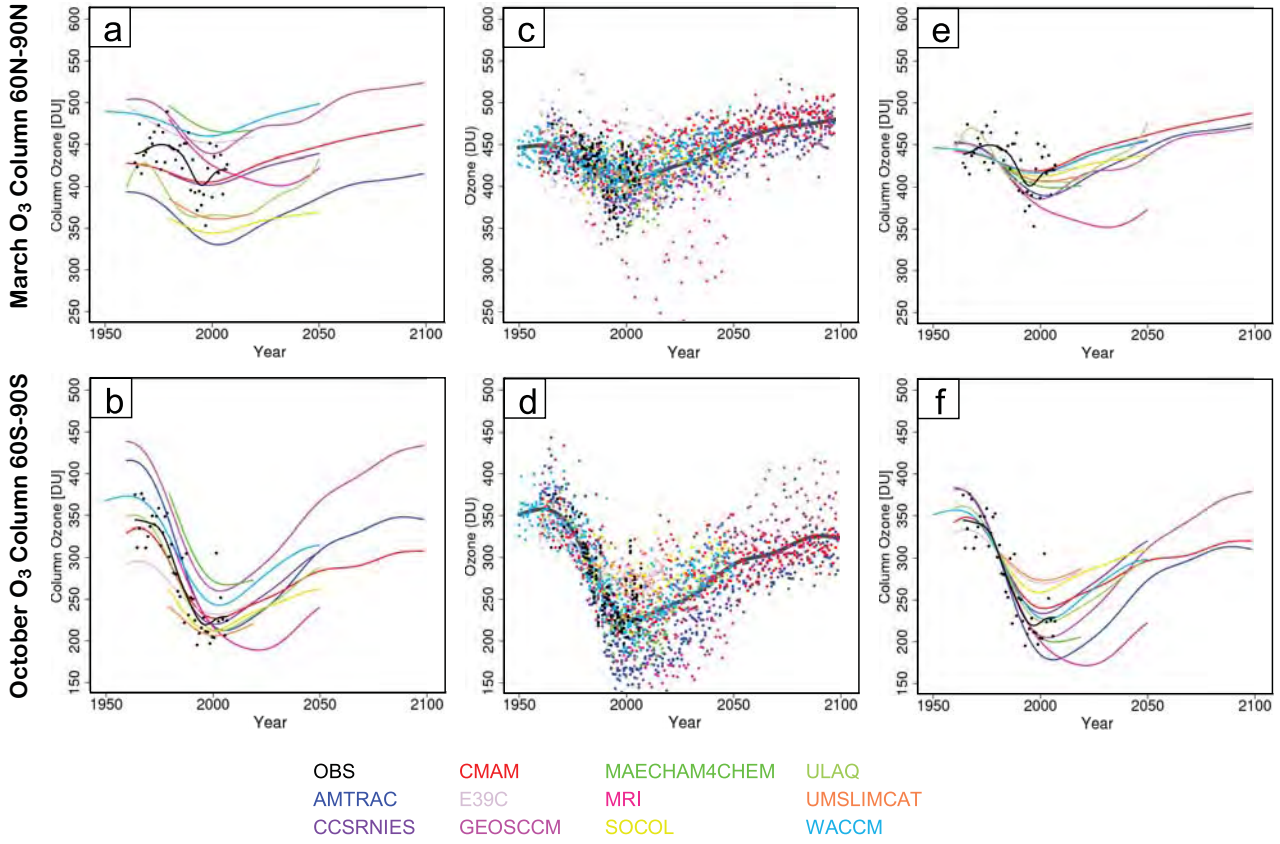

Figure B.2: Panels a and b: The initial estimate of the individual model trends $h_j(t)$ for the raw time series displayed in Figure B.1. This represents the first step in the TSAM analysis. Panels c and d: the 1980 baseline-adjusted time series data y'_{jk} following from (Equation B.7) with t_0 =1980. Panels e and f: The 1980 baseline-adjusted trend estimate $h'_j(t)$. This represents the second step in the TSAM analysis. The thick grey line in panels c and d represents the trend estimate $g'(t)$ for the simpler nonparametric additive model (9.9). For reference, following Eyring et al. (2007) smooth fits to the observations in these plots have been created by 30 iterations of a 1:2:1 filter (black lines).

Chapter 9), the thin plate splines are guaranteed to give smooth trend estimates and do not alter their properties at the ends of the series.

The first step in the TSAM analysis is to apply the nonparametric regression (Equation B.1) to the raw time series data. This is illustrated in panels a and b of **Figure B.2** by the IMT estimates $h_j(t)$ of the CCMVal-1 March 60°N-90°N and October 60°S-90°S total column ozone displayed in Figure B.1. (Note that, while the smooth trend estimates $h_j(t)$ extend over the full period (1950-2100), in Figure B.2a,b we have elected to display the $h_j(t)$ only over the period where data exists for each model.)

B.3 Baseline-adjustment of the trend estimates

The initial IMT estimates $h_j(t)$ in Figure B.2a, b reveal significant differences in the background values of column ozone - particularly in the Arctic (panel a). To facilitate a comparison of the trends across models, anomaly time series are constructed relative to a pre-ozone-hole baseline value of the index. While this is analogous to the procedure employed by Eyring *et al.* (2007), the smoothness of $h_j(t)$ allows a more robust definition of the baseline at a particular time t_0 (*i.e.*, $h_j(t_0)$), rather than from the average over some period about t_0. This results in the anomaly time series:

$$y_{jk}(t) - h_j(t). \qquad \text{(B.3)}$$

By construction, the anomaly time series (Equation B.3) is centred on a baseline value of zero at the time t_0. Here, we chose to have this baseline changed from zero to the multi-model mean of $h_j(t_0)$ resulting in the "t_0 baseline-adjusted time series":

$$y'_{jk}(t) = y_{jk} - h_j(t_0) + h(t_0) \qquad \text{(B.4)}$$

where

$$h(t_0) = \text{mean}_j[h_j(t_0)]. \qquad \text{(B.5)}$$

As discussed in Section 9.3, since the multi-model average of the IMT estimates $h(t_0)$ is a close approximation to the final multi-model trend estimate (MMT) derived in the third step of the TSAM analysis, the baseline adjustment may be viewed simply as forcing the anomaly time series to go roughly through the final MMT estimate at the reference date t_0.

The time series (B.4) contains all the information of (B.3) plus the multi-model average $h(t_0)$, which can be compared with observations. In the comparison of CCMVal-1 and CCMVal-2 we have used the baseline t_0 = 1980. Following (B.4), the 1980 baseline-adjusted time series data, y'_{jk} for the CCMVal-1 March 60°N-90°N and October 60°S-90°S total column ozone are displayed in Figure B.2c and d respectively. The corresponding 1980 baseline-adjusted non-parametric IMT estimates $h'_j(t)$ are presented in Figure B.2e and f. Following (B.1) and (B.4) the 1980 baseline-adjusted non-parametric smooth trend in our model is:

$$h'_j(t) = h_j(t) - h_j(t_0) + h(t_0) \qquad \text{(B.6)}$$

with

$$y'_{jk}(t) = h'_j(t) + \varepsilon_{jk}(t). \qquad \text{(B.7)}$$

Before moving on to the third step in the TSAM, we may ask if (9.8) represents one of the simplest models that satises the assumptions of our statistical model (*e.g.*, that the noise term $\varepsilon_{jk}(t)$ is independent from year-to-year, is normally distributed, and is drawn from the same underlying distribution with zero mean and similar variance). For example, we could have chosen the simpler nonparametric model:

$$y'_{jk}(t) = g'(t) + \hat{\varepsilon}_{jk}(t), \qquad \text{(B.8)}$$

where one trend estimate is made for all time series data instead of individual trend estimates for each model (B.7). This implicitly defines a different random noise component $\hat{\varepsilon}_{jk}(t)$. The nonparametric trend estimate $g'(t)$ is displayed as the thick grey line in panels c and d of Figure B.2. If (9.9) were a reasonable model for the data then, in addition to being an IMT, $g'(t)$ could also serve as the MMT thereby eliminating the need for the third step of the TSAM. Visual inspection of the smooth estimate $g'(t)$ to the 1980 baseline-adjusted time series y'_{jk} in Figure B.2c, d would suggest a reasonable fit. However, because we have built the analysis on a probabilistic model, the goodness of the $g'(t)$ and $h'_j(t)$ fits may be tested against the model's underlying assumptions.

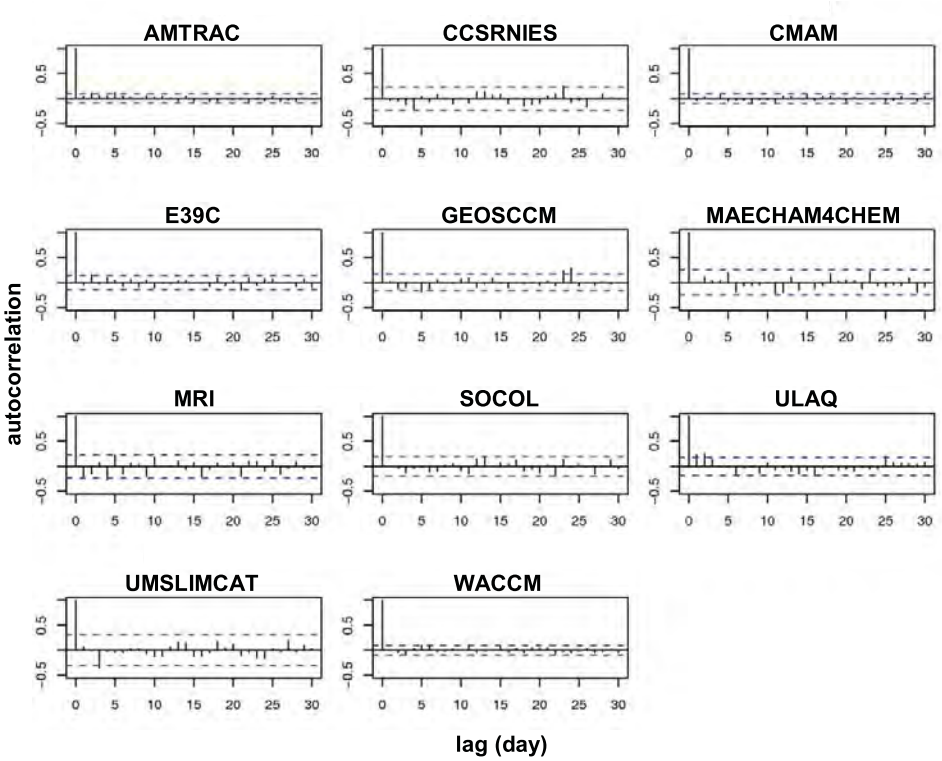

Figure B.3: Individual model autocorrelation functions for the residuals $\varepsilon_{jk}(t)$ for CCMVal-1 October total column ozone in the latitude band 60°S-90°S. This noise corresponds to the nonparametric model (9.8) with 1980 baseline trend estimates $h_j(t)$ displayed in Figure B.2f. The blue dashed lines represent 96% confidence limits for the sample autocorrelation function. This suggests that the assumption of year-to-year independence is a good one for the (B.7) model.

The year-to-year independence of the model noise term may be tested by calculating its autocorrelation function. In **Figure B.3** the autocorrelation function for the noise term $\varepsilon_{jk}(t)$ is displayed for each model for the nonparametric fit (B.7) to the CCMVal-1 October 60°S-90°S column ozone. The dashed blue lines in this figure represent 95% confidence limits. Lines that extend beyond these limits are considered to be sample correlations that are significantly different from zero. Inspection of all the models reveals that the assumption of year-to-year independence is a good one for the model (B.7). This is not, however, the case for the simpler model (B.8). The autocorrelation of the noise term $\hat{\varepsilon}_{jk}(t)$ is displayed in **Figure B.4** and displays significant violations of the assumption of year-to-year independence for several of the models.

Model assumptions related to the noise term may be further investigated by "notched box-and-whisker" plots. These are displayed for $\hat{\varepsilon}_{jk}(t)$ and $\varepsilon_{jk}(t)$ respectively in panels a and b of **Figure B.5** again for the CCMVal-1 October 60°S-90°S column ozone (see caption for details). From panel b we can see that the noise term $\varepsilon_{jk}(t)$ has a similar location and scale for each model, validating the model assumption that the residuals were drawn from the same distribution with zero mean and roughly the same variance. Again, the same cannot be said for the $\varepsilon_{jk}(t)$ residuals (panel a) suggesting that $g'(t)$ in (B.9) is not a good estimate of the trend.

We conclude, therefore, that (B.7) represents one of the simplest nonparametric additive models that is satisfied by the ozone indices considered in the two examples. (The same is basically true for the remainder of ozone-related indices analysed in Chapter 9).

B.4 Multi-model trend estimates

The final step of the TSAM analysis involves combining the IMT estimates $h'_j(t)$ to arrive at an MMT estimate:

$$h'(t) = \sum_j w_j(t) h'_j(t), \tag{B.9}$$

where the weights $w_j(t)$ have the properties

$$w_j(t) \geq 0 \text{ and } \sum_j w_j(t) = 1. \tag{B.10}$$

If the weights are assumed to be non-random, and the errors in the individual trends are assumed to be independent, then the standard error of the weighted sum is given by:

$$s^2_h(t) = \sum_j w^2_j(t) s^2_j(t), \tag{B.11}$$

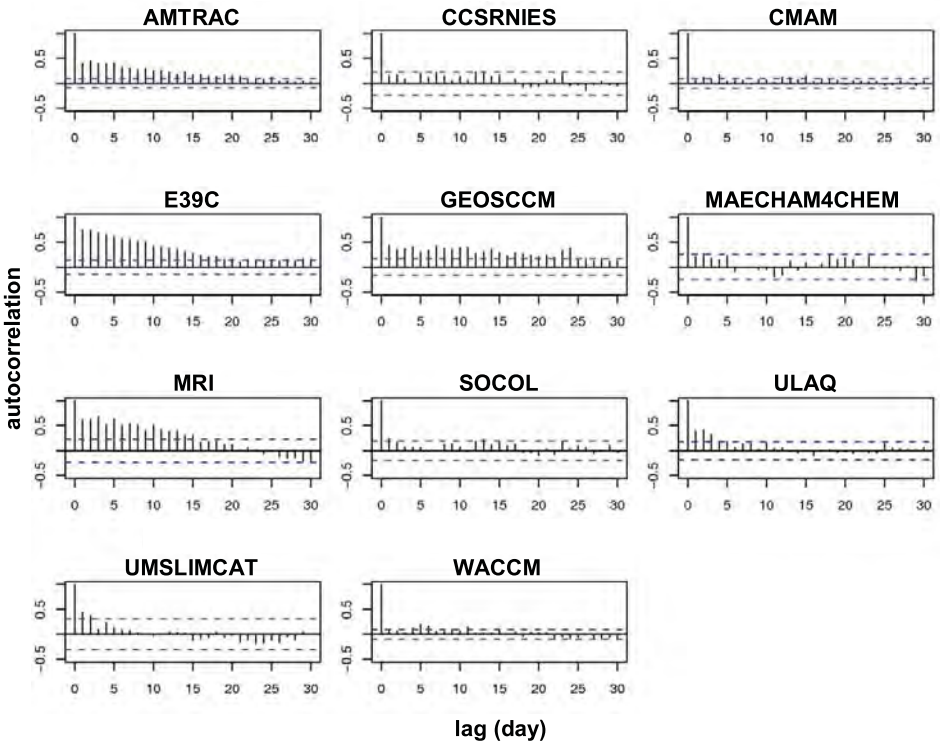

Figure B.4: Individual model autocorrelation functions for the noise term $\hat{\varepsilon}_{jk}(t)$ for CCMVal-1 October total column ozone in the latitude band 60°S-90°S. This noise corresponds to the simpler nonparametric model(9.9) with a 1980 baseline trend estimate g(t) displayed in Figure B.2d. The lines extending past the blue-dashed lines for several models indicates that the assumption of year-to-year independence is not well satisfied for the (B.8) model.

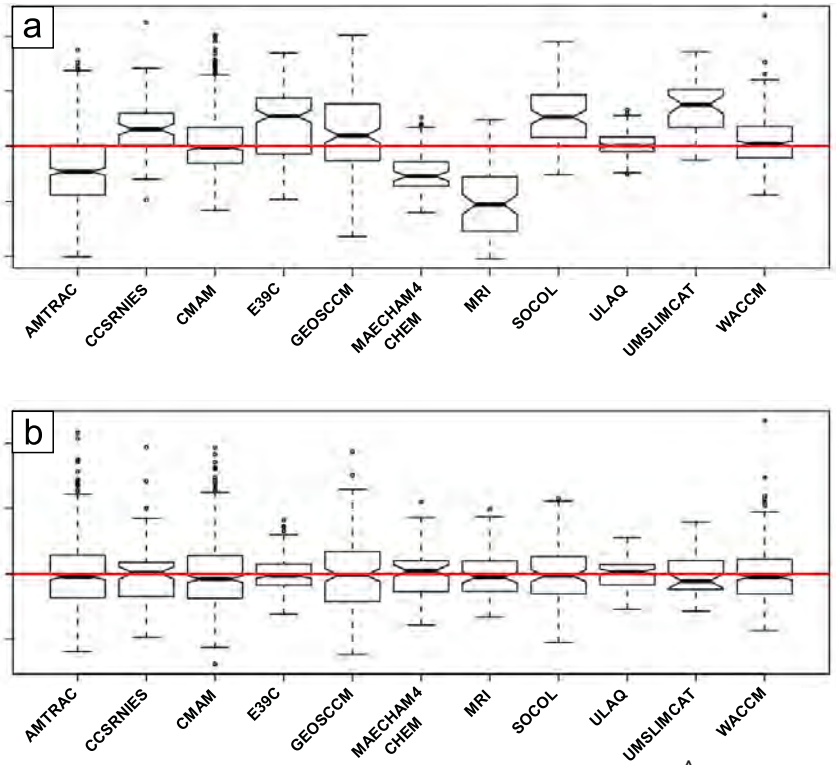

Figure B.5: Individual model notched box-and-whisker plots for the noise term $\hat{\varepsilon}_{jk}(t)$ corresponding to the simpler nonparametric additive model (B.8) (panel a) and for the noise term $\varepsilon_{jk}(t)$ corresponding to the nonparametric additive model (B.7). These apply to the CCMVal-1 October total column ozone in the latitude band 60°S-90°S. In these plots the central black line represents the median, the extent of the notches away from the median line indicates the 95% confidence interval of the median, the top and bottom of the boxes respectively represent the upper and lower quartiles, and the top and bottom whiskers extend out to 1.5 times the distance from the first to third quartiles. For the noise term $\varepsilon_{jk}(t)$ (panel b) the medians of all models fall within the notches and are close to zero. Also, the similar height of the boxes indicates that all models have a similar amount of variance away from the estimated trend $h'_j(t)$. For the noise term $\hat{\varepsilon}_{jk}(t)$, the means are significantly different and the inter-model variance is larger suggesting that (B.8) is not a suitable model for this data.

where $s_j(t)$ is the standard error of the trend estimate $h'_j(t)$, which can be calculated using standard expressions from linear regression (Woods, 2006). The standard error (B.11) can then be used to estimate the confidence and prediction intervals respectively as:

$$[h'(t) - 1.96s_h(t), h'(t) + 1.96s_h(t)] \qquad \text{(B.12)}$$

and

$$[h'(t) - 1.96\sqrt{(s^2_h(t) + s^2_\varepsilon)}, h'(t) + \sqrt{(s^2_h(t) + s^2_\varepsilon)}]. \qquad \text{(B.13)}$$

The 95% confidence interval in the trend gives the uncertainty in the trend estimate. In other words, there is a 95% chance that this interval will overlap the true trend. The interval is point-wise (rather than simultaneous) in that it represents the uncertainty in the trend at each year rather than being an interval for all probable trend curves over the whole period. The 95% prediction gives an idea of how much uncertainty their might be in a predicted index value for a particular year. In other words, there is a 95% chance that a particular index value on a specific year will lie in this interval. This interval is the combination of uncertainty in the trend estimate and the uncertainty due to natural interannual variability about the trend.

The specific choice of weights in (B.9) remains open. In general, we decide to base the construction of the weights on a statistical probability model with testable assumptions. Here, we have chosen a "random-effects" model to determine the weights. This model assumes that the trends for individual models $h'_j(t)$ are random samples from a "true" trend $\sim h'_j(t)$:

$$h'_j(t) = \sim h'_j(t) + \eta(t) \qquad \text{(B.14)}$$

where

$$\eta(t) \sim N(0, \lambda^2). \qquad \text{(B.15)}$$

The quantity λ^2 is included to account for additional variance between model trends that cannot be accounted for merely by sampling the uncertainty s^2_j. Using this random

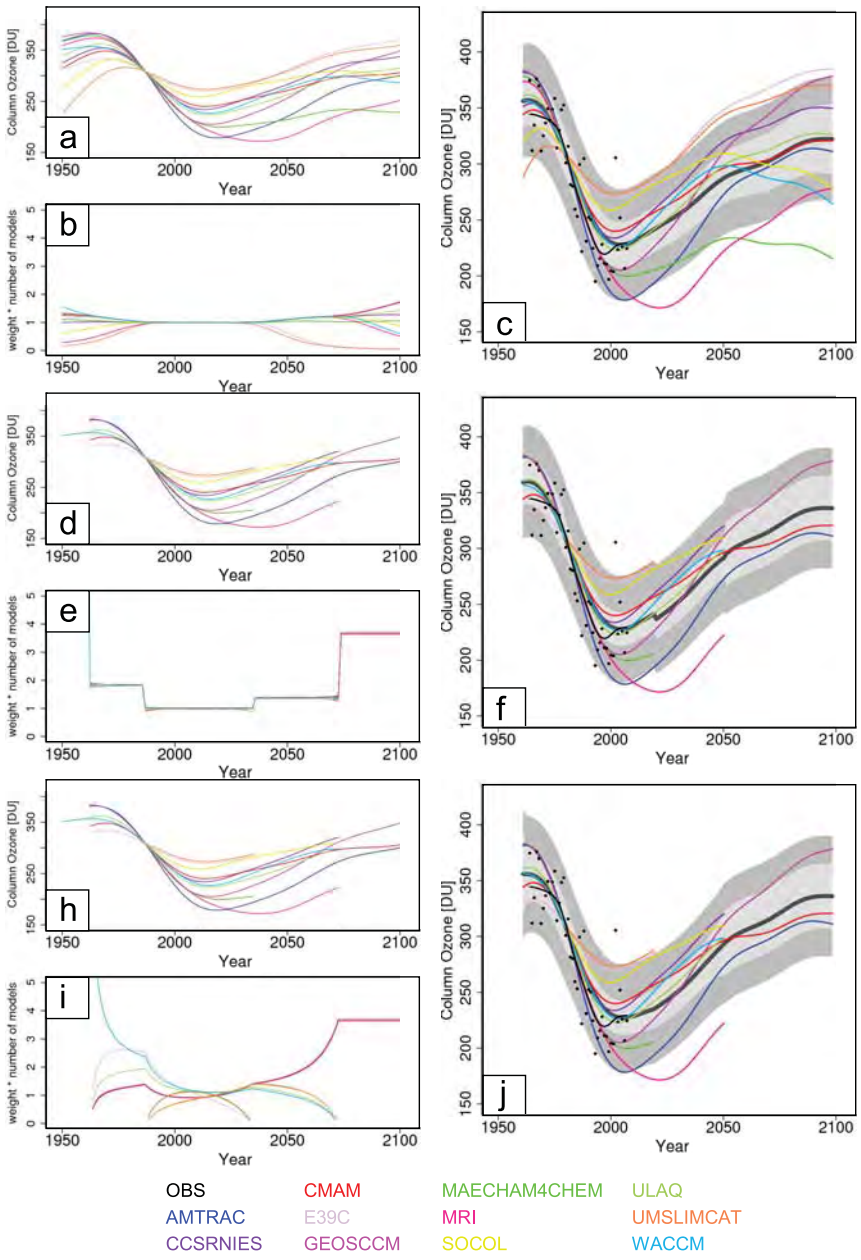

Figure B.6: For time series of CCMVal-1 October total column ozone in the latitude band 60°S-90°S are presented the individual model fits (panels a, d, and h), weights (panels b, e, and i), and trend (MMT) estimate (thick grey line in panels c, f, and j) for three approaches to determining the weights. Results from the "random-effects" model (B.17) are shown in panels a-c. One problem with this approach is that models can contribute to the final MMT estimate at times when no data exists of that model (i.e., in regions where $h'_j(t)$ represents an extrapolation). The introduction of prior weights (9.21) can help mitigate this problem. Results from the use of a simple on/offset of prior weights (having values of one where there is model data and zero where there is none) are presented in panels d-f. One artifact of this approach is that it causes discontinuities in the final MMT estimate. Finally, results from set of prior weights used for the present chapter, which employ a smoother quadratic taper from a value of 1 where time series data exists to a value of 0 where it is absent, is displayed in panels h-j.

effects model, (B.11) then generalises to:

$$s^2_h(t) = \sum_j w^2_j(t)(\lambda^2 + s^2_j(t)), \qquad \text{(B.16)}$$

which is used here to calculate intervals. Assuming this model is valid, a least-squares estimate of may be obtained from (B.9) employing the weights:

$$w_j(t) = w(t)/(\lambda^2 + s^2_j(t)) \qquad \text{(B.17)}$$

where

$$w^{-1}(t) = \sum_j (\lambda^2 + s^2_j(t))^{-1}. \qquad \text{(B.18)}$$

Specification of the weights $w_j(t)$ from (B.17) requires an estimate of the parameter λ^2. For this we have used the following iterative approach: An initial estimate of the true trend is obtained by calculating $h'_{\lambda=0}(t)$. Then, an iterative Newton-Raphson algorithm is employed to determine the λ that gives scaled residuals that have unit variance as is expected from (B.14):

$$\mathrm{var}\left(\frac{h'_j(t) - h'_{\lambda=0}(t)}{\sqrt{\lambda^2 + s^2_j(t)}} \right) = 1. \qquad \text{(B.19)}$$

Employing this model for the weights produces the MMT estimate $h'(t)$ for the 1980 baseline CCMVal-1 October 60°S-90°S column ozone displayed in **Figure B.6c**. The associated individual model trend estimates $h'_j(t)$ and weights $w_j(t)$ are respectively displayed in panels a and b of this figure. In this figure, the weights are scaled by the number of models so that a scaled weight of 1 implies a proportional contribution of that model to the MMT estimate.

While this formulation of weights provides a smooth final trend estimate $h'(t)$, for this example it highlights a potential problem - the individual model weights $w_j(t)$ are very insensitive to the absence of data in the original time series. For example, the time series for the MAECHAM4CHEM model (green) extends only over the period 1980-2019 (see Figure B.2). Its scaled weight, however, has a value of roughly 1 over the entire period 1960-2100 suggesting significant contributions of its trend estimate $h'_j(t)$ at times when there are no model data. The original idea behind this model for the weights was that the natural increase in standard errors $s^2_j(t)$ in the region where $h'_j(t)$ is extrapolated beyond the model data would cause the weights to decrease naturally towards zero. While Figure B.6b indicates that there is some tendency for the weights to display this behaviour, it clearly remains unphysical.

To correct this unphysical behaviour, we introduce the concept of prior weights $w^p_j(t)$ into the formulation such that the final weights now have the form:

$$w^p_j(t) = \frac{w^p_j(t) w_j(t)}{\sum_{j'} w^p_{j'}(t) w_{j'}(t)}, \qquad \text{(B.20)}$$

(with $w'_j(t)$ implicitly replacing $w_j(t)$ in expressions (B.11) and (B.17)). An example set of prior weights would be the "on/off" set: $w^p_j(t) = 1$ at times t when raw time series data exist for model j and $w^p_j(t) = 0$ otherwise. This prescription is illustrated in panels d-f of Figure B.6. It corrects the unphysical behaviour identified when $w_j(t)$ of (B.17) is used alone. However, this on/off prescription is still problematic in that it causes discontinuities in the MMT estimate Figure B.6f. The set of prior weights used for the Chapter 9 employs a smoother quadratic taper, from a value of 1 where time series data exists to a value of 0 where it is absent:

$$w^p_j(t) = \begin{cases} 1 - z^2 & \text{if } 0 \le z^2 \le 1 \\ 0 & \text{otherwise} \end{cases}, \qquad \text{(B.21)}$$

where

$$z = -1 + 2(t - t_{j,min})/(t_{j,max} - t_{j,min}), \qquad \text{(B.22)}$$

and where $[t_{j,min}, t_{j,max}]$ defines the period within which data exist for model j. This scheme is illustrated in panels h-j of Figure B.6.

Finally, the formulation of prior weights (B.20) allows a natural entry point for the specification of prior, time-independent, model weights based on performance metrics. Such metric based weights would take on values in the range [0, 1] and simply multiply $w^p_j(t)$ in the expression (B.20).

References

Eyring, V., D. W. Waugh, G. E. Bodecker, E. Cordero, H. Akiyoshi, J. Austin, S. R. Beagley, B. A. Boville, P. Braesicke, C. Brhl, N. Butchart, M. P. Chippereld, M. Dameris, R. Deckert, M. Deushi, S. M. Frith, R. R. Garcia, A. Gettelman, M. A. Giorgetta, D. E. Kinnison, E. Mancini, E. Manzini, D. R. Marsh, S. Matthes, T. Nagashima, P. A. Newman, J. E. Nielsen, S. Pawson, G. Pitari, D. A. Plummer, E. Rozanov, M. Schraner, J. F. Scinocca, K. Semeniuk, T. G. Shepherd, K. Shibata, B. Steil, R. S. Stolaarski, W. Tian, and M. Yoshiki, 2007: Multi-model projections of ozone recovery in the 21st century, 2007. *J. Geophys. Res.*, **112**, doi:10.1029/2006JD008332.

R Development Core Team, 2008. R: A language and environment for statistical computing. R Foundation for Statistical Computing, Vienna, Austria. ISBN 3-900051-07-0, URL http://www.R-project.org.

Woods, S.N., 2006. Generalized Additive Models: An Introduction with R, Chapman & Hall/CRC, London.